The Plasma Environments of Saturn's Moons Enceladus and Rhea: Modeling of Cassini Magnetic Field Data

Von der Fakultät für Elektrotechnik, Informationstechnik, Physik
der Technischen Universität Carolo-Wilhelmina
zu Braunschweig
zur Erlangung des Grades eines
Doktors der Naturwissenschaften
(Dr.rer.nat.)
genehmigte
Dissertation

von Hendrik Alexander Kriegel
aus Braunschweig

Bibliografische Information der Deutschen Nationalbibliothek

Die Deutsche Nationalbibliothek verzeichnet diese Publikation in der Deutschen Nationalbibliografie; detaillierte bibliografische Daten sind im Internet über `http://dnb.d-nb.de` abrufbar.

1. Referentin oder Referent: Prof. Dr. U. Motschmann
2. Referentin oder Referent: Prof. Dr. J. Saur
eingereicht am: 17. Dezember 2013
mündliche Prüfung (Disputation) am: 6. März 2014

ISBN 978-3-944072-02-9

uni-edition GmbH 2014
http://www.uni-edition.de

Printed in Germany

Vorveröffentlichungen der Dissertation

Teilergebnisse aus dieser Arbeit wurden mit Genehmigung der Fakultät für Elektrotechnik, Informationstechnik, Physik, vertreten durch den Mentor der Arbeit, in folgenden Beiträgen vorab veröffentlicht:

Publikationen

- Simon, S., J. Saur, **H. Kriegel**, F. M. Neubauer, U. Motschmann, and M. K. Dougherty (2011a), Influence of negatively charged plume grains and hemisphere coupling currents on the structure of Enceladus' Alfvén wings: Analytical modeling of Cassini magnetometer observations, *Journal of Geophysical Research (Space Physics)*, *116*, A04221, doi: 10.1029/2010JA016338
  The author's contribution: H.K. proposed the idea that the dust is responsible for the puzzling magnetic field structures and contributed to the interpretation of the results. The proof of the dust hypothesis and the analytical interaction model presented in this paper were developed by S.S. and J.S.

- **Kriegel, H.**, S. Simon, U. Motschmann, J. Saur, F. M. Neubauer, A. M. Persoon, M. K. Dougherty, and D. A. Gurnett (2011), Influence of negatively charged plume grains on the structure of Enceladus' Alfvén wings: Hybrid simulations versus Cassini Magnetometer data, *Journal of Geophysical Research (Space Physics)*, *116*, A10223, doi: 10.1029/2011JA016842
  The author's contribution: H.K. performed and analyzed the simulations, created the figures and wrote the manuscript of the article with the help of the co-authors.

- Simon, S. and **Kriegel, H.**, Saur, J., Wennmacher, A., Neubauer, F. M., Roussos, E., Motschmann, U. and Dougherty, M. K. (2012), Analysis of Cassini magnetic field observations over the poles of Rhea, *Journal of Geophysical Research (Space Physics)*, *117*, A07211, doi: 10.1029/2012JA017747
  The author's contribution: S.S. and H.K. contributed equally to this work: H.K. proposed the idea that a current in the wake generates the field perturbations and performed the simulations. Further, H.K. created the figures of the simulation results and helped in article writing.

- **Kriegel, H.**, S. Simon, P. Meier, U. Motschmann, J. Saur, A. Wennmacher, D. F. Strobel, and M. K. Dougherty (2014), Ion densities and magnetic signatures of dust pick-up at Enceladus, *Journal of Geophysical Research: Space Physics*, pp. n/a–n/a, doi: 10.1002/2013JA019440
  The author's contribution: H.K. performed and analyzed the simulations, created the figures and wrote the manuscript of the article with the help of the co-authors.

Tagungsbeiträge

- Kriegel, H., S. Simon, J. Müller, U. Motschmann, J. Saur,K. Glassmeier, and M. K. Dougherty, Hybrid Simulations of the Enceladus Plasma Interaction and Comparison with Cassini MAG Data, *Magnetospheres of the Outer Planets 2009, Köln, 27. - 31. Juli 2009*, (Vortrag)

- Kriegel, H., S. Simon, U. M. Motschmann, J. S. Saur, J. Mueller, C. Koenders, K. Glassmeier, and M. K. Dougherty, Impact of ion-neutral chemistry in the Enceladus plume on the global plasma interaction: a hybrid simulation approach, *AGU Fall Meeting 2009, San Francisco, 14.–18. Dezember 2009*, p. C1141, (Poster)

- Kriegel, H., S. Simon, U. Motschmann, J. Saur, J. Mueller, F. M. Neubauer, D. F. Strobel, K.-H. Glassmeier, and M. K. Dougherty , Enceladus' variable magnetospheric interaction: a hybrid simulation study, *EGU General Assembly 2010, Wien, 2. – 7. Mai 2010*, p. 2860, (Poster)

- Kriegel, H., Hybrid simulations of moon-magnetosphere interactions at Saturn, *AGU Fall Meeting 2010, San Francisco, 13. –17. Dezember 2010*, p. D5, (**eingeladener** Vortrag, ausgezeichnet mit dem "*Outstanding Student Paper Award*")

- Kriegel, H., Simon, S., Müller, J., Motschmann, U., Saur, J., Neubauer, F. M. Hybrid-Simulationen von Mond-Magnetosphären-Wechselwirkungen bei Saturn, *Jahrestagung der DGG gemeinsam mit der Arbeitsgemeinschaft Extraterrestrische Forschung und dem Fachverband Extraterrestrische Physik der DPG, Köln, 21. – 24. Februar 2011*, (Vortrag)

- Kriegel, H., S. Simon, U. Motschmann, J. Saur, F. M. Neubauer, A. M. Persoon, M. K. Dougherty, and D. A. Gurnett, Influence of negatively charged plume grains on the structure of Enceladus' Alfven wings: hybrid simulations versus Cassini MAG data, *Magnetospheres of the Outer Planets 2011, Boston, 11. – 15. Juli 2011*, (Vortrag)

- Kriegel, H. and Simon, S. and Motschmann, U. M. and Saur, J. and Neubauer, F. M. and Schmidt, J. and Teolis, B. D. and Dougherty, M. K., Hybrid simulations of Enceladus' plasma interaction: a multi-instrument survey, *AGU Fall Meeting 2011, San Francisco, 5. – 9. Dezember 2011*, B2018, (Vortrag)

- Kriegel, H. and Simon, S. and Motschmann, U. and Saur, J. and Neubauer, F. M., Hybrid simulations of dust-plasma interactions at Enceladus and comparison with Cassini data, *European Planetary Science Congress 2012, Madrid, 23. –28. September 2012* , 111, Link, (Vortrag)

- Kriegel, H., The impact of Enceladus' dust plume on the magnetic field and plasma, *AGU Fall Meeting 2012, San Francisco, 3.–7. Dezember*, (**eingeladener** Vortrag)

- Kriegel, H., Simulations of plasma-dust-neutral interactions at Enceladus, *Magnetospheres of the Outer Planets 2013, Athen, 8.–12. Juli 2013*, (**eingeladener** Vortrag)

Contents

Abstract

One of the most fascinating discoveries of the Cassini mission was the extended plume of water vapor and ice grains below Saturn's small moon Enceladus. The plume originates from geyser-like jets that are probably fed by a subsurface ocean of liquid water. These jets are located within surface fractures at the moon's south polar regions, the so-called "tiger stripes". After leaving their sources, the neutrals are ionized by means of photoionization and charge exchange with Saturn's magnetospheric plasma, thereby generating currents which perturb the plasma flow as well as Saturn's dipolar magnetic field. More precisely, these currents are closed by a system of field-aligned currents, the Alfvén wing.

In this thesis, analytical models as well as numerical simulations by means of the hybrid code A.I.K.E.F. (Adaptive Ion-Kinetic Electron-Fluid) are applied to study the interaction of the magnetospheric plasma with the Enceladean plume. In particular, the magnetic field perturbations generated by the interaction are analyzed and the simulation results are compared with Cassini Magnetometer (MAG) data obtained during the 20 Enceladus flybys (labeled E0 – E19), which took place between 2005 and 2013.

In a first study, it is shown that electron absorption by dust leads to a negative sign of the Hall conductivity and an associated reversal of the Hall current, which is referred to as the "Anti-Hall effect". The resulting twist of the magnetic field has been observed during all targeted Enceladus flybys so far. When including the dust, the simulations are in quantitative agreement with Cassini MAG data.

In a second study, the plasma simulations are combined with Monte-Carlo simulations of the 3D profiles of the water and dust plumes. Thereby, the improved model for the first time includes the effect of the distorted electromagnetic fields on the motion of the charged dust grains. Furthermore, the obtained neutral plume profiles are in excellent agreement with Cassini data, allowing to quantitatively analyze the ion densities within the plume. It is also demonstrated that the magnetic field signatures indicate the pick-up of negatively charged nanograins.

In addition, Cassini magnetic field observations from the only two polar flybys of Saturn's largest icy satellite Rhea are analyzed (R2 on 02 March 2010 and R3 on 11 January 2011). In-situ observations of exospheric neutral gas suggest Rhea to be embedded in a tenuous gas envelope. However, the interaction of this gas with the magnetospheric plasma does not cause any measurable contributions to the magnetic field draping pattern detected above the poles of the moon. Instead, it is shown that the finite length of Rhea's wake leads to a diamagnetic current that is responsible for generating a weak Alfvén wing pattern which has been detected by the Cassini spacecraft during the R2 and R3 encounters.

Kurzzusammenfassung

Eine der spektakulärsten Entdeckungen der Cassini-Mission war die Beobachtung einer großen Wolke aus Wasserdampf und nm- bis μm-großen Eispartikeln unterhalb von Saturns kleinem Eismond Enceladus, des sogenannten "Plumes". Dieser wird von geysirartigen Jets gebildet, die sich in Schluchten in der Südpolarregion, den sogenannten "Tigerstreifen", befinden und die vermutlich durch einen unterirdischen Ozean aus flüssigem Wasser gespeist werden. Nach dem Ausströmen werden die Neutralgasmoleküle durch Photoionisation und Ladungsaustausch mit Saturns magnetosphärischem Plasma ionisiert, wodurch sie Ströme erzeugen, die sowohl das Plasma als auch Saturns magnetisches Dipolfeld beeinflussen. Genauer gesagt werden diese Ströme durch ein System von feldparallelen Strömen, dem Alfvén-Flügel, geschlossen.

Das Ziel dieser Arbeit ist die Untersuchung der Wechselwirkung von Saturns magnetosphärischem Plasma mit Enceladus und seinem Plume. Hierzu werden sowohl analytische Modelle als auch numerische Simulationen mittels des Hybrid-Codes (Adaptive Ion-Kinetic Electron-Fluid) verwendet. Insbesondere werden die durch die Wechselwirkung erzeugten Magnetfeldstrukturen untersucht und die Ergebnisse mit Cassini Magnetometer (MAG) Messungen von den 20 Enceladus-Vorbeiflügen (E0 – E19), die zwischen 2005 und 2013 stattfanden, verglichen.

In einer ersten Studie wird gezeigt, dass die Absorption von Elektronen durch den Staub zu einem negativen Vorzeichen der Hall-Leitfähigkeit und einer damit verbundenen Umkehr des Hall-Stroms führt. Dieser Effekt wurde von uns "Anti-Hall Effekt" getauft. Die daraus resultierende Verdrehung der Magnetfeldlinien innerhalb des Alfvén-Flügels wurde während aller Enceladus-Vorbeiflüge gemessen. Durch die Einbeziehung des Staubes stimmen die Simulationsergebnisse quantitativ mit Cassini MAG-Daten überein.

In einer zweiten Studie werden die Plasmasimulationen mit Monte-Carlo Simulationen der 3D-Struktur des Neutralgas- und Staubplumes kombiniert. Dadurch berücksichtigt das Modell erstmalig den Einfluss der gestörten elektromagnetischen Felder auf die Bewegung der geladenen Staubteilchen. Darüber hinaus ist die Übereinstimmung der aus den Simulationen resultierenden Struktur des Neutralgasplumes mit Cassini-Messungen sehr gut, was eine quantitative Analyse der Ionendichten im Plume ermöglicht. Es wird zudem gezeigt, dass die gemessenen Magnetfeldsignaturen auf den Pick-up von negativ geladenen Nanoteilchen hinweisen.

Des Weiteren werden Magnetfeldmessungen von Cassini von den zwei einzigen polaren Vorbeiflügen an Saturns zweitgrößtem Mond Rhea (R2 am 2. März 2010 und R3 am 11. Januar 2011) analysiert. In-situ-Beobachtungen von exosphärischem Neutralgas zeigen, dass Rhea von einer dünnen Neutralgashülle umgeben ist. Die Wechselwirkung des Plas-

mas mit dem Neutralgas verursacht jedoch keine nennenswerten Magnetfeldstörungen über Rheas Polen. Stattdessen wird gezeigt, dass die endliche Länge von Rheas Plasma-Wake zu einem diamagnetischen Strom führt. Dieser Strom erzeugt wiederum einen schwachen Alfvén-Flügel, dessen Magnetfeldsignatur von Cassini während der R2- und R3-Vorbeiflüge detektiert wurde.

1 Introduction

Out of the 62 known Saturnian moons[1], the seven major ones have already been discovered in the 17th and 18th century. While Titan has first been observed by Christiaan Huygens in 1655, Saturn's second largest moon, Rhea, was discovered on 23 December 1672 by Giovanni Cassini along with Dione, Tethys and Iapetus. The inner satellites Enceladus and Mimas were discovered about 100 years later on 28 August 1789 and 17 September 1789, respectively, by Sir William Herschel [*Herschel* 1790]. However, it was not before 1847 that the current names of the moons were proposed by Herschel's son John [*Herschel* 1847]:

> "As Saturn devoured his children, his family could not be resembled round him, so that the choice lay among his brothers and sisters, the Titans and Titanesses. The name (...) Titan seemed to be indicated by the superior size of the Huygenian, while the three female appellatives (Rhea, Dione and Tethys) class together the three intermediate Cassinian satellites. The minute interior satellites (Enceladus and Mimas) seemed appropriately characterized by a return to male appellatives, chosen from a younger and inferior (though still superhuman) brood."

The first close-up images of these Titanesses and Titans as well as Saturn itself were captured during the flybys of the two Voyager spacecrafts in the 1980s. To further increase the knowledge of the giant planet and its moons and rings, the US *National Aeronautics and Space Administration* (NASA), the *European Space Agency* (ESA) and Italian space agency *Agenzia Spaziale Italiana* (ASI) designed the joint mission *Cassini-Huygens*. Launched in 1997, the spacecraft arrived at Saturn on 1 July 2004. On 14 January 2005, the Huygens probe was successfully delivered to Titan. The Cassini orbiter – equipped with twelve scientific instruments – completed its initial four-year prime mission of exploration in the Saturnian system in June 2008. The subsequent first extended mission, called the Cassini Equinox Mission, lasted until September 2010, while the second extended mission "Solstice" (named after the Saturnian summer solstice in May 2017) will hopefully be continued until September 2017 with ongoing success.

This thesis focuses on two particular members of Saturn's family of moons, namely the icy satellites Enceladus and Rhea. In addition, a tiny part of this work is dedicated to Enceladus' neighbor Dione. Although Enceladus was called a 'minute and inferior satellite' by John Herschel, this view has changed considerably with the spectacular discovery of the Enceladus plume – a large cloud of water vapor and ice grains emanating from the

[1] State: 2013

moon's south polar regions – by the Cassini Magnetometer [*Dougherty et al.* 2006]. The plume originates from geyser-like jets which are almost certainly being fed by a subsurface ocean of liquid water. The finding of present-day cryovolcanism promoted Enceladus to one of Cassini's main targets with 23 closed flybys scheduled for the whole mission. It turned out that Enceladus' plume constitutes the major source of neutral gas and plasma within the Saturnian magnetosphere. By chance, the name Enceladus is already linked to the moon's cryovolcanic activity. In Greek mythology, the giant Enceladus was defeated by the goddess Athena, who smashed the island of Silicy onto him. It is said that every now and then, Enceladus shifts his side in his grave, resulting in earthquakes and eruptions of Mount Etna[2]. Unlike Enceladus, Rhea is an inactive icy moon which possesses only a very thin atmosphere produced by sputtering [*Saur and Strobel* 2005]. The discovery that Rhea possesses a tenuous ring system on its own [*Jones et al.* 2008] could not be confirmed by optical observations [*Tiscareno et al.* 2010].

Enceladus and Rhea encircle the giant planet at distances of 3.95 and 8.74 Saturn radii (R_S), respectively. Both moons are therefore located well within Saturn's magnetosphere which has a sunward extent of about 20 R_S. Similar to Jupiter, the Saturnian magnetosphere is (at least partially) dominated by the fast rotation of the giant planet. Therefore, the magnetospheric plasma – which is mainly produced by ionization of the extended neutral torus generated by the Enceladean plume – corotates or at least sub-corotates with the planet. As the plasma flow velocity is larger than the Keplarian velocity of the moons, the ions and electrons continuously impinge on the surfaces and atmospheres of the satellites, whereas the plume acts like a strong, but displaced, dense atmosphere. Ionization of the neutral molecules of the plume by charge exchange with the magnetospheric plasma, photoionization and electron impacts and the subsequent pick-up of the new-born ions lead to the generation of electric currents. These currents and the associated perturbations of Saturn's dipolar magnetic field, as well as the modifications of the plasma flow and its density, are in the following referred to as 'plasma interaction'.

The primary aim of this thesis is to improve our understanding of the physical processes involved in the plasma interactions of Enceladus and Rhea on the basis of data collected by Cassini. Especially Cassini Magnetometer observations obtained along the trajectories of the various close flybys shall be analyzed and placed within a three-dimensional context. Eventually, these magnetic field signatures allow to draw conclusions on the properties of the obstacle that generated them, i. e. in particular the Enceladus plume and its underlying sources. To analyze the plasma structures, both, analytical and numerical modeling is applied. While an analytical description is most suitable to address the basic effects, a quantitative comparison with Cassini data requires a realistic model of the obstacle in a three-dimensional geometry which can only be achieved by numerical models.

Depending on the features which should be addressed, different approaches for the description of the plasma can be employed. The most simple one is Magnetohydrodynamics (MHD), treating the plasma as a single conducting fluid. The advantage of this rather crude approximation is the simplicity of the governing equations. These allow even with analytical models a profound discussion of the basic features of the respective interaction. When solved numerically, MHD codes are fast to run and achieve a high resolution. For example, the BATS'R'US code has been applied to study Enceladus' plasma interaction

[2] http://www.theoi.com/Gigante/GiganteEnkelados.html

by *Jia et al.* [2010b,c]. The major drawback of the MHD is, however, that neither the densities of different plasma species nor their different velocities can be resolved. The next, more sophisticated step in the hierarchy of the plasma descriptions is the multi-fluid approach, meaning that each plasma species is considered as its own fluid. For many space physics applications, a multi-fluid code is sufficient to cover most physical effects which are relevant on a global scale. Due to the closure of the equations, however, only a small number of moments of the distribution function is considered by the fluid approaches. Therefore, these models cannot account for non-Maxwellian velocity distributions like the ring distribution of the pick-up ions near Enceladus. In contrast to the fluid models, a fully kinetic description of both, electrons and ions, would theoretically include all possible effects. But, even with massive computational resources, it is not yet possible to simultaneously consider the vastly different masses of electrons and ions and the corresponding time scales.

Between the fluid and the full particle descriptions lies the hybrid approach, which treats the ions as particles and the electrons as a massless, charge-neutralizing fluid. One of the first three-dimensional hybrid codes with application to space physics has been developed by *Bagdonat and Motschmann* [2002a] (the "Braunschweig-Code"). In this thesis, its successor A.I.K.E.F. (Adaptive Ion-Kinetic Electron-Fluid) is applied, which is parallelized and allows to use an adaptive mesh [*Müller et al.* 2011]. A.I.K.E.F. and its precursor have already been used for the successful modeling of a large variety of plasma interactions in our solar system, e. g. the solar wind interaction of the terrestrial planets Mercury, Venus, Mars as well as the magnetospheric interaction of Saturn's largest moons Titan and Rhea (e.g, *Müller et al.* [2012], *Martinecz et al.* [2009], *Bößwetter et al.* [2004], *Simon et al.* [2007], *Roussos et al.* [2008a]). The code has also been used for a pilot study of Enceladus' plasma interaction [*Kriegel et al.* 2009]. Apart from A.I.K.E.F., a variety of other hybrid codes is currently applied by the space plasma physics community to the plasma interactions of the Saturnian moons, see e. g. *Ledvina et al.* [2004], *Omidi et al.* [2010, 2012] and *Lipatov et al.* [2012]. The advantage of the hybrid model is that the kinetic behavior of the ions is included, which is particularly important for Rhea, where the ion gyroradius is of about the same size as the radius of Rhea. At Enceladus, however, the ion gyroradii are significantly smaller than the moon's radius. Therefore, a fluid approach seems to be suitable for the description of Enceladus plasma interaction. However, the major result of this thesis is that the inclusion of charged dust grains is of vital importance for the correct description of the interaction. This plasma component could be integrated in the hybrid model without noteworthy modifications, while the available fluid simulation codes that are applied to Enceladus' plasma interaction by *Jia et al.* [2012] and *Paty et al.* [2011] seem to fail to include the heavy dust. Thus, the hybrid simulation code A.I.K.E.F. can be regarded as the appropriate choice for modeling the plasma interactions of the Titaness Rhea and the "little Titan" Enceladus.

Enceladus and its plume are embedded in a similar magnetospheric environment as the Jovian moon Io with its volcano-originating sulfur atmosphere. Io's interaction has already been studied extensively in the framework of the Voyager flybys and the Galileo mission to Jupiter in the 1980s and 1990s. The main aspect of Io's plasma interaction is the generation of a system of non-linear, standing Alfvén waves, the Alfvén wing [*Neubauer* 1980, 1998]. However, its plume makes Enceladus unique in several aspects: the south-polar

plume introduces an asymmetry compared to all other solar system objects which possess a rather symmetrical atmosphere/ionosphere. Therefore, particle absorption and current blockage at the surface mix up with the alfvénic interaction of the plume, resulting in afore unknown physical processes [*Saur et al.* 2007, *Kriegel et al.* 2009]. With regard to the so far poorly understood generation of the plume jets it is also important to determine the degree of plume variability. The magnetic field observations of the first three flybys have already proven to be a useful tool for the analysis of the variability [*Saur et al.* 2008]. The magnetic field perturbations will therefore be used to constrain the shape of the plume as well as the strength of its variability on a flyby-to-flyby base. In addition, the plume consists to a considerable amount of charged dust. The main result of this thesis is that this dust population makes "Enceladus Plume a New Kind of Plasma Laboratory"[3].

Like for Earth's moon, Rhea's plasma interaction is dominated by the absorption of particles at the surface and the resulting density cavity downstream of the moon. Prior to this work, only two Cassini flybys of Rhea were available, which confirmed the overall picture of the lunar-type plasma interaction [*Khurana et al.* 2008, *Roussos et al.* 2008a]. However, the trajectories of these flybys were located in Rhea's equatorial plane and therefore, a draping of the magnetic field lines around the thin atmosphere could not have been detected. Hence, one aim of this thesis is to investigate whether magnetic field observations of the two more recent, polar Rhea flybys match the expected structures of a lunar-type interaction.

This thesis is organized as follows: in chapter 2, an overview of the magnetospheric environment of Enceladus and Rhea will be provided. Furthermore, the trajectories of the 23 Enceladus and five Rhea flybys will be described. Chapter 3 presents the state of knowledge about Enceladus' and Rhea's plasma interactions prior to this thesis. The structures arising from plasma absorption at the moons' surfaces as well as the general properties of the Alfvén wing will be discussed. The hybrid code A.I.K.E.F. will be described in chapter 4. In particular, it will be elaborated on how ion-neutral reactions are included in the model. Moreover, the impact of the boundary conditions applied in the code will be analyzed. Our results are presented in chapters 5 – 7:

- Chapter 5 deals with the influence of charged dust on the structure of Enceladus' Alfvén wings in the context of Cassini magnetometer observations.
- In chapter 6, Monte-Carlo simulations of the Enceladus plume are combined with the hybrid code. Therefore, the full dust-plasma coupling in both directions is included, i. e. the dust is affected by the electromagnetic fields and plasma moments and vice versa. The improved model allows to constrain the ion densities within the plume and to analyze the magnetic signatures of dust pick-up at Enceladus.
- An analysis of Cassini magnetic field observations over the poles of Rhea is presented in chapter 7.

Finally, chapter 8 summarizes the results and gives an outlook to future work. In addition, a very brief overview about Dione's plasma environment will be provided in appendix C.

[3] http://www.nasa.gov/mission_pages/cassini/whycassini/cassini20120531.html

2 The Magnetospheric Environment of Enceladus and Rhea

2.1 Saturn's Icy Moons Enceladus and Rhea

The small moon Enceladus (radius $R_E = 252.1\,\text{km}$) and Saturn's second-largest moon Rhea ($R_{RH} = 763.5\,\text{km}$) encircle the giant planet on orbits with eccentricities of less than $\epsilon = 0.005$ (see table 2.1 for a list of the moons' main physical and dynamical properties). With a semi-major axis of 238,040 km or 3.95 Saturn radii (equatorial radius $R_S = 60,268\,\text{km}$), Enceladus is the fourteenth satellite when ordered by distance from Saturn. One bound rotation is carried out in about 1.37 days. Going further away from Saturn, Enceladus' nearest neighbors are Dione – which is connected to Enceladus through a 2:1 orbital resonance –, Tethys and Rhea. As the outermost of these four satellites, Rhea's orbit is located at 527,070 km or 8.74 R_S, leading to a rotation period of about 108h 25min. Since their surfaces are mostly covered with water ice, the four moons (Enceladus, Dione, Tethys, Rhea) and Enceladus' inner neighbor Mimas are also named Saturn's major icy moons. Their icy surfaces are also the reason why the moons have relatively high albedos and low temperatures – Enceladus has a visual geometric albedo of 1.38 [*Verbiscer et al.* 2007], which makes the moon even the most reflecting celestial body in the solar system. The corresponding surface temperature is only 76 K at the subsolar point [*Howett et al.* 2010]. When compared with Enceladus, Rhea's surface is rather dark with an albedo of 0.95. The surface temperature ranges between 53 K in the shadow and 99 K in the sunlight [*Howett et al.* 2010].

From the time of their discovery until the Voyager 1 spacecraft passed through the Saturnian system in November 1980, little more was known about the two satellites than their physical and dynamical characteristics (although the latest values from Cassini measurements are provided in table 2.1, most of these numbers have undergone only slight changes since the pre-Voyager era). This changed when Voyager 1 and 2 sent the first high-resolution images to Earth.

The images of Voyager 1 showed that Rhea's surface is more heavily cratered than those of the other outer moons indicating less resurfacing than at the other icy moons (cf. the image of Rhea obtained by Cassini in figure 2.1(a)). In agreement with this finding, Rhea seemed to be a relatively unspectacular and inactive satellite. Therefore it was a big surprise, when Cassini observations of absorption signatures of energetic electrons seemed to imply that Rhea possesses a ring system on its own [*Jones et al.* 2008]. However, the presence of this ring system has been ruled out by optical observations [*Tiscareno et al.*

Table 2.1: Overview about the main physical and dynamical properties of Enceladus and Rhea. The orbital characteristics are obtained from the satellites' ephemeris generated by the JPL HORIZONS system at http://ssd.jpl.nasa.gov.

Parameter	Enceladus	Rhea	Source
Mean Radius	R_E = 252.1 km	R_{RH} = 763.5 km	*Thomas* [2010]
Mass	$1.079 \cdot 10^{20}$ kg	$2.307 \cdot 10^{21}$ kg	*Thomas* [2010]
Mean density	1.609 g/cm^3	1.237 g/cm^3	*Thomas* [2010]
Escape velocity	239 m/s	635 m/s	calculated
Semi-major axis	238 040 km = 3.95 R_S	527 070 km = 8.75 R_S	JPL HORIZONS
Orbital period	1.370 d	4.518 d	JPL HORIZONS
Orbital excentricity	0.0047	0.001	JPL HORIZONS
Orbit inclination	0.009°	0.331°	JPL HORIZONS
Mean velocity	12.6 km/s	8.5 km/s	calculated
Rotation period	1.370 d	4.518 d	bound rotation
Sub-solar temperature	76 K	99 K	*Howett et al.* [2010]
Geometric albedo	1.38	0.95	*Verbiscer et al.* [2007]

2010]. When passing above Rhea's north pole during the second targeted Rhea flyby, Cassini's Ion and Neutral Mass Spectrometer (INMS) detected the presence of a tenuous exosphere around the moon [*Teolis et al.* 2010]. This exosphere, consisting mainly of molecular oxygen with a column density of $(3.4 \pm 0.7) \cdot 10^{16}$ cm^{-2} and a minor contribution of carbon dioxide, was found to be sustained by chemical decomposition of the surface water ice due to sputtering by Saturn's magnetospheric plasma. The detection of a dilute, sputtering-induced atmosphere around Rhea is consistent with the predictions of *Saur and Strobel* [2005], who had explored the possible existence of atmospheres around Saturn's icy satellites before the first Cassini flybys took place. As these predictions are based on the significantly higher energetic particle fluxes measured by Voyager, the column density obtained by *Saur and Strobel* [2005] is an order of magnitude higher than that present during the Cassini mission.

In contrast to Rhea, the images taken by the two Voyager spacecraft, combined with ground-based observations, gave the first hints pointing towards Enceladus' uniqueness:

- Enceladus orbits Saturn within the narrowest, but densest part of the extended E-ring which consists mainly of μm-sized ice particles.
- High-resolution Voyager 2 images showed a heterogeneous surface. It exhibits a geologic dichotomy with a cratered northern hemisphere while the southern hemisphere is nearly devoid of impact craters (see also figure 2.1(b) for a high resolution image obtained by Cassini).

These facts grew early speculations about cryovolcanic activity at Enceladus [*Terrile and Cook* 1981]. It was concluded that the lack of craters in the south must be caused by resurfacing processes within less than a few hundred million years. Furthermore, the

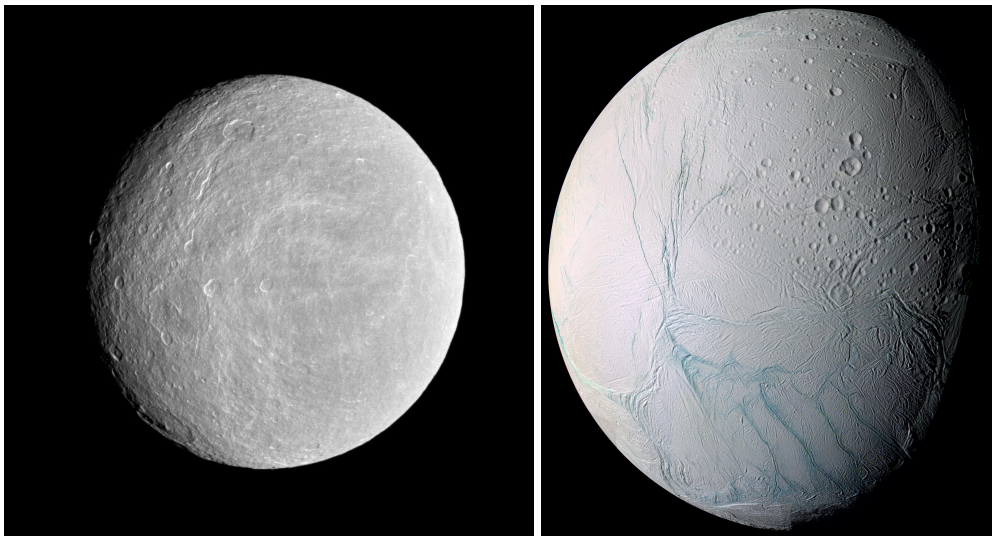

(a) (b)

Figure 2.1: (a) Cassini image of Rhea, obtained with the wide-angle camera of the Imaging Subsystem (ISS) on 21 Nov. 2009 from a distance of about 30,000 km [*Cassini Press Release PIA12648, NASA/JPL*] (b) False-color image of Enceladus obtained with the ISS narrow-angle camera on 14 July 2005. [*Cassini Press Release PIA06254, NASA/JPL*].

relatively short lifetime of E-ring particles of only a few thousand years requires that the ring must be constantly replenished. Therefore, Enceladus was suspected to be the main source of particles for the E-ring (see e. g. *Haff et al.* [1983], *Pang et al.* [1984]). However, it could not finally be concluded whether Enceladus is currently active.

In addition to the E-ring observations, in-situ Voyager and remote Hubble Space Telescope (HST) observations revealed that Saturn's magnetosphere is populated by an extended torus of OH molecules (see *Shemansky et al.* [1993], *Jurac and Richardson* [2005] and references therein). This torus extends out to a distance of approximately 8 R_S and assumes its peak density near the orbit of Enceladus. From these early observations, it was suggested that a source in the region near 4 R_S has to provide about 80% of the total OH source of 10^{28} H_2O/s [*Shemansky et al.* 1993].

As Cassini made its first two flybys at Enceladus in February and March 2005, the magnetometer (MAG, *Dougherty et al.* [2004]) indicated the presence of a conducting ionospheric plume at Enceladus [*Dougherty et al.* 2006]. Consequently, the altitude of the upcoming flyby in July 2005 was lowered from 1000 km to 173 km. During this flyby, various instruments onboard the spacecraft made the spectacular discovery of a large plume of water vapor and dust emanating from Enceladus' south polar regions [*Dougherty et al.* 2006, *Hansen et al.* 2006, *Porco et al.* 2006, *Spahn et al.* 2006, *Spencer et al.* 2006, *Tokar et al.* 2006]. A colored image of the dust plume is shown in figure 2.2(a).

It was found that the plume is formed by discrete jets that originate from the so-called "tiger stripes". These are four prominent, about 130 km long canyons named Alexandria, Baghdad, Cairo and Damascus[1]. On average, the tiger stripes are about 2 km wide, 500 m

[1]Features on Enceladus are named by the International Astronomical Union (IAU) after characters and places from the Arabian Nights.

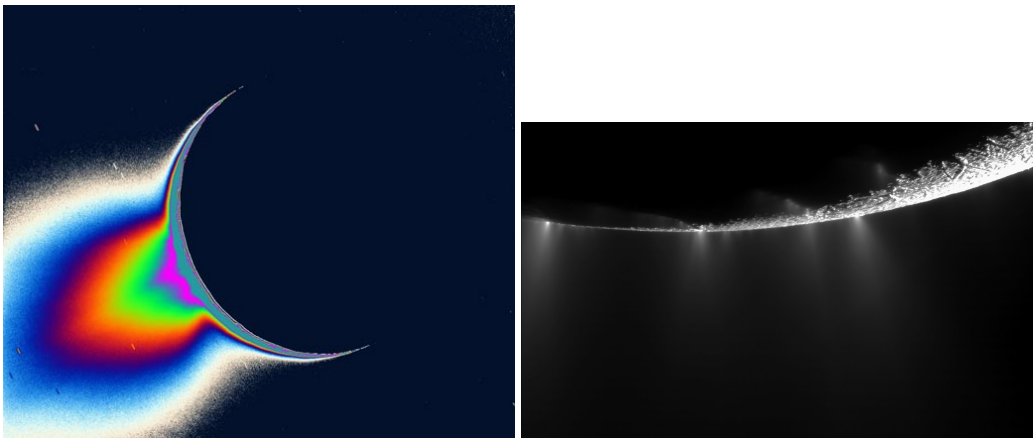

(a) (b)

Figure 2.2: (a) Enhanced and colorized image showing the large extent as well as the discrete jets of the plume above the south polar region [*Cassini Press Release PIA07759, NASA/JPL*]. (b) Mosaic created from two high-resolution images that were captured on 21 Nov. 2009 [*Cassini Press Release PIA11688, NASA/JPL*].

deep and flanked by about 100 m high ridges [*Porco et al.* 2006]. The jets are clearly visible in the Cassini image shown in figure 2.2(b). INMS measurements showed that the gaseous part of the plume consists to 90% – 96% of H_2O. Other constituents are CO_2 with a mixing ratio of 1.5% - 5.3% and ammonium (NH_3) with an abundance of about 1%. A variety of organic molecules with even lower abundances has also been detected [*Waite et al.* 2006, 2009]. Observations of the plume by the UltraViolet Imaging Spectograph (UVIS) during star occultations on two flybys suggest H_2O production rates of 150 – 300 kg/s or $5 \cdot 10^{27} - 1 \cdot 10^{28} H_2O/s$ [*Hansen et al.* 2006]. The dust part of the plume is made up by nanometer to micrometer-sized ice particles [*Spahn et al.* 2006]. Images of Cassini's Composite Infrared Spectrometer (CIRS) also revealed that strong thermal emissions corresponding to temperatures of 145 K and higher coincide with the location of the tiger stripes [*Spencer et al.* 2006]. A subsequent study by *Spitale and Porco* [2007] showed that particularly warm spots on the tiger stripes could be associated with eight sources of collimated dust (and probably also gas) jets. Since the properties of the plume are a major subject of this work, further findings are discussed prior to the results in chapters 5 and 6.

The neutral and dust particles emitted from Enceladus' south polar regions eventually feed the extended neutral torus and the E-ring, respectively. The neutral torus has also been observed with the Herschel Space Observatory, named after the discoverer of Enceladus. A plume source rate of $10^{28} H_2O/s$ appears to be consistent with the Herschel observations and the aforementioned HST observations by *Shemansky et al.* [1993], making Enceladus the ultimate source of neutrals for Saturn's magnetosphere [*Hartogh et al.* 2011]. The μm-sized ice particles of the E-ring nearly exclusively originate from the Enceladean plume [*Spahn et al.* 2006]. By modeling data from the Cosmic Dust Analyzer (CDA), *Kempf et al.* [2008] showed that the vertical structure of the E-ring is consistent with initial particle speeds around 230 m/s, which is close to the escape velocity. Thus, many ice grains fall back to Enceladus' surface, thereby explaining its high reflectance. Furthermore, the

displacement of the densest part of the E-ring by about 0.05 R_S outward from Enceladus' orbit can probably be explained with plasma drag on the dust particles.

Together with the discovery of Enceladus' cryovolcanic activity the question arises how such a tiny satellite could be geologically active. According to its mean density of $1.608\,\mathrm{g/cm^3}$ and shape with semi-major axes of $a = 256.6 \pm 0.3\,\mathrm{km}$, $b = 251.4 \pm 0.2\,\mathrm{km}$ and $c = 248.3 \pm 0.2\,\mathrm{km}$ [*Thomas* 2010], Enceladus could either be homogeneous and in hydrostatic equilibrium or differentiated into a rocky core and a H_2O layer, implying a non-hydrostatic state [*Porco et al.* 2006]. These authors also concluded that Enceladus is currently or has been in the past in a 1:4 spin-orbit libration resonance. However, no libration could be observed for a maximum detectable amplitude of 1.5°. *Schubert et al.* [2007] modeled the moon's thermal evolution and suggested that radiogenic heating from the decay of ^{26}Al shortly after Enceladus' formation could have lead to a rocky core of 165 km radius, an ocean of liquid water possessing a depth of about 70 km and an ice shell with a thickness of 15 km above it. These values yield a normalized moment of inertia of 0.31 and Enceladus' semi-major axes then imply that the moon is currently not in hydrostatic equilibrium. Furthermore, the heat imbalance of Enceladus due to the power of about 16 GW emitted at the south polar regions [*Howett et al.* 2011] rises difficulties in the understanding of the mechanisms which generate the plume. This heat flux cannot be explained by radiogenic heating [*Meyer and Wisdom* 2007]. However, tidal forces due to Enceladus' slightly eccentric orbit cause a lateral motion of the tiger stripe faults, making tidal shear heating the primary source of heat [*Nimmo et al.* 2007]. This further supports the presence of a subsurface liquid water ocean since tidal heating is most efficient if the ice shell is decoupled from the solid core by a liquid ocean [*Roberts and Nimmo* 2008]. Moreover, *Hurford et al.* [2009] showed that a physical libration at Cassini's detection limit of 1.5° increases the tidal heating by nearly a factor of five.

However, the issue for any of these models is that tidal heating under present-day orbital conditions does probably not balance the energy emitted from the south polar regions and thus, any subsurface water ocean would freeze out within the next hundred million years [*Meyer and Wisdom* 2007, *Roberts and Nimmo* 2008, *Běhounková et al.* 2012]. The energy required for subsequently melting the ice and generating an ocean of liquid water again is even considerably higher. In addition, energy drawn from the eccentricity would further circularize the orbit, although the 2:1 resonance with Dione might help to sustain a slightly elliptic orbit. It is therefore likely that Enceladus' orbit had a higher eccentricity in the past ($\epsilon > 0.015$) and that the current heat flux of Enceladus is not in steady state [*Roberts and Nimmo* 2008]. Therefore, *Běhounková et al.* [2012] suggested that the eccentricity may change periodically by about a factor of five on a time scale of hundred million years. Due to the numerous uncertainties, Enceladus' geological history may, however, remain a challenging research topic for many years.

Tidal dissipation as the primary source of heat implies that the tiger stripes are in different states of stress and tension during each orbit, allowing the vents to periodically open and close [*Hurford et al.* 2007]. In addition, *Hurford et al.* [2009] suggested that a physical libration of Enceladus significantly affects the stresses on the tiger stripes and therefore also the timing of the periodic eruptions. The diurnal variations of the plume activity have first been detected by *Hedman et al.* [2013]. These authors analyzed data from Cassini's Visual and Infrared Mapping Spectrometer (VIMS) and found that the horizontally in-

tegrated brightness of the plume is several times greater when Enceladus is close to its apocentre than at its pericentre.

The vapor and ice particles of the plume likely originate from boiling of a liquid H_2O reservoir at the triple point [*Porco et al.* 2006]. This reservoir is suggested to be located only a few meters below the surface. If cracks in this thin ice cap are formed, the water chamber is connected to space and the vapor pressure is released through the cracks, eventually forming the plume jets at sonic or even supersonic speeds. In agreement with this picture, *Schmidt et al.* [2008] showed that the size distribution and velocities of the dust grains are consistent with grain condensation and growth in small channels above a liquid water reservoir. In their model, the grains achieve their velocities by collisions with the channel walls and re-acceleration by the gas. *Postberg et al.* [2009] concluded that the small amount of sodium-rich E-ring grains detected by CDA strongly favors the presence of a liquid water ocean in contact with a rocky core. Therefore, the model of these authors suggests that the ocean contains low concentrations of NaCl and carbonates. *Postberg et al.* [2011] analyzed the composition of freshly ejected dust grains which had been detected by CDA. They found that salt-rich ice particles dominate the mass flux of the ejected grains, which is consistent with a size-dependent initial velocity distribution of the dust, producing heavier particles at speeds below the escape velocity. In consequence, most of the heavy, salt-rich grains do not escape into the E-ring. More recently, *Matson et al.* [2012] presented a hypothesis for a water circulation system, which could explain how the liquid water rises from the ocean below the ice shell – possessing a thickness of about 10 km – towards the chambers a few meters below the surface. They suggested that the tidal forces open cracks in the ice shell which are partially filled with water. The reduced pressure at the top of the water column leads to an exsolution of the low amount of CO_2, thereby lowering the density and further pushing the water towards the surface.

The question of why Enceladus' activity is concentrated at the pole is probably more easy to answer. *Nimmo and Pappalardo* [2006] showed that diapirism, i.e. an upwelling of low density material, yields a reorientation of the moon in the way that the diapir is situated closer to the satellite's spin axis. The diapir could be located either in the ice shell or the silicate core. *McKinnon* [2013] discussed how an irregularly shaped core could be formed and showed that this core would be consistent with the non-hydrostatic shape of Enceladus.

2.2 Plasma in Saturn's Inner and Middle Magnetosphere

Like the other gas giants, Saturn has a strong internal magnetic field. With a value of about $4.6 \cdot 10^{18}\,\mathrm{Tm}^3$, its dipole moment is more than five hundred times stronger than that of the Earth. However, due to Saturn's enormous size, the magnetic field reaches only about 20000 nT at the equator and is therefore weaker than the field at the surface of our home planet. Analysis of magnetometer observations from the Cassini prime mission have shown that the internal field is nearly exclusively dipolar with only negligible contributions of the higher moments [*Burton et al.* 2010]. Moreover, the dipole has a northward offset with respect to the rotational equator of about 0.036 R_S. The most peculiar feature of the internal field is the extremely small tilt of the dipole axis against the rotation

axis of less than 0.06° [*Cao et al.* 2011]. This finding is particularly interesting, because Cowling's theorem states that an axisymmetric magnetic field cannot be maintained by dynamo action. Hence, it is proposed that conducting layers above the dynamo region may symmetrize the magnetic field [*Stevenson* 1982, *Cao et al.* 2011].

The interaction of the solar wind with Saturn's magnetic field gives rise to a magnetosphere with an average magnetopause distance in the range of 21 – 27 R_S [*Kanani et al.* 2010]. Analysis of magnetometer data by *Arridge et al.* [2007] as well as a multi-instrument study of data collected during Cassini's Saturn Orbit Insertion (SOI) by *André et al.* [2008] showed that several regions inside the magnetosphere could be distinguished: the inner magnetosphere with a strongly dipolar magnetic field which extends until about $5R_S$, this region also coincides with the cold plasma torus; the quasi-dipolar middle magnetosphere with a dynamic plasma sheet from $5R_S$ to $12 - 15R_S$, and the outer magnetosphere where the magnetic field lines are stretched and form the magnetodisc. Cassini Plasma Spectrometer (CAPS) data from SOI also revealed that inside $10R_S$, the plasma density is significantly higher than in the outer magnetosphere. Therefore, this region is also referred to as the inner plasmasphere [*Sittler et al.* 2006]. The magnetospheric electrons and ions mainly originate from ionization of the extended neutral cloud supplied by Enceladus' plume as well as from sputtering of ring particles and the surfaces of the icy moons. These processes lead to the production of $(10^{27} - 10^{28.5})$ ions/s or about $(30 - 300)$ kg/s of plasma [*Sittler et al.* 2008, *Gombosi et al.* 2009]. The ions are mainly composed of H^+ and water group ions (W^+=O^+, OH^+, H_2O^+, H_3O^+). Inside 9 R_S, the water group ions dominate, while outside and at higher latitudes the proton abundance is higher [*Young et al.* 2005]. In contrast to previous expectations, hardly any nitrogen (<3%) from Titan's dense atmosphere is found within the magnetosphere [*Smith et al.* 2007].

The magnetic field is frozen into magnetospheric plasma that corotates with the planet. However, ions and electrons created by ionization or charge exchange from the neutral cloud or the satellites are "born" at the (slower) Keplarian speed. The convective electric field then accelerates those particles until their guiding centers acquire the corotation velocity of the plasma. This process is referred to as 'pick-up'. The local pick-up as well as collisions between the magnetospheric ions and the molecules of the neutral torus reduce the plasma bulk velocity and lead to a sub-corotation of the plasma flow [*Saur et al.* 2004a], since the ionospheric Pedersen conductance and the viscous torque between the neutral atmosphere and the ionosphere limits the momentum transfer from the planet to the magnetosphere (magnetosphere-ionosphere coupling, *Hill* [1979]). This is consistent with ion flow speeds derived from CAPS data by *Wilson et al.* [2009] that range between 50% and 80% of ideal corotation . Due to Saturn's fast rotation, the strong centrifugal forces cause the plasma to accumulate most distant to the rotational axis, i.e. near the equatorial plane. The newly produced plasma also leads to a density gradient that yields – in combination with the centrifugal forces – an outward transport of the plasma and eventually a stretching of the fields lines [*Arridge et al.* 2007]. Outside the radial location of the plasma source, the mass loaded magnetic flux tubes become unstable to the interchange instability (cf. e.g., *Southwood and Kivelson* [1987]). This instability involves the radial interchange of magnetic flux tubes, leading to a net flow of plasma outward

from the planet and the associated injections of energetic particles into the inner magnetosphere. More than 50 of these so-called "injection events" have been detected by the Magnetospheric Imaging Instrument (MIMI) (see e. g. *Mauk et al.* [2005] and *Müller et al.* [2010]). The interchange instability is also the reason for the highly dynamic middle magnetosphere around Rhea's orbit. In steady state, the magnetic flux should be conserved during the interchange processes. Since the dipole field decreases with L^{-3}, with L denoting the L-shell parameter, flux conservation requires the cross section A of a magnetic flux tube to increase with L^3. Assuming that the flux tube contains N particles within a volume of $A \cdot 2H$, where H is the plasma scale height (defined as the distance to the equatorial plane at which the plasma density has decreased to e^{-1}), the L-shell dependency of the plasma density can be approximated as $n \sim L^{-3}H^{-1}$. When it is further assumed that H is proportional to L (which is consistent with Cassini observations by *Moncuquet et al.* [2005]), one obtains

$$n \sim L^{-4} \quad . \tag{2.1}$$

Note that this estimate assumes outward transport of plasma initially caused by negative radial density gradients and is therefore not valid inside Enceladus' orbit.

From data collected during SOI by CAPS and the Radio and Plasma Wave Science (RPWS) instrument, *Sittler et al.* [2006] derived a first ion distribution for the inner plasmasphere which was roughly in agreement with the L^{-4}-dependency. The observed (perpendicular) temperature distributions as a function of L-shell parameter are given by (fig. 15 of *Sittler et al.* [2006])

$$k_B T_{\mathrm{H}^+} = 2.2 \left(\frac{L}{4}\right)^{2.5} \text{ eV} \tag{2.2}$$

for the protons (H^+) and

$$k_B T_{\mathrm{W}^+} = 35 \left(\frac{L}{4}\right)^{2} \text{ eV} \tag{2.3}$$

for water group ions (W^+). Since the azimuthal velocity v_ϕ increases linearly with L, the dependency of the temperature on L^2 is consistent with the conversion of kinetic energy to thermal energy by the thermalization of pick-up ions. Therefore, the different absolute values of T_{H^+} and T_{W^+} result from the different masses of the ion species. As the plasma scale height is proportional to $T^{1/2}$ (see e. g. *Persoon et al.* [2009]), equation (2.3) also justifies the assumption of $H \sim L$ that has been made in the derivation of equation (2.1). Furthermore, the ratio of the ion temperature perpendicular and parallel to the ambient magnetic field measured by CAPS [*Sittler et al.* 2006] is consistent with the findings of *Richardson and Sittler* [1990] from Voyager data, who found

$$T_{\mathrm{W}^+\perp} / T_{\mathrm{W}^+\parallel} = 5 \tag{2.4}$$

and

$$T_{\mathrm{H}^+\perp} / T_{\mathrm{H}^+\parallel} = 2 \quad . \tag{2.5}$$

This anisotropy may arise from the removal of the pick-up ions by charge exchange and recombination before isotropization can occur. This may also explain the smaller anisotropy of the protons which isotropize faster due to their lower mass [*Richardson and Sittler* 1990].

The SOI data also revealed the presence of two separate electron populations, a cold Maxwellian population ($E < 100\,\mathrm{eV}$) and a hot component ($E > 100\,\mathrm{eV}$) [*Young et al.* 2005]. The density of the cold population decreases with radial distance while its temperature increases. The main source of the cold electrons was found to be ionization of the neutral cloud [*Rymer et al.* 2007]. This is also consistent with the presence of two electron energy peaks at 20 eV and 42 eV in CAPS data which correspond to photoionization [*Schippers et al.* 2009]. The temperature of the cold electrons is correlated to the proton temperature according to (fig. 12 of *Sittler et al.* [2006])

$$k_B T_{\mathrm{H}^+} = \left(2.5\,(k_B T_{ec}[\mathrm{eV}])^{0.8} - 0.6\right)\,\mathrm{eV} \quad , \tag{2.6}$$

which indicates cooling/heating by Coulomb collisions between electrons and protons. In contrast to the cold population, the hot component increases in density and decreases in temperature with radial distance. Thus, the origin of the hot electrons is supposed to be not in the inner, but in the middle or outer magnetosphere [*Rymer et al.* 2007]. However, the exact transport mechanisms of these electrons from the middle to the inner magnetosphere are not yet fully understood.

Since the electron density n_e is related to the upper hybrid frequency f_{UH} and the magnitude of the magnetic field (B_0) by (cf. eq. (1) of *Persoon et al.* [2005])

$$n_e = \frac{f_{UH}[\,\mathrm{Hz}]^2 - (28 B_0[\mathrm{nT}])^2}{(8980)^2}\,\mathrm{cm}^{-3} \quad , \tag{2.7}$$

Persoon et al. [2005] used the upper hybrid resonance emissions detected by RPWS during the first five orbits to develop a model of the cold electron density profile in the inner magnetosphere from about $L = 4$ to $L = 9$. For the equatorial electron density, these authors found

$$n_e = k \left(\frac{1}{L}\right)^{\alpha} \quad , \tag{2.8}$$

with $k = 2.2 \cdot 10^4\,\mathrm{cm}^{-3}$ and $\alpha = 3.63 \pm 0.05$. Inside 5 R_S, however, the densities show a strong time variability. By excluding data from $R < 5R_S$ and with 14 equatorial orbits available, *Gurnett et al.* [2007] obtained the slightly different values of $k = 5.5 \cdot 10^4\,\mathrm{cm}^{-3}$ and $\alpha = 4.14$. By combining the results from the upper hybrid emissions with CAPS data, *Persoon et al.* [2009] improved the model and showed that for $L > 5R_S$, the equatorial ion densities exhibit a L-shell dependency of $n_{\mathrm{W}^+} \sim L^{-4.3}$ and $n_{\mathrm{H}^+} \sim L^{-3.2}$, respectively. All these descriptions of the density profiles are in very good agreement with the estimated dependency on L^{-4}, cf. equation (2.1). The electron temperature derived by *Persoon et al.* [2009] is

$$k_B T_{ec} = 0.11\,L^{1.98}\,\mathrm{eV} \quad . \tag{2.9}$$

By using data from the Langmuir Probe of the RPWS instrument, *Gustafsson and Wahlund* [2010] also derived the dependence of the electron temperature on L-shell from $3.5-7\,R_S$. These authors obtained

$$k_B T_{ec} = (0.04 \pm 0.02)\,L^{2.8\pm0.4}\,\mathrm{eV} \quad , \tag{2.10}$$

which is roughly consistent with the temperature model derived by *Persoon et al.* [2009] (equation (2.9)).

Another interesting aspect about Saturn and its magnetosphere is the exact value of Saturn's planetary rotation rate which is still under debate. Usually, variations in the auroral kilometric radio emissions are used to determine the rotation period of a gas planet (see *Zarka and Kurth* [2005] and references therein). In contrast to Jupiter, however, the Saturn Kilometric Radiation (SKR) does not allow to conclusively determine Saturn's internal rotation rate. Whereas the results from Voyager suggest a rotation period of 10 h 39 m [*Desch and Kaiser* 1981], Galileo and initial Cassini observations lead to a value of 10 h 45 min. Since Saturn's internal rotation rate could not have changed so significantly over such a short time span, the SKR period is likely not an exact measure of the internal rotation rate. However, plasma and magnetic field in the whole magnetosphere show a clear modulation with the SKR period (see e.g., *Andrews et al.* [2011]). Therefore, *Kurth et al.* [2008] introduced a longitude system with respect to the sub-solar longitude of the peak SKR emissions, called the SLS3 system which is valid until day 222 of 2007. *Gurnett et al.* [2007] showed that the electron densities derived from the upper hybrid frequency exhibit a sinusoidal variation with SLS3 longitude, e.g. at Enceladus' orbit the density varies from $n_0 = 45\,\mathrm{cm}^{-3}$ to $n_0 = 90\,\mathrm{cm}^{-3}$ for that time interval. Unfortunately, there is no longitude system covering the equinox or solstice mission, since it became evident that the period linked to Saturn's north pole is different from the southern period (cf. e.g, *Andrews et al.* [2010]). Yet it will be shown within this thesis that the appropriate value of the magnetospheric electron density has to be considered when modeling Enceladus' and Rhea's plasma interactions. Thus, the respective density has to be determined individually for each flyby from measurements like the RPWS upper hybrid frequency.

Apart from the rather low-energetic plasma, the inner magnetosphere is also populated by the highly energetic particles of the radiation belts. The energies of these particles range from hundreds of keV to tens of MeV. Their density and pressure are, however, orders of magnitude below those of the magnetospheric plasma described above. Hence, the high-energy particles do not contribute to the generation of the magnetic field structures in the vicinity of the moons and are not considered for the work presented in this thesis. However, measurements of the absorption signatures of the energetic particles by the Low Energy Magnetospheric Measurement System (LEMMS) of MIMI help to analyze the electromagnetic fields in the magnetosphere as well as in the environments of the moons (see e. g. *Roussos et al.* [2012] and *Krupp et al.* [2012, 2013]). These absorption features can be grouped into macro- and microsignatures. The former are permanent and azimuthally averaged structures in the radial distribution of the energetic particle fluxes while the latter are caused by absorption at the moons or rings. Because of the particles' sensitivity to gradient and curvature drift, the study of microsignatures requires a sophisticated model for the fields in the vicinity of the moon. Therefore, the results of our simulations presented in chapter 7 and appendix C are also used as input for an analysis of electron microsignatures at Rhea [*Roussos et al.* 2012] and Dione [*Krupp et al.* 2013], respectively.

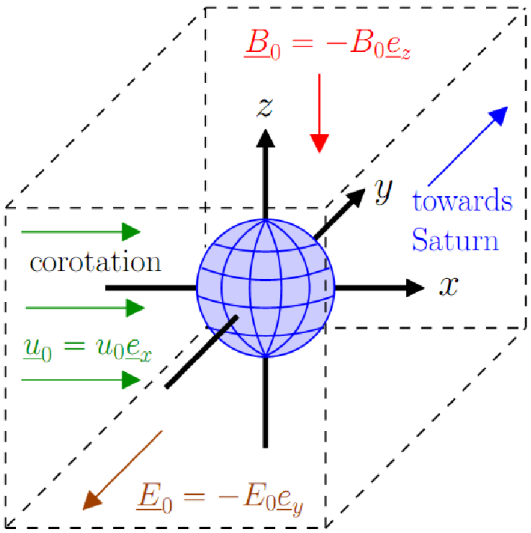

Figure 2.3: Sketch of the coordinate systems used throughout this work: the Enceladus Interaction System (ENIS) and the Rhea Interaction System (RHIS). Both systems are identical with regard to the plasma interaction, but they corotate with Enceladus or Rhea and their origin coincides with the center of the respective moon.

2.3 Coordinate System and Flybys

The orbits of the moons define natural interaction coordinate systems that will be used throughout this work, namely the Enceladus Interaction System (ENIS) and the Rhea Interaction System (RHIS). Its respective $(+x)$ axis is aligned with the direction of ideal corotation ($\underline{u}_0 = u_0\,\underline{e}_x$), and the $(+y)$ axis points towards Saturn. The z axis is perpendicular to the moon's orbital plane and completes the right-handed system, thereby being approximately antiparallel to the ambient magnetospheric field $\underline{B}_0 = -B_0\underline{e}_z$. The convective electric field $\underline{E}_0 = -\underline{u}_0 \times \underline{B}_0 = -E_0\underline{e}_y$ then points in negative y direction. The symbols $\underline{e}_x$, $\underline{e}_y$ and $\underline{e}_z$ denote the unit vectors along the axes. The origin of the coordinate system coincides with the center of the respective satellite. See also figure 2.3 for a sketch of the coordinate system.

Until the end of 2013, Cassini had performed 200 elliptical orbits around Saturn. During that time, Cassini had accomplished a large number of close flybys of the icy satellites, including 20 flybys of Enceladus and five flybys of Rhea. Only three more Enceladus encounters and no further visit of Rhea are scheduled for the remaining years of the Cassini mission. In the following, the flybys are described in more detail and a list of the properties of the Enceladus and Rhea encounters is provided in tables 2.2 and 2.3, respectively. For instance, the Saturn Local Times (SLT) and the Sub-Solar Latitudes (SSL) of all flybys are listed. This information is necessary to infer whether Enceladus or Rhea were located in Saturn's geometric shadow with respect to the sun during the time of the flyby and therefore, no photoionization occurred. Illustrations of SLT and SSL are provided in figure 2.4. A satellite orbiting Saturn at an average distance L is located in the planet's

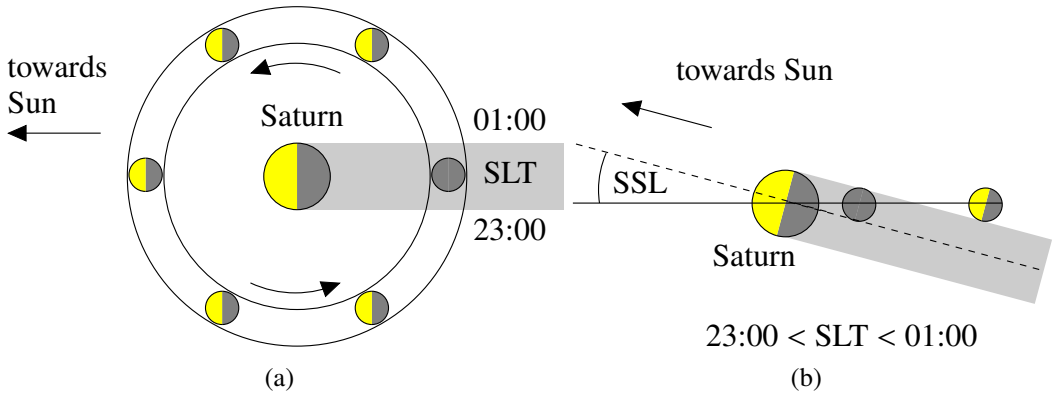

Figure 2.4: Illustration of (a) Saturn Local Time (SLT) and (b) Sub-Solar Latitude (SSL). Enceladus is approximately located in Saturn's shadow from 23:00 SLT to 01:00 SLT and |SSL| < 15°, whereas the shadow is roughly given by the same local times, but smaller latitudes of |SSL| < 6.5° for Rhea. See inequality (2.11) for the exact definition of the shadow.

shadow if

$$L \sqrt{\sin^2\left(\frac{\mathrm{SLT}}{24\,\mathrm{h}} \cdot 360^\circ\right)\cos^2(\mathrm{SSL}) + \sin^2(\mathrm{SSL})} < 1 \quad , \tag{2.11}$$

and considering only local times at Saturn's night side, i. e. 18 h < SLT < 6 h. Therefore, Saturn's shadow roughly corresponds to local times from 23:00 SLT to 01:00 SLT and |SSL| < 15° (Enceladus) or |SSL| < 6.5° (Rhea). Cassini's approximate trajectory during the flybys can be deduced from the latitude and longitude of closest approach and the velocity vector. As discussed in the previous section, the upstream electron densities n_0 vary according to the moon's longitude with respect to the SKR period [*Gurnett et al.* 2007]. Thus, the densities estimated from measurements of the upper hybrid frequency by RPWS are provided in tables 2.2 and 2.3 as well. The values for Enceladus were taken from *Jia et al.* [2010b, 2011] and *Kriegel et al.* [2011] (flybys E3 – E13), derived by *A. Persoon, [priv. comm.]* (flybys E14 – E16) or estimated from RPWS full resolution wideband spectrograms available at the Planetary Data System (http://pds.nasa.gov).

2.3.1 Enceladus Flybys

In this work, the Enceladus flybys are labeled sequentially E0 – E19. The number sequence starts with zero, since the first flyby, E0, was originally planned as a non-targeted flyby, but it was already relatively close to Enceladus and, more important, gave the first hints towards the plume. In the literature, another nomenclature is used occasionally, in which the number of Cassini's orbit is followed by the suffix 'EN', e. g. E1 would be identical to 004EN.

Chronologically, the available flybys occurred in sequences of two, three or four encounters over a duration of a few months. The first series of encounters (E0, E1 and E2 in 2005) occurred upstream of the moon, i.e. the spacecraft did not pass through the center of the plume. The second sequence of encounters (E3 – E6) took place in 2008. These were the first flybys which passed directly through the plume. In November 2009 and mid 2010, the flybys E7 – E8 and E9 – E11 were performed. At the end of 2010, the two only

north polar flybys E12 and E13 took place. Two additional series with three flybys each in autumn 2011 (E14 – E16) and spring 2012 (E17 – E19) complete the set of accomplished flybys so far. Three further flybys (E20 – E22) will take place at the end of 2015.

To better visualize the flyby trajectories, the flybys are grouped into five categories according to their trajectories and one additional category for the three future flybys:

- There are three flybys which do not possess a counterpart with a similar trajectory, namely E0, E2, and E15. Their trajectories are displayed in fig. 2.5. The distant encounters E0 and E15 were directed towards Saturn and occurred far upstream or downstream of Enceladus, respectively. Both trajectories were nearly parallel to the equatorial plane. The closest approach of E0 took place north and upstream of the moon, while that of E15 was slightly south and more than $5R_E$ downstream of Enceladus. The E2 flyby was located upstream of the plume, possessing a south-to-north trajectory that is also oriented towards Saturn.

- The flybys E1, E10 and E16 possess similar trajectories which are parallel to the equatorial plane at $z = -1.5R_E$, upstream of the plume and directed towards Saturn (see fig. 2.6). When crossing the (x, z)-plane, Cassini was located about $2R_E$ upstream of Enceladus.

- E3 – E6 constitute are series of highly inclined flybys during which Cassini passed steep through the plume from downstream and north of Enceladus to upstream and south. The trajectories are shown in fig. 2.7. E3 features the highest inclination of these flybys and also included an inbound motion. The other three flybys possessed nearly the same inclination, but E6 was located about $0.5R_E$ further downstream than E4 and E5. The velocity during these encounters was a factor of two higher than for the other flybys.

- Encounters E7, E9, E14 and E17 – E19 were all equatorial flybys parallel to the moon's orbital plane at $z = -1.5R_E$ and crossed through the center of the plume with a closest approach near Enceladus' south pole. For E7 and E9, the trajectories were oriented from upstream to downstream and away from Saturn (outbound), while E14, E17, E18 and E19 were directed towards Saturn (see fig. 2.8). E14, E17 and E18 possessed nearly identical trajectories. The E19 trajectory was parallel to that of these three flybys, but located about $0.35R_E$ further upstream.

- The remaining four encounters constitute of two pairs, E8/E11 and E12/E13 (see fig. 2.9). All four flybys were roughly parallel to the equatorial plane, although E11 features a small northward tilt of about 15°. E8 and E11 were located far south of Enceladus at $z = -7.3R_E$ and $z \approx -11R_E$, respectively. E12 and E13 were both north polar flybys and directed outbound. These two encounters possessed a nearly identical direction, but the closest approach of E12 was located about $1R_E$ further downstream than that of E13.

- No predicted trajectories are available for the future flybys E20 – E22. Their approximate trajectories can, however, be constructed from the planned location of closest approach and the estimated velocity vector of Cassini at that point (see figure 2.10). During all three planned encounters, Cassini is going to move parallel

to the equatorial plane. E20 is located about $7R_E$ above Enceladus' north pole, whereas E22 is going to take place about $20R_E$ below the south pole. In contrast, E21 is similar to E7 and E9 and will therefore pass through the plume close to the south pole.

While the Magnetometer onboard Cassini is independent from the orientation of the spacecraft, the particle detectors (INMS, CAPS, CDA) need to point towards the ram direction to collect useful data. The flybys with a suitable spacecraft pointing for these instruments were E2, E3, E5, E7, E10, E14, E17 and E18.

In addition, four occultations of the sun or a star by Enceladus' plume were observed by Cassini UVIS: the first occultation of the star γ Orionis took place during the E2 flyby [*Hansen et al.* 2006]. Analysis of these data allowed to determine the column density of the plume. During the second observation on 24 October 2007, the plume occulted the star ζ Orionis [*Hansen et al.* 2008]. The only occultation of the sun occurred during the E10 flyby [*Hansen et al.* 2011]. During both occultations, UVIS observed supersonic gas jets with a higher density, superimposed on the plume background. The E15 encounter was designed to enable a dual stellar occultation of two of the three stars in Orion's belt. However, the results from this observation have not yet been published.

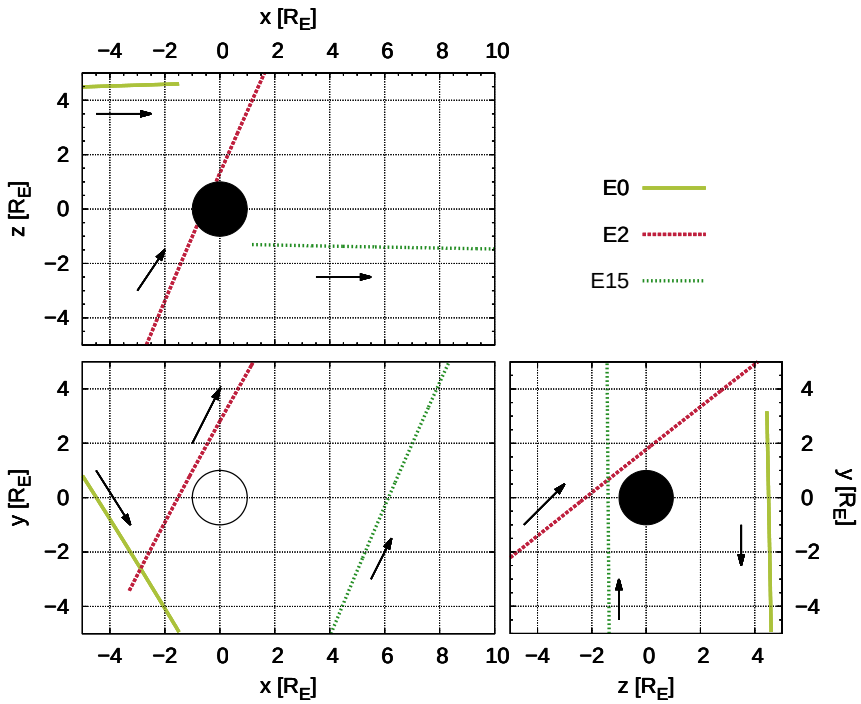

Figure 2.5: Trajectories of E0, E2, and E15, projected onto the planes of ENIS.

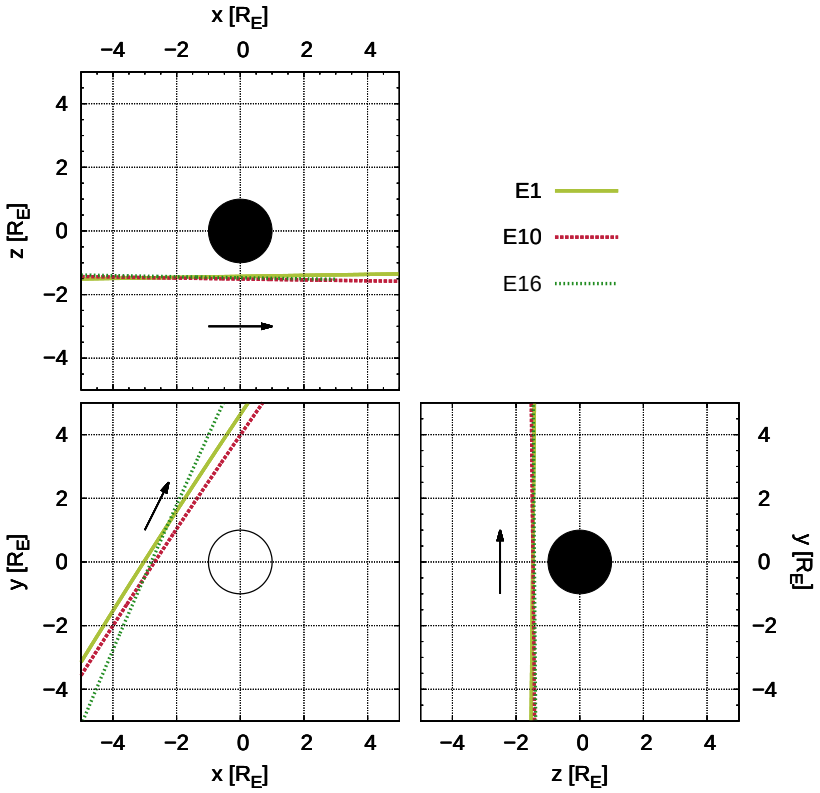

Figure 2.6: Trajectories of E1, E10, and E16, projected onto the planes of ENIS.

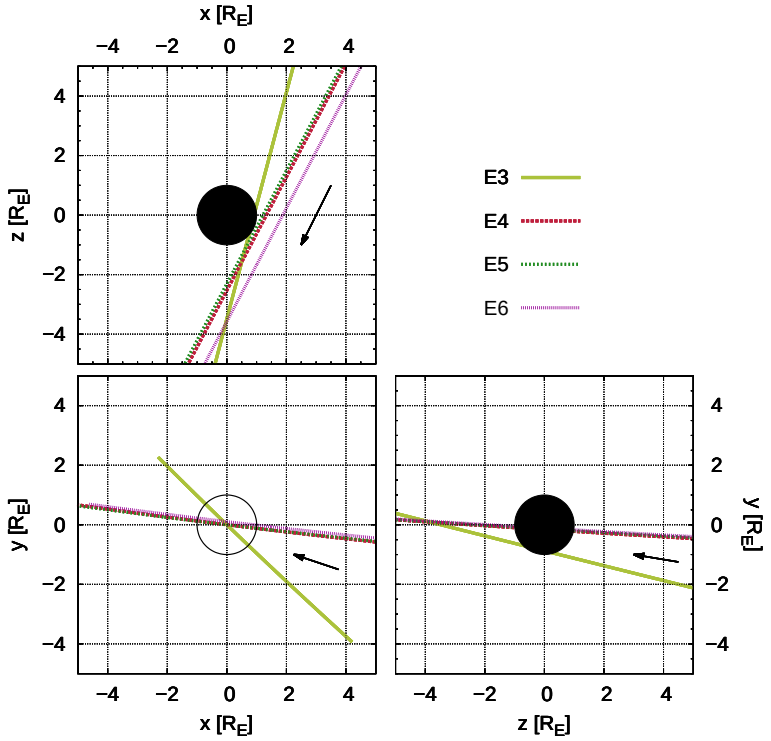

Figure 2.7: Trajectories of E3 – E6, projected onto the planes of ENIS.

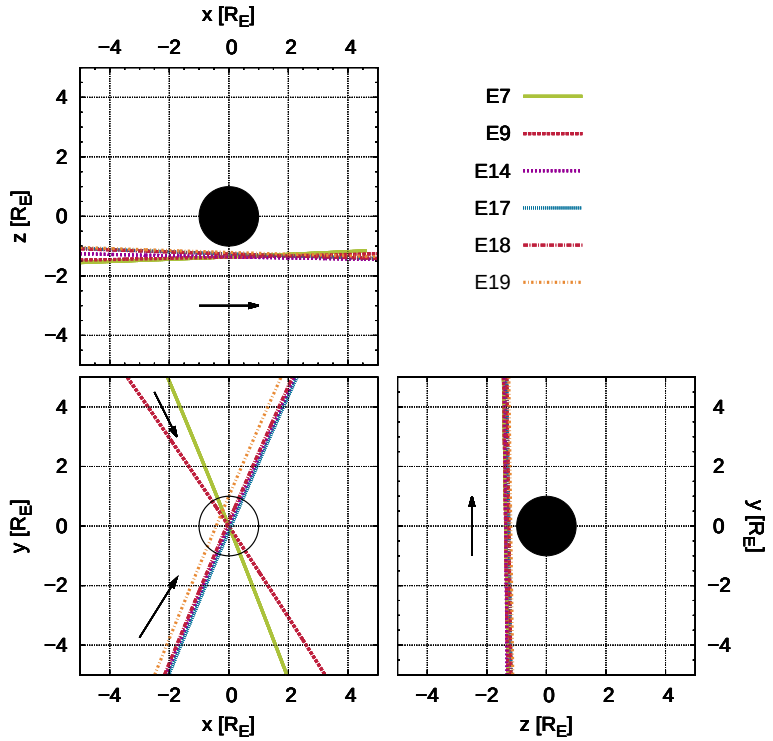

Figure 2.8: Trajectories of E7, E9, E14 and E17 – E19, projected onto the planes of ENIS.

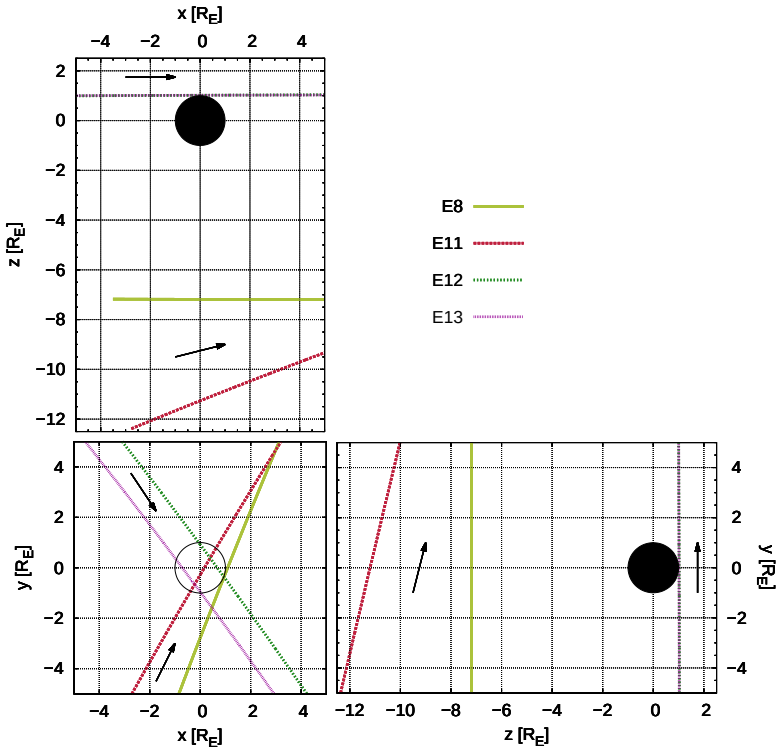

Figure 2.9: Trajectories of E8, E11, E13, and E13, in ENIS coordinates.

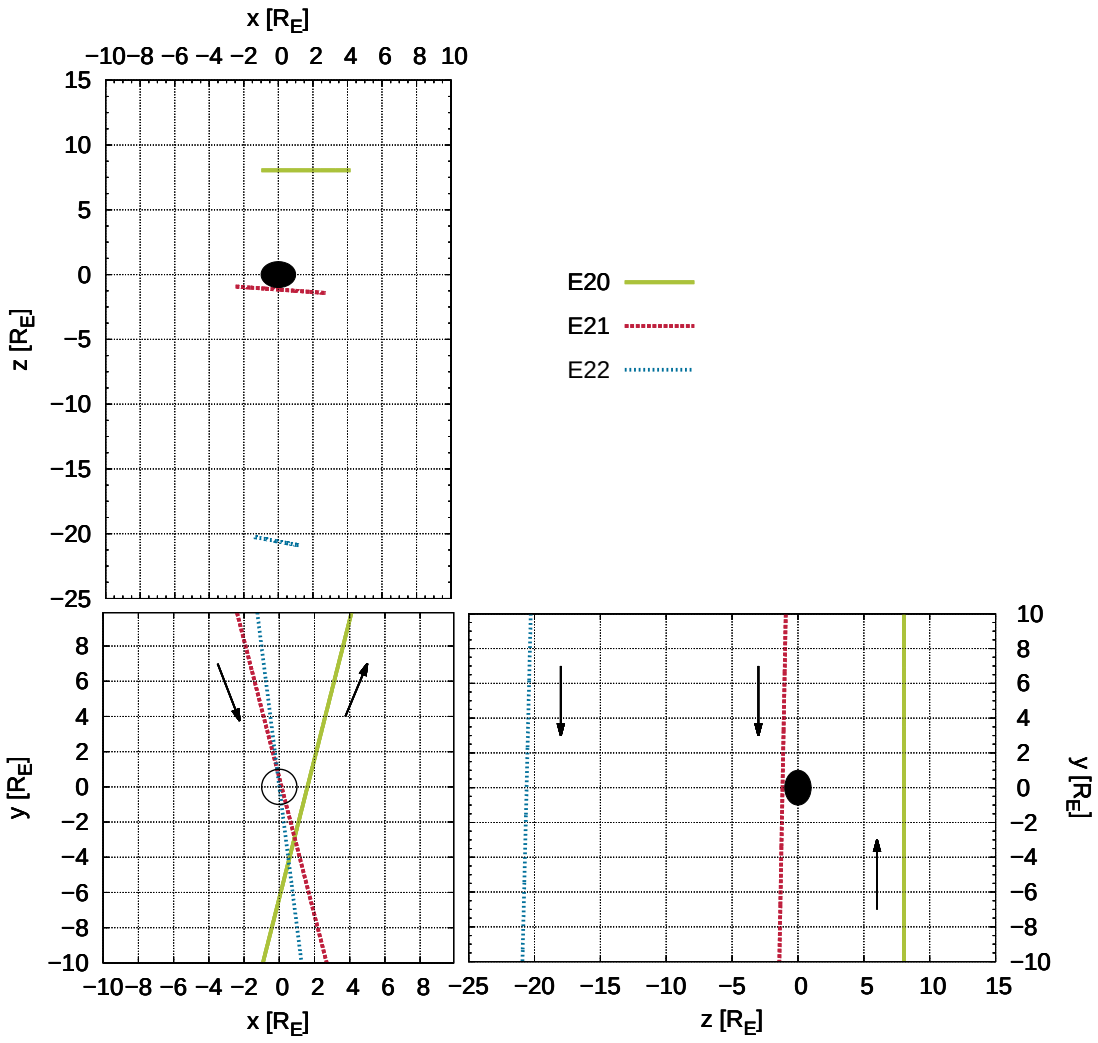

Figure 2.10: Approximate trajectories of the future flybys E20, E21 and E22.

Table 2.2: Overview about the Enceladus flybys of the entire Cassini mission. Information on closest approach (time, date and distance) as well as Enceladus' corresponding Saturn Local Time (SLT) and sub-solar latitude (SSL) are provided. The trajectory can be reconstructed from the planetographic longitude and latitude of closest approach and Cassini's velocity vector. The upstream plasma density n_0 is estimated from measurements of the upper hybrid frequency by RPWS.

Flyby	Rev.	Date		Year	(DOY)	Time [UTC]	SLT [h]	SSL [°]	Alt [km]	Long. [°]	Lat. [°]	v_x	v_y	v_z	v [km/s]	n_0 [cm^{-3}]
E0	003	17	Feb	2005	(048)	03:30:29	22.6	-22.6	1261	239.6	50.1	3.5	-5.7	0.1	6.7	90
E1	004	9	Mar	2005	(068)	09:08:02	17.0	-22.4	500	303.3	-29.9	3.6	5.5	0.1	6.6	60
E2	011	14	Jul	2005	(195)	19:55:21	17.1	-21.1	171	326.2	-23.0	2.6	4.8	6.1	8.2	65
E3	061	12	Mar	2008	(072)	19:06:12	23.2	-8.0	52	134.1	-20.4	-3.5	3.4	-13.5	14.4	90
E4	080	11	Aug	2008	(224)	21:06:18	22.7	-5.6	51	96.9	-27.2	-8.2	1.0	-15.7	17.7	55
E5	088	9	Oct	2008	(283)	19:06:40	22.5	-4.7	26	96.7	-28.5	-8.2	1.0	-15.7	17.7	90
E6	091	31	Oct	2008	(305)	17:14:51	22.5	-4.4	171	92.5	-27.7	-8.2	1.0	-15.7	17.7	45
E7	120	2	Nov	2009	(306)	07:41:57	10.9	1.3	98	126.4	-89.2	2.9	-7.2	0.1	7.7	60
E8	121	21	Nov	2009	(325)	02:09:56	3.7	1.6	1596	111.9	-83.4	2.9	7.2	0.0	7.8	45
E9	130	28	Apr	2010	(118)	00:10:17	9.3	4.0	99	151.5	-89.1	3.6	-5.4	0.1	6.5	75
E10	131	18	May	2010	(138)	06:04:39	3.9	4.1	440	303.4	-33.5	3.6	5.4	-0.1	6.5	65
E11	136	13	Aug	2010	(225)	22:30:51	3.6	5.5	2554	34.7	-78.5	3.4	5.8	1.4	6.8	60
E12	141	30	Nov	2010	(334)	11:53:59	8.8	7.1	46	53.6	61.8	3.7	-5.0	0.0	6.3	55
E13	142	21	Dec	2010	(355)	01:08:27	8.8	7.4	49	232.9	60.6	3.7	-5.0	0.0	6.2	65
E14	154	1	Oct	2011	(274)	13:52:26	23.8	11.4	98	198.5	-89.8	3.0	6.8	-0.1	7.4	85
E15	156	19	Oct	2011	(292)	09:22:12	23.8	11.6	1234	112.8	-13.8	2.9	6.9	-0.1	7.5	90
E16	156	6	Nov	2011	(310)	04:58:53	23.8	12.1	498	294.0	-29.3	3.0	6.7	-0.1	7.4	105
E17	163	27	Mar	2012	(087)	18:30:09	0.6	13.8	73	123.0	-86.9	3.0	6.9	-0.1	7.5	110
E18	164	14	Apr	2012	(105)	14:01:38	0.6	13.9	73	284.2	-87.0	3.0	6.9	-0.1	7.5	100
E19	165	2	May	2012	(123)	09:31:29	0.5	14.3	73	291.7	-71.9	2.9	6.9	-0.1	7.5	70
E20	223	14	Oct	2015	(287)	10:41:30	12.2	25.4	1838	104.3	79.1	2.1	8.3	0.0	8.5	-
E21	224	28	Oct	2015	(301)	15:22:47	20.8	25.4	48	68.8	-83.7	2.1	-8.2	-0.2	8.5	-
E22	228	19	Dec	2015	(353)	17:49:20	21.3	25.7	4998	352.9	-88.4	1.2	-9.5	-0.3	9.5	-

Table 2.3: Overview of the five close Rhea flybys of the Cassini mission. The upstream density is estimated from *Roussos et al.* [2012]; the background magnetic field $\underline{B_0}$ is obtained from MAG data at closest approach.

Flyby	Rev.	Date		Year	(DOY)	Time [UTC]	SLT [h]	SSL [°]	Alt [km]
R1	018	26	Nov	2005	(330)	22:37:38	12.0	-19.2	502
R1.5	049	30	Aug	2007	(242)	01:19:01	8.5	-10.6	5726
R2	127	2	Mar	2010	(061)	17:40:35	23.3	3.2	101
R3	143	11	Jan	2011	(011)	04:53:25	13.3	7.7	70
R4	183	9	Mar	2013	(068)	18:17:28	1.1	17.5	1000

Flyby	Long. [°]	Lat. [°]	v_x	v_y	v_z	v	n_0 [cm^{-3}]	$(B_{0,x}, B_{0,y}, B_{0,z})$ [nT]
			[km/s]					
R1	88.7	-10.4	-0.1	7.3	0.0	7.3	4	(0.9,1.3,-28.2)
R1.5	84.3	5.4	0.7	-6.6	0.1	6.7	6 - 8	(0.4,1.3,-21.3)
R2	256.1	81.7	-1.8	8.4	0.0	8.6	3.5 - 4.5	(4.6,2.8,-22.1)
R3	96.9	-76.3	-1.1	-8.0	0.0	8.0	8	(3.1,1.5,-21.4)
R4	173.4	18.3	-3.0	2.4	8.4	9.3	-	(1.4,1.1,-21.0)

2.3.2 Rhea Flybys

The five Rhea encounters consist of four targeted flybys labeled R1 – R4 and a more distant, non-targeted flyby termed "R1.5". In analogy to the Enceladus flybys, information on these flybys are summarized in table 2.3. As already mentioned, the magnetosphere exhibits a high level of variability at Rhea's orbit. Therefore, the upstream density ranges from $n_0 = 4\,\mathrm{cm}^{-3}$ to $n_0 = 8\,\mathrm{cm}^{-3}$ for the different flybys. A column for the background magnetic field has also been added, since the field strength changes by more than 10% from flyby to flyby. Plots of the electron density and the magnetic field for the first four flybys can be found in the work of *Roussos et al.* [2012]. Please note that for R4, the density has not yet been presented in the literature and plots showing the upper hybrid frequency are also not yet available at the Planetary Data System.

Figure 2.11 displays the trajectories of the five encounters. The R1 flyby on 26 Nov. 2005 was located downstream of Rhea, parallel to the equatorial plane at $z = -0.3R_{RH}$ and directed towards Saturn. During this flyby, Cassini passed directly through Rhea's central wake. In contrast to that, the non-targeted R1.5 flyby crossed Rhea's distant wake at about $9R_{RH}$ and above the equatorial plane at $z = 0.8R_{RH}$. During R1.5, Cassini moved towards negative y . As can be seen in figure 2.11, Cassini passed above Rhea's north pole during R2, approaching the moon from the Saturn-averted side. Within the interval shown in the figure, the flyby trajectory was nearly parallel to the $(z = 0)$-plane and only slightly inclined with respect to the y axis: in the inbound region of R2 (i.e. for $y < 0$), Cassini was located in the downstream half space (i.e. at $x > 0$), whereas in the outbound segment $(y > 0)$, the spacecraft traveled through the upstream half space $(x < 0)$. The subsequent R3 encounter occurred below Rhea's south pole and featured a strong similarity to the geometry of R2. Again, the spacecraft trajectory was nearly parallel to the $(z = 0)$-plane and possessed only a small inclination against the y axis. However, during R3 Cassini was

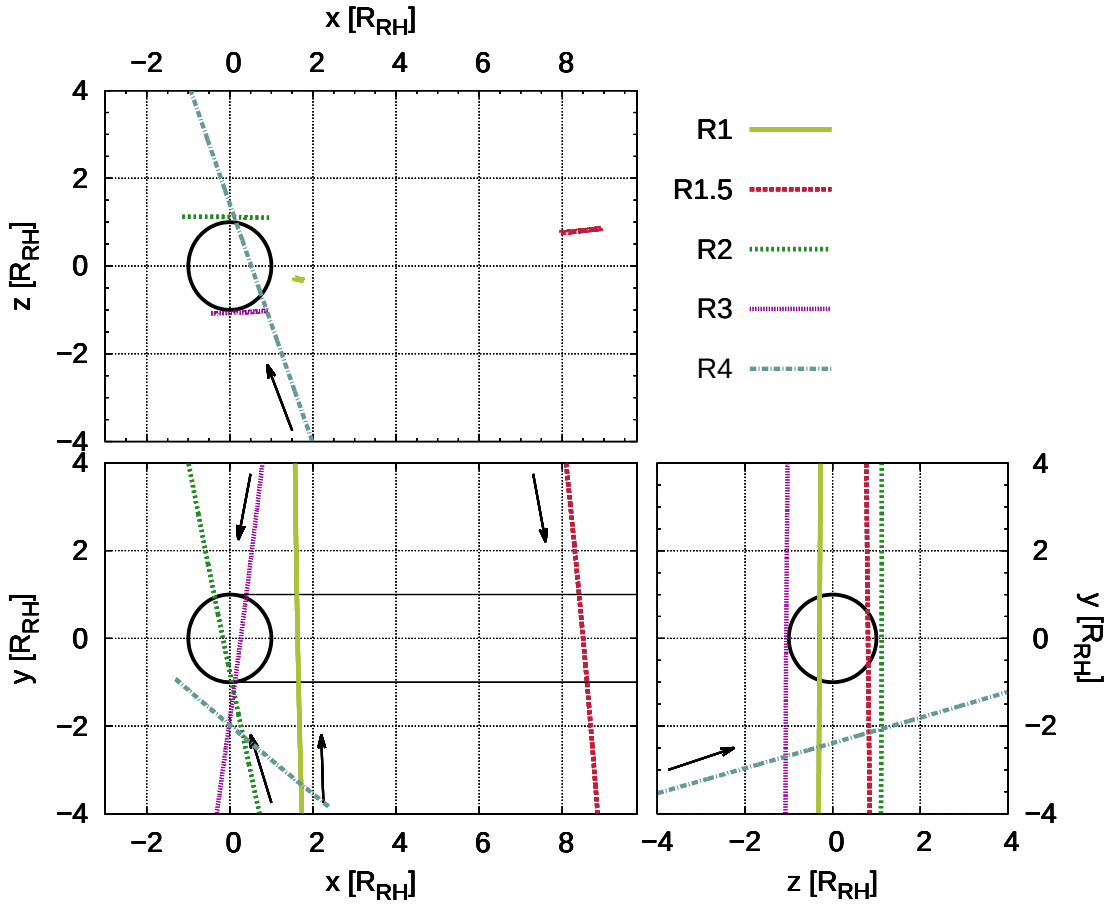

Figure 2.11: Cassini's trajectories for the five Rhea flybys in RHIS coordinates. The thin black lines denote the outer boundaries of Rhea's geometric plasma shadow, i.e. the cylinder $\sqrt{y^2 + z^2} = R_{RH}$ for $x \geq R_{RH}$.

located downstream of Rhea ($x > 0$) in the Saturn-facing half space ($y > 0$), whereas the segment of the flyby trajectory in the Saturn-averted half space ($y < 0$) lead through the ($x < 0$) half space. As can also be seen from figure 2.11, closest approach of both flybys was located at a distance of about only $0.1R_{RH}$ above the surface of Rhea. During the northbound R4 encounter on 09 March 2013, the spacecraft achieved a closest approach altitude of 1000 km(= $1.3R_{RH}$), i.e. about an entire order of magnitude larger than during R2 and R3. In contrast to the other flybys, R4 possessed a south-to-north trajectory and passed by the moon at its Saturn-averted side.

2.4 Upstream Plasma Conditions at Enceladus and Rhea

While in section 2.2, an overview of the plasma properties in Saturn's inner and middle magnetosphere was provided, Enceladus' and Rhea's plasma environments according to the observations from the various close flybys will be specified in this section. A sketch of the moons' plasma environment is presented in figure 2.12. The parameters described

here characterize the default upstream plasma (marked by the hat) used for the discussion of Enceladus' and Rhea's plasma interactions. An overview of the most important parameters is provided in table 2.4.

MAG data showed that at Enceladus, the magnetic field is dipolar with a magnitude of $\hat{B}_0 = 325\,\mathrm{nT}$ [*Dougherty et al.* 2006]. CAPS observations during the E2 flyby confirmed that Enceladus is embedded in a dense plasma of electrons, hydrogen and water group ions (W^+=$\{O^+, OH^+, H_2O^+, H_3O^+\}$) with a density of $\hat{n}_0 = 70.5\,\mathrm{cm}^{-3}$ [*Tokar et al.* 2006]. For the different flybys, the densities are in the range of $n_0 = 45 - 110\,\mathrm{cm}^{-3}$ as listed in table 2.2. The average ion mass is $m_i = 17.6\,\mathrm{amu}$ [*Tokar et al.* 2006]. For an ideally corotating plasma with a velocity of $u_{0,\mathrm{Sat.}} = 39\,\mathrm{km/s}$ in the Saturn-centered frame, the flow speed relative to Enceladus' slower orbital velocity ($v_E = 12.6\,\mathrm{km/s}$, see table 2.1) is given by $\hat{u}_0 = u_{0,\mathrm{Sat.}} - v_E = 26.4$ km/s. However, it was found that the ion bulk speed u_0 is about 80% of the ideal coratation, i. e. $u_0 = 30.4\,\mathrm{km/s} - 12.6\,\mathrm{km/s} = 17.8\,\mathrm{km/s}$ relative to Enceladus [*Wilson et al.* 2009]. According to the CAPS measurements from E2 [*Tokar et al.* 2006] and the SOI observations summarized in equation (2.3), the ion temperature is about $k_B T_i = 35\,\mathrm{eV}$. As already mentioned, the electrons can be divided into a cold Maxwellian population, photoelectrons and a hot (suprathermal) population. The temperature of the cold electron population is approximately $k_B T_{ec} = 1.35\,\mathrm{eV}$ [*Tokar et al.* 2006], which is roughly consistent with equations (2.9) and (2.10). Since the treatment of the photoelectrons and the suprathermal population was improved from chapter 5 to chapter 6, their temperatures will be discussed in the respective chapters.

Near Rhea's orbit, the background magnetic field is still nearly dipolar. During R2 and R3, it possessed a magnitude of about $\hat{B}_0 = 21\,\mathrm{nT}$, which is slightly smaller than observed during the initial R1 flyby in 2005 (see table 2.3). The number density of the magnetospheric water group ions (average mass $m_i = 17\,\mathrm{amu}$) is about $\hat{n}_0 = 6\,\mathrm{cm}^{-3}$ and the temperature is $kT_i = 200\,\mathrm{eV}$ (cf. table 1 in *Khurana et al.* [2008] and table 2 in *Wilson et al.* [2009]), which is roughly consistent with equation (2.3). Measurements of thermal ion properties from the R1 encounter and the more distant, non-targeted R1.5 flyby suggest plasma velocities of 57.6 km/s and 60.0 km/s, respectively [*Wilson et al.* 2010]. Compared to the full corotation speed of 86.4 km/s, i. e. $\hat{u}_0 = 86.4\,\mathrm{km/s} - 8.5\,\mathrm{km/s} = 77.9\,\mathrm{km/s}$ relative to Rhea (see table 2.1), the plasma sub-corotates by about 30%. As an average of the two flybys, $u_0 = 50\,\mathrm{km/s}$ is used as the velocity of the incident magnetospheric flow relative to Rhea. Based on data from CAPS, *Sittler et al.* [2006, 2007] derived a temperature of $k_B T_{ec} = 10\,\mathrm{eV}$ for the thermal electrons at Rhea's L-shell, i.e. their value is more than an order of magnitude smaller than the value for the ions (see equation (2.9)).

From these upstream flow conditions, the characteristic parameters of Enceladus' and Rhea's plasma interactions can be derived. These are also listed in table 2.4. The characteristic velocity is the Alfvén speed,

$$\underline{v}_A = \frac{\underline{B}_0}{\sqrt{\mu_0 n_i m_i}} \quad , \tag{2.12}$$

which assumes values between $|\underline{v}_A| = v_A = 162\,\mathrm{km/s}$ and $v_A = 253\,\mathrm{km/s}$ at Enceladus, and between $v_A = 39\,\mathrm{km/s}$ and $v_A = 56\,\mathrm{km/s}$ at Rhea. Hence, the alfvénic Mach number

$$M_A = \frac{u_0}{v_A} \tag{2.13}$$

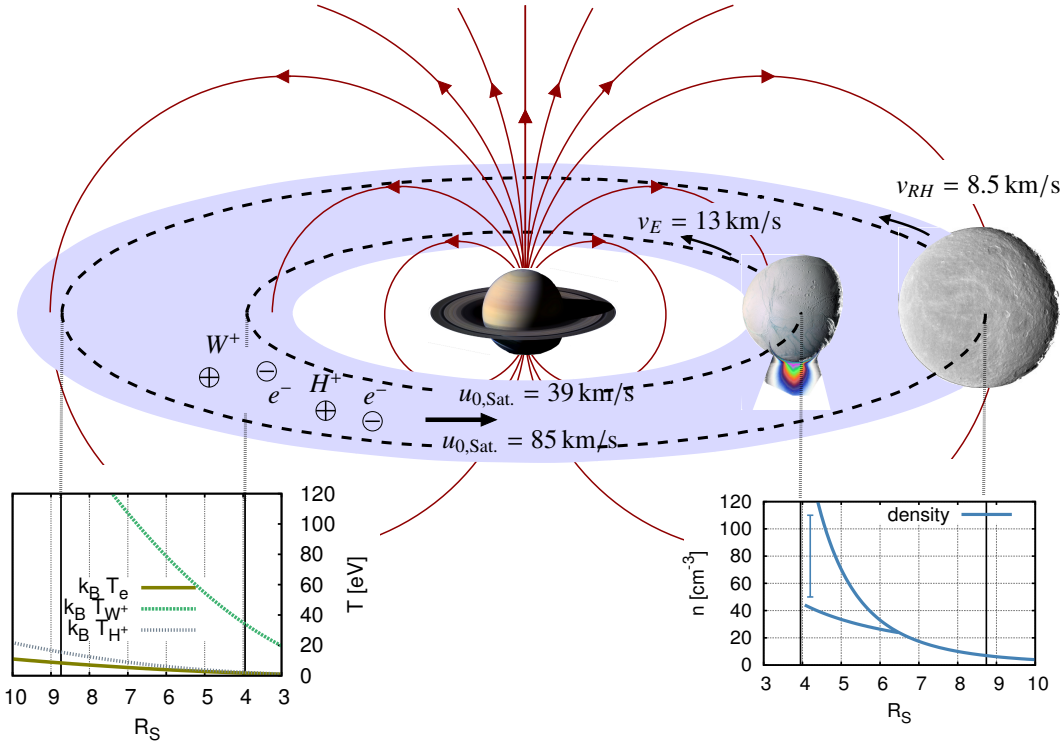

Figure 2.12: Summary of Enceladus' and Rhea's magnetospheric environment (not to scale). On their Keplarian orbits at $3.95R_S$ and $8.74R_S$, the two icy moons are overtaken by the (sub)-corotating magnetospheric plasma consisting of electrons, protons and water group ions (velocity $u_{0,\mathrm{Sat.}}$ in a non-rotating frame of reference). The profiles of plasma densities and temperatures in the inner magnetosphere are shown in the bottom plots (cf. equations (2.2),(2.3), (2.9) and (2.8)). The strength of Saturn's dipole field decreases from about $B_0 = 325\,\mathrm{nT}$ at Enceladus to about $B_0 = 21\,\mathrm{nT}$ at Rhea.

is $M_A = 0.07 - 0.11$ (Enceladus) and $M_A = 0.90 - 1.27$ (Rhea). The plasma beta is given by

$$\beta_\alpha = \frac{\hat{n}_0 k_B T_\alpha}{\frac{\hat{B}_0^2}{2\mu_0}} \quad , \tag{2.14}$$

yielding $\beta_i = 0.0094$ and $\beta_e = 0.0004$ for ions and electrons at Enceladus, respectively. At Rhea, the betas are considerably larger with $\beta_i = 1.10$ and $\beta_e = 0.05$. The sound speed is given by

$$c_s = v_A \sqrt{\kappa \frac{(\beta_i + \beta_e)}{2}} \quad , \tag{2.15}$$

where κ denotes the adiabatic exponent with $\kappa = 2$. This value takes into account that the magnetic field reduces the degrees of freedom to two. The resulting sonic Mach numbers $M_S = u_0/c_S$ are $M_S = 0.89$ for Enceladus and $M_S = 1.02$ for Rhea. The maximum velocity of the fast magnetosonic wave defines the magnetosound speed

$$c_{MS} = \sqrt{v_A^2 + c_S^2} \quad . \tag{2.16}$$

The ranges of the corresponding magnetosonic Mach numbers $M_{MS} = u_0/c_{MS}$ are $M_{MS} = 0.07 - 0.11$ (Enceladus) and $M_{MS} = 0.68 - 0.80$ (Rhea). The length scales of Rhea's

Table 2.4: Properties of Enceladus' and Rhea's magnetospheric environments as measured by Cassini during the flybys. See text for the definitions of the derived values.

		Enceladus	Rhea
Quantity	Symbol	Values	
Magnetic field (default value)	$\hat{B}_0$	325 nT	21 nT
Plasma density (range)	$n_e = n_i$	45 – 110 cm^{-3}	4 – 8 cm^{-3}
Plasma density (default value)	$\hat{n}_0$	70.5 cm^{-3}	6 cm^{-3}
Thermal electron temperature	$k_B T_{ec}$	1.35 eV	10 eV
Ion temperature	$k_B T_i$	35 eV	200 eV
Ion corotation speed	$\hat{u}_0$	26.4 km/s	77.9 km/s
Ion bulk speed	u_0	17.8 km/s	50 km/s
Average ion mass	m_i	17.6 amu	17 amu
		Derived values	
Alfvénic Mach number	M_A	0.07 – 0.11	0.90 – 1.27
Sonic Mach number	M_S	0.89	1.02
Magnetosonic Mach number	M_{MS}	0.07 – 0.11	0.68 – 0.80
Ion gyroradius	r_g	15 km $0.06R_E$	654 km $0.86R_{RH}$
Inverse gyrofrequency	Ω_i^{-1}	0.6 s	8.4 s
Electron plasma beta	β_e	0.0004	0.05
Ion plasma beta	β_i	0.0094	1.10

plasma interaction are determined by the ion gyroradius

$$r_g = \frac{m_i \hat{u}_0}{e\hat{B}_0} \quad , \tag{2.17}$$

yielding $r_g = 15\,\mathrm{km} = 0.06R_E$ upstream of Enceladus and $r_g = 654\,\mathrm{km} = 0.86R_{RH}$ at Rhea. In contrast, the length scales of Enceladus' plasma interaction are determined by the extent of the plume and the pick-up tail [*Kriegel et al.* 2009]. A characteristic time scale is provided by the inverse ion gyrofrequency

$$\Omega_0^{-1} = \frac{m_i}{e\hat{B}_0} \quad , \tag{2.18}$$

i. e. $\Omega_0^{-1} = 0.6\,\mathrm{s}$ and $\Omega_0^{-1} = 8.4\,\mathrm{s}$ for Enceladus and Rhea, respectively.

Hence, the plasma impinging on Enceladus is subalfvénic and submagnetosonic, i.e. similar to the environment of Jupiter's moon Io. Rhea is exposed to a trans-alfvénic and submagnetosonic flow. These incident flow conditions are qualitatively similar to those at the other large icy satellites Tethys [*Simon et al.* 2009a] and Dione [*Simon et al.* 2011a]. In the next chapter, the general picture of the plasma interaction of an obstacle exposed to such a plasma flow will therefore be discussed.

3 Basics of Enceladus' and Rhea's Plasma Interaction

In this chapter, the foundations of the understanding of the plasma structures arising from the interaction of Saturn's magnetospheric plasma with Enceladus and Rhea will be laid. Since Rhea does not possess a significant ionosphere[1], the structures resulting from plasma absorption at the surface of an icy moon will be briefly described in section 3.1. Moreover, previous studies of Rhea's interaction are summarized. The main part of this chapter deals, however, with the theoretical background of the Alfvén wing, i.e. the magnetic field structures caused by the subalfvénic plasma interaction of a conducting obstacle (section 3.2). Since it will be demonstrated within this thesis that the plasma structures of both, Enceladus and Rhea, reveal new aspects of the properties and the generation of an Alfvén wing, its analytical description will be presented in some detail. In section 3.4, an overview of the state of knowledge on Enceladus' plasma interaction apart from the results presented in this thesis is provided. In particular, the open questions which are addressed in this work will be pointed out in section 3.5.

3.1 Interaction of an Inert Moon

For any planetary body that possesses neither an intrinsic magnetic field nor a substantial ionosphere, the impinging plasma is simply absorbed at the surface of the body. This absorption results in the formation of an extended density cavity in the downstream region. The shape of this density cavity, its refilling and the associated currents and magnetic field structures have already been analyzed by a number of authors. The plasma environments of the icy moons Rhea and Tethys have been studied by e.g., *Khurana et al.* [2008], *Roussos et al.* [2008a] and *Simon et al.* [2009b], whereas the interaction of Enceladus' absorbing body has been analyzed in a preceding study [*Kriegel et al.* 2009].

Perpendicular to the magnetic field, the density cavity is approximately restricted to the width of the moons' geometric shadow with respect to the plasma flow. Parallel to the magnetic field, the depletion region expands along the magnetic field lines and forms a two-dimensional, symmetric cone (cf. fig. 1 of *Roussos et al.* [2008a]). The structure of the wake region can be explained from different points of view:

The most illustrative description is provided by the motion of single particles, cf. figure 3.1. Due to the high thermal velocity of the upstream plasma ($v_{th} \gtrsim u_0$), many particles

[1] The magnetic significance of Rhea's ionosphere is discussed in chapter 7.

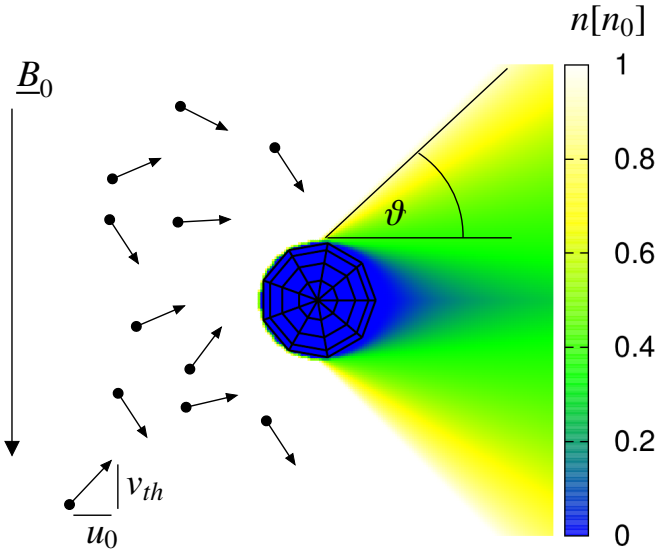

Figure 3.1: Plasma density resulting from absorption at the surface of an icy moon. The density contours are plotted according to equation (3.1) for $u_0 = c_s$, which is approximately valid for Rhea.

possess a large field-aligned velocity component which is comparable to the bulk speed. These particles may impinge on the surface of the moon at high latitudes. On the downstream side, these missing particles lead to a region of reduced density not only in the geometric shadow, but also in a cone-like region extending along the field lines. Assuming a Maxwellian velocity distribution, the standard deviation of the distribution of the field-aligned velocity ($\overline{v_\parallel}$), therefore roughly defines the opening angle $\vartheta \approx \arctan \overline{v_\parallel}/u_0$ of the cone [*Khurana et al.* 2008]. Similarly, the thermal motion also explains the refilling of the core shadow by particles which penetrate into the wake with large field-aligned velocities. Perpendicular to magnetic field, the gyration prevents the free thermal motion of the ions. If the gyroradii are small compared to the obstacle, the particles cannot enter the wake and in consequence, the width of the wake is nearly identical to the diameter of the moon.

A more sophisticated explanation for the structure of the plasma density downstream of an absorbing obstacle has been discussed by *Roussos et al.* [2008a]. When considering plasma expansion into the geometrical shadow under the initial condition that this region is completely devoid of plasma, one obtains the following expression for the density in the (x, z)-plane (eq. (7) of *Roussos et al.* [2008a])

$$n(x,z) = \begin{cases} n_0 \exp\left[-\left(\dfrac{(-|z|+1)\,u_0}{(x-x_{limb})\,c_S} + 1\right)\right] & ; \quad \dfrac{(-|z|+1)\,u_0}{(x-x_{limb})\,c_S} > -1 \\ n_0 & ; \quad \dfrac{(-|z|+1)\,u_0}{(x-x_{limb})\,c_S} \leq -1 \end{cases} , \tag{3.1}$$

where x_{limb} is the location of the limb along the x axis and c_s denotes the sound speed (see eq. (2.15)). The density resulting from equation (3.1) is also shown in figure 3.1. This density profile is in agreement with hybrid simulations with the precursor of the A.I.K.E.F. code performed by *Roussos et al.* [2008a] for Rhea and by *Simon et al.* [2009b] for Tethys. In addition, plasma absorption by the solid body of Enceladus has been simulated by

means of the A.I.K.E.F. in a preceding study [*Kriegel et al.* 2009].

A third point of view to analyze the structure of the wake is given by the superposition of the magnetohydrodamic modes launched at the surface of the obstacle [*Neubauer* 1998]. Such an analysis has been carried out by *Wiehle et al.* [2011] for the Earth moon and by *Vernisse et al.* [2013] in a more general study of the interaction of an absorbing obstacle.

A peculiar feature of Rhea's plasma interaction stems from the large gyroradii of the magnetospheric upstream ions which are almost comparable to the radius of Rhea (cf. table 2.4). Therefore, the absorption of magnetospheric particles at the moon's surface is expected to possess a pronounced asymmetry with respect to the direction of the convective electric field. In chapter 7, it shall be discussed how the large gyroradii of the ions impinging on Rhea modify the shape of the plasma wake. At Tethys ($r_g = 30.9\,\mathrm{km} = 0.06 R_T$) and Dione ($r_g = 92.3\,\mathrm{km} = 0.16 R_D$), asymmetries due to finite gyroradius effects are expected to play a far less important role (where R_j, $j = T, D$, denotes the respective satellite radius, values of r_g derived from table 1 in *Khurana et al.* [2008]).

The discussion above focused only on the ions. Due to the higher mobility, the electrons refill the wake more quickly. To maintain quasi-neutrality, the ions are dragged into the wake by ambipolar fields. On scales larger than the Debye length, these processes can be approximated by the gradient of the electron pressure in the momentum equation. Higher electron temperatures therefore yield a faster refilling of the wake (see *Simon et al.* [2009b]).

The density gradients at the boundaries of the wake are associated with diamagnetic currents which drag the magnetic field lines into the wake (see also figure 1 of *Simon et al.* [2009b]). In other words, the deficit of plasma pressure is compensated by an enhanced magnetic field pressure. A quantitative verification of the pressure balance will be presented together with the discussion of magnetic field signatures measured during the polar Rhea flybys R2 and R3 in section 7.2.1.

Apart from the magnetic field structures resulting from the plasma wake, the solid body itself interacts with the magnetic field. This has already been discussed in *Kriegel* [2009] and *Kriegel et al.* [2009] and shall only be briefly summarized. In stationary state, any currents generated within a possible conducting interior of the moons – such as Enceladus' liquid water ocean – have to flow through the crust and close outside the obstacle. Thus, the conductivity of the crust is crucial for the formation of stationary current systems in the interior and the associated reaction of the magnetic field to the obstacle, regardless of the conductivity of deeper regions below the crust. The crusts of Saturn's icy moons can be regarded as an insulating layer of ice, which is why no significant current is able to flow through the surface [*Neubauer* 1998]. If the background field exhibited a significant time variation like the Jovian magnetic field at the orbits of the Galilean moons, induction within a subsurface ocean would generate a measurable contribution to the magnetic field outside the moon, see e.g. *Seufert et al.* [2011]. On the one hand, the background magnetic field at Enceladus can be regarded as stationary on the time scale of the flybys ($\sim$ min). Further long-time variations like the field modulation with the SKR period (cf. section 2.2) as well as the plume variability along the orbit (see section 2.1) induce only negligible secondary magnetic fields. On the other hand, Rhea is embedded in a rather dynamical magnetospheric environment, but the moon's interior is very likely an undifferentiated and insulating mixture of ice and rock [*Anderson and Schubert* 2007]. Therefore,

both moons should not generate a noticeable perturbation of the magnetic field directly by the presence of their solid bodies, but the perturbations are caused in the plasma wake and by the plume. Consequently, the magnetic field should freely diffuse through the moons. This is the reason why these objects are also called "inert" (= non-reacting) moons.

The hybrid simulations of Tethys' plasma environment by *Simon et al.* [2009b] showed that this picture of the plasma interaction of such an inert moon is consistent with MAG data from the only targeted Tethys flyby. In addition, the simulations of *Roussos et al.* [2008a] successfully explained MAG data from the R1 flyby of Rhea, further confirming the picture of the plasma interaction described above. In contrast, analysis of MAG data from the Dione D1 flyby by *Simon et al.* [2011a] showed a weak draping of the magnetic field lines around the moon, thereby indicating the presence of a tenuous atmosphere around Dione. These magnetic field perturbations were not present in MAG data from the subsequent D2 encounter, since this flyby passed through the wake in the equatorial plane [*Simon et al.* 2011a]. Thus, the R1 flyby of Rhea was probably not suitable to decide whether Rhea's thin atmosphere has a noticeable effect on the magnetic field structures or if Rhea's plasma environment can be fully explained in terms of the plasma interaction of an inert moon.

Thus, two major questions regarding Rhea's magnetospheric interaction will be addressed in chapter 7 of this thesis:

- Cassini's more recent Rhea flybys R2 and R3 are the first flybys that did not pass through the wake in the equatorial plane, but close to Rhea's poles. Do MAG data from these flybys comply with the understanding of Rhea's plasma interaction described above?

- What additional effects arise from the large gyroradii of the upstream plasma?

3.2 The Alfvén Wing

In the following, the interaction of a magnetized, subalfvénic plasma with a *conducting* obstacle, i. e. a volume with a conductivity perpendicular to the magnetic field that is larger than the perpendicular conductivity of its surrounding, is discussed. For simplicity, it is assumed that the plasma flows perpendicular to the magnetic field. Later, this general scenario will be specified to the interaction of Saturn's magnetospheric plasma with the Enceladean plume. As this scenario is similar to the interaction of the ionosphere of the Jovian moon Io with Jupiter's magnetospheric plasma, many aspects of this theory have been developed in the context of Voyager and Galileo observations at Io by e.g., *Neubauer* [1980], *Goertz* [1980], *Neubauer* [1998] and *Saur et al.* [1999]. It should be noted that this type of interaction scenario is not restricted to the moon-magnetosphere interactions at Saturn or Jupiter, but similar interactions also occur between some extrasolar planets and their respective stellar winds [*Saur et al.* 2013].

In the MHD approximation, the interaction of the plasma with any obstacle generates a fast mode, a slow mode and an Alfvén mode. Since the group velocity of the fast mode is isotropic, it may be considered as a type of spherical wave. Conservation of energy

then requires that the amplitude of the fast mode decreases with distance to the obstacle. In contrast, slow and Alfvén mode transport energy primarily along the magnetic field. However, the compressional slow mode does not possess field-aligned currents which could close the perpendicular currents generated by the obstacle. In consequence, only the Alfvén mode contributes significantly to the stationary structures in the far field [*Neubauer* 1998]. Thus, stationary non-linear alfvénic solutions of the MHD equations shall be discussed. At first, general properties of these solutions will be derived. Subsequently the associated current systems and magnetic field perturbations are described before these are eventually connected to the conductivity of the obstacle.

3.2.1 General Properties of the Alfvén Wing

Before commencing the analytical description of the Alfvén wing, at first a more illustrative model is discussed. When the magnetized plasma impinges on the obstacle, the magnetic field lines are continuously disturbed in its vicinity and drape around the volume with higher perpendicular conductivity. This draping of the magnetic field lines propagates as Alfvén waves along the field. While the waves propagate with the Alfvén speed, the obstacle moves relative to the plasma with a velocity $\underline{u}_0$ (perpendicular to $\underline{B}_0$). In the rest frame of the obstacle, the Alfvén waves therefore form a two-dimensional, Mach cone like, stationary structure, the *Alfvén wing*, as sketched in figure 3.2(a).

The superposition of the undisturbed Alfvén speed $\underline{v}_{A,0}$ and the upstream plasma velocity $\underline{u}_0$ defines the Alfvén characteristics (see figure 3.2(b))

$$\underline{\mathcal{L}}_0^{\pm} = \underline{u}_0 \pm \underline{v}_{A,0} \quad . \tag{3.2}$$

For a southward orientation of the background field ($\underline{B}_0 = -B_0\underline{e}_z$) that corresponds to the environments of the Saturnian and Jovian satellites, the upper sign ("+") refers to the southern part of the wing whereas the lower sign ("−") denotes the northern wing. The angle between the Alfvén characteristics and the background field is given by

$$\tan\theta_A = \frac{|\underline{u}_0|}{|\underline{v}_{A,0}|} = M_A \quad . \tag{3.3}$$

From the simple picture sketched in figure 3.2(a), a basic property of the Alfvén wing can already be derived. Considering a completely homogeneous and stationary plasma flow, the Alfvén waves should propagate undisturbed. Therefore, all plasma quantities should be constant along the Alfvén characteristics, implying that the Alfvén wing extends to infinity.

In reality, however, the Alfvén waves generated by the obstacle propagate through regions with spatially varying Alfvén velocity due to changes in the plasma density or the magnetic field strength. These gradients in the propagation velocity lead to a reflection of the waves, which particularly occurs at the parent planet's ionosphere for moon-magnetosphere interactions or at the corona of the central star in planet-star interactions. In addition, Alfvén waves may be partially reflected at the boundaries of the plasma torus in Saturn's or Jupiter's magnetosphere. Three cases are possible for the resulting interaction:

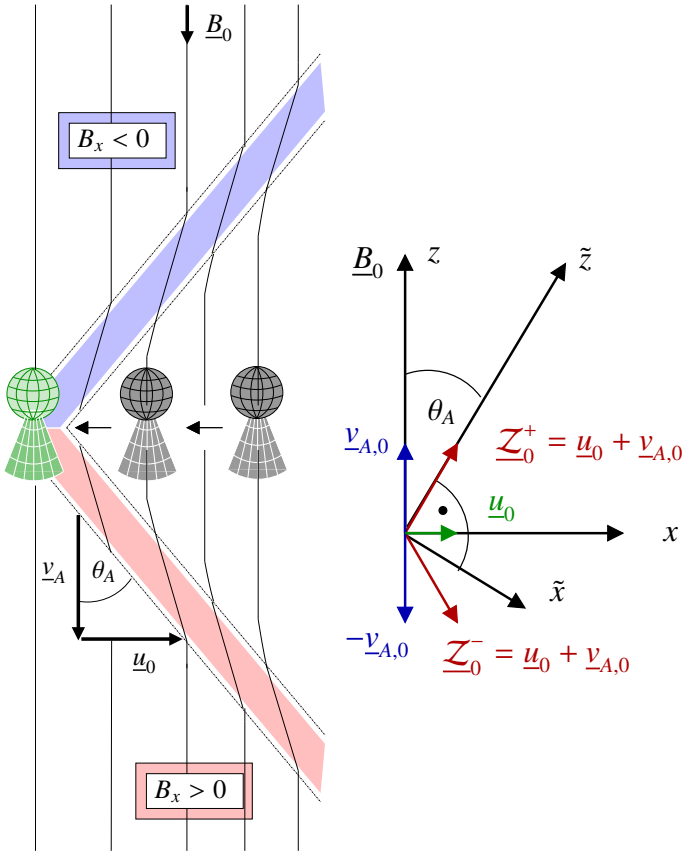

(a) (b)

Figure 3.2: Illustration of Alfvén wing and coordinate system. (a) Alfvén waves generated by the interaction between the magnetospheric plasma and Enceladus' plume propagate along the field lines while Enceladus moves relative to the plasma. The resulting stationary and two-dimensional, Mach cone like structure is the *Alfvén wing*. (b) Alfvén characteristics $\underline{\mathcal{Z}}_0^{\pm}$ and wing coordinate system, where $\tilde{z}$ is aligned with $\underline{\mathcal{Z}}_0^+$.

1. The reflected waves reach their source region around the obstacle. Therefore, the associated current system is closed in the parent planet's ionosphere and the ionospheric conductances act back on the current systems. In such a case, the description as Alfvén wing is not adequate any more. Instead, the resulting interaction has been referred to as 'unipolar inductor model'. For the case of Io, this approach has e.g. been applied by *Goldreich and Lynden-Bell* [1969], *Hill and Pontius* [1998].

2. When the reflected waves do not return to the obstacle, the interaction is decoupled from the parent planet or star. In this case, the far field is not characterized by the ionospheric conductivity, but only by the properties of the undisturbed plasma. Current closure occurs formally at infinity. This type of interaction is termed the ideal or pure Alfvén wing model.

3. For the intermediate case, i.e. a partial feedback between the obstacle and the reflecting boundary, no quantitative model of the mixed nonlinear Alfvén wave disturbance system exists [*Saur et al.* 2004b].

To check which of the models is the appropriate choice for the description of Enceladus' plasma interaction, the local plasma convection time τ_c has to be compared with the Alfvén travel time τ_A. The latter is defined as the time that is required for an Alfvén wave to travel from the moon to the parent planet's ionosphere and back to the moon while τ_c is the time which is needed for a plasma element to cross the interaction region. If τ_A is large compared to τ_c, the interaction is not influenced by the planet's ionosphere and the interaction is best described by the Alfvén wing model. For the average conditions at Enceladus, *Saur et al.* [2007] calculated $\tau_A \sim 300 - 400\,\mathrm{s}$ and $\tau_c \sim 10\,\mathrm{s}$. Thus, $\tau_A \gg \tau_c$ is well fulfilled at Enceladus and the Alfvén wing model is suitable to describe the plasma interaction of Enceladus. A detailed study of the reflections of Enceladus' Alfvén wings at Saturn's ionosphere (which do nevertheless occur) can be found in the work of *Jacobsen* [2011].

Although, the work presented in this thesis focuses on Enceladus' local interaction, i.e. the region within a few R_E around the moon, effects of the far field interaction, which include Saturn and the magnetosphere, shall be briefly discussed. The most prominent far field effect is the generation of an auroral footprint of the Alfvén wing in Saturn's ionosphere by acceleration and precipitation of electrons into the ionosphere. The UV, IR and radio emissions of the footprint therefore indicate where the Alfvén wing reaches the ionosphere (see, e.g. *Clarke et al.* [2004] for a discussion of Io's footprint in Jupiter's ionosphere). Io's primary footprint (leading spot) as well as multiple footprints of the reflected Alfvén wings have even been observed remotely by the HST [*Bonfond et al.* 2008, 2009]. Enceladus' footprint is unlikely more difficult to observe than that of Io due the significantly lower energy flux towards the ionosphere: Enceladus' interaction generates about 10^8 W, compared to a power of $\sim 10^{12}$ W in the Io scenario (values are theoretical Poynting fluxes calculated by *Saur et al.* [2013]; the observable power is even two orders of magnitude lower). In agreement with that, *Pryor et al.* [2011] reported on the detection of the Enceladus' footprint by UVIS in 3 out of 313 images which were in principle favorable for the detection of the footprint. More recent data increased these numbers to 6 detections out of 316 images [*Gurnett and Pryor* 2012]. Interestingly, the size of the footprint is considerably larger than the moon's diameter, indicating that the source region extends as far as $20R_E$. The brightness of the footprint varies even when it is visible by a factor of about three, suggesting a strong variability in the plume source rate. Since the images of the footprint were obtained on 26 August 2008 (about two weeks after the E4 flyby), the plume was probably particularly active at that time. *Pryor et al.* [2011] also report on the detection of field-aligned ion and electron beams by CAPS, which are likely associated with the reflection of the Alfvén wing. As discussed by *Jacobsen* [2011], the magnetometer observations obtained inbound of the E4 flyby show wave-like field perturbations that seem to be related to these particle beams of the reflected wing. However, it remains puzzling why the E4 flyby was the only encounter that exhibited such a signature.

3.2.2 Mathematical Derivation

In the following, the analytical description of the Alfvén wing developed by *Neubauer* [1980] is summarized. A stationary, alfvénic solution implies

$$\partial_t(...) = 0 \quad ; \qquad |\underline{B}| = |\underline{B}_0| = \text{const} \quad ; \qquad \varrho = \varrho_0 = \text{const} \quad , \tag{3.4}$$

where ϱ denotes the plasma mass density. Consequently, the pressure

$$p = p_0 \left(\frac{\varrho}{\varrho_0} \right)^{\kappa} = p_0 = \text{const} \tag{3.5}$$

remains constant. In this expression, κ is the adiabatic index. The subscript "0" denotes quantities from the undisturbed regions upstream of the obstacle, whereas the quantities without "0" may be perturbed due to the interaction. With the assumptions (3.4) and (3.5), the ideal MHD equations

$$\partial_t \varrho + \partial_{\underline{x}} \cdot \left(\varrho \underline{u} \right) = 0 \tag{3.6}$$

$$\begin{aligned} \varrho \partial_t \underline{u} + \varrho \left(\underline{u} \cdot \partial_{\underline{x}} \right) \underline{u} &= -\partial_{\underline{x}} p + \underline{j} \times \underline{B} \\ &= -\partial_{\underline{x}} p + \frac{1}{\mu_0} \left\{ -\frac{\partial_{\underline{x}} \underline{B}^2}{2} + \left(\underline{B} \cdot \partial_{\underline{x}} \right) \underline{B} \right\} \end{aligned} \tag{3.7}$$

$$\partial_t \underline{B} = -\partial_{\underline{x}} \times \underline{E} = \partial_{\underline{x}} \times \left(\underline{u} \times \underline{B} \right) \tag{3.8}$$

reduce to

$$\partial_{\underline{x}} \cdot \underline{u} = 0 \tag{3.9}$$

$$\left(\underline{u} \cdot \partial_{\underline{x}} \right) \underline{u} = \left(\underline{v}_A \cdot \partial_{\underline{x}} \right) \underline{v}_A \tag{3.10}$$

$$\left(\underline{u} \cdot \partial_{\underline{x}} \right) \underline{v}_A = \left(\underline{v}_A \cdot \partial_{\underline{x}} \right) \underline{u} \quad . \tag{3.11}$$

The symbols have the usual meaning, i.e. $\underline{u}$, $\underline{j}$, $\underline{E}$ and $\underline{B}$ denote plasma velocity, current, electric field and magnetic field. Note that the current is expressed according to Ampère's law in the low-frequency limit, i.e.

$$\underline{j} = \frac{1}{\mu_0} \partial_{\underline{x}} \times \underline{B} \quad . \tag{3.12}$$

By adding and subtracting equations (3.10) and (3.11) it can be shown that constancy of the Alfvén characteristics $\underline{\mathcal{Z}}^{\pm}$ – which are also termed *Elsässer variables* or *Riemann invariants* – is a solution of the non-linearized MHD equations:

$$(3.10) \pm (3.11) \quad \Rightarrow \quad \left(\underline{u} \cdot \partial_{\underline{x}} \right) \left(\underline{u} \pm \underline{v}_A \right) = \left(\underline{v}_A \cdot \partial_{\underline{x}} \right) \left(\underline{v}_A \pm \underline{u} \right) \tag{3.13}$$

$$\Rightarrow \quad \left(\left(\underline{u} \mp \underline{v}_A \right) \cdot \partial_{\underline{x}} \right) \left(\underline{u} \pm \underline{v}_A \right) = 0 \tag{3.14}$$

$$\Leftrightarrow \quad \left(\underline{\mathcal{Z}}^{\mp} \cdot \partial_{\underline{x}} \right) \underline{\mathcal{Z}}^{\pm} = 0 \tag{3.15}$$

and thus, $\underline{\mathcal{Z}}^{\pm}$ is constant with[2]

$$\underline{\mathcal{Z}}^{\pm} = \underline{u} \pm \underline{v}_A = \underline{u}_0 \pm \underline{v}_{A,0} = \underline{\mathcal{Z}}_0^{\pm} \quad . \tag{3.16}$$

[2]Note added in proof: More precisely, $\underline{\mathcal{Z}}^{+}$ is constant along $\underline{\mathcal{Z}}^{-}$ and vice versa. The solution of eq. (3.15) that is to be discussed here – characterizing the Alfvén wing – is given by eq. (3.16).

With respect to the following calculations, it may also be useful to provide the magnitude of $\underline{\mathcal{Z}}^{\pm}$,

$$|\underline{\mathcal{Z}}^{\pm}| = |\underline{u}_0 \pm \underline{v}_{A,0}| = \sqrt{u_0^2 + v_{A,0}^2 \pm 2u_0 v_{A,0} \cos\left(\measuredangle \underline{u}_0, \underline{v}_{A,0}\right)} \tag{3.17}$$

$$= v_{A,0}\sqrt{1 + M_A^2} \quad . \tag{3.18}$$

It is now helpful to apply a coordinate system $\underline{\tilde{x}} = (\tilde{x}, \tilde{y}, \tilde{z})$, where the positive $\tilde{z}$-axis is aligned with the characteristics. Without loss of generality, $\tilde{z}$ shall be aligned with $\underline{\mathcal{Z}}^{+}$. The $\tilde{x}$-axis is perpendicular to $\tilde{z}$ and located in the plane defined by the background magnetic field $\underline{B}_0$ and the plasma flow $\underline{u}_0$. $\tilde{y}$ is perpendicular to both, $\tilde{x}$ and $\tilde{z}$. The orientation of $\tilde{y}$ is chosen such that the coordinate system is right-handed. See also figure 3.2(b) for an illustration of this Alfvén wing coordinate system. Since the coordinate system which is mainly used in this work is the interaction system of the respective satellite (ENIS or RHIS), the physical quantities then need to be transformed from the wing coordinate system $(\tilde{x}, \tilde{y}, \tilde{z})$ to the interaction coordinate system (x, y, z). This transformation is given by

$$\tilde{x} = \frac{1}{\sqrt{1 + M_A^2}} (\pm x - M_A z) \tag{3.19}$$

$$\tilde{y} = y \tag{3.20}$$

$$\tilde{z} = \frac{1}{\sqrt{1 + M_A^2}} (M_A x \pm z) \quad , \tag{3.21}$$

with the upper sign denoting the northern wing and the lower sign referring to the southern wing.

In the Alfvén wing coordinate system, writing equation (3.16) separately for the three components and considering only the upper sign yields

$$u_{\tilde{x}} + v_{A,\tilde{x}} = 0 \tag{3.22}$$

$$u_{\tilde{y}} + v_{A,\tilde{y}} = 0 \tag{3.23}$$

$$u_{\tilde{z}} + v_{A,\tilde{z}} = \text{const} \quad . \tag{3.24}$$

It follows then that

$$\frac{\partial}{\partial \tilde{z}} u_a = -\frac{\partial}{\partial \tilde{z}} v_{A,a} \quad , \tag{3.25}$$

where the subscript 'a' denotes the components in the Alfvén wing coordinate system, $a \in \{\tilde{x}, \tilde{y}, \tilde{z}\}$. Inserting equations (3.22) – (3.24) and (3.25) in (3.14) (lower sign) yields

$$\left[\left(u_{\tilde{z}} + v_{A,\tilde{z}}\right) \partial_{\tilde{z}}\right] \left(u_a - v_{A,a}\right) = 0 \tag{3.26}$$

$$\left(u_{\tilde{z}} + v_{A,\tilde{z}}\right) \left(\partial_{\tilde{z}} u_a - \partial_{\tilde{z}} v_{A,a}\right) = 0 \tag{3.27}$$

$$2\left(u_{\tilde{z}} + v_{A,\tilde{z}}\right) \left(\partial_{\tilde{z}} u_a\right) = 0 \quad , \tag{3.28}$$

and therefore,

$$\frac{\partial}{\partial \tilde{z}} \underline{u} = \underline{0} \quad . \tag{3.29}$$

In a similar manner it can be shown that

$$\frac{\partial}{\partial \tilde{z}} \underline{B} = \underline{0} \quad . \tag{3.30}$$

The same conclusion can be achieved, if $\tilde{z}$ is aligned with the southern characteristic $\underline{\mathcal{Z}}^-$. Therefore, velocity, magnetic field, electric field and current are constant along the characteristics of the Alfvén wing.

For a discussion of the current loops, the current is divided into a part $\underline{j}_{\tilde{\perp}}$ perpendicular to $\underline{\mathcal{Z}}^+$ and a part $\underline{j}_{\tilde{\parallel}} = j_{\tilde{\parallel}}\, \underline{e}_{\tilde{z}} = j_{\tilde{z}}\, \underline{e}_{\tilde{z}}$ along the wing. Taking the divergence yields

$$\partial_{\underline{\tilde{x}}} \cdot \underline{j} = \partial_{\underline{\tilde{x}}} \cdot \underline{j}_{\tilde{\perp}} + \partial_{\underline{\tilde{x}}} \cdot \underline{j}_{\tilde{\parallel}} = \partial_{\underline{\tilde{x}}} \cdot \underline{j}_{\tilde{\perp}} + \partial_{\tilde{z}} j_{\tilde{z}} = \partial_{\underline{\tilde{x}}} \cdot \underline{j}_{\tilde{\perp}} = 0 \quad . \tag{3.31}$$

The interpretation of equation (3.31) is that the perpendicular currents form closed current loops, independent of the parallel currents. From Ampere's law, the currents perpendicular to the wing can be expressed as (equation (13) of *Neubauer* [1980])

$$\underline{j}_{\tilde{\perp}}(\tilde{x}, \tilde{y}) = (j_{\tilde{x}}, j_{\tilde{y}}, 0) = \frac{1}{\mu_0}(\partial_{\tilde{y}} B_{\tilde{z}}, -\partial_{\tilde{x}} B_{\tilde{z}}, 0) = \frac{1}{\mu_0}\left(\partial_{\underline{\tilde{x}}} B_{\tilde{z}} \times \underline{e}_{\tilde{z}}\right) \quad . \tag{3.32}$$

To derive the parallel current, the divergence of the electric field is taken. Constancy of $\underline{\mathcal{Z}}^+$ implies $\partial_{\underline{x}} \times \underline{\mathcal{Z}}^+ = 0$ and thus,

$$\begin{aligned} \partial_{\underline{x}} \cdot \underline{E} &= \partial_{\underline{x}} \cdot \left(-\underline{u} \times \underline{B}\right) \\ &= \partial_{\underline{x}} \cdot \left[-\left(\underline{\mathcal{Z}}^+ - \frac{\underline{B}}{\sqrt{\mu_0 \rho}}\right) \times \underline{B}\right] \\ &= \underline{\mathcal{Z}}^+ \cdot \mu_0 \underline{j} = \mu_0 v_A \sqrt{1 + M_A^2}\, j_{\tilde{z}} \quad . \end{aligned} \tag{3.33}$$

Therefore, the current along the Alfvén characteristics can be expressed as

$$j_{\tilde{z}} = \Sigma_A \partial_{\underline{x}} \cdot \underline{E} = -\Sigma_A \partial_{\underline{x}}^2 \psi \quad , \tag{3.34}$$

with the electric potential ψ and the Alfvén conductance

$$\Sigma_A = \frac{1}{\mu_0 v_A \sqrt{1 + M_A^2}} \quad . \tag{3.35}$$

This conductance can be interpreted as a conductor situated perpendicular to the Alfvén characteristics with a uniform height-integrated conductivity Σ_A [*Neubauer* 1980, 1998, *Goertz* 1980].

The magnetic field perturbations perpendicular to the wing ($\underline{B}_{\tilde{\perp}}$) can be derived from the electric field according to

$$\begin{aligned} \underline{e}_{\tilde{z}} \times \underline{E} &= \underline{e}_{\tilde{z}} \times (-\underline{u} \times \underline{B}) \\ &= \underline{e}_{\tilde{z}} \times \left(-(\underline{\mathcal{Z}}^+ \mp \frac{\underline{B}}{\sqrt{\mu_0 \rho}}) \times \underline{B}\right) \\ &= +(\underline{e}_{\tilde{z}} \cdot \underline{\mathcal{Z}}^+)\underline{B} - (\underline{e}_{\tilde{z}} \cdot \underline{B})\underline{\mathcal{Z}}^+ \\ &= v_A \sqrt{1 + M_A^2}\, \underline{B} - B_{\tilde{z}}\, v_A \sqrt{1 + M_A^2}\, \underline{e}_{\tilde{z}} \\ &= v_A \sqrt{1 + M_A^2}\, \underline{B}_{\tilde{\perp}} \quad . \end{aligned} \tag{3.36}$$

Finally, we find for the magnetic field of the Alfvén wing (see *Neubauer* [1980])

$$\underline{B}_{\tilde{\perp}} = (B_{\tilde{x}}, B_{\tilde{y}}, 0) = \left(\underline{e}_{\tilde{z}} \times \underline{E}\right) \mu_0 \Sigma_A \quad . \tag{3.37}$$

The parallel field component is obtained by considering the constancy of $\underline{B}$,

$$\underline{B}_{\tilde{\parallel}} = (0, 0, B_{\tilde{z}}) = \pm \sqrt{B_0^2 - \tilde{B}_\perp^2} \quad . \tag{3.38}$$

Instead of the electric field, it is sometimes more convenient to consider the electric potential ψ. Faraday's law and $\partial_{\tilde{z}}(...) = 0$ imply $E_{\tilde{z}}(\tilde{x}, \tilde{y}, \tilde{z})$ to be constant. At large distances to the wing, i.e. $\sqrt{\tilde{x}^2 + \tilde{y}^2} \to \infty$, the electric field should be identical to the unperturbed field $\underline{E}_0 = -\underline{u}_0 \times \underline{B}_0 = -E_0\, \underline{e}_y = -E_0\, \underline{e}_{\tilde{y}}$. Therefore, it is $E_{\tilde{z}} = 0$ and the electric field can be written as

$$\underline{E} = -\partial_{\underline{\tilde{x}}} \psi = (-\partial_{\tilde{x}}\psi, -\partial_{\tilde{y}}\psi, 0) = (E_{\tilde{x}}, E_{\tilde{y}}, 0) \quad . \tag{3.39}$$

In ENIS (or RHIS) coordinates, the magnetic field components $\left(B_x, B_y, B_z\right)$ associated with the Alfvén wing can eventually be expressed as (see also *Simon et al.* [2011b] with $\partial_z \psi = 0$)

$$B_x = \frac{1}{\sqrt{M_A^2 + 1}} \left\{ \mp M_A \Gamma \pm \mu_0 \Sigma_A \frac{\partial \psi}{\partial y} \right\} \quad ; \tag{3.40}$$

$$B_y = \frac{1}{\sqrt{M_A^2 + 1}} \mu_0 \Sigma_A \left\{ \mp \frac{\partial \psi}{\partial x} + M_A \frac{\partial \psi}{\partial z} \right\} \quad ; \tag{3.41}$$

$$B_z = \frac{1}{\sqrt{M_A^2 + 1}} \left\{ -\Gamma - M_A \mu_0 \Sigma_A \frac{\partial \psi}{\partial y} \right\} \quad , \tag{3.42}$$

with

$$\Gamma = \sqrt{B_0^2 - \mu_0^2 \Sigma_A^2 \left\{ \frac{1}{M_A^2 + 1} \left(\pm \frac{\partial \psi}{\partial x} - M_A \frac{\partial \psi}{\partial z} \right)^2 + \left(\frac{\partial \psi}{\partial y} \right)^2 \right\}} \quad . \tag{3.43}$$

At large distances to the wing – i.e., $\sqrt{x^2 + y^2} \to \infty$ – the B_x and the B_y perturbations decrease to zero, whereas $B_z \to -B_0$. Note that although the $\tilde{z}$ component of the electric field vanishes in the wing coordinate system ($\partial_{\tilde{z}}\psi = 0$), this does *not* necessarily imply $\partial_z \psi = 0$ in the interaction coordinate system.

In the case of Enceladus, these expressions could be further simplified, since the magnetic field perturbations in the far field do not depend on z for two reasons: The electron collision frequency is clearly below the electron cyclotron frequency ($\nu_e \ll \Omega_e$), and therefore the conductivity parallel to the magnetic field is large compared to the perpendicular conductivity. In consequence, the parallel electric field can be considered negligible [*Neubauer* 1998]. For the low Alfvénic Mach number at Enceladus ($M_A \approx 0.1$) and corresponding small angle $\theta_A < 10°$, it is also clear that $\tilde{z}$ approximately coincides with z. Thus, at Enceladus electric field and electric potential do not depend on z, i.e. $\partial_z \psi = 0$.

It should be pointed out that this analytical description of the Alfvén wing is based on the ideal MHD equations *without* source or collision terms arising from the obstacle. Thus,

the solution discussed above is valid only in the far field, i.e. sufficiently far away from the obstacle. Furthermore, this general solution does not explicitly include the properties of the obstacle, although its size and conductivity determine the electric potential ψ as will be shown in the following sections.

3.2.3 Pedersen and Hall Currents

The coupling between the far field Alfvén wing solution and the conducting obstacle is provided by the closure of the perpendicular currents arising from the interaction of the plasma flow with the obstacle.

Therefore, a derivation of the perpendicular current after *Neubauer* [1998] and *Simon et al.* [2011b] will be presented in the following. While previously the MHD approach was used, it is now necessary to consider a multi-fluid approach. In addition, the general conducting obstacle is now specified by a cloud of neutral gas which can be ionized and/or which leads to collisions between the neutrals and the charged plasma. For a plasma fluid α, the momentum equation then reads

$$\begin{aligned} n_\alpha m_\alpha \frac{d\underline{u}_\alpha}{dt} &= -\partial_{\underline{x}} p_\alpha + q_\alpha n_\alpha (\underline{E} + \underline{u}_\alpha \times \underline{B}) \\ &\quad - \sum_n n_\alpha m_\alpha \nu_{\alpha,n} (\underline{u}_\alpha - \underline{u}_n) - \sum_n S_{\alpha,n} m_\alpha (\underline{u}_\alpha - \underline{u}_n) \qquad (3.44) \\ &= -\partial_{\underline{x}} p_\alpha + q_\alpha n_\alpha (\underline{E} + \underline{u}_\alpha \times \underline{B}) - \sum_n n_\alpha m_\alpha \tilde{\nu}_{\alpha,n} (\underline{u}_\alpha - \underline{u}_n) \quad . \qquad (3.45) \end{aligned}$$

The parameters m_α and $\nu_{\alpha,n}$ are the mass and the ion-neutral collision frequency of each species, respectively. The subscript 'n' denotes possible different neutral species. In the last step, the collision frequency $\nu_{\alpha,n}$ and the source term $S_{\alpha,n}$ have been merged into the effective collision frequency $\tilde{\nu}_{\alpha,n}$ according to (see e.g. *Neubauer* [1998])

$$\tilde{\nu}_{\alpha,n} = \frac{S_{\alpha,n}}{n_\alpha} + \nu_{\alpha,n} \quad . \qquad (3.46)$$

Now, four simplifying assumptions are made: first, the velocity of the neutrals shall be small compared to the velocity of the plasma species ($|\underline{u}_n| \ll |\underline{u}_\alpha|$). Thereby, the momentum equation simplifies to

$$n_\alpha m_\alpha \frac{\mathrm{d}\underline{u}_\alpha}{\mathrm{d}t} = -\partial_{\underline{x}} p_\alpha + q_\alpha n_\alpha (\underline{E} + \underline{u}_\alpha \times \underline{B}) - n_\alpha m_\alpha \tilde{\nu}_\alpha \underline{u}_\alpha \quad , \qquad (3.47)$$

where

$$\tilde{\nu}_\alpha = \sum_n \nu_{\alpha,n} \quad . \qquad (3.48)$$

Second, the electric field and magnetic field shall be given by $\underline{E} = \underline{E}_0 = -E_0 \underline{e}_y = -u_0 B_0 \underline{e}_y$ and $\underline{B} = \underline{B}_0 = -B_0 \underline{e}_z$, respectively. Third, the thermal pressure is assumed to be negligible compared to dynamic and magnetic pressure, in agreement with the very low plasma beta at Enceladus (cf. table 2.4). Fourth, the plasma flow shall be stationary, i.e. $m_\alpha \mathrm{d}\underline{u}_\alpha/\mathrm{d}t = 0$. Solving equation (3.47) for the bulk speed $\underline{u}_\alpha$ of each component then yields

$$\underline{u}_\alpha = \frac{1}{B_0}\begin{pmatrix} \frac{\tilde{\nu}_\alpha\Omega_\alpha}{\tilde{\nu}_\alpha^2+\Omega_\alpha^2} & -\frac{\Omega_\alpha^2}{\tilde{\nu}_\alpha^2+\Omega_\alpha^2} & 0 \\ \frac{\Omega_\alpha^2}{\tilde{\nu}_\alpha^2+\Omega_\alpha^2} & \frac{\tilde{\nu}_\alpha\Omega_\alpha}{\tilde{\nu}_\alpha^2+\Omega_\alpha^2} & 0 \\ 0 & 0 & \frac{\Omega_\alpha}{\tilde{\nu}_\alpha} \end{pmatrix} \cdot \underline{E}_0 \quad , \tag{3.49}$$

where Ω_α denotes the gyrofrequency of species α that is negative for electrons and positive for ions, in agreement with the notation used by *Simon et al.* [2011b].
For an ion species j, the (effective) collisions therefore yield a drift motion according to

$$u_{j,x} = u_0 \frac{\Omega_j^2}{\tilde{\nu}_j^2+\Omega_j^2} \quad , \tag{3.50}$$

$$u_{j,y} = -u_0 \frac{\tilde{\nu}_j\Omega_j}{\tilde{\nu}_j^2+\Omega_j^2} \quad . \tag{3.51}$$

The direction of the drift is given by $\underline{u}_j = u_0 \frac{\Omega_j}{\sqrt{\Omega_j^2+\tilde{\nu}_j^2}}(\cos\phi, -\sin\phi, 0)$, where the angle ϕ reads

$$\tan\phi = \left|\frac{u_{j,y}}{u_{j,x}}\right| = \frac{\tilde{\nu}_j}{\Omega_j} \quad . \tag{3.52}$$

The associated current density

$$\underline{j} = \sum_\alpha n_\alpha q_\alpha \underline{u}_\alpha \tag{3.53}$$

can be computed according to

$$\underline{j} = \underline{\underline{\sigma}} \cdot \underline{E} = \sigma_P \underline{E} + \sigma_H \frac{\underline{B}\times\underline{E}}{B} + \sigma_\parallel (\underline{E}\cdot\underline{B})\frac{\underline{B}}{B^2} \quad , \tag{3.54}$$

where the conductivity tensor with Pedersen conductivity σ_P, Hall conductivity σ_H and parallel conductivity $\sigma_\parallel$ is given by

$$\underline{\underline{\sigma}} = \begin{pmatrix} \sigma_P & \sigma_H & 0 \\ -\sigma_H & \sigma_P & 0 \\ 0 & 0 & \sigma_\parallel \end{pmatrix} \quad . \tag{3.55}$$

The elements of the conductivity tensor can be expressed as

$$\sigma_P = \sum_\alpha \frac{n_\alpha q_\alpha^2}{m_\alpha}\frac{\tilde{\nu}_\alpha}{\tilde{\nu}_\alpha^2+\Omega_\alpha^2} = \sum_\alpha \frac{n_\alpha q_\alpha}{B_0}\frac{\tilde{\nu}_\alpha\Omega_\alpha}{\tilde{\nu}_\alpha^2+\Omega_\alpha^2} \quad ; \tag{3.56}$$

$$\sigma_H = -\sum_\alpha \frac{n_\alpha q_\alpha^2}{m_\alpha}\frac{\Omega_\alpha}{\tilde{\nu}_\alpha^2+\Omega_\alpha^2} = -\sum_\alpha \frac{n_\alpha q_\alpha}{B_0}\frac{\Omega_\alpha^2}{\tilde{\nu}_\alpha^2+\Omega_\alpha^2} \quad ; \tag{3.57}$$

$$\sigma_\parallel = \sum_\alpha \frac{n_\alpha q_\alpha^2}{m_\alpha\tilde{\nu}_\alpha} \quad . \tag{3.58}$$

Instead of including ionization and the resulting pick-up in the Pedersen conductivity by means of the effective collision frequency, it is also possible to introduce a separate pick-up conductivity (cf. *Goertz* [1980]). For the sake of completeness, the derivation of the pick-up conductivity is summarized below. Due to ionization, a certain number of electrons (S_e) and ions (S_i) is produced per unit volume and time. In agreement with $|\underline{u}_n| \ll |\underline{u}_\alpha|$, it is assumed that ions and electrons are generated at rest. After acceleration by the electromagnetic fields, their guiding centers are displaced by

$$y_{guid} = r_{g,\alpha} \frac{q_\alpha}{|q_\alpha|} \quad , \tag{3.59}$$

where $r_{g,\alpha}$ is the gyroradius of ions ($\alpha = i$) and electrons ($\alpha = e$), respectively. The current resulting from pick-up can therefore be expressed as

$$\underline{j} = \sum_{\alpha=i,e} S_\alpha \, r_{g,\alpha} \, e \, \frac{\underline{E}}{|\underline{E}|} = \sigma_{pick} \underline{E} \quad , \tag{3.60}$$

with the pick-up conductivity

$$\sigma_{pick} = \sum_{\alpha=i,e} \frac{S_\alpha \, m_\alpha}{B_0^2} \quad . \tag{3.61}$$

If the effective collision frequency does not include collisions, i.e.

$$\tilde{\nu}_\alpha = \frac{S_\alpha}{n_\alpha} \quad , \tag{3.62}$$

the Pedersen conductivity converges to the pick-up conductivity in the limit $\tilde{\nu}_\alpha \ll \Omega_\alpha$:

$$\sigma_P = \sum_{\alpha=i,e} \frac{n_\alpha \, q_\alpha}{B_0} \frac{\tilde{\nu}_\alpha \Omega_\alpha}{\tilde{\nu}_\alpha^2 + \Omega_\alpha^2} \rightarrow \sum_{\alpha=i,e} \frac{n_\alpha \, q_\alpha}{B_0} \frac{\tilde{\nu}_\alpha}{\Omega_\alpha} = \sum_{\alpha=i,e} \frac{n_\alpha \, q_\alpha}{B_0} \frac{S_\alpha / n_\alpha}{\Omega_\alpha} = \sum_{\alpha=i,e} \frac{S_\alpha \, m_\alpha}{B_0^2} = \sigma_{pick} \tag{3.63}$$

and the Hall conductivity becomes zero.

Please note that additional contributions to the currents may not be caused by collisions or pick-up but for example pressure gradients which were neglected above. However, it is not possible to assign a conductivity to e.g. the diamagnetic current caused by pressure gradients, because this current is not proportional to the electric field.

3.2.4 Potential Equation

In the following, the perpendicular current arising from the interaction of the neutral atmosphere with the flow of magnetized plasma (equation (3.54)) will be connected to the Alfvén wing. For this calculation, the interaction coordinate system (x, y, z) will still be used and it is assumed that $\partial_z \psi = 0$ (see last paragraph of section 3.2.2). Initially, these calculations were carried out by *Wolf-Gladrow et al.* [1987] and *Neubauer* [1998],

whereas the computation shown here follows the summary of *Simon et al.* [2011b].

Exactly like in equation (3.31), the divergence of the current is split up into a parallel and a perpendicular contribution,

$$\partial_{\underline{x}} \cdot \underline{j}_{\perp} = -\partial_z \cdot j_{\parallel} \quad . \tag{3.64}$$

Integrating this equation yields

$$j_{\parallel}(z_{max}) - j_{\parallel}(z_{min}) = \int_{z=z_{min}}^{z_{max}} \partial_{\underline{x}} \cdot \underline{j}_{\perp} \, \mathrm{d}z \quad , \tag{3.65}$$

where z_{min} and z_{max} denote the lower and upper boundary of the integration, respectively. Inserting the electric potential ψ into the perpendicular current arising from Pedersen and Hall conductivity (equation (3.54)) gives

$$\underline{j}_{\perp} = -\left\{\sigma_P \frac{\partial \psi}{\partial x} + \sigma_H \frac{\partial \psi}{\partial y}\right\} \underline{e}_x - \left\{\sigma_P \frac{\partial \psi}{\partial y} - \sigma_H \frac{\partial \psi}{\partial x}\right\} \underline{e}_y \tag{3.66}$$

and thus,

$$\partial_{\underline{x}} \cdot \underline{j}_{\perp} = -\left\{\sigma_P \partial^2_{\underline{x}} \psi + \left(\frac{\partial \sigma_P}{\partial x} - \frac{\partial \sigma_H}{\partial y}\right)\frac{\partial \psi}{\partial x} + \left(\frac{\partial \sigma_P}{\partial y} + \frac{\partial \sigma_H}{\partial x}\right)\frac{\partial \psi}{\partial y}\right\} \quad . \tag{3.67}$$

Inserting this equation in eq. (3.65) and introducing the height-integrated conductivities

$$\Sigma_{P,H} = \int_{z_{min}}^{z_{max}} \sigma_{P,H}(x, y, z) \, \mathrm{d}z \tag{3.68}$$

results in

$$j_{\parallel}(z_{max}) - j_{\parallel}(z_{min}) = \Sigma_P \partial^2_{\underline{x}} \psi + \left(\frac{\partial \Sigma_P}{\partial x} - \frac{\partial \Sigma_H}{\partial y}\right)\frac{\partial \psi}{\partial x} + \left(\frac{\partial \Sigma_P}{\partial y} + \frac{\partial \Sigma_H}{\partial x}\right)\frac{\partial \psi}{\partial y} \quad . \tag{3.69}$$

To specify the upper and lower boundaries of the integration as well as the parallel current at these boundaries, two cases are considered:

(1) The neutral gas cloud envelops a solid obstacle like an icy satellite and the magnetic field lines intersect the satellite. Without loss of generality, the analysis is restricted to the northern hemisphere. The lower boundary of the integration (z_{min}) can then be identified with the surface of the satellite (see figure 3.3). According to the discussion in section 3.1, no current flows through the surface of the icy moon and therefore, it is

$$j_{\parallel}(z_{min}) = 0 \quad . \tag{3.70}$$

The upper boundary can formally be set to infinity, where the Alfvén wing model allows to express the parallel current as (cf. equation (3.34))

$$j_{\parallel}(z_{max}) = -\Sigma_A \partial^2_{\underline{x}} \psi \quad . \tag{3.71}$$

In this case, the integral (3.68) sums up all conductivity north of the solid obstacle. Inserting equations (3.70) and (3.71) into (3.69) yields the final form of the potential equation:

$$(\Sigma_P + \Sigma_A)\,\partial^2_{\underline{x}}\psi + \left(\frac{\partial\Sigma_P}{\partial x} - \frac{\partial\Sigma_H}{\partial y}\right)\frac{\partial\psi}{\partial x} + \left(\frac{\partial\Sigma_P}{\partial y} + \frac{\partial\Sigma_H}{\partial x}\right)\frac{\partial\psi}{\partial y} = 0 \quad . \tag{3.72}$$

The same result can be obtained for the southern hemisphere.

(2) As illustrated in figure 3.3, further upstream or downstream of the obstacle the integration along z may not intersect the solid body. In that case, the lower boundary has to be set to $z_{min} = -\infty$ and the parallel current at z_{min} is also given by the corresponding Alfvén wing far field current,

$$j_{\parallel}(z_{min}) = +\Sigma_A \partial^2_{\underline{x}}\psi \quad . \tag{3.73}$$

The potential equation is accordingly modified to

$$(\Sigma_P + 2\Sigma_A)\,\partial^2_{\underline{x}}\psi + \left(\frac{\partial\Sigma_P}{\partial x} - \frac{\partial\Sigma_H}{\partial y}\right)\frac{\partial\psi}{\partial x} + \left(\frac{\partial\Sigma_P}{\partial y} + \frac{\partial\Sigma_H}{\partial x}\right)\frac{\partial\psi}{\partial y} = 0 \quad . \tag{3.74}$$

However, the integral (3.68) now contains all conductivity above and below the equatorial plane. Note that equation (3.74) assumes the form of equation (3.72), if the conductivities σ_P and σ_H are symmetric with respect to $z = 0$ and the integration is performed from $z = 0$ to $z = z_{max}$.

A more general form of the potential equation which also includes the unipolar inductor model has been derived by *Saur* [2004] and *Saur et al.* [2007].

3.2.5 Solution of the Potential Equation

To analytically solve the potential equation (3.72), which is an elliptic partial differential equation of second order with variable coefficients, the obstacle is assumed to possess a cylindrical symmetry. In two-dimensional polar coordinates $\underline{x} = (r\cos\varphi, r\sin\varphi, 0)$, the potential equation reads

$$\frac{1}{r}\frac{\partial}{\partial\varphi}\left[(\Sigma_P + \Sigma_A)\frac{\partial\psi}{\partial\varphi}\right] + \frac{\partial}{\partial r}\left[r\,(\Sigma_P + \Sigma_A)\frac{\partial\psi}{\partial r}\right] + \frac{\partial\Sigma_H}{\partial r}\frac{\partial\psi}{\partial\varphi} - \frac{\partial\Sigma_H}{\partial\varphi}\frac{\partial\psi}{\partial r} = 0 \quad . \tag{3.75}$$

The overall idea is now to approximate the obstacle by subdomains with constant conductances. Within each of these volumes, the potential equation reduces to the two-dimensional Laplace equation

$$\partial^2_{\underline{x}}\psi(x, y) = 0 \quad , \tag{3.76}$$

the general solution of which is given by

$$\psi(r,\varphi) = \sum_{k=1}^{\infty}\left\{r^k(a_k\cos k\varphi + b_k\sin k\varphi) + r^{-k}(g_k\cos k\varphi + h_k\cos k\varphi)\right\} \quad . \tag{3.77}$$

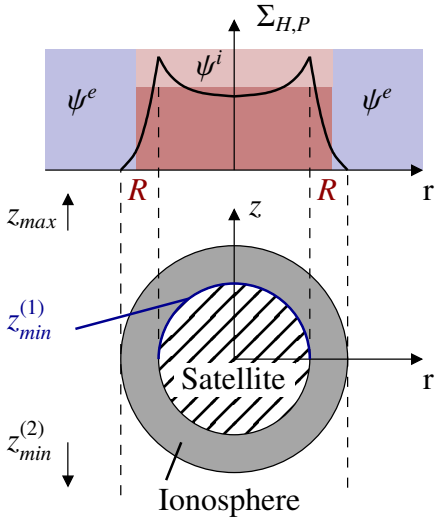

Figure 3.3: Illustration of height-integrated conductivity profiles and associated integration boundaries, adapted from *Neubauer* [1998]. Integration over the conductivity of the ionosphere along z yields the profiles of the conductances Σ_P and Σ_H as indicated by the black line in the upper part of the figure. The upper integration boundary is $z_{max} = +\infty$, whereas the lower boundary may be given by the obstacle ($z^{(1)}_{min}$) or by $z^{(2)}_{min} = -\infty$. For the analytical solution derived by *Neubauer* [1998] and *Saur et al.* [1999], the obstacle is approximated by constant conductances inside $r < R$ (marked in dark red) and zero outside. The corresponding electric potentials are denoted as ψ^i and ψ^e, respectively.

Here, the term for $k = 0$ has been ignored, since an additive constant in the potential has no influence on the physical fields. The problem therefore 'reduces' to the determination of the coefficients a_k, b_k, g_k and h_k within the different subdomains according to the appropriate boundary conditions.

The basic solution presented here was first derived by *Saur et al.* [1999]. In that work, the conductivity distribution of the obstacle is approximated by a cylindrical volume with constant conductances inside of a radius R (region 'i') and zero outside (region 'e'), i.e. two subdomains are considered (cf. figure 3.3). The corresponding potentials are ψ^i and ψ^e, respectively. This solution has been extended by *Saur* [2004] to elliptical cylinders, allowing to model an elliptically shaped ionosphere. The boundary conditions are:

1. $\psi(r, \varphi)$ has to be continuous everywhere, including the boundaries between the subdomains.

2. For $r \to \infty$, the solution has to be identical to the unperturbed potential, i.e.

$$\psi(r \to \infty, \varphi) = \psi_0 = E_0 r \sin\varphi \quad . \tag{3.78}$$

   In the outermost domain, the coefficients a_k and b_k are therefore equal to zero for $k > 1$.

3. $\psi(r, \varphi)$ must not diverge in the domain containing $r = 0$ and thus, the corresponding coefficients g_k and h_k have to be zero for $k \geq 1$.

4. Integration of the potential equation (3.75) across the surface of the cylinder in an interval $[R-\epsilon, R+\epsilon]$ with $\epsilon \to 0$ yields the jump condition (eq. (A2) of *Saur et al.* [1999])

$$\lim_{\epsilon \to 0} \left\{ r\left(\Sigma_P + \Sigma_A\right) \frac{\partial \psi(r,\varphi)}{\partial r} + \Sigma_H \frac{\partial \psi(r,\varphi)}{\partial \varphi} \right\} \Bigg|_{R-\epsilon}^{R+\epsilon} = 0 \quad . \tag{3.79}$$

The solution originally derived by *Saur et al.* [1999] from the boundary conditions 1. – 4. is given by

$$\psi^i = \psi_0 - E_p \left[\cos\theta_p \, r \sin\varphi + \sin\theta_p \, r \cos\varphi \right] \qquad r < R \quad , \tag{3.80}$$

$$\psi^e = \psi_0 - E_p \left(\frac{R}{r}\right)^2 \left[\cos\theta_p \, r \sin\varphi + \sin\theta_p \, r \cos\varphi \right] \qquad r > R \quad . \tag{3.81}$$

In the above expressions, E_p denotes the magnitude of the perturbation electric field with

$$E_p = E_0 \sqrt{\frac{\Sigma_P^2 + \Sigma_H^2}{\Sigma_H^2 + (\Sigma_P + 2\Sigma_A)^2}} \quad . \tag{3.82}$$

The angle θ_p is defined by

$$\tan\theta_p = \frac{2\Sigma_A \Sigma_H}{\Sigma_H^2 + \Sigma_P(\Sigma_P + 2\Sigma_A)} \quad . \tag{3.83}$$

Thus, the electric field $\underline{E}_i = \underline{E} - \underline{E}_p$ is constant inside the cylinder $r < R$. Furthermore, $\underline{E}_i$ is reduced and twisted with respect to the undisturbed electric field. It should be pointed out that the solution of *Saur et al.* [1999] was the first that included the Hall conductivity and the associated Hall effect, resulting in the twist of $\underline{E}_i$.

Due to the translation invariance of the Alfvén wing along the characteristics, the electric field is not only reduced within the cylindrical obstacle, but along the whole Alfvén wing. Therefore, the volume inside the radius R shall be referred to as the *non-tilted* flux tube of the obstacle, i.e. the surface of the flux tube is given by $\sqrt{x^2 + y^2} = R$. This flux tube is illustrated in figure 3.4(a). With regard to the application to the "real" situation, however, it should be remembered that the Alfvén wing coordinate system is different from the interaction coordinate system ($\tilde{z} \neq z$). More precisely, the Alfvén characteristics include an angle $\theta_A = \arctan M_A$ to the z axis (cf. figure 3.2). Hence, it may sometimes be useful to consider the *tilted* flux tube that shall be defined as $\sqrt{\tilde{x}^2 + \tilde{y}^2} < R$ (see figure 3.4(b)).

To decide whether an atmosphere could generate any noticeable perturbations of the plasma environment, the magnitude of the perturbation electric field, E_p, could be compared with the undisturbed electric field E_0 (equation (3.82)). If the Hall conductance is neglected, the Alfvén conductance of the ambient magnetospheric plasma has to be compared against the Pedersen conductance of the ionosphere. These two quantities define the *interaction strength parameter* [*Saur et al.* 1999, *Saur and Strobel* 2005]

$$\overline{\alpha} \equiv \frac{\Sigma_P}{\Sigma_P + 2\Sigma_A} \qquad (0 \leq \overline{\alpha} \leq 1) \quad . \tag{3.84}$$

If $\overline{\alpha} = 0$, the atmosphere does not make any contribution at all to the plasma interaction ($E_p \to 0$), while in the other extreme case of $\overline{\alpha} = 1$ (implying $\Sigma_P \gg \Sigma_A$), the perturbations

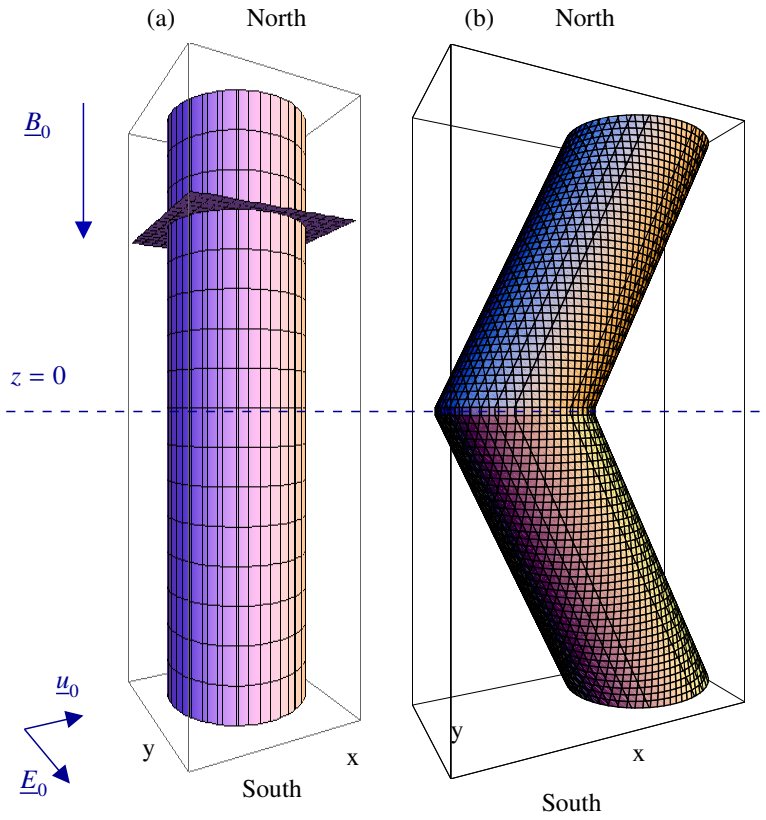

Figure 3.4: Models of the flux tube. (a) The flux tube is described as a non-tilted cylinder; that is, its surface is defined by $r = \sqrt{x^2 + y^2} = R$. (b) To account for the tilt of the Alfvén characteristics against the direction of the background magnetic field $\underline{B}_0$, both the northern and southern segments of the cylinder have been tilted by an angle of arctan M_A in positive x direction. Please note that for illustration purposes, the influence of the tilt is exaggerated. For Enceladus, the tilt angle against the north-south direction is of the order of only arctan $M_A \approx 7°$. In addition, a plane perpendicular to the northern wing is shown. Figure adapted from *Simon et al.* [2011b].

caused by the presence of the atmosphere reach their maximum possible value and the plasma flow within the wing tubes is decelerated to complete stagnation ($E_p \rightarrow E_0$).

Transformed back to Cartesian coordinates, the components of the electric field inside the flux tube ($r < R$) following from equation (3.80) read

$$E_{i,x} = -\frac{\partial \psi^i}{\partial x} = \frac{2E_0 \Sigma_H \Sigma_A}{\Sigma_H^2 + (\Sigma_P + 2\Sigma_A)^2} \tag{3.85}$$

$$E_{i,y} = -\frac{\partial \psi^i}{\partial y} = \frac{-2E_0 \Sigma_A (\Sigma_P + 2\Sigma_A)}{\Sigma_H^2 + (\Sigma_P + 2\Sigma_A)^2} \quad . \tag{3.86}$$

Incorporating these expressions into the Alfvén wing far field solution (equations (3.40) – (3.42)) yields the magnetic field perturbations within the Alfvén flux tube as a function of the conductances Σ_P and Σ_H,

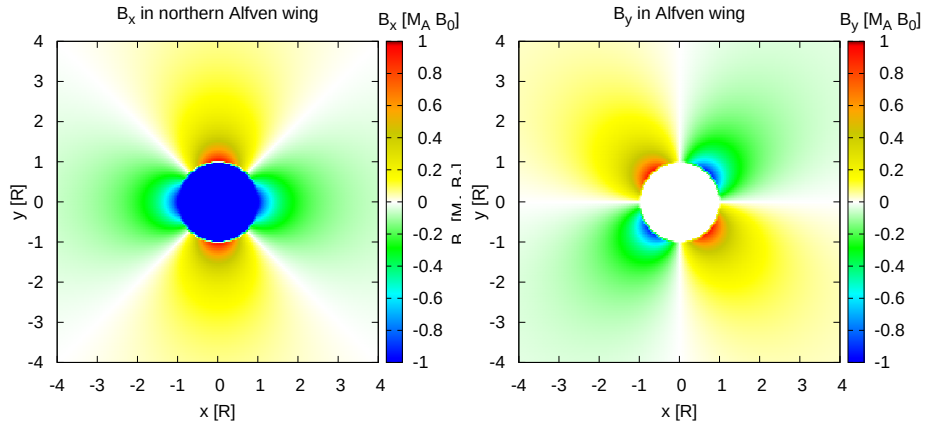

Figure 3.5: Magnetic field perturbations of the Alfvén wing far field solution in a plane perpendicular to the northern wing as illustrated in figure 3.4. B_x and B_y are obtained from equations (3.40) – (3.41) and (3.80) – (3.81) with $\Sigma_H = 0$ and $\Sigma_P \gg \Sigma_A$. The obstacle is given by a cylinder with constant conductances for $x^2 + y^2 < R^2$ and zero outside.

$$B_x = \frac{1}{\sqrt{1+M_A^2}} \left\{ \pm \frac{2\mu_0 E_0 \Sigma_A^2 (\Sigma_P + 2\Sigma_A)}{\Sigma_H^2 + (\Sigma_P + 2\Sigma_A)^2} \right. \\ \left. \mp M_A \sqrt{B_0^2 - \frac{\left(2\mu_0 E_0 \Sigma_A^2\right)^2}{(\Sigma_H^2 + (\Sigma_P + 2\Sigma_A)^2)^2} \left(\frac{\Sigma_H^2}{1+M_A^2} + (\Sigma_P + 2\Sigma_A)^2 \right)} \right\} \tag{3.87}$$

$$B_y = \pm \frac{2\mu_0 E_0 \Sigma_A^2}{\sqrt{1+M_A^2}} \frac{\Sigma_H}{\Sigma_H^2 + (\Sigma_P + 2\Sigma_A)^2} \tag{3.88}$$

Outside the flux tube, the expressions for B_x and B_y become even more lengthy. Instead of providing these expressions here, figure 3.5 displays plots of the B_x and B_y perturbations of the Alfvén wing far field solution in a plane perpendicular to the northern wing in the simplified case of $\Sigma_H = 0$ and $\overline{\alpha} \to 1$. The resulting vectors of the perpendicular magnetic field perturbations $\underline{B}_\perp = (B_x, B_y, 0)$ are shown in figure 3.6.

The field configuration displayed in figures 3.5 and 3.6 can also be regarded as the magnetic field of a two-dimensional magnetic dipole aligned with the x axis due to the current distribution along the characteristics [*Neubauer* 1980]. This parallel current is given by

$$j_z(r,\varphi) = -\Sigma_A \partial_{\underline{x}}^2 \psi = -2E_0 \Sigma_A \{g_e \sin\varphi + h_e \cos\varphi\} \delta(r-R) \tag{3.89}$$

with the coefficients

$$g_1^e = -\frac{\Sigma_H^2 + \Sigma_P(\Sigma_P + 2\Sigma_A)}{\Sigma_H^2 + (\Sigma_P + 2\Sigma_A)^2} \tag{3.90}$$

$$h_1^e = -\frac{2\Sigma_H \Sigma_A}{\Sigma_H^2 + (\Sigma_P + 2\Sigma_A)^2} \quad . \tag{3.91}$$

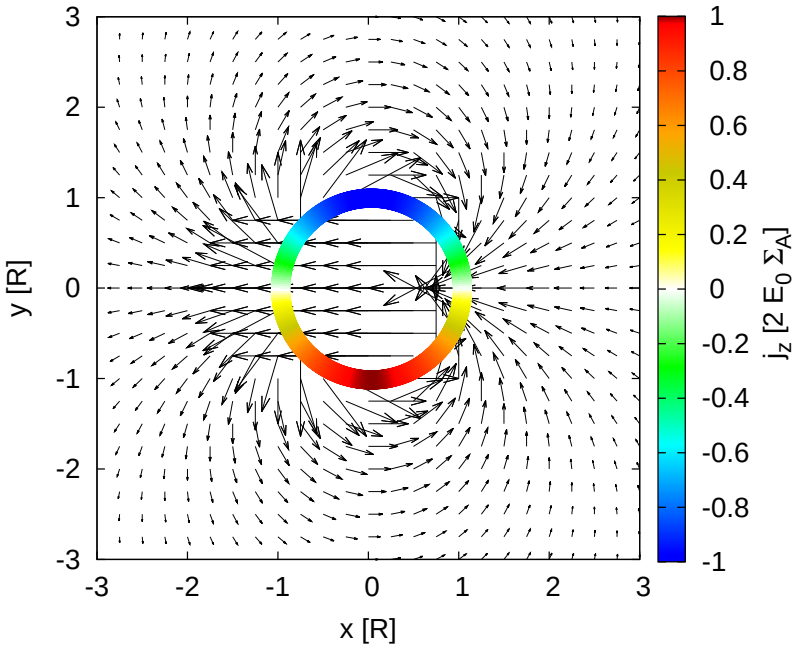

Figure 3.6: Parallel current along the Alfvén characteristics and vectors of the magnetic field perturbations corresponding to figure 3.5. Although the current flows only at the surface of the flux tube, the current is shown on a ring with finite thickness for illustration purposes.

For the solution derived above, i.e. for constant conductances inside a cylinder and zero outside, the field-aligned currents $j_z(x, y)$ are therefore confined to the surface of the flux tube. The zero crossing of $j_z(\varphi)$, i.e. the orientation of the two-dimensional dipole depends on the Hall conductance Σ_H. In analogy to the plots of the magnetic field perturbations, the extreme case $\Sigma_H = 0$ and $\Sigma_P \gg \Sigma_A$ is considered, yielding

$$j_z(r, \varphi) = -2E_0\Sigma_A \sin\varphi \; \delta(r - R) \quad . \tag{3.92}$$

Figure 3.6 shows the distribution of j_z along the mantle of the cylinder superimposed on the field perturbation vectors corresponding to figure 3.5. In the $(+y)$ hemisphere, the currents flows towards the obstacle, while at $y < 0$, the current flows away from the obstacle. In the southern wing, the situation is reversed. Thus, the parallel alfvénic current is indeed fed by the perpendicular (Pedersen and Hall) currents within the obstacle, which was exactly the starting point for the derivation of the potential equation.

In section 5.3 we will discuss further properties of this solution like the associated flow velocities of electrons and ions.

3.3 The Alfvén Wing of Enceladus (Hemisphere Coupling)

For the description of Enceladus' interaction, the general solution presented in the previous section was expanded by *Saur et al.* [2007] to account for the asymmetry introduced by the south polar plume, i.e. the different conductivity north and south of the moon. This modification always has to be taken into account when different conductivities in the northern and southern hemisphere are separated by a current-blocking obstacle. In that

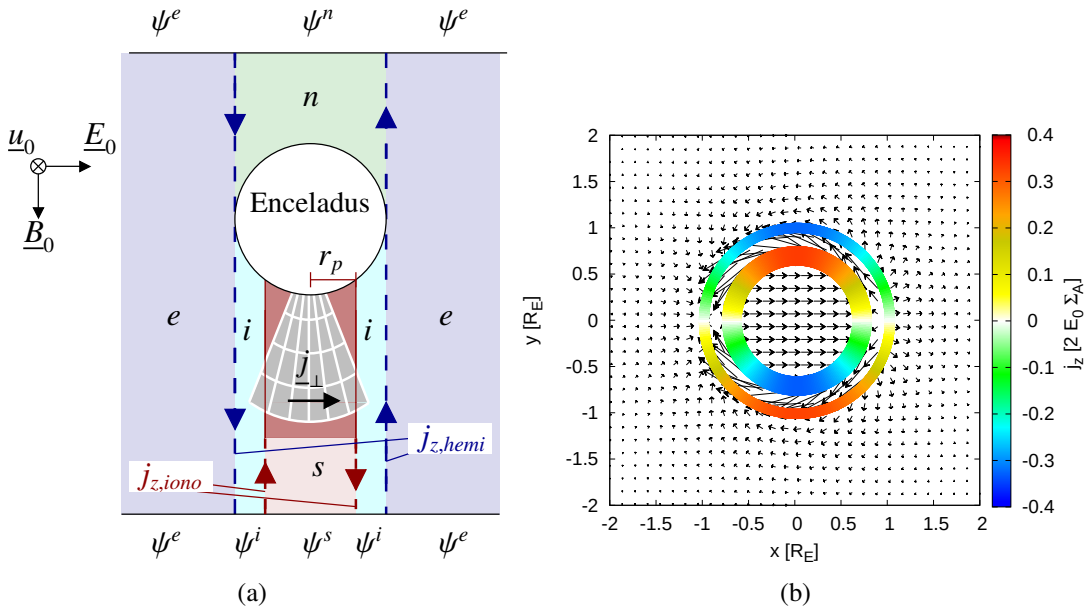

Figure 3.7: Panel (a) displays the domains considered for the analytical solution of Enceladus' asymmetric Alfvén wing. Figure adapted from *Saur et al.* [2007]. Panel (b) shows the magnitude of wing-aligned ionospheric and hemisphere coupling currents in the far field solution of the southern wing for a plume with radius $r_p = 0.7R_E$ and the corresponding vectors of the magnetic field perturbations. Again, the surface currents are shown on rings with finite thickness for illustration purposes. See text for further explanations.

case, equation (3.65) yields different potentials for the northern and southern hemisphere. These potentials are connected with each other via the potential outside the Enceladus flux tube.

Note that for the solution discussed in the previous section, the field-aligned currents are confined to the mantle of the cylinder with constant conductances (cf. figure 3.6). In this simplified scenario, the currents are therefore only blocked by Enceladus, if the plume is approximated by a cylinder with radius r_p, which is smaller than Enceladus, i.e. $r_p < R_E$. Thus, at least four different subdomains have to be considered: first, the exterior domain ('e') whose inner boundary is the Enceladus flux tube. Second, a domain bounded by the extent of the south polar plume and Enceladus' surface. Third, a domain 'i' between the second domain and the exterior. Fourth, a domain 'n' north of Enceladus and bounded by the flux tube and the exterior region (see figure 3.7(a)). The potential equation (3.72) is then solved in analogy to the cylindrical gas cloud (section 3.2.2). An additional boundary condition arises from the coupling of the potentials of the northern and southern hemisphere by integrating equation (3.65) radially across the flux tube from $R_E - \epsilon$ to $R_E + \epsilon$ with $\epsilon \to 0$ (see eq. (9) of *Saur et al.* [2007] for a more general form of this condition):

$$2 \left.\frac{\partial \psi^e}{\partial r}\right|_{r=R_E} = \left.\frac{\partial \psi^n}{\partial r}\right|_{r=R_E} + \left.\frac{\partial \psi^s}{\partial r}\right|_{r=R_E} . \tag{3.93}$$

The solution derived by *Saur et al.* [2007] demonstrates that the different conductances north and south of Enceladus result in different electric potentials and consequently different magnetic field perturbations, electric fields and plasma flow velocities in the northern

and southern hemisphere. This implies that although northern and southern potential are not directly linked, the northern potential is nevertheless affected by the southern plume. The coupling between the two hemispheres creates an additional surface current system which is tangential to the Enceladus flux tube,

$$j_{z,hemisphere}(r,\varphi) = 2E_0\Sigma_A \{g_e \sin\varphi + h_e \cos\varphi\} \delta(r - R_E) \quad . \tag{3.94}$$

The wing-aligned current flowing at the surface of the 'plume-cylinder', i.e. $x^2 + y^2 = r_p^2$ can be expressed as

$$j_{z,iono}(r,\varphi) = \frac{4E_0\Sigma_A R_E^2}{r_p^2} \{g_i \sin\varphi + h_i \cos\varphi\} \delta(r - r_p) \quad , \tag{3.95}$$

where the coefficients are given by eqs. (17) – (23) of *Saur et al.* [2007]. Similar to figure 3.7, both currents are displayed in figure 3.7(b) for $\Sigma_H = 0$, $\Sigma_P \gg \Sigma_A$ and $r_p = 0.7R_E$. According to this analytical solution, the hemisphere coupling current system should always be present, if the Alfvénic, wing-aligned currents are (partially) blocked at the moon's surface. As sketched in figure 1 of *Saur et al.* [2007], this even includes the case in which the plume's diameter is larger than the flux tube but the conductivity is largest below the south pole.

To account for the finite conductivity in the outer regions of the plume, *Simon et al.* [2011b] further extended the solution of *Saur et al.* [2007] by considering even more subdomains. These authors showed that their results are in good agreement with Cassini MAG data from several Enceladus flybys.

It should be pointed out that the field-aligned currents on the mantle of the conducting cylinder are surface currents due to the model assumption of constant conductances within this cylinder. These currents generate a magnetic field discontinuity at the surface of the plume flux tube (see figure 3.5). However, if the conductances were not constant, these currents would be distributed over the whole cross-section of the cylinder and no discontinuity would occur. In contrast, the hemisphere coupling currents are always true surface currents, regardless of the model assumptions. These currents therefore produce real and observable magnetic field discontinuities across the northern and southern Enceladus flux tube. At the time of the study of *Saur et al.* [2007], the Cassini spacecraft had not crossed this boundary, but as was shown by *Simon et al.* [2011b], these discontinuities indeed seem to be present at Enceladus (see also chapters 5 and 6).

3.4 Enceladus' Plasma Interaction: Measurements and Further Studies

After these theoretical descriptions of the plasma structures in Enceladus' environment, the basic insights resulting from Cassini observations – apart from the findings of this thesis – will be summarized. Note that this section focuses on the plasma structures, while the different models will be discussed in section 4.6.

The first in-situ observations of plasma structures generated by the plume were already made during the E0 and E1 flybys in February and March 2005 by the Cassini Magnetometer [*Dougherty et al.* 2006]. The observed magnetic field signatures indicated a

draping of the field lines around an ionospheric obstacle south of Enceladus, consistent with the formation of an Alfvén wing. The magnetic field structures also suggested a slow down of the plasma within the plume. The picture of an Alfvénic interaction could be further confirmed during the subsequent E2 encounter. Moreover, the observed signatures exhibited the expected magnetic field pile-up upstream of the plume.

During the E2 flyby, CAPS observed strong deflections in the plasma flow at least $27R_E$ away from Enceladus. Close to Enceladus, the plasma was found to be strongly slowed down [*Tokar et al.* 2006]. It was concluded that the data are consistent with charge exchange between the magnetospheric ions and the neutrals in Enceladus' plume and the subsequent pick-up of these newly generated ions. Although photo- and impact ionization of neutrals could in principle lead to the same structures, RPWS did not detect a significant increase of the plasma density during E2 ($\gtrsim 20\%$) and therefore, charge exchange was suggested to be the dominant process for the plasma slow down and the deflections [*Tokar et al.* 2006]. By applying a steady-state model of the electrodynamic coupling between Enceladus and Saturn based on the unipolar inductor, *Tokar et al.* [2006] and *Pontius and Hill* [2006] found that the amount charge exchange required to generate the observed flow deflections corresponds to a total mass loading rate of more than 100 kg/s.

As more flybys became available, CAPS detected freshly-produced water group ions (O^+, OH^+, H_2O^+, H_3O^+) close to Enceladus [*Tokar et al.* 2009]. Within the plume, the CAPS ram anodes measured ions at energies corresponding to Cassini's flyby velocity, which implies a (nearly) stagnating plasma flow within the plume. It is noteworthy that the slow down of the plasma was measured four to six R_E north of Enceladus. The observations of flow perturbations north of Enceladus are consistent with Cassini approaching the northern Alfvén wing.

INMS measurements during the E3 flyby showed that out of the water group ion species, H_3O^+ is predominant within the plume [*Cravens et al.* 2009]. Another study of the ion-neutral chemistry in the plume has been presented by *Fleshman et al.* [2010a], further confirming the importance of H_3O^+. A more detailed discussion of this findings will be presented in section 6.4.1.

Burger et al. [2007] developed a 3D Monte-Carlo model of the neutral plume to simultaneously explain INMS and UVIS data. By including a detailed model of charge exchange and ionization, these authors calculated a mass loading rate of $2-3$ kg/s, i.e. two orders of magnitude smaller than the value obtained by *Tokar et al.* [2006]. Furthermore, *Burger et al.* [2007] suggested a plasma slow down to about 10 km/s which is less than 50% of the corotation speed but still significantly more than a stagnant plasma flow.

Khurana et al. [2007] modeled the magnetic field data collected during the E0 – E2 flybys in 2005 in order to quantify the strength of Enceladus' plasma interaction. These authors concluded that the effective diameter of the plume as an obstacle to the plasma flow is at least $6R_E$, and the draping center[3] of the magnetic field lines is displaced by more than $2R_E$ south of Enceladus and downstream by at least $1R_E$. In contrast to *Pontius and Hill* [2006], *Khurana et al.* [2007] estimate the total mass loading within $5R_E$ of Enceladus to

[3]Note that in the work of *Khurana et al.* [2007] and *Jia et al.* [2010b,c], the term "momentum loading center" is used. Because the center is derived from the draping of the magnetic field lines, this location is more appropriately described as the "draping center", especially since the draping center does not necessarily coincide with the region of highest momentum loading.

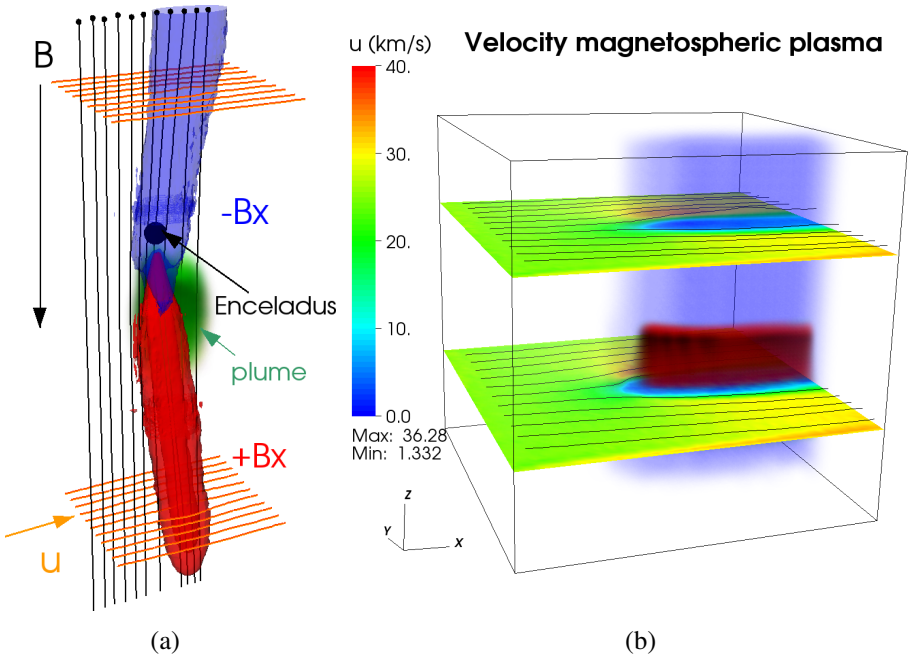

Figure 3.8: Results from preceding hybrid simulations of Enceladus' plasma interaction [*Kriegel et al.* 2009]. (a) B_x perturbations of Enceladus' Alfvén wing. (b) Deflection of the plasma flow around the wing. The region shown in dark red indicates the increased pick-up ion density.

be less than 3 kg/s, consistent with the value of *Burger et al.* [2007].

The same magnetic field data were also analyzed by *Saur et al.* [2008]. These authors applied a two-fluid plasma model in combination with a Biot-Savart model and presented evidence for a temporal variability in the activity of the jets. They derived a production rate for the water molecules of 1600 kg/s during E0 and 200 kg/s for E1 and E2, i. e. a difference of a factor of eight between these flybys. In that work, the authors applied an analytical plume model that was adjusted to INMS data from the E2 flyby. They found that MAG data seem to indicate changes of the regions with strongest plume activity from downstream (E0) to upstream (E1, E2).

In a pilot study, first self-consistent simulations of Enceladus' plasma interaction were presented in *Kriegel* [2009] and *Kriegel et al.* [2009]. It was systematically analyzed how Enceladus' low-conducting body and plasma absorption at the surface as well as ionization and pick-up in the plume contribute to the overall structure of the interaction region. By isolating the contribution of the plasma-absorbing body of Enceladus, it was found that plasma absorption at the surface of the moon gives rise to the expected shape of the density cavity. Furthermore, the magnetic field diffuses through the solid body of Enceladus almost unaffected. These findings are in agreement with the processes described in section 3.1 If the plume is included, an Alfvén wing system is triggered that controls the structure of Enceladus' plasma environment. Figure 3.8 displays the results of these hybrid simulations. Panel 3.8(a) shows the B_x perturbations which clearly extend along the Alfvén characteristics. The plasma flow is deflected around the Alfvén wings as shown in figure 3.8(b). In that study, charge exchange was not taken into account, but only photoionization and electron impacts. As derived in section 3.2.3, all three processes

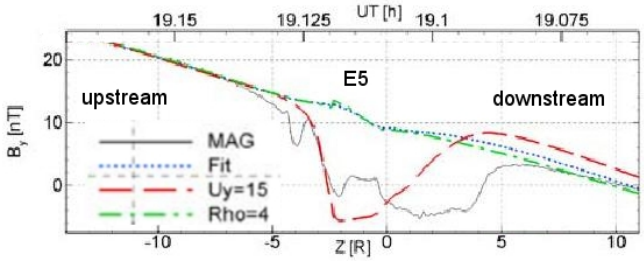

Figure 3.9: Simulation results of *Jia et al.* [2010c] (after fig. 2 of that work). The plot shows the measured B_y perturbation during E5 (black), and the results for different simulation setups. The dashed line (red) shows the results for a simulation that includes a Saturnward component of the upstream plasma of $u_{0,y} = 15\,\mathrm{km/s}$.

determine the currents via the effective collision frequency. Therefore, an increase of the ionization frequency is able to compensate for a lack of charge exchange. The major difference is the resulting ion density, which is obviously higher for an increased ionization frequency. It was demonstrated that the pick-up tail of the newly generated ions possesses a 2D structure due to the small gyroradii (cf. red volume in figure 3.8(b)). The simulations also showed a pile-up of the magnetic field in front of the plume and a reduced magnetic field strength in the downstream region due to the perpendicular currents within the plume. By comparing the results with MAG data from E0 – E2, evidence was found for a variation of the activity and the positions of the active jets that contribute to the plume in agreement with *Saur et al.* [2008]. Quantitatively, however, the inferred plume variability was different for the two studies as *Kriegel et al.* [2009] derived a factor of two between E1 and E2, whereas the model of *Saur et al.* [2008] suggests a rather constant plume for these flybys. Although the simulation results presented in *Kriegel et al.* [2009] show in general a good agreement with Cassini MAG data, there is an apparent mismatch between the simulated B_y perturbations and MAG data during E2 (see fig. 7 of *Kriegel et al.* [2009]).

Omidi et al. [2010] carried out a similar hybrid simulation study to compare the influence of the absorbing body with that of the plume. These authors showed that charge exchange and ionization result in the generation of ion cyclotron waves. In addition, they studied the impact of the plume on the plasma structures and found that neutral densities at the surface of up to $n_{n0} \sim 10^6\,\mathrm{cm}^{-3}$ do not cause noticeable perturbations of the plasma. Densities of $n_{n0} \sim 10^8\,\mathrm{cm}^{-3}$ are required to generate a strong Alfvén wing. By comparing modeled ion energy spectra with CAPS observations from E3, *Omidi et al.* [2010] also found that base densities of $n_{n0} \sim 5 \cdot 10^8\,\mathrm{cm}^{-3}$ and a corresponding mass loading rate of $\sim 4\,\mathrm{kg/s}$ are in agreement with CAPS data, which is also consistent with the values derived by *Khurana et al.* [2007] and *Saur et al.* [2008].

In a series of three papers *Jia et al.* [2010b,c,d] carried out a very detailed study of Enceladus' plasma interaction by means of MHD simulations. In the first part, *Jia et al.* [2010d] performed case studies to isolate the structures caused by an absorbing body and an atmosphere alone, similar to the work of *Kriegel et al.* [2009]. In contrast to the latter, *Jia et al.* [2010d] also compared the importance of charge exchange with photo- and electron impact ionization. They found that charge exchange has the dominant impact on field perturbations and plasma flow pattern. In the second study, *Jia et al.* [2010c] compared

their results with MAG data from the E2 and E5 flybys to analyze the shape of the plume. They found that the magnetic field signatures agree best with a plume opening angle of $10° - 20°$ and a tilt angle of $10°$ towards downstream which is also in agreement with *Kriegel et al.* [2009]. Furthermore, their model suggests that mass loading in the plume is less efficient close to the surface of the moon, although the neutral density is highest near the surface. Their modeled ion densities show an increase of about 50% due to photo- and electron impact ionization. Currents arising from charge exchange, however, generate over 90% of the strength of the field perturbations. Although their results were in good agreement with the observed B_x and B_z components for both flybys, B_y was not reproduced by the simulations as shown in figure 3.9. This is similar to the results of *Kriegel et al.* [2009], who found a disagreement between simulated and measured B_y component for the E2 flyby (cf. fig. 7 in that work). Therefore, *Jia et al.* [2010c] suggested that an upstream velocity component towards Saturn is required to explain the observed B_y perturbations. Furthermore, *Jia et al.* [2010c] found that variations in the gas production rate cause significant variations in the B_z perturbations, while variations in the upstream density mainly modify the B_x and B_y perturbations. This finding is in agreement with the theoretical point of view developed in the previous sections: On the one hand, the B_z perturbation is not part of the Alfvén wing far field solution, but it is directly generated by the perpendicular Pedersen and Hall currents in the plume. The strength of these currents therefore increases with higher neutral densities. On the other hand, the B_x perturbation in the center of the Alfvén wing in the far field (equation (3.87)) can be approximated as $B_x \approx \overline{\alpha} M_A B_0$. For $\overline{\alpha} \to 1$, the B_x perturbations depend only on the upstream density, $B_x \sim \sqrt{n_0}$. In their third study, *Jia et al.* [2010b] analyzed the variability of the plume by considering the strength of the B_z perturbations. It was found that the maximum variation of the gas production rate is about 30% which is a clearly lower variability than the factor of eight between E0 and E1/E2 derived by *Saur et al.* [2008]. The plasma momentum loading rate ranges from 0.8 to 1.9 kg/s, which is consistent with previous studies. The model of *Jia et al.* [2010b] also required that the momentum loading rate per neutral density is reduced close to the surface by orders of magnitude compared to larger distances. It it suggested that a depletion of hot electrons and a decrease in the charge exchange rate may explain the reduction of the momentum loading rates close to the south pole.

Another important finding has been made by analyzing data that has been collected by the RPWS Langmuir probe during the E2 encounter: the presence of a significant imbalance between the number densities of free electrons and ions, coinciding with an increase in the density of submicron dust grains [*Wahlund et al.* 2009, *Yaroshenko et al.* 2009]. Thus, this void in the electron density is suggested to arise from electron absorption by dust. In agreement with that, analysis of the upper hybrid frequency emissions recorded by RPWS during E3 indicated an electron dropout to below $n_e = 20\,\mathrm{cm}^{-3}$ within the plume [*Farrell et al.* 2009]. The density of charged dust corresponding to the difference of electron and ion densities observed by the Langmuir Probe during E3 has been used by *Shafiq et al.* [2011] to infer characteristics of the charged dust population. These authors concluded that the Debye length of these charged dust grains is large compared to the average distance between the grains and hence, the charged dust has to be taken into account as an additional plasma constituent. Interpretation of Langmuir Probe data from the steep flybys E3 – E6 has also been performed by *Morooka et al.* [2011]. These authors suggested enormous ion densities of $30,000 - 100,000\,\mathrm{cm}^{-3}$ due to ionization within the plume,

whereas the suggested electron densities are in the range of $2,000 - 4,000\,\mathrm{cm}^{-3}$, thereby implying that more than 90% of the electrons are absorbed by the dust. However, *Morooka et al.* [2011] did not present any quantitative estimates with regard to the processes generating these extremely high densities.

Apart from the indirect hints towards the presence of charged dust by the discrepancy of electron and ion densities, there is also direct evidence for charged nanograins in the plume reported by the CAPS. Although originally designed for detecting electrons and ions in a wide energy range, the instrument detected high counting rates at energies $> 1\,\mathrm{keV}$ when Cassini was traveling through the plume. These were interpreted as the signatures of charged nanograins [*Jones et al.* 2009]. The nanograins were observed as collimated jets and seem to be separated according to their charges and masses. Interestingly, both, positive and negative grains were observed. Further analysis of these data by *Coates et al.* [2010] indicated the presence of negative ions, i.e. negatively charged water group clusters with masses up to 72 amu. *Hill et al.* [2012] used CAPS data from E3 and E5 to derive the densities of the nanograins. These authors suggested that the density of the negative nanograins reached values of up to $2600\,e/\mathrm{cm}^{-3}$ during E3, whereas the density of the positive grains is about three orders of magnitude lower.

In addition, RPWS recorded strong broadband whistler mode emissions, called auroral hiss [*Gurnett et al.* 2011]. It is suggested that the electrons generating the auroral hiss are accelerated by parallel electric fields in a region very close to the moon. A survey of the auroral hiss observations of all 20 flybys has been carried out by *Leisner et al.* [2013]. These authors found that all emissions are generated by field-aligned electron beams either in the region upstream and Saturnward of Enceladus or downstream and at the Saturn-averted side.

More recently, *Ozak et al.* [2012] analyzed CAPS electron data from E5 by applying a two-stream electron transport model. Their modeled electron fluxes agree well with CAPS data, thereby suggesting that photoelectrons with energies between 10 eV and 70 eV are consistent with the data. Furthermore, *Ozak et al.* [2012] concluded that ion production due to electron impacts is only about 20% that of photoionization. However, the photoelectrons considered by *Ozak et al.* [2012] are mainly of magnetospheric origin. In constrat, *Coates et al.* [2013] showed that photoelectron locally produced within the plume had been detected by CAPS during nearly all Enceladus encounters. These authors suggested that the plume photoelectrons increase the electron flux at energies of about 20 eV by about a factor of two and thus, photoelectrons have to be taken into account as an additional ionization source.

3.5 Summary of Enceladus' Plasma Interaction and Open Questions

The plasma interaction of Enceladus features the unique situation in which an absorbing body is placed *above* the plume as an ionosphere-type obstacle. Therefore, the resulting interaction with the subalfvénic flow of magnetospheric plasma contains aspects of both scenarios. Previous studies, however, indicate that the plasma structures generated by the plume dominate the overall interaction and the structures caused by plasma absorption

at the moon (see section 3.1) are less important at Enceladus [*Kriegel et al.* 2009, *Jia et al.* 2010d]. Within the plume, the neutral molecules are mainly ionized due to charge exchange and to a lesser extent by photoionization and electron impacts. The momentum and mass loading of a few kg/s of ions leads to a nearly stagnant plasma flow in the center of the plume as observed by CAPS [*Tokar et al.* 2006]. Furthermore, ionization and ion-neutral collisions result in the generation of Pedersen and Hall currents in the plume. These transverse currents cause a magnetic pile-up region at the ramside of the plume and reduce the magnetic field strength in the downstream region. In the rest frame of the incident plasma, these currents are closed by the field-aligned currents of a stationary, non-linear system of Alfvén waves, the Alfvén wing. Transformed to the rest frame of the moon, the currents flow along the Alfvén characteristics $\underline{\mathcal{Z}}^{\pm}$, which are tilted towards the corotation direction by an angle of $\theta_A \approx 5^\circ - 10^\circ$ with respect to the background field. In the far field (i.e. where the magnetic field generated by Pedersen and Hall currents can be neglected), the wing current system exhibit translation symmetry along the wing characteristics (see e.g. *Neubauer* [1980, 1998], *Saur et al.* [1999] and references therein). The associated magnetic field perturbations have been detected by Cassini MAG during all Enceladus encounters. Furthermore, *Saur et al.* [2007] proposed an additional current system that arises from the partial blockage of the Alfvénic field-aligned currents by the solid body of the moon. This current system connects Enceladus' northern and southern hemispheres and therefore, it is referred to as 'hemisphere coupling currents'. Since these currents are surface currents flowing on field lines tangential to Enceladus, they cause discontinuities in the magnetic field which have been observed by Cassini MAG.

Overall, a broad and detailed understanding of Enceladus' plasma interaction was already available prior to this thesis. However, a comparison between Cassini MAG data and preceding hybrid simulations [*Kriegel et al.* 2009] as well as MHD simulations by *Jia et al.* [2010b,c] also revealed some apparent mismatches which seem to contradict the theory depicted in this chapter. In addition, the presence of charged dust has not been taken account by these studies. Thus, the following issues shall be addressed within this thesis:

- Various measurements indicate that the negatively charged dust within the plume exhibits densities comparable to the ion densities [*Yaroshenko et al.* 2009, *Shafiq et al.* 2011, *Morooka et al.* 2011, *Hill et al.* 2012]. Thus, the main topic of this thesis is to investigate what effects on the plasma structures are caused by the presence of the charged dust.

- What is the reason for the striking difference between modeled and measured B_y perturbations? If the explanation was a radial flow component of the magnetospheric plasma as suggested by *Jia et al.* [2010c], how does such a flow pattern fit in the understanding of Saturn's magnetosphere (see section 2.2)? What other explanations are possible and how could they be integrated into the existing theoretical framework? These questions will be addressed and answered in chapter 5.

- The models of *Khurana et al.* [2007] and *Jia et al.* [2010b,c] indicate that the draping center is displaced from the surface to the south and downstream. *Jia et al.* [2010b] proposed that a reduction of the reaction and ionization rates may yield this shift of the draping center. It will therefore be analyzed in chapters 5 and 6,

whether and under what assumptions, the hybrid simulations in combination with data from the steep Enceladus flybys E3 – E6 can reproduce this location of the draping center. In this sense, MAG data shall also be used as a sensitive probe to further constrain the structure and properties of the neutral plume.

- Between 2009 and 2014, 13 additional Enceladus flybys took place that had not been analyzed in the simulation studies of *Jia et al.* [2010b,c] and *Kriegel et al.* [2009]. Do the (magnetic field) data collected along these trajectories confirm our understanding of Enceladus plasma interaction or do new questions arise? With more flybys available, the variability of the plume is also to be constrained in more detail in chapter 5.

- Although charge exchange has the dominant impact on the plasma flow, photoionization and electron impacts are responsible for the increased ion density in the plume. In chapter 6, the combination of a detailed model of the reaction and ionization rates with a sophisticated model of the neutral plume shall allow to quantitatively determine the increase of the ion density.

4 Hybrid Simulation Code A.I.K.E.F.

In this chapter, the main features of the simulation model are described. After a brief overview about the hybrid approach and the simulation code A.I.K.E.F., the unique aspects of the modeling of Enceladus' plasma interaction are discussed. In particular, the implementation of collisions and reactions is discussed in some detail. Furthermore, the boundary conditions applied within the simulation model will be described and their influence on the physical structures will be analyzed. Finally, an overview of the existing models of Enceladus' plasma interaction is provided.

4.1 Hybrid Approach: Basic Assumptions and Equations

Since the hybrid model used in this work has already been described in detail in the literature (e. g. *Bagdonat and Motschmann* [2002b], *Simon* [2007]), the assumptions and equations of the hybrid model will only be briefly reviewed. For a more general overview about hybrid models and their implementations, the reader is referred to *Winske et al.* [2003].

The hybrid approach treats the electrons as a massless, charge-neutralizing fluid. Since the ions are represented by individual particles, the model can handle multiple ion species and does not require any assumptions on the velocity distribution of the ions. The approximation of electrons as a fluid is well fulfilled if the time and spatial scales of the investigated processes are clearly larger than the electron gyration period and the electron gyration radius, respectively.

The hybrid model used in this thesis is based on three basic assumptions:

- The electron mass m_e is neglected,

$$m_e \approx 0 \quad . \tag{4.1}$$

- The plasma is assumed to be quasi-neutral, i. e. for a plasma consisting of $\alpha = 1, ..., N$ species with densities n_α and charges q_α, it is

$$\sum_{\alpha=1}^{N} q_\alpha n_\alpha = 0 \quad . \tag{4.2}$$

  Therefore, the length scales are assumed to be much larger than the Debye length λ_D, which assumes values of a few meters in the vicinity of Enceladus and some tens of meters near Rhea.

- The Darwin-Approximation [*Bagdonat* 2004] is used which means that the displacement current is neglected. Ampère's law then reads

$$\partial_{\underline{x}} \times \underline{B} = \mu_0 \underline{j} \quad . \tag{4.3}$$

  Thus, all velocities have to be well below the speed of light.

From these few assumptions, the basic equations of the model can be derived.

To show how even a negatively charged ion or dust species can be included in the framework of the hybrid model, the general derivation of the equation for the electric field is reviewed. The electron momentum equation for zero electron mass and isotropic pressure reads

$$\underline{E} = -\underline{u}_e \times \underline{B} - \frac{\partial_{\underline{x}} p_e}{e n_e} + \eta \underline{j} \quad , \tag{4.4}$$

where $\underline{u}_e$ denotes the electron bulk speed and p_e is the electron pressure. The last term describes the diffusion of the electromagnetic fields through a medium of finite resistivity η or corresponding conductivity $\sigma = 1/\eta$, which may arise from the moon's solid body, see section 4.5.1. In addition, this resistivity mimics the effects of electron-ion collisions or wave-particle scattering. Using the definition of the current $\underline{j}$,

$$\underline{j} = \sum_\alpha q_\alpha n_\alpha \underline{u}_\alpha = \sum_j q_j n_j \underline{u}_j - e n_e \underline{u}_e \quad , \tag{4.5}$$

and rearranging for the electron velocity $\underline{u}_e$ yields

$$\underline{u}_e = \frac{\sum_j q_j n_j \underline{u}_j - \underline{j}}{e n_e} = \frac{\sum_j q_j n_j \underline{u}_j - \underline{j}}{\sum_j q_j n_j} \quad , \tag{4.6}$$

where $\underline{u}_{\alpha/j}$ denotes the bulk velocity of species α/j. In the last step, the quasi-neutrality condition (4.2) has been used. It may be defined that here and in the following, the subscript 'α' runs over all *plasma* species (ions and electrons) while the subscript 'j' is only used for the *ion* species.

Inserting equations (4.2), (4.6) and (4.3) into (4.4) finally yields the equation for the electric field in the hybrid model:

$$\underline{E} = -\frac{\sum_j q_j n_j \underline{u}_j}{\sum_j q_j n_j} \times \underline{B} + \frac{(\partial_{\underline{x}} \times \underline{B}) \times \underline{B}}{\mu_0 \sum_j q_j n_j} - \frac{\partial_{\underline{x}} p_e}{\sum_j q_j n_j} + \eta \frac{\partial_{\underline{x}} \times \underline{B}}{\mu_0} \quad . \tag{A}$$

The substitution

$$\frac{\sum_j q_j n_j \underline{u}_j}{\sum_j q_j n_j} = \underline{u}_i \tag{4.7}$$

leads to the more common form of equation (A) that is usually given in the literature. Note that in this general case, $\underline{u}_i$ is the *charge-averaged* ion velocity, which is identical to the

number-density averaged velocity only in the simple case with singly-charged, positive ion species. Therefore, $|\underline{u}_i|$ may become larger than each species' bulk velocity $|\underline{u}_j|$, if negatively charged ion or dust species are involved.

It should be noted that the denominators in equation (A) must not be zero. Thus, a minimum positive charge density $\rho_{\min}$ is introduced. If the density at some point in the simulation box drops below that threshold, the denominators are set equal to $\rho_{\min}$ to avoid that the field diverges. The value of the minimum charge density $\rho_{\min}$ is set to $\rho_{\min} = 0.1en_0^*$ and $\rho_{\min} = 0.15en_0^*$ for the simulations presented in chapter 5 and 6, respectively, what corresponds to 10 % (15 %) of the upstream ion density n_0^*.

When considering $\rho_{\min}$, the model is capable of handling a *negatively* charged ion or dust species without any modifications. In section 6.3, it will be shown that dust (subscript 'D') can be described as a heavy, negatively charged ion species. Assuming that the dust may be charged with ξ electrons, i. e.

$$\varrho_D = -e\xi n_D \quad , \tag{4.8}$$

it is

$$\sum_j q_j n_j = \sum_{\substack{j \\ q_j>0}} q_j n_j - e\xi n_D > \rho_{\min} \quad . \tag{4.9}$$

In this hybrid model, the equation of state for the electrons is provided by an adiabatic law for the pressure:

$$p_e = \sum_j p_{e,j} = \sum_j p_{e,j0} \left(\frac{n_{e_j}}{n_{e,j0}} \right)^\kappa \quad . \tag{B}$$

The quantities $p_{e,j0}$ and $n_{e,j0}$ denote pressure and density of the undisturbed upstream plasma. The adiabatic exponent κ is set to $\kappa = 2$. This choice considers that the magnetic field reduces the degrees of freedom of the electrons to two (see e.g, *Bagdonat* [2004] and *Simon* [2007]). The subscript 'j' indicates that different electron populations are assigned to the respective ion species. This description takes into account that the temperature of the upstream electrons may be considerably different from that of the ionospheric electrons. The approach of different electron populations is a good approximation only in regions where these populations do not mix. Otherwise, this concept may lead to contradictory results, see *Ranocha* [2013]. However, it should be pointed out that due to the low electron plasma beta of only $\beta_e = 0.0004$ at Enceladus (cf. table 2.4), the electron pressure has a negligible impact on the plasma structures. Apart from the adiabatic law, other ways to close the set of equations are also possible, for instance a study that included the time evolution of the electron pressure in the hybrid model has recently been presented by *Ranocha* [2013].

Finally, the time evolution of the magnetic field can be obtained by applying Faraday's law to eq. (A),

$$\partial_t \underline{B} = \partial_{\underline{x}} \times \left(\underline{u}_i \times \underline{B}\right) - \partial_{\underline{x}} \times \left(\frac{\partial_{\underline{x}} \times (\partial_{\underline{x}} \times \underline{B})}{\mu_0 \sum\limits_j q_j n_j} \right) - \partial_{\underline{x}} \times \left(\frac{\eta}{\mu_0} \partial_{\underline{x}} \times \underline{B} \right) \quad . \tag{C}$$

Note that due to the adiabatic law, the curl of the pressure term vanishes and this term does not appear in equation (C).

Since the ions are treated as particles, they may be generated or lost by ionization, recombination, reactions or absorption at the satellite's surface. The motion of an individual particle 'p' is governed by the Lorentz force according to

$$\frac{d\underline{x}_{p,j}}{dt} = \underline{v}_{p,j} \qquad ; \qquad \frac{d\underline{v}_{p,j}}{dt} = \frac{q_j}{m_j} \left(\underline{E}' + \underline{v}_{p,j} \times \underline{B} \right) \quad , \tag{D}$$

where the modified electric field $\underline{E}' = \underline{E} - \eta \underline{j}$ is required to conserve the total momentum of the system [*Bagdonat* 2004].

4.2 Numerical Implementation

The implementation of the hybrid model used in this work is the simulation code A.I.K.E.F. (Adaptive Ion-Kinetic Electron-Fluid) [*Müller et al.* 2011]. It is the successor of the "Braunschweig Code" which has been applied to the plasma interaction of various objects in the solar system within the last decade. In particular, A.I.K.E.F. had already been used for the preceding study of Enceladus' plasma interaction [*Kriegel et al.* 2009] whereas the Braunschweig-Code had been applied for simulations of Rhea's plasma interaction by *Roussos et al.* [2008a]. A detailed description of the numerical aspects of A.I.K.E.F. is given by *Müller et al.* [2011]. Therefore, just a short summary and some details which are complementary to the aforementioned studies will be provided here.

A.I.K.E.F. operates on Cartesian meshes, where the resolution can locally be increased according to the structures of interest. The refinement is implemented as "Hybrid Block Adaptive Mesh Refinement" (AMR). The mesh is decomposed into equally sized blocks (L_0-blocks). Each block is again divided into eight octants. If a certain criterion is fulfilled (either predefined or dynamically computed during simulation runtime), the octant becomes a new block of the next higher level of refinement. The cell size of this new block is therefore a factor of two smaller. This method allows a good adjustment of the regions of higher mesh resolution to the features of interest together with an efficient computation. Theoretically, an arbitrary number of refinement levels may be used. However, it turned out that calculations with more than four levels (L_0, L_1, L_2, L_3) take too long for our purposes. The code is parallelized via the Message Passing Interface (MPI) such that each process is assigned a certain number of blocks. The number of blocks handled by a process is adjusted in the way that the workload of all processes is similar. For the simulations performed for this thesis, the computation time speedup of A.I.K.E.F. scales almost linearly with the number of processors until at least 128 CPUs. Therefore, and due to the available computational resources, nearly all simulations were carried out on 128

CPUs.

A.I.K.E.F. is a *Particle-in-Cell* code, which means that the macroscopic physical quantities are computed only at the mesh nodes of the simulation grid while the ions (which are represented by macroparticles with the same charge-to-mass ratio as the real particles) can move freely within the cells. The contribution of a macroparticle to the macroscopic moments at the mesh nodes of the respective cell as well as the electromagnetic fields at the particle's position are inter-/extrapolated with the trilinear *Cloud-in-Cell* method. However, the different cells sizes of the mesh require some additional procedures for the particles: when moving from a lower to s higher level of refinement, one cell is divided into eight smaller cells. In consequence, a certain number of macroparticles in the larger cells (typically $\sim$ 100) would yield on average a factor of eight less macroparticles in the smaller cells. When crossing even more levels, e.g. from L_0 to L_3, some cells of L_3 may be completely devoid of particles. The opposite effect occurs when starting with about 100 macroparticles in the highest level and moving into larger cells. In this case, the number of macroparticles in the cells of L_0 would be drastically enhanced, yielding a very inefficient and slow computation. Therefore, the number of macroparticles in each cell is adjusted next to the refinement boundaries. On the one hand, this is done by splitting one particle into two if there are too few macroparticles in the respective cell. On the other hand, three particles are merged into two if there are too many particles. Details on the splitting and merging in A.I.K.E.F. can be found in *Müller* [2012].

The electric field is advanced in time via the *Current Advance Method* [*Matthews* 1994]. The convective term and the Hall term of the magnetic field equation,

$$\partial_t \underline{B} = \partial_{\underline{x}} \times \left(\underline{u}_i \times \underline{B} \right) - \partial_{\underline{x}} \times \left(\frac{\partial_{\underline{x}} \times (\partial_{\underline{x}} \times \underline{B})}{\mu_0 \sum\limits_j q_j n_j} \right) = f(\underline{B}) \tag{4.10}$$

are advanced in time by means of a second-order cyclic *leap-frog* algorithm, which is explicit in time (see section 4.3.1 of *Bagdonat* [2004] and references therein). The major disadvantage of this algorithm is that the numerical solution may be artificially amplified compared to the analytical solution which makes the simulation unstable. Therefore, an additional smoothing procedure has to be performed (see section 4.4). The diffusion term of the magnetic field equation,

$$\partial_t \underline{B} = -\partial_{\underline{x}} \times \left(\frac{\eta}{\mu_0} \partial_{\underline{x}} \times \underline{B} \right) = g(\underline{B}) \quad , \tag{4.11}$$

is more difficult to numerically solve due to the sharp gradient of the resistivity η at the surface of the moon (see section 4.5.1 for a discussion of the obstacles' resistivity). If the leap-frog algorithm was applied to equation (4.11), a stable simulation would require a significantly smaller time step and an associated longer simulation time. Thus, an implicit Crank-Nicolson algorithm

$$\frac{\underline{B}^{n+1} - \underline{B}^n}{\Delta t} = \frac{1}{2} \left(g(\underline{B}^{n+1}) + g(\underline{B}^n) \right) \tag{4.12}$$

is applied to advance the diffusion term from time step n to time step $n+1$. This algorithm has the advantage that the numerical amplification is always equal to one. To solve this

implicit equation, the iterative *Successive-Over-Relaxation* (SOR) scheme is used,

$$\underline{B}^{new} = (1 - \omega_{SOR})\underline{B}^{old} + \omega_{SOR}\underline{B}^{*} \quad . \tag{4.13}$$

Here, $\underline{B}^{*}$ is a function of the coefficients and differential operators of equation (4.11). The overrelaxation parameter ω_{SOR} guarantees convergence for $1 < \omega_{SOR} < 2$. The exact value of ω_{SOR} which enables the fastest convergence can be determined only empirically for each simulation scenario. For further details on the implementation of the SOR scheme, the reader is referred to the appendix of *Wang* [2012].

The code is implemented on an *un*-staggered mesh, that is $\underline{E}$ and $\underline{B}$ are computed on the same mesh nodes. This requires an additional "divergence cleaning" method to ensure that $\partial_{\underline{x}} \cdot \underline{B} = 0$ is fulfilled: first, the (numerical) divergence of $\underline{B}$ is used to determine a potential Φ_{dB} by

$$\partial^2_{\underline{x}}\Phi_{dB} = -\partial_{\underline{x}} \cdot \underline{B} \quad . \tag{4.14}$$

Poisson's equation for the potential Φ_{dB} is solved again with the SOR method. Second, the calculated Φ_{dB} is used to obtain the corrected (divergence-free) magnetic field according to

$$\underline{B}_{corrected} = \underline{B} + \partial_{\underline{x}}\Phi_{dB} \quad . \tag{4.15}$$

Apart from the amplification error of the leap-frog algorithm, the numerical stability of the simulations is affected by the finite number of macroparticles in the cells. The macroscopic plasma moments calculated at the grid nodes, like ion density and velocity, always exhibit some level of fluctuations. Therefore, using a higher number of macroparticles stabilizes the simulations at the expense of computational time. Furthermore, the Courant-Friedrichs-Lewy criterion states that no information (which include the particles) should propagate faster than one mesh spacing per time step Δt. Otherwise, any explicit numerical scheme gets instable. For the simulations of Enceladus, however, the Courant criterion would in principle allow for very large Δt, e.g. for the fastest particles – moving with about 60 km/s (bulk speed plus twice the thermal speed) – and a cell size of 10 km a time step of $\Delta t < 0.1$ s seems to be sufficient. However, the combination of small denominators in the field equations due to negatively charged dust in the plume and the strong resistivity gradient at the surface of the obstacle require a smaller time step for the stability of the simulations of $\Delta t < 10^{-2}$ s.

It should also be noted that all calculations in A.I.K.E.F. were carried out with normalized quantities (indicated by a ' * '), i. e.

$$A^{*} = \frac{A_{\mathrm{SI}}}{A_{0,\mathrm{SI}}} \quad , \tag{4.16}$$

where A_{SI} denotes the physical quantity in SI units and $A_{0,\mathrm{SI}}$ is the background value in SI units.

4.3 Collisions, Reactions and Ionization

In many cases, the interaction of the plasma flow with a neutral gas cloud (like Enceladus' plume) is most important for the overall plasma interaction of the respective object. It will

therefore be described how the ion-neutral interactions are incorporated into the simulation model. It should be pointed out that the *plasma* simulation model A.I.K.E.F. considers the neutral gas as a stationary, fluid-like background. This is, however, a reasonable assumption, since in any case where the neutrals become important for the dynamics of the ions, the neutral density has to be considerably larger than the ion density. In Saturn's neutral-dominated magnetosphere, this is fulfilled nearly everywhere. For instance, the density of the neutral torus at Enceladus' orbit is about $n_n \sim 10^4\,\mathrm{cm}^{-3}$ [*Smith et al.* 2010] compared to an ion density of $n_i \sim 10^2\,\mathrm{cm}^{-3}$ (cf. table 2.4). Within the plume, the neutral density even increases up to $n_n \sim 10^9\,\mathrm{cm}^{-3}$, compared to ion densities of the order of $n_i \sim 10^3\,\mathrm{cm}^{-3}$ (see chapter 6). Thus it is assumed that for each position $\underline{x} = (x, y, z)$ the neutral density $n_n(\underline{x})$ and the neutral velocity $\underline{u}_n(\underline{x})$ are given and do not change during the simulation. The shape of the used three-dimensional neutral density and velocity profiles $n_n(\underline{x})$ and $\underline{u}_n(\underline{x})$ is described in chapters 5 and 6.

In the current simulation model, three physical processes how this neutral cloud interacts with the plasma are considered:

- Binary elastic collisions between an ion and a neutral. Since the ions are usually significantly faster than the neutrals, the ion transfers momentum to the neutral. After the collision, the ion moves with the former kinetic energy of the neutral, but the physical properties of the ion do not change.

- Bimolecular, resonant (i.e. elastic) ion-molecule reactions between an ion of species j_1 and a neutral molecule N_1, producing an ion of species j_2 and a neutral N_2 according to

$$j_1^+ + \mathrm{N}_1 \longrightarrow j_2^+ + \mathrm{N}_2 \quad . \tag{4.17}$$

  Most relevant for planetary ionospheres are charge exchange processes, i. e. a proton transfers from j_1^+ to N_1 or an electron from N_1 to j_1^+. In that case, it is $j_2^+ = (\mathrm{HN}_1)^+$ or $j_2^+ = {\mathrm{N}_1}^+$ and N_2 has to be such that the stoichiometry of the reaction is fulfilled. In *resonant* charge exchange processes, the reactants maintain their kinetic energy after the reaction. In this way, elastic collisions could technically be regarded as a special case of resonant reactions with $j_1^+ = j_2^+$ and $\mathrm{N}_1 = \mathrm{N}_2$, although the physical processes are different.

- Ionization of a neutral in the sense that an additional ion-electron pair is created, which is possible by photoionization due to a photon with energy $h\nu$,

$$h\nu + \mathrm{N}_1 \longrightarrow \mathrm{N}_2 + j_1^+ + e^- \quad , \tag{4.18}$$

  or electron impact ionization,

$$e^- + \mathrm{N}_1 \longrightarrow \mathrm{N}_2 + j_1^+ + 2e^- \quad . \tag{4.19}$$

Whether the interaction between an ion and a neutral results in an elastic collision or charge exchange depends on the involved ion and neutral species as well as on their relative kinetic energy. For common energies within ionospheres ($\sim$ eV), elastic collisions occur mostly between *unlike* ion and neutrals. The corresponding interaction can be approximated by Maxwell molecule collisions (see appendix A and *Schunk and Nagy*

[2009]). The reaction between an ion and its *parent* neutral can usually be described by resonant charge exchange. There are also reactions (which mostly involve a proton transfer) that are accidently resonant [*Schunk and Nagy* 2009]. Which collisions and reactions are considered has to be specified individually for a given scenario (see sections 5.4.1 and 6.1.2). In this chapter, only the general implementation of these processes is described.

Since the ions are represented by individual particles within the hybrid model, a natural way of describing the collisions and reactions is to include a collision/reaction probability for each particle. Therefore, an expression for this probability will be derived in section 4.3.1. Afterwards, it is shown how these statistical collisions are related to the known ionospheric currents of the fluid description (cf. section 3.2.3). The implementation of the photo- and electron impact ionization is described in section 4.3.3.

4.3.1 Reaction Probability and Implementation

The collisions between an ion and a neutral shall occur with an average collision time τ between two collisions or the corresponding length λ. It is clear that the occurrence of a collision in an interval Δw (in space or time) is independent of whether a collision took place in the previous interval or not. Furthermore, the probability that the ion undergoes a collision within the interval Δw is proportional to the length of Δw. This interval is also considered to be small, i.e. not more than one collision happens within Δw. These assumptions (memorylessness or independent increments, stationary increments and rareness) correspond to a Poisson process and therefore, the associated probability distribution is a Poisson distribution.

Thus, the probability that an ion survives a time t without a reaction is given by

$$P(t) = P(t=0)\exp\left(-\frac{t}{\tau}\right) \quad , \tag{4.20}$$

where τ is the average time between reactions, depending on the cross section $\sigma(v_{rel})$ for the respective reaction, the neutral density $n_n(\underline{x})$ at the particle's position $\underline{x}$ and its velocity v_{rel} relative to the neutral. Instead of the cross section, often the reaction rate coefficient $k_{j_1 j_2}(v_{rel}) = \sigma(v_{rel})\, v_{rel}$ is used.

The probability that an ion undergoes a reaction in the next time interval dt is then given by $p\,dt$ with

$$p = \frac{d}{dt}\left(1 - P(t)\right)\Big|_{t=0} = \frac{1}{\tau} = \sigma(v_{rel}) n_n(\underline{x}) v_{rel} = k_{j_1 j_2}(v_{rel})\, n_n(\underline{x}) \quad , \tag{4.21}$$

where $P(t=0) = 1$, since the particle 'lives' at the beginning of the time interval.

These statistical reactions are implemented in A.I.K.E.F. by calculating the reaction probability $p\,\Delta t$ for each particle within the next numerical time step Δt and comparing it against a random number $r \in [0;1]$. If $p\,\Delta t > r$, the ion of species j_1 undergoes a reaction and is deleted, while a new one of species j_2 is created. The initial velocity of the new particle is set to the velocity $\underline{u}_n$ of the neutrals.

If more than one reaction is possible for a particle of species j_1 (e. g. H_2O^+ may react to H_3O^+ or resonant charge exchange occurs and the product is again H_2O^+), the reac-

tion probability p is the probability that *any* reaction occurs for this particle. Therefore, $k_{j_1}(v_{rel})$ is calculated as the sum of all possible reactions of species j_1, i.e.

$$k_{j_1}(v_{rel}) = \sum_j k_{j_1 j}(v_{rel}) \quad . \tag{4.22}$$

Which of the reactions $j_1 \rightarrow j_2$ takes place is then determined statistically according to the ratio $k_{j_1 j_2}(v_{rel})/k_{j_1}(v_{rel})$.

In previous hybrid simulation studies with A.I.K.E.F. and its predecessor, the equation of motion of a particle 'p' of species j was given by [*Bagdonat* 2004]

$$\frac{d\underline{v}_{p,j}}{dt} = \frac{q_j}{m_j}\left(\underline{E} + \underline{v}_{p,j} \times \underline{B}\right) - k_j n_n (\underline{v}_{p,j} - \underline{u}_n) \quad , \tag{4.23}$$

where the last term on the right-hand side has also been referred to as a 'drag force'. In this way, the kinetic motion of individual particles is combined with the fluid description of collisions (cf. equation (3.45)). Obviously, this semi-kinetic approach only applies for collisions and does not include reactions.

4.3.2 Comparison of Statistical Collisions and Fluid Drag Force

In the following, it will be demonstrated how statistical collisions and drag force are related with each other. Therefore, the motion of a test particle subject to collisions is analyzed.

It is assumed that the particle moves in constant electric and magnetic fields with $\underline{B}_0 = -B_0 \underline{e}_z$ and $\underline{E}_0 = -E_0 \underline{e}_y$. Without collisions, a test particle with initial velocity zero then performs a cycloidal motion which can be expressed as

$$\begin{aligned} x(t) &= r_g(\Omega t - \sin \Omega t) \\ y(t) &= r_g(\cos \Omega t - 1) \\ z(t) &= \text{const} \quad , \end{aligned} \tag{4.24}$$

where r_g and Ω are the gyroradius and the gyrofrequency, respectively.

After a time $t = t_c$, the cycloidal motion may be interrupted by a collision . In agreement with $v_{ion} \gg u_{neutral}$, the particle's velocity is set to zero at the time of the collision. Afterwards, the particle is accelerated by the electric field and begins to perform a new cycloid as sketched in figure 4.1.

The average velocity of the particle in an interval t_c between two collisions is given by

$$< v_x >_{t_c} = \frac{x(t_c) - x(0)}{t_c} = \frac{r_g(\Omega t_c - \sin \Omega t_c)}{t_c} \tag{4.25}$$

$$< v_y >_{t_c} = \frac{y(t_c) - y(0)}{t_c} = \frac{r_g(\cos \Omega t_c - 1)}{t_c} \quad . \tag{4.26}$$

The guiding center moves along the direction $\underline{v}_G = (v_0 \cos\phi, -v_0 \sin\phi, 0)$, with ϕ given by

$$\tan\phi = \frac{< v_y >_{t_c}}{< v_x >_{t_c}} = \frac{\cos \Omega t_c - 1}{\Omega t_c - \sin \Omega t_c} \quad . \tag{4.27}$$

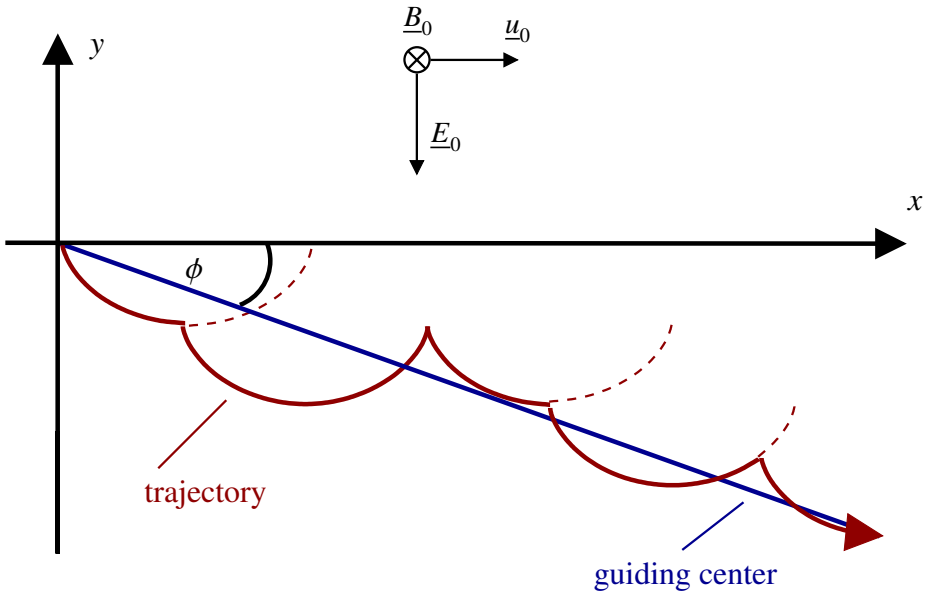

Figure 4.1: Sketch of the cycloidal motion of a positively charged particle, interrupted by collisions. The particle's guiding center moves on average along a line which forms an angle ϕ with the undisturbed motion.

Note that $\tan\phi$ oscillates around the fluid expression from equation (3.52) if $t_c = \tilde{\nu}_i^{-1}$. However, the collisions occur statistically around an average collision time τ according to the probability given by equation (4.21). Thus, the average velocity for one particle within a large or even infinite time with many collisions is computed by integrating over the velocities for all possible collision times $t_c \in [0, \infty]$, weighted with the respective probability density $\left(-\frac{dP}{dt}\right)$ that describes a collision within dt. However, one has to be careful that the average velocity is *not* the average over all $< \underline{v} >_{t_c}$ weighted with the probability, since the velocities $< \underline{v} >_{t_c}$ that belong to shorter t_c, contribute less to the average, because they cover a shorter way. For instance, the average velocity for covering a distance Δx within a time interval Δt is not given by the sum of the average velocities in the sub-intervals "1" and "2" with $\Delta x = \Delta x_1 + \Delta x_2$ and $\Delta t = \Delta t_1 + \Delta t_2$,

$$< v >= \frac{\Delta x}{\Delta t} = \frac{\Delta x_1 + \Delta x_2}{\Delta t_1 + \Delta t_2} \neq \frac{\Delta x_1}{\Delta t_1} + \frac{\Delta x_2}{\Delta t_2} \quad . \tag{4.28}$$

Instead, the average velocities have to be weighted with the relative length of the interval,

$$< v >= \frac{\Delta x_1}{\Delta t_1}\frac{\Delta t_1}{\Delta t_1 + \Delta t_2} + \frac{\Delta x_2}{\Delta t_2}\frac{\Delta t_2}{\Delta t_1 + \Delta t_2} \quad . \tag{4.29}$$

Thus, $< \underline{v} >_{t_c}$ also has to be weighted with t_c/τ:

$$<< \underline{v} >_{t_c} >= \int_0^\infty dt_c \frac{\underline{x}(t_c)}{t_c}\frac{t_c}{\tau}\left(-\frac{\mathrm{d}P}{\mathrm{d}t}\right) \quad . \tag{4.30}$$

Inserting equations (4.24) and (4.20) into (4.30) finally yields

$$<< v_x >_{t_c}> = \int_0^\infty dt_c r_g(\Omega t_c - \sin\Omega t_c)\frac{1}{\tau^2}\exp\left(-\frac{t_c}{\tau}\right)$$
$$= u_0 \frac{\Omega^2}{1/\tau^2 + \Omega^2} \tag{4.31}$$

and

$$<< v_y >_{t_c}> = \int_0^\infty dt_c r_g(\cos\Omega t_c - 1)\frac{1}{\tau^2}\exp\left(-\frac{t_c}{\tau}\right)$$
$$= -u_0 \frac{\Omega/\tau}{1/\tau^2 + \Omega^2} \quad . \tag{4.32}$$

These velocities are exactly the same as the drift velocities obtained from the fluid approach trough Pedersen and Hall currents in section 3.2.4 (equations (3.50) and (3.51)), if τ is replaced by the inverse collision frequency, $\tau = \tilde{\nu}_i^{-1}$. Therefore, the statistical description of the collisions is a microscopic model of Pedersen and Hall conductivities and the drag force.

4.3.3 Photoionization and Electron Impact Ionization

The model includes photoionization and electron impact ionization as described by equations (4.18) and (4.19), respectively. For both processes, new ions are inserted into the simulation during each time step according to

$$\partial_t n_i(\underline{x}) = \nu_{io}(\underline{x}) n_n(\underline{x}) \quad , \tag{4.33}$$

where $\nu_{io}(\underline{x})$ denotes the ionization frequency with contributions from photoionization (ν_{ph}), electron impact ionization (ν_e) and a possible additional effective ionization frequency ν^* (see section 6.1.3),

$$\nu_{io}(\underline{x}) = \nu_{ph} + \nu_e + \nu^* \quad . \tag{4.34}$$

The values used for the ionization frequencies are discussed in sections 5.4.1 and 6.1.3. The initial velocity of the newly generated ions is given by the neutral velocity $\underline{u}_n(\underline{x})$ and superimposed random velocities components according to thermal fluctuations.

Two different implementations of these ion production processes are included in A.I.K.E.F.:

1. The "rejection-method": a certain number N of macroparticles is inserted into the simulation (typically $N \sim 10^3$) during each Δt. For each particle, coordinates $\underline{x}$ within the simulation box are generated as random numbers. The coordinates of a particle are rejected and new coordinates generated as long as

$$\frac{J(\underline{x})}{J_{max}} \frac{\nu_{io}(\underline{x}) n_n(\underline{x})}{\nu_{io,max} n_{n,max}} < r \tag{4.35}$$

with $r \in [0;1]$ being another random number. In this way, the coordinates that are most likely generated correspond to the location of the highest ion production. The subscript 'max' denotes the maximum ion production. J is the determinant of the Jacobian matrix, which has to be considered if not Cartesian coordinates, but e.g. spherical coordinates (r, ϑ, φ) are generated, since a uniform distribution of the angles ϑ and φ does not yield a uniform distribution of the resulting positions. Each particle is assigned the same "weight" w, i.e. each particle contributes equally to the density. This contribution is determined according to the number of new particles (N) and according to the ion production rate integrated over the whole simulation box,

$$w = \frac{\int \nu_{io}(\underline{x}) n_n(\underline{x}) \mathrm{d}V}{N} \Delta t \quad . \tag{4.36}$$

This equation represents the integrated version of equation (4.33) for N particles with equal weight w. Therefore, the rejection method is most suitable in cases where $\nu_{io}(\underline{x})$ and $n_n(\underline{x})$ are defined by analytical expressions and the integral can be evaluated. The advantage of this method is that it generates a high number of macroparticles in the few cells with high ion production rate – which are typically the regions of particular interest – and less particles elsewhere.

2. The second possibility is to inject exact one macroparticle in each cell, but drop the claim that all particles are generate with an equal weight. Instead, each particle's contribution to the density shall be defined by $\nu_{io}(\underline{x}) \cdot n_n(\underline{x})$. The coordinates of the particle within the cell are chosen randomly. This method has the advantage that only the local values $\nu_{io}(\underline{x})$ and $n_n(\underline{x})$ are required instead of an integrated quantity. However, in regions of high neutral density the ions are represented by a significantly lower number of macroparticles compared to the rejection method. In contrast, particles are also inserted in regions with low neutral density what may not be the case for the rejection method. Furthermore, the number of cells is usually much larger than 10^3 and the resulting high total number of macroparticles would drastically slow down the simulation. Therefore, the method is adjusted such that the probability to insert a macroparticle is set to k^{-1}, with $k > 1$. If the particle is inserted, its contribution to the density is consequently increased by the factor k. By adjusting the value of k a similar number of new macroparticles is produced as by the rejection method.

Within this thesis, both methods have been used for the ionization processes in Enceladus' plume: the rejection method has been applied for the simulations presented in chapter 5, where an analytical model of the plume has been used while the second implementation was more suitable for the simulated neutral plumes in chapter 6. With regard to possible future improvements – like an electron impact ionization rate which changes during the simulation runtime according to the local electron density – the second implementation should be preferred.

4.4 Numerical Damping (Smoothing)

As mentioned in section 4.2, it is necessary to apply a smoothing procedure in order to improve the numerical stability. On the one hand, the smoothing avoids too strong local gradients in the electromagnetic fields. On the other hand, structures with characteristic length scales comparable to or smaller than the grid size cannot be described correctly within the model and therefore, these structures have to be damped.

The smoothing of a scalar quantity $A_{[i,j,k]}$ at a grid node $[i, j, k]$ ($i, j, k \in \mathbb{Z}$) can be carried out in two ways (see also *Bagdonat* [2004]):

1. A 'simple' smoothing procedure where an average of the fields at the neighbor grid points ($\overline{A_{[i,j,k]}}$) is added to $A_{[i,j,k]}$ at each grid node according to

$$A^{\text{new}}_{[i,j,k]} = (1 - \eta_{sm}) A_{[i,j,k]} + \eta_{sm}\, \overline{A_{[i,j,k]}} \tag{4.37}$$

   with

$$\overline{A_{[i,j,k]}} = \sum_{a,b,c=-1}^{1} A_{[i+a,j+b,k+c]}\, W_{[a,b,c]} \tag{4.38}$$

   and the weighting factors

$$W_{[a,b,c]} = \frac{1}{8}\, 2^{-(a^2+b^2+c^2)} \quad . \tag{4.39}$$

   These factors take into account, how far a node $[i + a, j + b, k + c]$ with $a, b, c \in \{-1, 0, 1\}$ is away from the node $[i, j, k]$ (see fig. 3.10 of *Simon* [2007]). The strength of the smoothing is determined by the parameter η_{sm}.

2. The second possibility is the use of a small, global value of η in the diffusion term of equation (A), in addition to the resistivity of the obstacle. Physically, a value of η different from zero would be the result of wave-particle scattering or electron-ion collisions. For numerical stability, η has to be chosen somewhat larger than the real value.

Before the impact of the smoothing on the results presented in this thesis is analyzed, it may be instructive to compare the two smoothing procedures. As has been pointed out by *Müller et al.* [2011], the simple smoothing procedure is similar to a Laplace operator in finite differences and therefore acts in a similar manner as diffusion. Since A.I.K.E.F. is currently used by a large number of people, it may be of some interest to learn about the smoothing strength of the two methods relative to each other, i.e. to find a relation between the smoothing parameters η_{sm} and η.

On the one hand, rewriting equation (4.37) yields

$$A^{\text{new}}_{[i,j,k]} = A_{[i,j,k]} - \eta_{sm} \cdot f(A_{[i,j,k]}) \quad , \tag{4.40}$$

where the abbreviation $f(A_{[i,j,k]}) = A_{[i,j,k]} - \overline{A_{[i,j,k]}}$ has been introduced. On the other hand, the diffusion term in the magnetic field equation reads

$$\partial_t \underline{B} = -\partial_{\underline{x}} \times \left(\frac{\eta}{\mu_0} \partial_{\underline{x}} \times \underline{B} \right) \quad . \tag{4.41}$$

Rewritten for discrete time steps one obtains

$$\frac{\underline{B}^{t+\Delta t} - \underline{B}^{t}}{\Delta t} = -\partial_{\underline{x}} \times \left(\frac{\eta}{\mu_0} \partial_{\underline{x}} \times \underline{B}^{t} \right) \tag{4.42}$$

and

$$\underline{B}^{t+\Delta t} = \underline{B}^{t} - \frac{\eta \Delta t}{\mu_0} \left(\partial_{\underline{x}} \times (\partial_{\underline{x}} \times \underline{B}^{t}) \right) \quad . \tag{4.43}$$

In the last step, η is assumed to be constant, i. e. $\eta \neq \eta(\underline{x})$. With $\partial_{\underline{x}} \cdot \underline{B} = 0$, it is $\partial_{\underline{x}} \times (\partial_{\underline{x}} \times \underline{B}) = -\partial_{\underline{x}}^2 \underline{B}$. The spatial derivatives in finite differences for the components of $\underline{B}$ at grid node $[i, j, k]$ for an equidistant Cartesian grid yield for, e.g. the B_x component,

$$\begin{aligned} B^{t+\Delta t}_{x,[i,j,k]} = B^{t}_{x,[i,j,k]} + \frac{\eta \Delta t}{\mu_0} \Bigg(& \frac{B^{t}_{x,[i+1,j,k]} - 2B^{t}_{x,[i,j,k]} + B^{t}_{x,[i-1,j,k]}}{\Delta x^2} \\ & \frac{B^{t}_{x,[i,j+1,k]} - 2B^{t}_{x,[i,j,k]} + B^{t}_{x,[i,j-1,k]}}{\Delta x^2} \\ & \frac{B^{t}_{x,[i,j,k+1]} - 2B^{t}_{x,[i,j,k]} + B^{t}_{x,[i,j,k-1]}}{\Delta x^2} \Bigg) \quad . \end{aligned} \tag{4.44}$$

For formal analogy to equation (4.40), this expression is rewritten as

$$\begin{aligned} B^{t+\Delta t}_{x,[i,j,k]} &= B^{t}_{x,[i,j,k]} - \frac{\eta \Delta t}{\mu_0 \Delta x^2} \left(B^{t}_{x,[i,j,k]} - \sum_{a,b,c=-1}^{1} B_{[i+a,j+b,k+c]} \, \tilde{W}_{[a,b,c]} \right) \\ &= B^{t}_{x,[i,j,k]} - \frac{\eta \Delta t}{\mu_0 \Delta x^2} \left(B^{t}_{x,[i,j,k]} - \overline{B^{t}_{x,[i,j,k]}} \right) \\ &= B^{t}_{x,[i,j,k]} - \frac{\eta \Delta t}{\mu_0 \Delta x^2} \, g(B^{t}_{x,[i,j,k]}) \quad , \end{aligned} \tag{4.45}$$

where the new weighting factors

$$\tilde{W}_{[a,b,c]} = \delta_{a0}\delta_{b0} + \delta_{b0}\delta_{c0} + \delta_{a0}\delta_{c0} - 8\,\delta_{a0}\delta_{b0}\delta_{c0} \tag{4.46}$$

have been introduced. δ_{ab} denotes the Kronecker-delta. The average $\overline{B^{t}_{x,[i,j,k]}}$ and the abbreviation $g(B^{t}_{x,[i,j,k]}) = B^{t}_{x,[i,j,k]} - \overline{B^{t}_{x,[i,j,k]}}$ are introduced in analogy to equation (4.40).
By comparing equations (4.40) and (4.45), one may identify

$$\eta_{sm} \hat{=} \frac{\eta \Delta t}{\mu_0 \Delta x^2} = \frac{\eta^* \Delta t^*}{(\Delta x^*)^2} \tag{4.47}$$

where the quantities $(...)^*$ correspond to normalized units with $\eta^* = \eta e n_0 / B_0$. Therefore, the smoothing parameter η_{sm} depends on grid resolution and time step if a similar amount of numerical diffusion should be achieved. Note that in the diffusion term, only the six nearest neighbors of a node are considered, while the 'simple' smoothing includes 26 neighbors. One should also keep in mind that A.I.K.E.F. advances the diffusion term in time using an implicit Crank-Nicolson algorithm, whereas the explicit Euler method has been used in the derivation of equation (4.45) for simplicity (see section 4.2).

Table 4.1: Global normalized variance σ_l^{fluc} of the magnetic field components B_l to compare the two smoothing procedures. The smoothing parameter η_{sm} corresponds to the smoothing where a weighted average of the neighbors is used according to equation (4.40) while η^* is the resistivity applied for the diffusion term.

η_{sm}	η^*	σ_x^{fluc}	σ_y^{fluc}	σ_z^{fluc}
0.1	-	$1.5 \cdot 10^{-7}$	$1.5 \cdot 10^{-7}$	$3.1 \cdot 10^{-7}$
-	1	$1.5 \cdot 10^{-7}$	$1.6 \cdot 10^{-7}$	$3.9 \cdot 10^{-7}$
0.05	-	$3.7 \cdot 10^{-7}$	$3.6 \cdot 10^{-7}$	$6.9 \cdot 10^{-7}$
-	0.5	$2.7 \cdot 10^{-7}$	$2.6 \cdot 10^{-7}$	$5.2 \cdot 10^{-7}$
0.02	-	$8.7 \cdot 10^{-7}$	$8.6 \cdot 10^{-7}$	$1.7 \cdot 10^{-6}$
-	0.2	$6.8 \cdot 10^{-7}$	$6.8 \cdot 10^{-7}$	$1.3 \cdot 10^{-6}$
0.01	-	$1.5 \cdot 10^{-6}$	$1.5 \cdot 10^{-6}$	$3.0 \cdot 10^{-6}$
-	0.1	$1.2 \cdot 10^{-6}$	$1.2 \cdot 10^{-6}$	$2.4 \cdot 10^{-6}$

To check the accuracy of the correspondence (4.47), a series of test simulations with different values of η_{sm} and η was carried out. Since the smoothing is a general aspect of the simulation code and is not particularly related to Enceladus' or Rhea's plasma interaction, normalized units are used in the following. The test simulations only include plasma flowing at a velocity of $u_0^* = 1$ through a uniform box with periodic boundaries without any obstacle. The temperature corresponds to $\beta_i = \beta_e = 0.1$. Furthermore, the solar wind is initialized with a uniform magnetic field $\underline{B}_0^* = (0, 0, -1)$. The cell size is $\Delta x^* = 0.1$ and the time step is set to $\Delta t^* = 0.001$. Due to the numerical fluctuations, the magnetic field evolves slightly during the simulation. After 100 time steps, the global normalized variance σ_l^{fluc} of the magnetic field component B_l was calculated as

$$\sigma_l^{fluc} = \frac{\sum\limits_{i,j,k} \left(B_{l,[i,j,k]} - B_{0,l} \right)^2}{\sum\limits_{i,j,k} [i, j, k]} \quad . \tag{4.48}$$

In this expression, the sums run over all mesh nodes and the denominator corresponds to a normalization by the number of nodes by summing up all triples $[i, j, k]$. Since the variance decreases with increasing smoothing, σ_l^{fluc} can be regarded as a measure for the strength of the smoothing. The results are listed in table 4.1. They confirm that both smoothing strategies lead to a roughly similar level of fluctuations σ_l^{fluc} when η_{sm} and η are related by the correspondence (4.47). The minor differences of σ_l^{fluc} result from the different number and weight of the neighbor nodes included in the averaging. Due to the background magnetic field pointing in $(-z)$ direction, σ_z^{fluc} is about twice as large as $\sigma_{x/y}^{fluc}$. Surprisingly, the fluctuations scale approximately linearly with the smoothing strength.

Since the simulations presented in chapters 5 and 6 intend to characterize Enceladus' plume based on the strength of the magnetic field perturbations, it is necessary to quantify the influence of the smoothing on the simulated magnetic field. Thus, the most simple test scenario for the generation of an Alfvén wing is used. In this scenario, cold plasma streams through a cylindrical obstacle that is aligned with the z axis. Within the obstacle, the plasma undergoes elastic collisions with a constant collision frequency of $\nu_{in} = \Omega_i$. At each collision, the particle's velocity is set to zero. Hence, this test scenario is identical

to the approach of constant conductances within a cylindrical obstacle, which has been used for the derivation of the analytical solution of the Alfvén wing (cf. section 3.2.5). This test scenario therefore allows a quantitative comparison between simulations and analytical solution and will also be applied in sections 4.5.2 and 5.3.

In agreement with our default Enceladus parameters listed in table 2.4, the density of the plasma is $n_0 = 70.5\,\mathrm{cm}^{-3}$, the background magnetic field is given by $\underline{B}_0 = (0, 0, -325\,\mathrm{nT})$, the velocity is $u_0 = 26.4\,\mathrm{km/s}$ and the ion mass is 17.6 amu. The size of the simulation box is $L_x \times L_y \times L_z = 30R_E \times 25R_E \times 100R_E$, since it is adjusted to the nearly field-aligned Alfvén wing. A uniform grid with a cell size of $\Delta x = 0.26R_E$ is applied. To avoid any boundary effects (see section 4.5.2), the simulation is not run until stationarity, but stopped before the Alfvén wing can reach the top and bottom boundaries of the box, i.e. the simulation time is $\tau = \tau_A = 40R_E/v_A \approx 90\,\mathrm{s}$. The radius and the height of the cylinder are set to $2R_E$, yielding height-integrated conductivities of

$$\Sigma_P = \Sigma_H = \int_0^{2R_E} \mathrm{d}z \frac{ne}{B_0} \frac{1}{2} = 8.8\,\mathrm{S} \quad .$$

From equations (3.87) and (3.88) the B_x and B_y perturbations inside the flux tube of the northern Alfvén wing can then be calculated to

$$B_x = -0.6 M_A B_0 \quad , \quad B_y = 0.2 M_A B_0 \quad .$$

These theoretical perturbations for an ideal Alfvén wing will now be compared with simulation results for different values of the smoothing resistivity ($\eta^* \in \{0.01, 0.02, 0.05, 0.1\}$). For convenience, the resistivity is provided in normalized units, the corresponding SI units can be obtained from $\eta = \eta^* B_0/(en_0)$. Figure 4.2(a) shows the B_x perturbation in the northern Alfvén wing for a smoothing of $\eta^* = 0.05$. To enable a more quantitative analysis, the B_x perturbations for the different strengths of the smoothing are compared in figure 4.2(b) along the northern Alfvén characteristic (black line in panel (a)). In all four simulations, the perturbation is strongest at $z = 5R_E$ which results from contributions of the Pedersen and Hall currents. The weaker perturbations at $z > 30R_E$ result from Alfvén waves that are generated at the begin of the simulation when the plasma flow within the obstacle has not yet been slowed down to the stationary values. Therefore, the region at $z > 30R_E$ could be regarded as the front of the Alfvén wing, which is, however, not part of the stationary solution. Only in between, i.e. from about $z = 10R_E$ to $z = 25R_E$, the results should be compared with the Alfvén wing far field solution. For the two lowest smoothing values of $\eta^* = 0.01$ (red line) and $\eta^* = 0.02$ (blue line), the simulated field perturbations are very close to the analytical value. For a resistivity of $\eta^* = 0.05$, the magnitude of B_x is reduced by about 10% and B_x is not constant along the characteristic, but exhibits a stronger gradient towards larger z. The strongest smoothing even leads to a decrease of the B_x perturbation to $B_x = -0.45 M_A B_0$ at $z = 25R_E$, i.e. a reduction by about 25% compared to the analytical value.

These results suggest to choose the resistivity smaller or equal than $\eta^* = 0.02$ to avoid any noticeable influence of the smoothing on the results. However, the Enceladus simulations including the solid body and the plume have proven to require a smoothing of at least $\eta^* = 0.05$ for numerical stability. Thus, when interpreting the simulation results, it has to

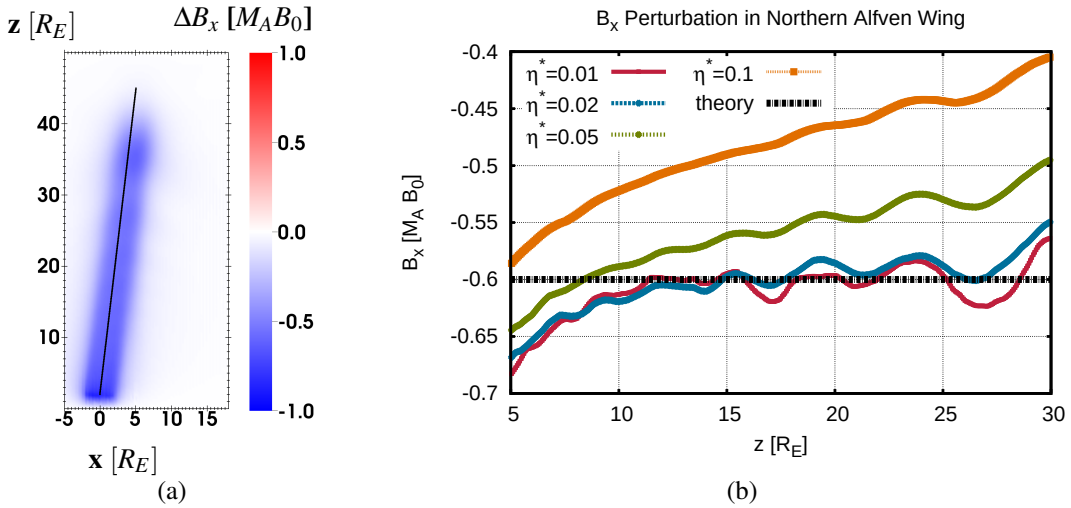

Figure 4.2: B_x perturbation of the northern Alfvén wing in the ($y = 0$)-plane (panel (a)) and along the Alfvén characteristic for different strengths of the smoothing (panel (b)).

be taken into account that the magnetic field perturbations are reduced by up to 10% due to the smoothing.

A value of $\eta^* = 0.05$ is also consistent with *Winske et al.* [2003], who suggested as a 'rule-of-thumb' to limit the magnetic diffusion length to about $p = 10 - 20\%$ of the smallest cell size for numerical stability. This results in

$$\eta^* \geq p\, u^*\, \Delta x^* \quad , \tag{4.49}$$

where u^* is a characteristic velocity, i.e. the Alfvén speed, $u^*1 = 1$. The smallest cell size is $\Delta x = 0.26 R_E \approx 0.5 l_0$, i. e. $\Delta x^* = 0.5$, which yields (with $p = 0.1$)

$$\eta^* \geq 0.05 \quad . \tag{4.50}$$

Therefore, $\eta^* = 0.05$ is used for all simulations shown in this work. The corresponding value of η_{sm} is $\eta_{sm} = 3\%$ for a time step of $\Delta t = 0.015 \Omega_i^{-1}$. In SI units, this resistivity corresponds to

$$\eta = 1.4 \cdot 10^3 \Omega\mathrm{m} \quad , \tag{4.51}$$

or the equivalent plasma conductivity

$$\sigma = \frac{1}{\eta} \approx 7 \cdot 10^{-4}\, \mathrm{S/m} \quad . \tag{4.52}$$

This value is three orders of magnitude smaller than the resistivity applied for the solid bodies of Enceladus and Rhea. However, this value is also orders of magnitude higher than the anomalous resistivity that would arise from wave-particle scattering or electron-ion collisions. Therefore, the resistivity outside the obstacle should not be associated with these effects, but only with smoothing that is required for numerical stability.

4.5 Boundary Conditions

The boundary conditions applied within a simulation may have an even stronger influence on the results than the smoothing. In general, there are two types of boundaries that have to be handled by the code: the inner boundary at the surface of the solid obstacle and the outer boundaries which confine the simulation box.

4.5.1 Inner boundary

The inner boundary has already been described in detail by *Kriegel et al.* [2009]. On the one hand, every particle, which impinges on the surface of the moon's solid body, is removed from the simulation. On the other hand, no boundary condition is applied to the electromagnetic fields. $\underline{E}$ and $\underline{B}$ are calculated self-consistently from the hybrid equations within the entire computational domain including the interior of the satellite. The distinction between the exterior and the interior is exclusively controlled by $\underline{u}_i$, ρ_i and η. The velocity $\underline{u}_i$ and the reciprocal density $1/\rho_i$ are set to zero within the obstacle. For numerical reasons, however, a discontinuity in the density cannot be handled by the code. Thus, only for the calculation of the fields, we set the density in the interior to the very low value of $1 \cdot 10^{-6} \cdot n_0 *$. In order to avoid a strong resistivity gradient at the surface, we apply a resistivity profile with a continuous transition from $\eta = 0$ (or $\eta =$ const in case it is also used as smoothing) in the plasma to a finite resistivity η_0 in the moon's interior.

This continuous resistivity profile is either realized by smearing out the constant resistivity of the interior by means of repeated smoothing of the resistivity at the begin of the simulation (equation (4.40)) or by setting $\eta(\underline{x})$ according to a spherically symmetric Fermi profile,

$$\eta(r) = \eta_0 \frac{1}{\exp\left[(r - R_\eta)\, a_\eta\right] + 1} \quad . \tag{4.53}$$

On the one hand, the parameters R_η and a_η have to be adjusted such that the artificial resistivity outside the obstacle is as small as possible. On the other hand, too sharp gradients destabilize the field solvers and may require very small time steps. Therefore, these parameters have to be chosen carefully for a good trade-off between simulation time and artificial plasma resistivity.

The modeling of the moons' interior as described above assumes that these objects could be described by a homogeneous resistivity. As has already been discussed in section 3.1, the icy moons' nearly insulating crusts are the reason why they can be described – under stationary conditions – as homogeneous low-conducting obstacles. The value of η_0 or the corresponding conductivity could be specified from two points of view. First, measurements of the electrical properties of the surfaces in principle constrain the conductivity of the crusts. However, the available measurements yield a wide range of possible conductivities, e.g. pure water ice has a conductivity of the order of $\sigma_{ice} \sim 10^{-9}\,\mathrm{S/m}$ but even minor impurities may increase the conductivity by orders of magnitude. Second, the magnetic field should diffuse freely through the satellites and therefore, the conductivity of the obstacles has to be chosen such that the magnetic diffusion time inside the obstacles

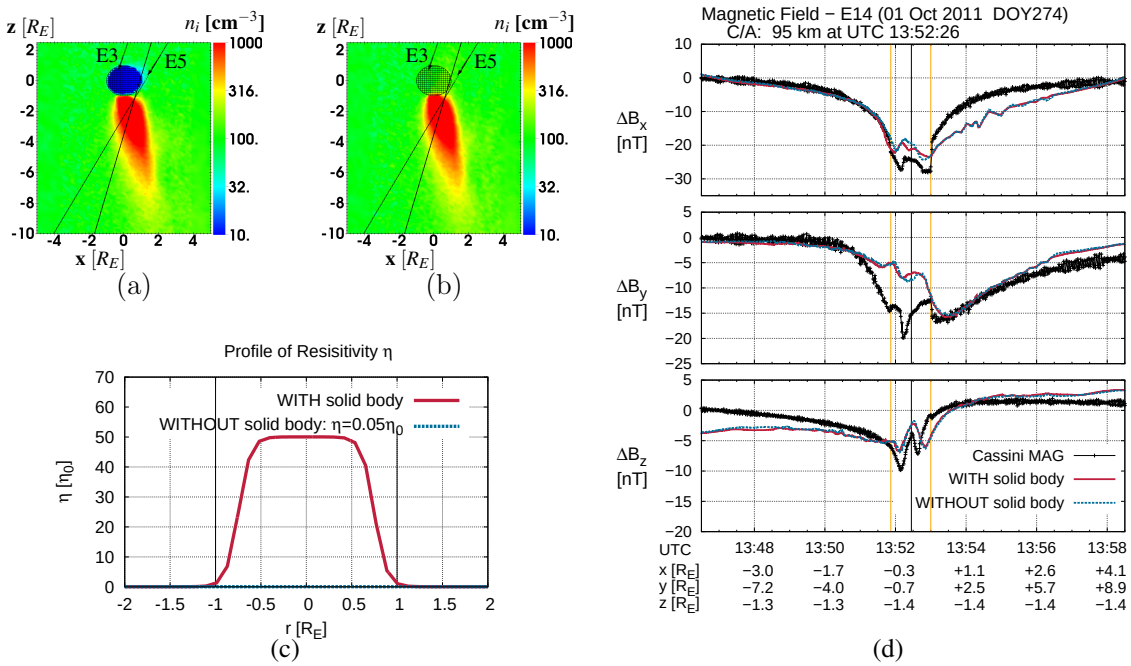

Figure 4.3: Test of the inner boundary for the Enceladus simulations. Two simulations are shown: (1) including Enceladus as solid obstacle, the resulting ion density is displayed in panel (a), (2) without solid obstacle, the corresponding density is shown in panel (b). Plot (c) displays the resistivity profiles. Plot (d) shows simulated magnetic field components for the E14 flyby.

is significantly smaller than the plasma convection time around it,

$$\tau_{diff} \approx \mu_0 \sigma \left(2R_j\right)^2 \ll \tau_{conv} \approx \frac{2R_j}{u_0} \quad , \tag{4.54}$$

where R_j denotes the radius of the respective satellite ($j = E, RH$). For both satellites, this condition is fulfilled for a conductivity of the order of $\sigma \sim 10^{-7}$ S/m, what is also close to estimates for the Terrestrial moon. In consequence, a conductivity of $\sigma = 7 \cdot 10^{-7}$ S/m is used for all Enceladus simulations presented in this thesis, whereas a value of $\sigma = 9 \cdot 10^{-7}$ S/m is applied for Rhea.

It should be pointed out that for any simulation scenario, it has to be carefully checked whether and how much the resistivity profile affects the results. To compare the plasma structures generated by the resistive obstacle with the effect of an ionosphere, either of them could be disabled for test simulation purposes. For Enceladus, such a comparison is shown in figure 4.3. Two simulations are compared with each other: (1) an Enceladus simulation with parameters as described in chapter 6. The resulting ion density is zero inside the moon and increased in the plume (panel 4.3(a), see also figure 6.7(c)). The resistivity profile is described by the solid red line in plot 4.3(c). (2) the same simulation except that no solid obstacle is included. Therefore, no effect of the moon on the ion density is visible (cf. panel 4.3(b)). Moreover, the resistivity is now constant, $\eta = 0.05\eta_0$. As an example, panel 4.3(d) displays the resulting magnetic field perturbations along the E14 trajectory for both simulations. The physics of these magnetic field signatures will be discussed in section 6.5.3; here it is only important to notice that the simulated magnetic

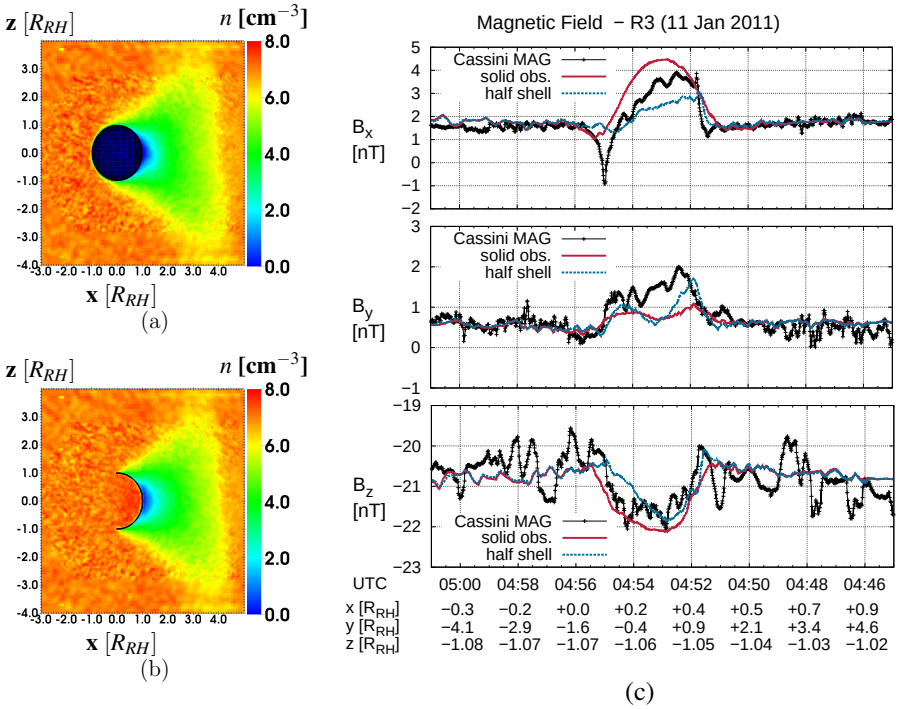

Figure 4.4: Test of the inner boundary for the Rhea simulations. Two simulations are shown: (1) including Rhea as solid obstacle, the resulting ion density is displayed in panel (a). For simulation (2), the solid obstacle is replaced by a "particle-absorbing half-sphere". The corresponding density is shown in panel (b). Plot (c) displays simulated magnetic field components for the R3 flyby.

field structures of both simulations are nearly identical. Thus, the inner boundary and also the solid body of Enceladus have no influence on the magnetic field structures for this close flyby.

For Rhea it is, however, more complex to isolate the influence of the inner boundary since not an ionosphere or plume, but the wake determines the plasma structures. Therefore, a suitable test scenario should encompass the wake, but not the solid obstacle. Although it seems to be a contradiction, this case can be realized numerically. Despite neither the solid obstacle nor its resistivity is included, a wake similar to that of a solid obstacle can be generated by deleting each particle which crosses the surface of the open half-sphere $x^2 + y^2 + z^2 = R_{RH}^2$ with $x > 0$ from inside to outside. In analogy to figure 4.3, figure 4.4 shows the results of two simulations: (1) a Rhea simulation with upstream conditions corresponding to the R3 flyby. The details of the simulation setup are described in chapter 7. (2) the same simulation, but the solid body of Rhea is replaced by the particle-absorbing half-sphere. Panels 4.4(a) and(b) display the resulting plasma densities in the (x, z)-plane, while the associated magnetic field structures along the R3 flyby are shown in panel 4.4(c). The wake generated by the half-sphere has indeed a shape very similar to that caused by the absorbing moon. Minor differences arise from the different onset of the absorption near the north and south pole. This is because for the solid obstacle, some particles with a large field-aligned velocity component may be absorbed at $x < 0$, but would never cross the half-sphere. The different density profile near the pole is also

responsible for the deviations between the simulated magnetic field perturbations along the R3 flyby, that is very close to the south pole. However, it should be pointed out that the overall magnetic field structures are very similar for both simulations and are therefore not caused by artificial effects of the inner boundary, but are solely generated in Rhea's wake.

4.5.2 Outer boundaries

The outer boundaries of the simulation box can be either described as *inflow* or *outflow* boundaries. A.I.K.E.F. is capable of setting the boundary type for particles, velocity field, electric field and magnetic field independently. In the case of particles, inflow means that the outermost cells are filled with new particles during each time step, whereas for outflow conditions, no particles are filled in these cells during simulation runtime and particles which enter these cells are removed from the simulation. When using inflow conditions for the fields, the outermost mesh nodes are kept at the background values. In contrast to that, the fields' values from their inner neighbors are copied to the outer nodes for outflow conditions. These conditions can be applied separately for every face $(\pm x, \pm y, \pm z)$ of the simulation box.

Due to the high thermal velocity of the ions within Saturn's magnetosphere, a significant fraction of the particles possesses a noticeable velocity component perpendicular to the magnetic field. A small fraction of particles even has a velocity component opposite to the bulk speed of the plasma. If outflow conditions were applied at the box faces perpendicular or opposite to the plasma flow, these particles would be missing. The loss of plasma pressure would even yield a pressure gradient that drags the particles out of the box (see *Simon* [2007] for a detailed discussion of the particle boundary conditions). Therefore, inflow conditions for the particles are used at all faces of the box. For the fields, it turned out that the magnetic field slightly starts to 'diffuse out of the box' after several thousand time steps if outflow conditions are used. Thus, for the fields every face of the box is set to inflow as well. However, for the short simulation time of the simulations that are presented in chapter 5, outflow conditions do also work.

Furthermore, the boundaries have to be modified to avoid reflections of the Alfvén wing at the $\pm z$ boundaries of the simulation box. These reflections occur for both, inflow and outflow conditions, and are also present in the simulations of *Omidi et al.* [2010]. To date, we are not aware of any boundary condition that could prevent the reflection of the wing. The solution implemented in A.I.K.E.F. is therefore to avoid that the Alfvén wing reaches the boundary. This is achieved by setting a slowly increasing resistivity towards the $\pm z$ boundaries. As described in section 4.4, this resistivity damps the currents and field perturbations of the wing. However, it is important that the gradient in η does not become too large, otherwise the Alfvén wing will be reflected at this gradient.

As empirical value, a resistivity of $\eta^* = 5$ with a linear gradient over $\Delta z = 15 R_E$ towards the upper and lower boundary of the box has proven appropriate. This resistivity is two orders of magnitude larger than the smoothing value, but still one order of magnitude below the resistivity of the obstacle. Moreover, it turned out that damping at the $+x$ boundary further decreased the occurrence of boundary artifacts. Therefore, the linear gradient was slightly modified to an "inverse hyper-ellipsoid". The resulting resistivity

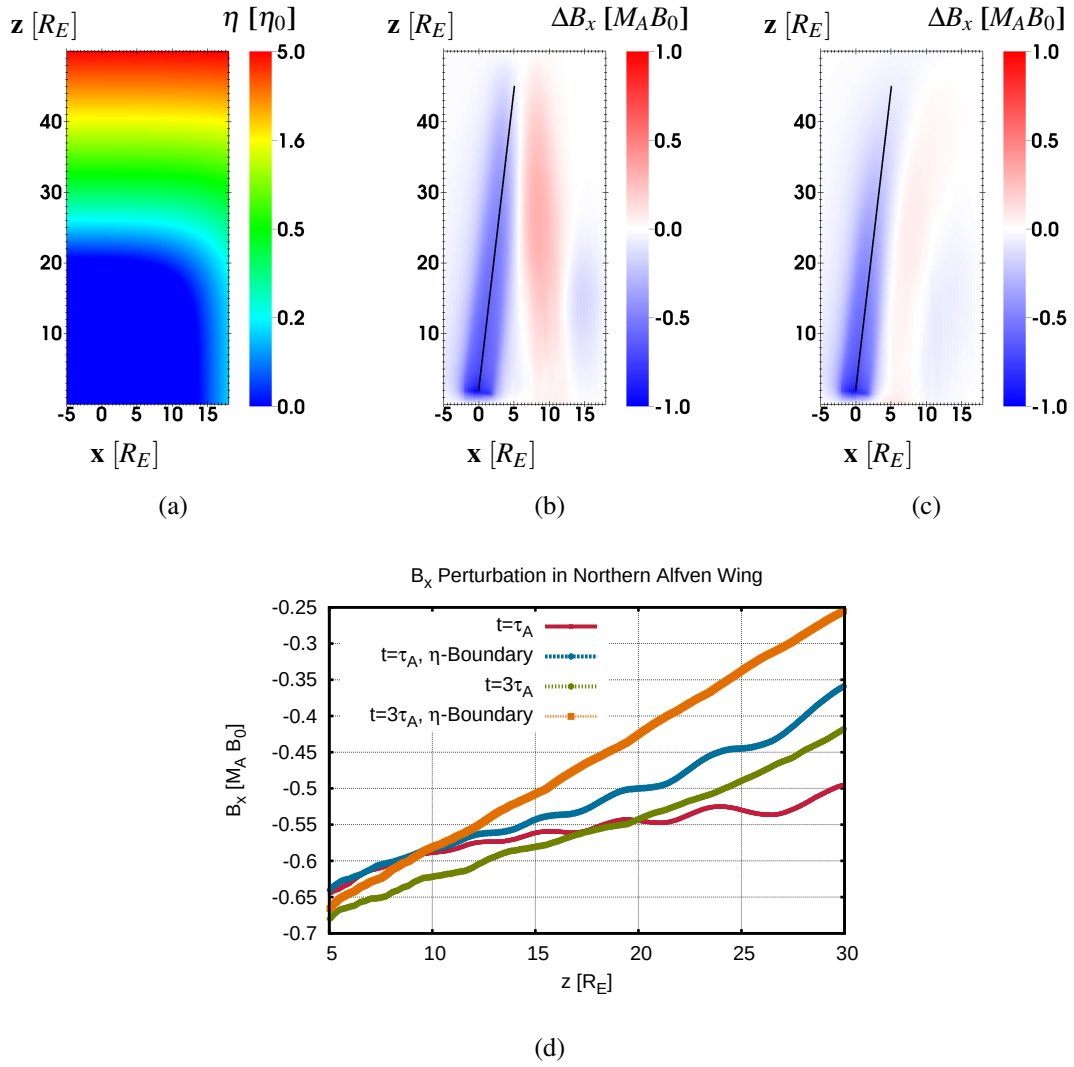

Figure 4.5: Modified boundary with increased resistivity near the $\pm z$ boundaries (panel (a)) to avoid reflections of the Alfvén wing. Plot (b) shows the B_x perturbation of a simulation without the modified boundary where the Alfvén wing is reflected, while panel (c) displays a run where the Alfvén wing is damped by the increased η. Panel (d) shows a comparison of the two simulations along the Alfvén characteristic (black lines in (b) and (c)) before ($t = \tau_A$) and after ($t = 3\tau_A$) the Alfvén wing is reflected.

distribution is shown in figure 4.5(a).

To investigate how strong this modified boundary impacts the plasma structures, again the field perturbations within the Alfvén wing are considered. The same basic scenario to generate an Alfvén wing is applied as in the analysis of the smoothing in section 4.4, but now including the resistive boundary. This simulation, however, is not stopped before the Alfvén wing reaches the boundary, but run three times longer ($\tau = 3\tau_A \approx 270\,\mathrm{s}$). The resulting B_x perturbation in the northern Alfvén wing is shown in figure 4.5(b) for a simulation without the modified boundary and in panel 4.5(c) for a simulation including this resistive boundary. The reflected Alfvén wing is clearly visible in figure 4.5(b) as

the region of positive B_x at about $x = 10R_E$. In contrast, no reflected wing can be seen in plot 4.5(c). For a quantitative analysis, the B_x perturbations are also shown along the Alfvén characteristic in figure 4.5(d). The two simulations are shown before the Alfvén wing reaches the boundary, i.e. after $t = \tau_A$, and also after the reflection has occurred at the time $t = 3\tau_A$. Northward of $z = 12R_E$, the increased resistivity leads to the desired damping of the B_x perturbation. For the simulation without increased resistivity, the superposition of the original and the reflected wing also leads to a reduced B_x perturbation at $z > 20R_E$. Interestingly, both simulation produce at $t = 3\tau_A$ a slightly larger perturbation. Most important is, however, the fact that the simulation including the resistive boundary generates a similar perturbation close to the obstacle and does prevent the reflection of the wing. Thus, this resistive boundary is an appropriate choice for modeling stationary Alfvén wing structures within a finite-sized simulation box.

4.6 Further Simulation Codes for Enceladus and Rhea

Finally, A.I.K.E.F. shall be compared with other existing simulation codes that have been applied to the plasma interactions of Enceladus and Rhea.

In the case of Rhea, only the "Braunschweig-Code" has been used for simulations of Rhea's plasma environment [*Roussos et al.* 2008a]. It turned out that the A.I.K.E.F.'s inner boundary condition – which was already implemented in that version of the Braunschweig-Code – is particularly suitable to model the inert moons. In contrast, Enceladus has been modeled by a number of authors apart from our preceding study [*Kriegel et al.* 2009].

Saur et al. [2008] used an updated version of the two-fluid plasma model of *Saur and Strobel* [2005] for Enceladus' plasma interaction. The model calculates the modifications of electron and ion density, velocity, and temperature by aeronomic reactions with a given neutral gas distribution (such as electron impact ionization and charge exchange). The model also computes the 3D electric current system driven by the interaction, from which the associated magnetic field perturbations are calculated by means of Biot-Savart-Integrals [*Saur et al.* 2002]. Due to the analytical description of the inner boundary, the model naturally includes the hemisphere coupling currents. Overall, the model of *Saur et al.* [2008] is similar to first-order perturbation theory and – although producing excellent results – does not self-consistently include the modifications of the plasma flow patterns by the perturbed magnetic field.

A series of hybrid simulation studies of Enceladus' plasma interaction was carried out by *Omidi et al.* [2010, 2012]. In contrast to A.I.K.E.F., the hybrid code of these authors is not capable of using an adaptive or hierarchical mesh. Instead, the calculations are run on a uniform Cartesian grid with massive computational resources to achieve a resolution of up to 17 km, similar to our model. Furthermore, the initial magnetic field is kept constant within the obstacle. In contrast to the assumption of adiabatic electrons in A.I.K.E.F., the electron pressure is determined assuming isothermal electrons. In addition, *Omidi et al.* [2010] did not implement a damping of the Alfvén wings near the boundaries. Therefore, their simulations are run only until the Alfvén wing reaches the $\pm z$ boundaries of the simulation box. Similar to our studies, *Omidi et al.* [2012] included dust as a heavy, negatively charged ion species. While the work presented in this thesis mainly focuses

on the magnetic field structures, *Omidi et al.* [2010, 2012] analyzed wave generation and energy spectra. Furthermore, these authors did not include a detailed model of the ion-neutral chemistry which will prove necessary for a quantitative comparison with Cassini magnetometer data.

The hybrid code developed by the group of *P. Trávníček* from the Space Plasma Group at the Astronomical Institute of the Academy of Sciences of the Czech Republic has also been applied to Enceladus by *Stverak et al.* [2009]. These authors, however, did never present their results in a peer-reviewed journal .

The MHD simulation code BATS-R-US (Block Adaptive Tree Solar-wind Roe Upwind Scheme) developed at the University of Michigan has been applied to Enceladus' plasma interaction by *Jia et al.* [2010b,c,d]. This MHD code uses similar parameters as applied for the simulations with A.I.K.E.F., e. g. the simulation domain is $80R_E \times 80R_E \times 80R_E$ which is similar to our model in the z direction, but larger in x and y direction because BATS-R-US is only capable of square meshes. By using a multiscale grid system, *Jia et al.* achieved a resolution of 10 km, which is slightly better than our resolution. In their model, the surface of Enceladus is the inner boundary of the calculation domain. The plasma is absorbed at Enceladus' surface, while the gradient of the magnetic field is set to zero across the boundary. From these parameters, BATS-R-US seems to be equally suitable to study Enceladus' plasma interaction as A.I.K.E.F. However, the major result of this thesis is the vital importance of charged dust for the plasma structures. Consequently, *Jia et al.* [2012] applied the multi-fluid version of BATS-R-US to study the effect of charged dust. Although it is in principle possible to include the charged dust even within the MHD framework (see the recent study by *Blöcker* [2013]), *Jia et al.* have not yet succeeded to qualitatively explain Cassini MAG observations at Enceladus that are associated with charged dust.

A multi-fluid simulation model has also been applied to Enceladus by *Paty et al.* [2011]. Similar to *Jia et al.*, these authors have not yet successfully included the charged dust and no peer-reviewed publication was available at the time of this writing.

In summary, A.I.K.E.F. is due to both, numerical implementation and capabilities inherent to any hybrid model, the only simulation code that has already been successfully applied to the plasma interactions of Enceladus and Rhea and which is also suitable to address the open questions arising from measurements in the vicinity of the two moons.

5 Influence of Negatively Charged Plume Grains on the Structure of Enceladus' Alfvén Wings

The following chapter has been published in wide parts before submission of the thesis. The copyright holder of the pre-publications is the American Geophysical Union, and the cited parts are reprinted with permission. The publications can be found under the following references:
Simon, S., J. Saur, **H. Kriegel**, F. M. Neubauer, U. Motschmann, and M. K. Dougherty (2011a), Influence of negatively charged plume grains and hemisphere coupling currents on the structure of Enceladus' Alfvén wings: Analytical modeling of Cassini magnetometer observations, *Journal of Geophysical Research (Space Physics)*, *116*, A04221, doi: 10.1029/2010JA016338
Kriegel, H., S. Simon, U. Motschmann, J. Saur, F. M. Neubauer, A. M. Persoon, M. K. Dougherty, and D. A. Gurnett (2011), Influence of negatively charged plume grains on the structure of Enceladus' Alfvén wings: Hybrid simulations versus Cassini Magnetometer data, *Journal of Geophysical Research (Space Physics)*, *116*, A10223,
doi: 10.1029/2011JA016842

5.1 Magnetic Field Observations at Enceladus

At the end of chapter 3, it has been discussed that our previous hybrid simulations as well as MHD simulations by *Jia et al.* [2010c] failed to explain some key features of Enceladus' plasma interaction like the orientation of the measured B_y perturbation (at least within a local interaction model) and the location of draping center. To investigate these puzzling issues, we will at first discuss the magnetic field signatures obtained during Cassini's E5 – E9 and E11 flybys at Enceladus, which are displayed in figure 5.1. For better visualization only the magnetic field *perturbations* ($\Delta B_x, \Delta B_y, \Delta B_z$) caused by Enceladus are shown. To subtract the background field from the data, we have fitted a dipole field to the intervals between 10 and 20 minutes before and after closest approach.

For all flybys except for E8 and E11, Cassini observed a negative B_x perturbation, indicating that the spacecraft passed through the center of the northern Alfvén wing although Cassini was located below the south pole. This means that Cassini crossed the interaction region *between* the south pole of Enceladus and the draping center. Surprisingly,

the B_y perturbations from all these flybys exhibited a negative sign. During E8 and E11, the spacecraft flew through the southern Alfvén wing and the measured magnetic field perturbations were positive for both, B_x and B_y.

For the component in the direction of the background field (B_z), only a negative perturbation was measured during all flybys so far. Since the background field is directed towards negative z, Cassini passed only through regions of enhanced $|\underline{B}|$. In other words, the spacecraft intersected the magnetic pile-up region, but did not penetrate the corresponding magnetic field decrease in the downstream region. The step-like shape of the B_z perturbations of E7 (panel 5.1(c)) results from artifacts caused by the reduced resolution of the MAG instrument[1].

The analytical solution for the magnetic field perturbations of the Alfvén wing derived in section 3.2.5 showed that the bending of the field lines yields a negative B_x component in the northern and a positive B_x within the southern wing flux tube. In addition, the Hall current within the plume gives rise to a component along the Saturn-Enceladus-line (B_y). In the far field (i.e. where the magnetic field arising from Pedersen and Hall currents can be neglected), the wing current system and the associated magnetic field perturbations exhibit translation symmetry along the wing characteristics. This also implies that the orientation of the B_y component, even at large distances to Enceladus, is determined by the value of the Hall conductance of the local interaction region. In equations (3.87) – (3.88), the magnetic field perturbations inside the Alfvénic flux tube were given as a function of the constant height-integrated Pedersen and Hall conductivities Σ_P and Σ_H inside a cylindrical plume. According to equation (3.88), the sign of B_y in the northern or southern wing is determined by the sign of the Hall conductance, or more precisely,

$$\Sigma_H > 0 \quad \rightarrow \quad \begin{cases} B_y > 0 \quad \text{and} \quad B_x < 0 \quad \text{(northern Alfvén wing)} \\ B_y < 0 \quad \text{and} \quad B_x > 0 \quad \text{(southern Alfvén wing)} \end{cases} . \tag{5.1}$$

Obviously, the measured *positive* correlation between the signs of the B_x and B_y perturbations seems to contradict the previous understanding of the Alfvén wing.

Since E5 – E7 and E9 passed through the *center* of the plume, the Alfvén wing *far field* solution is, however, not strictly applicable for these flybys. In contrast, closest approach of E8 and E11 took place far away from the center of the plume, i.e. at distances of $6.3R_E$ and $10.1R_E$, respectively. Therefore, the magnetic perturbations measured during these flybys should correspond to the Alfvén wing far field solution. In turn, it is a reasonable assumption (which was unambiguously confirmed by our simulations), that the signs of the B_x and B_y perturbations observed during E5 – E7 and E9 in the near-field of the northern Alfvén wing are identical to the signs of ΔB_x and ΔB_y in the northern Alfvén wing far field.

There are in principle only three possibilities which could explain the observed magnetic field signatures. First, Cassini did not pass through the Alfvénic flux tube, but instead

[1] As we mentioned in *Simon et al.* [2011b], the instrument has been in low-resolution mode (with a range of $\pm 10,000$ nT sampled with 14 bits yielding a digital resolution of 1.22 nT) for periapsis and waited too long before the autoranging unit switched it to high-resolution mode (with a range of ± 400 nT and a corresponding digital resolution of 49 pT). The observed magnetic field varies in coarse steps in sensor coordinates. Because of the performed coordinate transformations, the x, y, and z signals mix and produce the artifacts visible in this plot. However, these signatures do not modify the overall features of the observed field signature, and for our purposes, they are only of minor quantitative relevance.

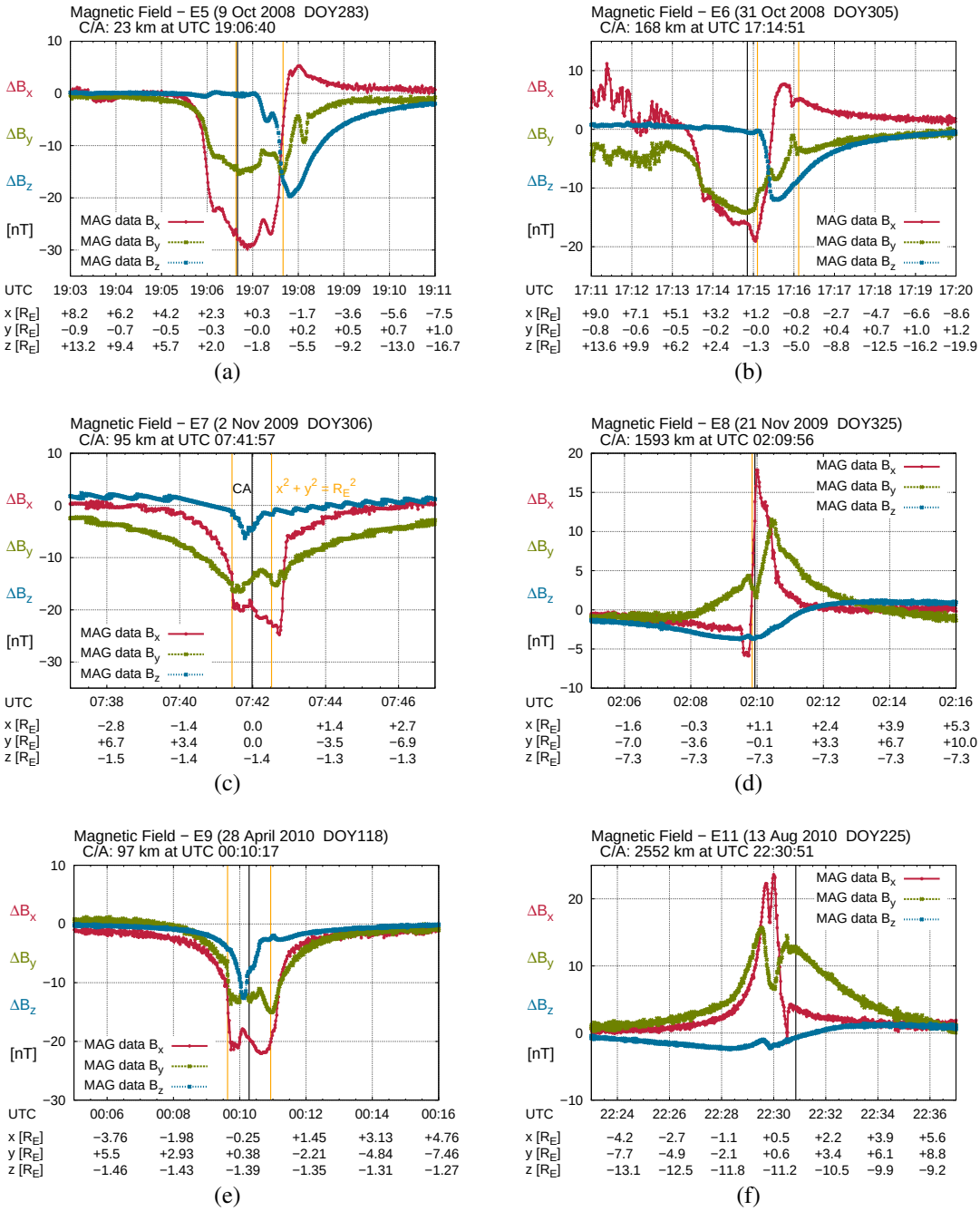

Figure 5.1: Cassini magnetometer observations from Enceladus flybys (a) E5, (b) E6, (c) E7, (d) E8, (e) E9 and (f) E11. In all plots, the B_x component is denoted in red, B_y and B_z are shown in green and blue, respectively. The vertical black lines mark the time of closest approach to Enceladus, whereas the orange lines denote the intersection points between Cassini's trajectory and the surface of the non-tilted flux tube that is defined by $\sqrt{x^2 + y^2} = R_E$.

remained in the outer regions of the Alfvén wing. As displayed in figure 3.5, in certain regions it would then be possible to observe a positive correlation between B_x and B_y. For the analytical solution with constant conductances inside a cylinder with radius R and using two-dimensional polar coordinates $(x, y) = (r\cos\varphi, r\sin\varphi)$, these regions are given by $r > R$ and the four sectors $0° < \varphi < 45°$, $90° < \varphi < 135°$, $180° < \varphi < 225°$ and $270° < \varphi < 315°$. However, this explanation is highly unlikely since the trajectories of E5 – E7 and E9 intersected the z axis within $2R_E$ to the south pole and therefore probably crossed through the center of the plume. Moreover, all test simulations including a tilted plume – to shift one of these sectors in Cassini's path – failed to explain the observations. Thus, MAG data seem indeed to show the field perturbations inside the Alfvénic flux tube.

Second, the ENIS might be inappropriate to describe Enceladus' Alfvén wing. For the analytical solution, it was assumed that x is aligned with the direction of the magnetospheric plasma flow, while y is perpendicular to the flow. If the plasma flow was directed inward by an angle ϕ as suggested by *Jia et al.* [2010c], the analytical solution is valid only for the new coordinates $x_{new} = x\cos\phi + y\sin\phi$ and $y_{new} = -x\sin\phi + y\cos\phi$. Hence $B_x < 0$ and $B_y < 0$ can be transformed into $B_{x,new} < 0$ and $B_{y,new} > 0$. Therefore, *Jia et al.* [2010c] suggested that Enceladus' magnetosphere interaction cannot be solely described in terms of a local model, i.e. not only processes in the moon's immediate vicinity, but also the large-scale dynamics within Saturn's magnetosphere have to be taken into account. These authors proposed that an imbalance of the radial forces in the magnetosphere leads to inward motion of the plasma at Enceladus' orbit. By including an upstream flow velocity that is tilted against the direction of ideal corotation by about $\phi = 30°$ towards Saturn, *Jia et al.* [2010c] indeed succeeded in reproducing Cassini MAG observations from the E5 flyby. However, apart from the missing quantitative physical justification, this approach failed in reproducing the B_y perturbations observed during the earlier E2 encounter.

Third, the Hall conductance Σ_H may assume negative values, yielding

$$\Sigma_H < 0 \quad \rightarrow \quad \begin{cases} B_y < 0 \quad \text{and} \quad B_x < 0 \quad \text{(northern Alfvén wing)} \\ B_y > 0 \quad \text{and} \quad B_x > 0 \quad \text{(southern Alfvén wing)} \end{cases} . \tag{5.2}$$

At first glance, a negative Hall conductance seems to be "unphysical". However, it was discussed at the end of chapter 3 that within the plume, a large amount of dust is charged by the electrons, and consequently the number of "free" electrons is reduced. Therefore, the dust should be regarded as an additional plasma component (see also section 5.4.3). In this chapter, we will thus demonstrate how negatively charged dust leads to a negative sign of the Hall conductance, thereby explaining Cassini Magnetometer observations.

5.2 Anti-Hall Effect: Analytical Derivation

In section 3.2.3, the Hall conductivity was derived as (equation (3.57))

$$\sigma_H = -\sum_\alpha \frac{n_\alpha q_\alpha}{B_0} \frac{\Omega_\alpha^2}{\tilde{\nu}_\alpha^2 + \Omega_\alpha^2} \quad . \tag{5.3}$$

Let us now consider a plasma consisting of electrons, ions and negatively charged dust. As will be discussed in section 5.4.3, the sizes of the dust grains range from nm to μm

and the grains may be charged with $1 - 1000$ electrons, resulting in a charge-to-mass ratio of the dust which is at least three orders of magnitude smaller than that of the ions. Therefore, the gyrofrequency of the dust is negligible and the dust does not contribute to the sum in equation (5.3). Since the dust leads to a measurable imbalance between electrons and ions, it has nevertheless to be included in the quasi-neutrality condition, yielding

$$en_e = \sum_j q_j n_j - e\xi n_D \quad , \tag{5.4}$$

where the term $-e\xi n_D$ denotes the charge density of the dust grains. If the dust grains with density n_D possessed the same size, each of the grains would be charged with ξ electrons. Furthermore, the electron collision frequency ν_e is clearly exceeded by the electron gyrofrequency Ω_e, $\nu_e \ll \Omega_e$ [*Saur et al.* 2007]. By incorporating this approximation and the quasi-neutrality condition in equation (5.3), the Hall conductivity can be written as

$$\sigma_H = + \sum_j \frac{n_j q_j}{B_0} \frac{\tilde{\nu}_j^2}{\tilde{\nu}_j^2 + \Omega_j^2} - \frac{e\xi n_D}{B_0} \tag{5.5}$$

$$= \frac{1}{B_0} \sum_j q_j n_j \frac{\tilde{\nu}_j^2}{\tilde{\nu}_j^2 + \Omega_j^2} - e\xi n_D \quad , \quad . \tag{5.6}$$

It is obvious from equation (5.6) that σ_H becomes negative, if

$$e\xi n_D > \sum_j q_j n_j \frac{\tilde{\nu}_j^2}{\tilde{\nu}_j^2 + \Omega_j^2} \quad . \tag{5.7}$$

For one single-charged ion species, this condition simplifies to

$$\xi n_D > n_i \frac{\tilde{\nu}_i^2}{\tilde{\nu}_i^2 + \Omega_i^2} \quad . \tag{5.8}$$

The same approach does not lead to a reversal of the Pedersen conductivity:

$$\sigma_P = \sum_\alpha \frac{n_\alpha q_\alpha}{B_0} \frac{\Omega_\alpha \tilde{\nu}_\alpha}{\tilde{\nu}_\alpha^2 + \Omega_\alpha^2} \tag{5.9}$$

$$= \frac{1}{B_0} \left(\sum_j q_j n_j \frac{\tilde{\nu}_j \Omega_j}{\tilde{\nu}_j^2 + \Omega_j^2} \right) \quad . \tag{5.10}$$

In contrast to the Hall conductivity, the Pedersen conductivity is thus not modified by the negatively charged dust – at least not when the dust grains are assumed to be at rest.

The Pedersen and Hall currents are illustrated in figure 5.2. Due to $\tilde{\nu}_e \ll \Omega_e$, the electrons are not noticeably affected by the neutral gas and perform an undisturbed cycloidal motion with bulk velocity $\underline{u}_e = u_0 \underline{e}_x$.[2] In contrast, the effective collision frequency of the

[2]Note added in proof: More precisely, the electrons can complete many undisturbed cycloids before undergoing a collision. If electron and ion collision frequencies are of similar order of magnitude, both plasma components nevertheless possess a similar mean free path. After the collision, the electrons are accelerated on the small scale of the electron gyroradius. Therefore, these collisions do not result in a noticeable motion in y direction and the electron motion can be approximated by the bulk velocity $\underline{u}_e = u_0 \underline{e}_x$.

ions ($\tilde{\nu}_i$) is on the same order as the gyrofrequency Ω_i. Furthermore, the neutral velocity is considerably smaller than the ion velocity and is therefore neglected. Thus, the ions start a new cycloid with initial velocity zero after each collision (see also figure 4.1). The resulting drift motion has been derived in section 3.2.3 (equations (3.50) and (3.51)). Since the electron motion does not lead to an electron bulk velocity along the y direction, the Pedersen current is generated only by the ion bulk velocity $u_{i,y}$ due to the collisions. The x component of the current (Hall current) is caused by the difference of the reduced ion current density ($en_i u_{i,x}$) and (nearly) unperturbed electron current density ($en_e u_0$), yielding a Hall current directed in negative x direction. If the Hall current was not included, the perpendicular current would be directed towards negative y. Therefore, the Hall current leads to a clockwise rotation of the perpendicular current (in the (x, y) plane), what is referred to as the Hall effect (see e.g. *Saur et al.* [1999]). The electron current density is reduced if a certain fraction of the electrons is absorbed by immobile dust grains, for instance a dust charge density of $\xi n_D = 0.1 n_i$ was assumed in figure 5.2(b). If the inequality (5.6) is fulfilled, the ion current density becomes larger than the electron current density. In consequence, the Hall current becomes positive and the resulting perpendicular current is rotated counterclockwise. In *Simon et al.* [2011b], we entitled this effect as *Anti-Hall effect* and in the following, we may refer to inequality (5.6) as the "Anti-Hall condition'.

Although the gyrofrequency of the dust was considered negligible, the finite velocity of the dust grains shall be considered as an additional contribution to the currents,

$$\underline{j} = \sigma_P \underline{E} + \sigma_H \frac{\underline{B}_0 \times \underline{E}}{B_0} - e\xi n_D \underline{u}_D \quad , \tag{5.11}$$

where $\underline{u}_D$ denotes the bulk velocity of the dust grains. The Hall current (j_x) is then given by

$$j_x = e u_0 \left\{ -\frac{n_i \nu_i^2}{\nu_i^2 + \Omega_i^2} + \xi n_D \left(1 - \frac{u_{D,x}}{u_0} \right) \right\} \quad . \tag{5.12}$$

It is evident that the Anti-Hall effect is reduced by the factor $\left(1 - \frac{u_{D,x}}{u_0}\right)$, if $u_{D,x} > 0$. This is consistent with the picture derived above, since the dust current density ($-e\xi n_D u_{D,x}$) leads to a smaller Hall current for $u_{D,x} > 0$. The Anti-Hall condition with finite grain velocity then reads

$$e\xi n_D \left(1 - \frac{u_{D,x}}{u_0} \right) > \sum_j q_j n_j \frac{\tilde{\nu}_j^2}{\tilde{\nu}_j^2 + \Omega_j^2} \quad . \tag{5.13}$$

The grain velocity also modifies the Pedersen current according to

$$j_y = -u_0 e \left(n_i \frac{n_i \Omega_i}{\nu_i^2 + \Omega_i^2} + \xi n_D \frac{u_{D,y}}{u_0} \right) \quad , \tag{5.14}$$

which is therefore enhanced by a grain velocity in positive y direction.

To show that the Anti-Hall effect is indeed able to generate the observed magnetic field structures, an improved version of the analytical model for Enceladus' Alfvén wing described in section 3.2.5 has been applied in *Simon et al.* [2011b]. By approximating the

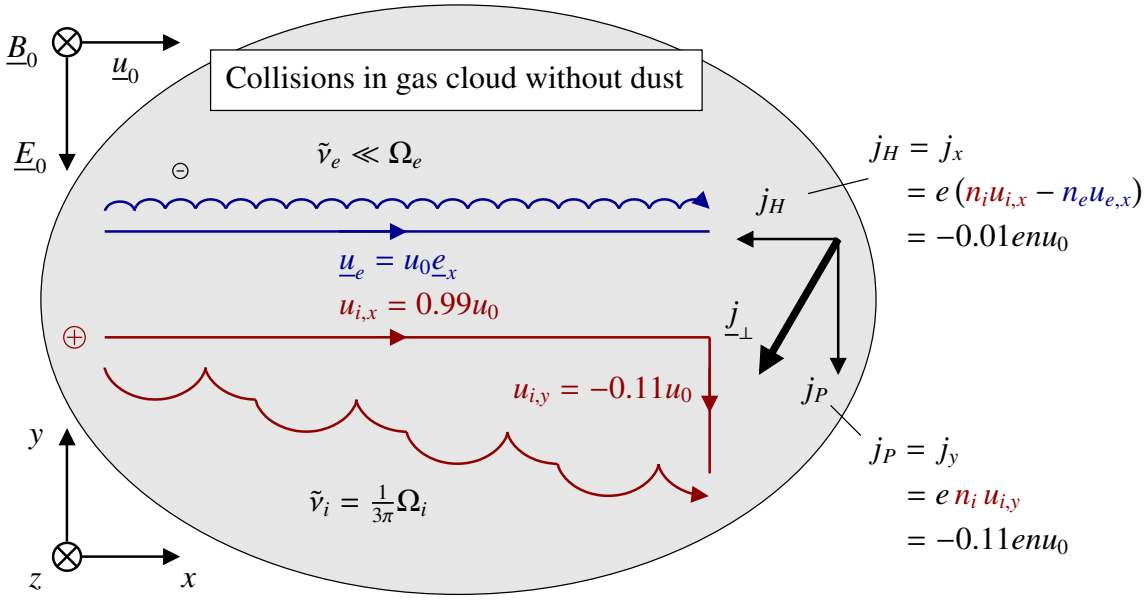

(a)

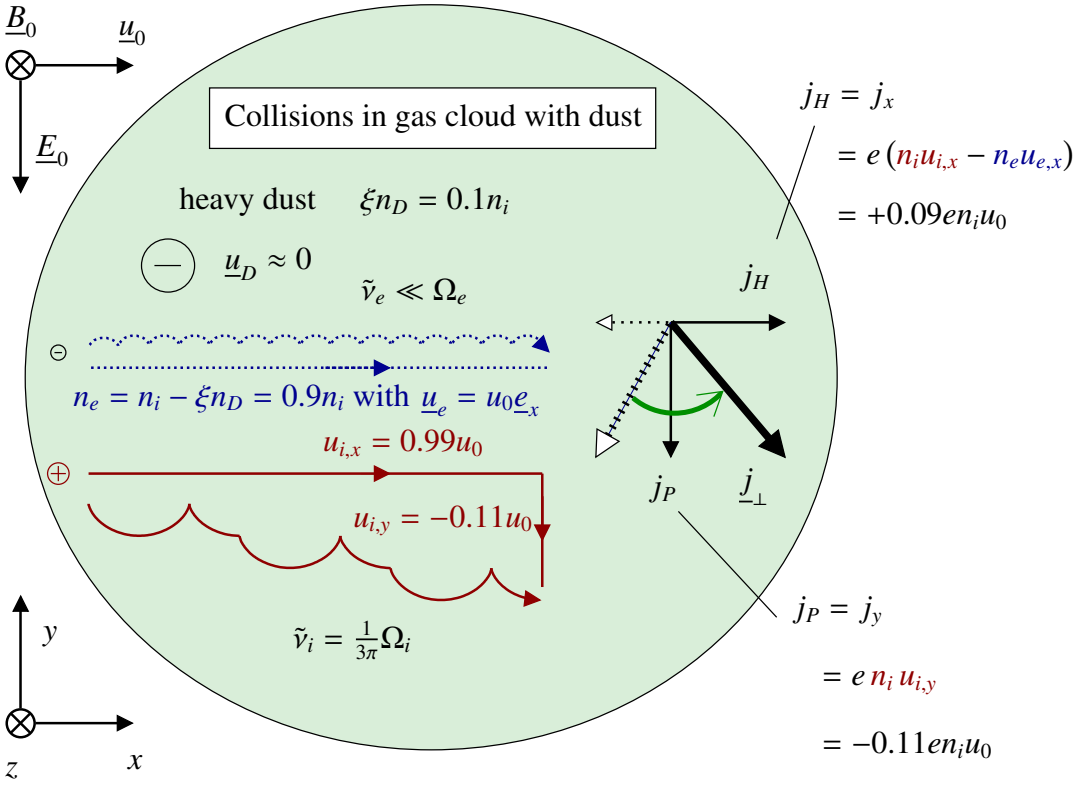

(b)

Figure 5.2: Illustration of the Hall effect and the Anti-Hall effect. The figure shows a cut through a homogeneous gas cloud in a plane perpendicular to the magnetic field. Within the cloud, the ions undergo collisions. At the time of the collision, their velocity is set to zero. The resulting drift motion of ions and electrons is sketched for a collision frequency of $\tilde{\nu}_i = \frac{\Omega_i}{3\pi}$, corresponding to collisions after 1.5 cycloids. The ion drift velocity is calculated from equations (3.50) and (3.51). Panel (a) displays the resulting currents for a gas cloud without dust, whereas panel (b) illustrates the situation when 10% of the electrons are absorbed by heavy dust grains which are assumed to be at rest. In consequence, the Hall current j_H reverses its direction and the perpendicular current $\underline{j}_\perp$ is rotated counterclockwise.

plume by several coaxial cylinders with constant conductances Σ_P and Σ_H, MAG data obtained during the flybys E3 – E9 (partly presented in section 5.1) were qualitatively reproduced. However, the model confines the field-aligned currents to the surfaces of the plume cylinders (see also 3.2.5), causing artificial spikes and discontinuities in the magnetic field which have obviously not been measured by Cassini MAG. Since in reality, the neutral density and thus, the collision frequency decrease with distance to Enceladus' south pole, the model presented in *Simon et al.* [2011b] also does not include a realistic description of the magnetic pile-up in front of the plume, as visible in the B_z component. Moreover, the analytical model can handle only a plume geometry that exhibits cylindrical symmetry around the z axis. Hence, comparing the magnetic field signatures obtained from that model to observations does not allow to constrain the shape, density and especially a possible tilt of the plume, as indicated by e.g., *Kriegel et al.* [2009]. Therefore, a numerical model needs to be applied to Enceladus' plasma interaction. In the next section, we will demonstrate that the negatively charged dust can be described within our hybrid model. It will be shown that we are able to reproduce the correlation between the signs of B_x and B_y, as observed in the Alfvén wings of Enceladus. We also analyze the asymmetric ion flow deflection caused by the presence of negatively charged dust which has not been done with the analytical model presented in *Simon et al.* [2011b].

5.3 Anti-Hall Effect: Simulations

In order to show the principle effect of the electron-absorbing dust, we apply the same simplified interaction scenario for the generation of an Alfvén wing as in section 4.4: a plasma of water group ions undergoes collisions with a constant collision frequency $\tilde{\nu}_i = 0.5\Omega_i$ within a cylindrical volume, where Ω_i is the ion gyrofrequency. The upstream conditions are identical to the 'real' Enceladus scenario (see table 5.1). The cylinder with height 4 R_E and radius 3 R_E is centered at the origin of the ENIS system, while the solid body of Enceladus is *not* included in this test scenario. Furthermore, the cylinder is filled with a uniform density ξn_D of negative dust, which is treated as a heavy, negatively charge plasma species. From eq. (5.8), we expect the Anti-Hall effect to occur for dust charge densities of $\xi n_D > 0.2 n_i$. Therefore, we consider two different cases: $\xi n_D = 0$ (case 1) and $\xi n_D = 2n_i/3$ (case 2).

Figure 5.3 shows the results without any dust (case 1) in the left column compared to those with $\xi n_D = 2/3 n_i$ (case 2, right column). Plots (a) and (b) show the B_y component of the Alfvén wings generated by the cylindrical obstacle. One can clearly see the small inclination angle of the Alfvén wing against the background field of $\arctan M_A = 7°$. The effect of the dust is best illustrated by the currents parallel to the Alfvén characteristics ($\approx j_z$) in a plane perpendicular to the wings, shown here at $z = +7.5 R_E$ (cf. plots (e) and (f)). With zero Hall effect, i. e. for $\xi n_D = 0.2 n_i$, the maximum of these currents would be located at the y axis (see figure 3.6). For $\xi n_D = 0$, the Hall effect rotates these currents clockwise, while a dust charge density of $\xi n_D = 2n_i/3$ causes a rotation counterclockwise (Anti-Hall effect). The resulting B_y component is displayed for both cases in the same plane (see plots 5.3(c) and 5.3(d)). It can clearly be seen from plots 5.3(a) – (d) that in the interior of the northern Alfvén fluxtube, B_y is positive without and negative with dust. Within the southern wing, the opposite situation occurs. Outside the fluxtube, the

wing-aligned currents yield a quadrupole-like structure of the B_y component.

For this simple scenario, we can quantitatively compare the hybrid model results with the analytical Alfvén wing solution: equations (5.6) and (5.10) allow to calculate the conductivities, integration from $z = 0$ to the top of the cylinder yields the conductances and from equations (3.87) and (3.88) we obtain the corresponding constant magnetic field perturbations in the far field inside the fluxtube. In case 1, we get a Pedersen conductance of $\Sigma_P = 7\,\mathrm{S}$, a Hall conductance of $\Sigma_H = 3.5\,\mathrm{S}$ and $B_y = \pm 5\,\mathrm{nT}$ ('+': north, '−': south). Case 2 ($\xi n_D = 2/3\, n_i$) yields $\Sigma_P = 7\,\mathrm{S}$, $\Sigma_H = -8\,\mathrm{S}$ and $B_y = \mp 9\,\mathrm{nT}$. This is in good agreement with what can be obtained from figure 5.3. For $\xi n_D = 0.2 n_i$ one gets $\Sigma_H = 0$ and therefore, a B_y perturbation of approximately zero (not shown here, but confirmed by simulation). Thus, we have shown that the reversal of the Hall current due to dust is not only an effect of the analytical, first-order perturbation theory applied in *Simon et al.* [2011b], but can also be reproduced by our self-consistent simulation.

In *Simon et al.* [2011b], only the results for the magnetic field perturbations were presented, while the hybrid model automatically also calculates currents and ion velocity. For a better understanding of the flow perturbations and currents associated with Hall and Anti-Hall effect, we compare our simulations with analytical results derived by *Saur et al.* [1999] for the same cylindrical geometry. For the electric field, the electron velocity and the perpendicular current inside the cylinder, these authors derived

$$\underline{E} = \underline{E}_0 + E_P \begin{pmatrix} \sin\Theta_P \\ \cos\Theta_P \end{pmatrix} \quad , \tag{5.15}$$

$$\underline{u}_e = u_e \begin{pmatrix} \cos\Theta_{twist} \\ \sin\Theta_{twist} \end{pmatrix} \tag{5.16}$$

and

$$\underline{j}_\perp = -j_\perp \begin{pmatrix} \sin\Theta_P \\ \cos\Theta_P \end{pmatrix} \quad , \tag{5.17}$$

where the angles are given by

$$\tan\Theta_P = \frac{2\Sigma_A\Sigma_H}{\Sigma_H^2 + \Sigma_P(\Sigma_P + 2\Sigma_A)} \tag{5.18}$$

and

$$\tan\Theta_{twist} = \frac{\Sigma_H}{\Sigma_P + 2\Sigma_A} \quad , \tag{5.19}$$

respectively. As in chapter 3, Σ_A denotes the Alfvén conductance.

All these equations are still valid when including dust in the cylinder. For the derivation of the ion velocity, however, *Saur et al.* [1999] used the explicit definition of Hall and Pedersen conductivities, depending on collision and gyration frequency. For the plasma with electrons, one single-charged species of water group ions and dust, the Hall conductivity

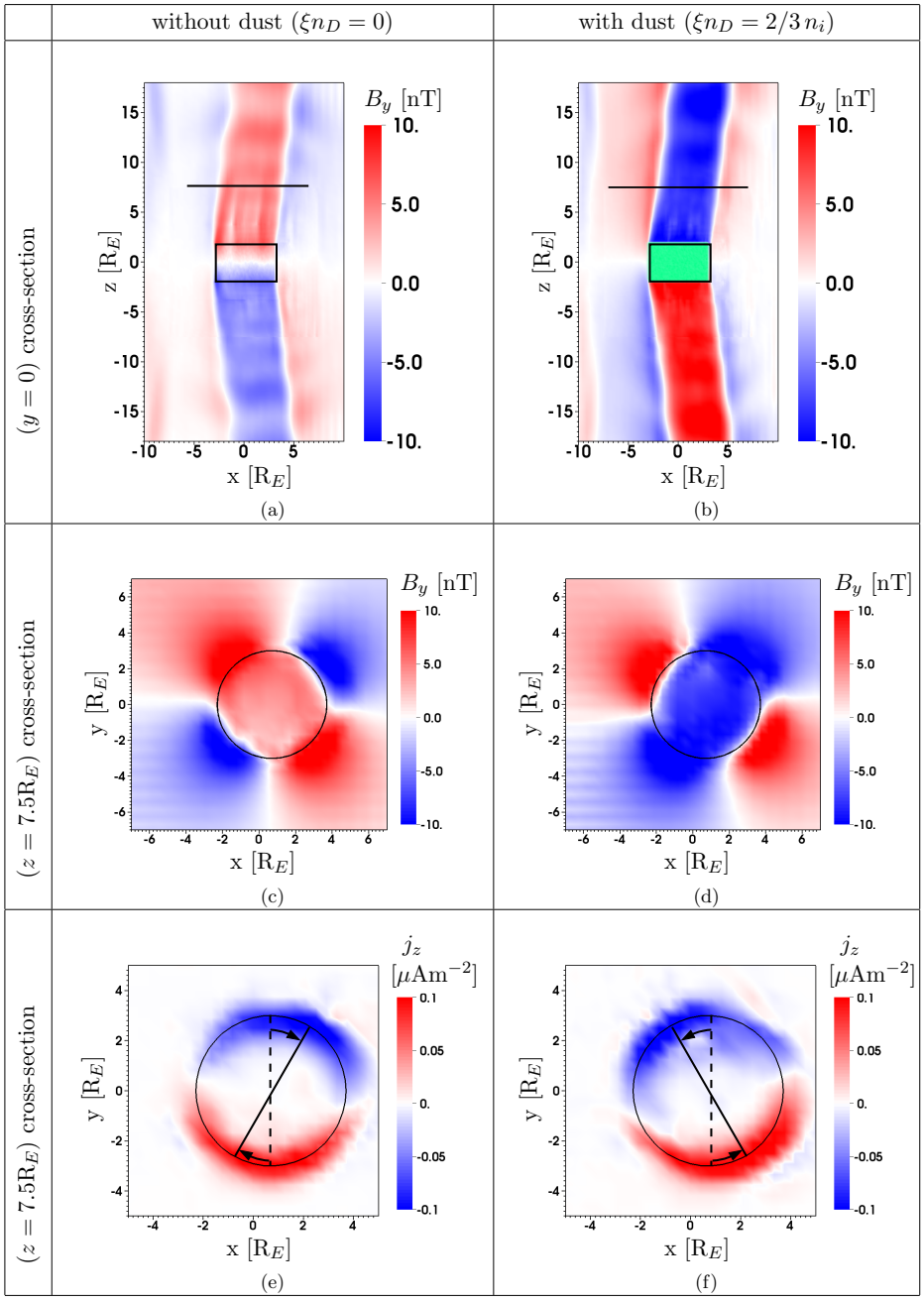

Figure 5.3: Results from hybrid simulations in order to show the principle effect of negatively charged dust grains on the plasma interaction. Plots (a) and (b) illustrate the scenario: the plasma, which flows in $(+x)$ direction, undergoes collisions within a cylindrical volume (denoted by the black rectangle), leading to the generation of Alfvén wings, as illustrated by B_y. The left-hand column shows the results without any dust, while for the results shown in the right-hand column the cylindrical volume is filled with a constant density of $\xi n_D = 2n_i/3$ (illustrated by the green area in plot (b)). The four lower panels display a plane roughly perpendicular to the Alfvén wings (indicated by the black lines in (a) and (b)). The circle of radius $3R_E$ shows the approximate position of the Alfvén tube. Due to the small angle between the wings and the background magnetic field of about only $\arctan M_A = 7°$ (also visible in (a) and (b)), these currents are mainly given by j_z (cf. plots (e) and (f)). Without any dust, the Hall effect rotates these currents clockwise, while the dust-associated Anti-Hall effect causes a counter-clockwise rotation. This explains the different signs of the B_y component in the four top panels.

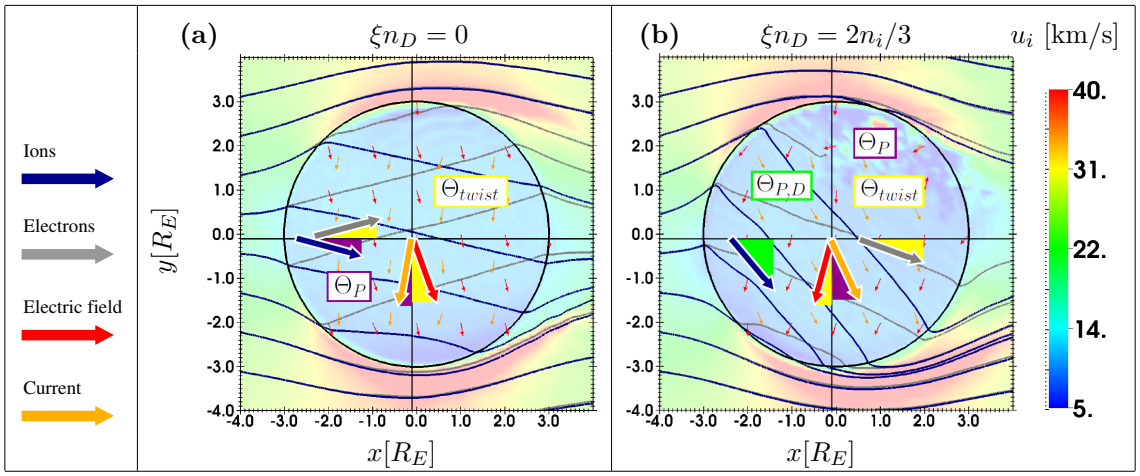

Figure 5.4: The plots show the directions of the electric field (red), the perpendicular current (orange), the electron velocity (given by $\underline{E} \times \underline{B}$, gray) and the ion velocity (blue) for the same uniform cylinder filled with neutral gas as discussed in figure 5.3. We consider two different cases: no dust ($\xi n_D = 0$) and a uniform dust density of $\xi n_D = 2n_i/3$. Without dust, all quantities are twisted around the z axis due to the Hall effect (see also *Saur et al.* [1999], figure 9), while the electron absorption by dust (plot (b)) yields an Anti-Hall effect, which reverses the directions of the twist of electron velocity, electric field and current due to the negative sign of the Hall conductivity. The ions, however, are deflected away from Saturn in both cases. The dust even enhances their deflection.

(equation (5.6)) becomes

$$\sigma_H = \frac{en_i}{B}\frac{\tilde{\nu}_i^2}{\tilde{\nu}_i^2 + \Omega_i^2} - \frac{e}{B}\xi n_D = \sigma_{Hi} - \frac{en_i}{B}k \quad , \tag{5.20}$$

where the absorption parameter $k = \xi n_D / n_i$ has been introduced. The symbol σ_{Hi} denotes the Hall conductivity in an electron-ion plasma without dust, the corresponding conductance is Σ_{Hi}. Analogous to eq. A16 of *Saur et al.* [1999], we obtain for the ion velocity

$$\underline{u}_i = |\underline{u}_i| \begin{pmatrix} \cos\Theta_{P,D} \\ -\sin\Theta_{P,D} \end{pmatrix} \quad , \tag{5.21}$$

with

$$\tan\Theta_{P,D} = \frac{2\Sigma_{Hi}\Sigma_A + k\Sigma_P\tilde{\Sigma}_{Hi}}{2\Sigma_A\Sigma_P + (1-k)(\Sigma_{Hi}^2 + \Sigma_P^2)} \quad , \tag{5.22}$$

and the abbreviation

$$\tilde{\Sigma}_{Hi} \equiv \frac{\Sigma_{Hi}^2 + \Sigma_P^2}{\Sigma_{Hi}} \quad . \tag{5.23}$$

One can easily verify that for $k \to 0$ also $\Theta_{P,D} \to \Theta_P$. To understand the implications of the above equations, figure 5.4 shows our simulation results for the directions of fields, currents and velocities in the ($z = 0$) plane. For case 1, i. e. without dust, our results are

shown in plot 5.4(a). One can clearly see the deflection of electric field, electron velocity, current and ion velocity with the angles Θ_P and Θ_{twist}. From equations (5.18), (5.19) we get $\Theta_{twist} \approx \Theta_P \approx 13°$, which is in good agreement with our simulation results.

The situation gets different with dust. In an electron-ion plasma without dust, a vanishing Hall conductance $\Sigma_H \approx 0$ implies $\tilde{\nu}_i \approx 0$ and therefore no deflection of electric field, electron velocity, current and ion velocity. With dust, however, the modified quasi-neutrality condition ($n_i = n_e + \xi n_D$) yields $\Sigma_H \approx 0$, but $\Sigma_{Hi} \neq 0$ and therefore $\Theta_{PD} \neq 0$. Thus, what we can learn from eqs. (5.18), (5.19) and (5.22) is that only the ions should undergo a deflection. Physically this deflection is a result of the Pedersen current, where in the case of electrons attached to dust only the ions but not the charged dust particles move with respect to Enceladus.

In case 2, the direction of rotation of electric field, current, and electron velocity reverses, since the Hall current reverses its sign. The ion flow, however, does not change its flow direction from $-y$ to $+y$, but the deflection away from Saturn gets even stronger, since it can be seen from eq. (5.22) that $\Theta_{P,D} > \Theta_P$ for $k > 0$. This has the remarkable consequence that for the ions, the dust enhances the asymmetries, while for electrons, electric field and current the direction of rotation is reversed. The angles for case 2 are $\Theta_{twist} = -28°$, $\Theta_P = -20°$ and $\Theta_{P,D} = 54°$, which match well with figure 5.4(b).

It is therefore shown that A.I.K.E.F. is able to reproduce the sign of the observed B_y perturbation according to the presence of negatively charged dust, i. e. the Anti-Hall effect is successfully included in the model. The results are in quantitative agreement with the analytical theory of the Alfvén wing. For a quantitative comparison with Cassini data, however, a realistic model of the plume needs to be included. Hence, we extend our previous hybrid model of Enceladus' plasma interaction [*Kriegel et al.* 2009] such that we now include momentum loading via charge exchange as well as the electron absorption by dust. The following problems are addressed:

- We compare Cassini magnetometer data with our simulations that include a realistic neutral plume model *and* negative dust.
- Based on this comparison, we estimate variations in plume activity and a possible tilt of the plume for the flybys E5 – E9 and E11.

5.4 Modeling Enceladus

The hybrid model and the A.I.K.E.F. code have already been described in chapter 4. Here, we will therefore summarize only the numerical and physical parameters which are used for the simulations presented in this chapter. Furthermore, the models of the neutral and dust plume are described.

5.4.1 Simulation Parameters and Geometry

As discussed in section 2.2, the magnetospheric plasma impinging on Enceladus consists mainly of O^+, OH^+, H_2O^+ and H_3O^+ [*Tokar et al.* 2006, 2008]. To study the basic effect

of the dust on Enceladus' Alfvén wings, however, we consider only a single species of water group ions (W^+) with an average mass of m_i = 17.5 amu. We assume that the ions flow at the ideal corotation velocity of $\underline{u}_0$ = (26.4,0,0) km/s relative to Enceladus. As discussed in section 2.2, Cassini observations show evidence for a sub-corotation of the upstream flow [*Wahlund et al.* 2005, 2009, *Wilson et al.* 2009], whereas our assumption of ideal corotation was mainly made to improve numerical stability. However, this does not affect our conclusions, since we are interested in the general plasma structures and *relative* variations of the plume. Assuming that all upstream ion species have roughly equal abundances [*Tokar et al.* 2006], the major reactions with the neutral water molecules of the plume yield an average rate of $k_{\alpha\beta} = k_{W^+} = 2.2 \cdot 10^{-9}\mathrm{cm}^3/\mathrm{s}$ (see e.g. appendix of *Fleshman et al.* [2010b]). A more detailed analysis of the ion neutral chemistry will be presented in the next chapter. The electron pressure (equation (B)) includes contributions from two electron populations: a warm population with $k_B T_{ew}$=100 eV, which makes up a fraction of 0.5% of the total electron density and a cold population with $k_B T_{ec}$ = 1.35 eV. The background magnetic field is approximated by a dipole field which is fitted to the unperturbed upstream field of the respective flyby. At the center of Enceladus, the field is approximately given by $\underline{B}_0 = (0, 0, -325\,\mathrm{nT})$. The density of the upstream plasma is set individually for each flyby according to the values listed in table 2.2. An overview about the physical parameters is provided in table 5.1. Those values which are not mentioned here in the text have been adopted from table 2.4.

Photoionization and electron impact ionization are considered as ionization processes. The photoionization rate for water is $\nu_{photo} = 4.4 \cdot 10^{-9}/\mathrm{s}$ at 9.5 AU for quiet solar conditions [*Burger et al.* 2007]. This rate is kept spatially constant, since none of the flybys discussed here occurred in Saturn's geometric shadow and the plume is assumed to be optically thin. The electron impact ionization is mainly carried by the warm electron population which possesses a rate coefficient of $I_e = 4.5 \cdot 10^{-8}\mathrm{cm}^3/\mathrm{s}$ [*Fleshman et al.* 2010b]. We neglect any variations in the local ionization rate due to the energy loss of the electrons when moving through the plume.

The size of our simulation box is $20R_E \times 20R_E \times 70R_E$ for the simulations presented in this chapter. Because of the south-polar plume and the associated structures, Enceladus is not placed at the center of the box, but at 4/7 of the box height. We use a hierarchical mesh that is adaptive in space but static in time, with up to three levels of refinement: L_0, L_1, L_2. At the coarsest level (L_0), the resolution is $\Delta_{L_0} = 53\mathrm{km} = 0.21R_E$, while it is $\Delta_{L_2} = \frac{1}{4}\Delta_{L_0} = 13\mathrm{km} = 0.05R_E$ in the highest level. The spatial extension of the refinement levels is illustrated by the plots of our mesh in figures 5.5(a) and 5.5(d). Due to limited computational resources, we were not able to perform every simulation with the highest resolution, but only the final (best fit) runs. All other runs are carried out using a mesh with only two levels of refinement (L_0, L_1), since we did not notice a remarkable dependency of our results on the grid resolution. The ions and the dust are represented by 100 macroparticles per species, yielding a total of more than one billion macroparticles in the simulation. The physical and numerical parameters are summarized in table 5.1. Further numerical aspects like boundary conditions and smoothing are described in sections 4.5 and 4.4.

Table 5.1: Physical and numerical parameters used in the simulations. [1]Upstream density adjusted to each flyby according to values listed in table 2.2. [2]Dipole magnetic field fitted to the unperturbed upstream field of the respective flyby.

Parameter	Symbol and Value
Plasma velocity	$u_0 = 26.4\,\mathrm{km/s}$
Plasma number density	$n_0 = 45 - 90\,\mathrm{cm}^{-3}$ [1]
Magnetic field at (0,0,0)[2]	$\underline{B}_0 = (0, 0, -325)\,\mathrm{nT}$
Species included	$\mathrm{W}^+ \mathrel{\hat{=}}$ water group ions
Ion mass	$m_i = 17.5\,\mathrm{amu}$
Alfvénic Mach number	$M_A = 0.10 - 0.15$
Ion temperature	$k_B T_i = 35\,\mathrm{eV}$
Cold electron temperature	$k_B T_{ec} = 1.35\,\mathrm{eV}$
Hot electron temperature	$k_B T_{eh} = 100\,\mathrm{eV}$
Density fraction of hot electrons	$0.5\%\, n_0$
Opening angle (gas plume)	$H_\vartheta = 7.5°$
Opening angle (dust plume)	$H_\vartheta = 15°$
Charge exchange rate coefficient	$k_{W^+} = 2.2 \cdot 10^{-9}\,\mathrm{cm^3 s^{-1}}$
Photoionization rate	$\nu_{Ph} = 4.4 \cdot 10^{-9}\,\mathrm{s^{-1}}$
Electron impact rate coefficient	$I_e = 4.5 \cdot 10^{-8}\,\mathrm{cm^3 s^{-1}}$
Box (x)	$-7.5R_E \leq x \leq +12.5R_E$
Box (y)	$-10R_E \leq y \leq +10R_E$
Box (z)	$-40R_E \leq z \leq +30R_E$
Mesh spacing L_0	$\Delta_{L_0} = 53\,\mathrm{km} = 0.21R_E$
Mesh spacing L_2	$\Delta_{L_2} = \frac{1}{4}\Delta_{L_0} = 13\,\mathrm{km} = 0.05R_E$
Time step	$\Delta t = 0.015\Omega_i^{-1} = 8.4 \cdot 10^{-3}\,\mathrm{s}$
Simulation time	$10000\Delta t = 150\Omega_i^{-1} = 84\,\mathrm{s}$
Smoothing	$\eta_{sm} = 6\%$
Conductivity of interior	$\sigma = 7 \cdot 10^{-7}\,\mathrm{S/m}$
Macroparticle per Cell	100

5.4.2 Modeling the Plume

We model the neutral density according to the single-plume model given by *Saur et al.* [2008]. The density profile is given by

$$n_n(r, \vartheta, \varphi) = n_{n,0} \left(\frac{R_E}{r}\right)^2 \exp\left[-\left(\frac{\vartheta}{H_\vartheta}\right)^2\right] \exp\left[\frac{R_E - r}{H_d}\right] \quad , \tag{5.24}$$

where $n_{n,0}$ denotes the base density on Enceladus' surface. The parameters r and ϑ are the radial distance from the center of Enceladus and the polar angle, respectively. H_ϑ denotes the angular width of the plume. The third term arises from the gravitation of Enceladus. We set H_d equal to the Hill radius of 948 km.

Simulations based on Cassini UVIS measurements suggest that the neutrals ejected from the south polar regions have a surface density on the order of $10^{10} - 10^{11}\,\mathrm{cm}^{-3}$ [*Tian et al.* 2007]. This base density is related to the plume production rate Q according to

$$n_{n,0} = \frac{Q}{A u_n R_E^2} \quad , \tag{5.25}$$

where $A = 0.054$ is an integration constant due to the opening angle of the plume (see *Jia et al.* [2010c]). Assuming a neutral speed of $u_n = 1$ km/s, a surface density of 10^{10} cm^{-3} corresponds to a plume production rate of $3 \cdot 10^{28}$ H_2O/s.

Measurements and simulations indicate a variation in the activities of the jets [*Saur et al.* 2008, *Kriegel et al.* 2009, *Teolis et al.* 2010, *Tenishev et al.* 2010, *Smith et al.* 2010]. Therefore, $n_{n,0}$ is treated as a free parameter to model the source strength for the individual flybys. We vary $n_{n,0}$ between different simulation runs in steps of $1 \cdot 10^{10}$ cm^{-3}.

Spitale and Porco [2007] showed that the plume consists of at least eight jets. However, *Saur et al.* [2008] showed that a multi-plume model might not be necessary to reproduce MAG data. The effect of the single jets on the global shape of the plume is mainly given by variations in the location of active regions, which may yield a global tilt of the plume. For each flyby, we therefore tested different tilts of the plume in order to achieve best possible agreement with MAG data. In the ENIS system, the symmetry axis of the plume has the direction $(\cos\varphi_0 \sin\vartheta_0, \sin\varphi_0 \sin\vartheta_0, \cos\vartheta_0)$, with $\varphi_0 \in [0°; 360°]$ and $\vartheta_0 \in [90°; 180°]$. These angles correspond to planetographic latitude (Lat.) and longitude (Lon.) on Enceladus' surface as follows: $90° - \vartheta_0 = $ Lat.(°) and the correlation between φ_0 and Lon. is given by $(0° \mathrel{\widehat{=}} 90°\text{W}, 90° \mathrel{\widehat{=}} 0°\text{W}, 180° \mathrel{\widehat{=}} 270°\text{W}, 270° \mathrel{\widehat{=}} 180°\text{W})$. Please note that the angle φ_0 is measured in counter-clockwise direction (with respect to the ENIS system), whereas the value of Lon. increases when moving clockwise around Enceladus. Since these additional parameters strongly increase the number of necessary simulations, we at first checked, if a tilt of the symmetry axis towards planetary latitudes of $-80°$ along the $\pm x$ and $\pm y$ axis yielded any notable improvement when comparing our results with Cassini MAG data. If that was the case, we further varied the latitude in steps of $\vartheta_0 = 5°$ and the longitude in steps of $\varphi_0 = 22.5°$ to find the optimal set of parameters.

From UVIS observations during a star occultation on 24 October 2007, *Hansen et al.* [2008] obtained a Mach number of the gas of about $M = 1.5$, which is in agreement with simulations [*Tian et al.* 2007, *Smith et al.* 2010, *Tenishev et al.* 2010]. Assuming a gas temperature of 150 K (that is a thermal speed of $v_{th} = 455$ m/s), this yields an outgassing velocity of $u_n = 680$ m/s. More recent data suggest a even higher velocity of $M = 4$ [*Hansen et al.* 2010]. A Mach number in the range of 1.5 – 4 corresponds to opening angles of the individual jets of $\arctan(v_{th}/u_n) = 30° - 15°$. However, as we use a single-plume model, the opening angle H_ϑ includes both, ejection speed and location of the vents. We found that our simulations yield a considerably better agreement with a more confined plume and therefore set $H_\vartheta = 7.5°$ (see also section 5.5.2). With regard to the dynamics of the ions, however, we found that a neutral velocity on the order of 1 km/s does not have a noteworthy influence on the outcome of the simulation. For simplicity, we therefore neglect the neutrals' velocity in the ionization processes, i.e. the newly generated ions start with initial velocity zero.

5.4.3 Dusty Plasma Parameters

According to *Farrell et al.* [2010] and *Shafiq et al.* [2011], the charged submicron-sized dust grains in the Enceladus plume may be considered an additional plasma constituent, since the inter-grain distance for dust densities of $n_D \geq 10^{-1}\,\mathrm{cm}^{-3}$ is smaller than the effective dusty plasma Debye length of $\lambda_{Eff} \sim 1\,\mathrm{m}$. Assuming spherical grains with a mass density of $\rho = 10^3\,\mathrm{kg/m}^3$ (water ice) and an average number of $\xi = 50$ electrons for a grain size of $0.03\,\mu m$ and $\xi = 8000$ for a grain size of $1\,\mu m$, the charge-to-mass ratio ranges from $q_D/m_D = 3 \cdot 10^{-1}\,\mathrm{C/kg}$ to $q_D/m_D = 7 \cdot 10^{1}\,\mathrm{C/kg}$ [*Shafiq et al.* 2011]. Therefore, we consider the charged dust as an additional plasma species with a charge-to-mass ratio of $q_D/m_D = 5.5\,\mathrm{C/kg} = 10^{-6}\,q_{W^+}/m_{W^+}$. Due to this small charge-to-mass ratio, this averaged dust species does practically not move during the simulation runtime, which is on the order of a few minutes. We would like to note that this would still be true for nanometer-sized grains with a significantly larger charge-to-mass ratio of $q_{D,nm}/m_{D,nm} \sim 10^{-4}\,q_{W^+}/m_{W^+}$, since the accelerating electric field is strongly reduced within the center of the plume (see section 5.5). Moreover, the resulting dust charge density can also be interpreted to include a fraction of positively charged grains as reported by *Jones et al.* [2009], because only the total dust charge density is taken into account by our simulations. The presence of positively charged grains would then just mean that the density of the negative grains is even larger.

The source strength of the dusty part of the plume is characterized analogously to the gas plume by the density $\xi n_{D,0}$ of charged dust at the south pole, which is varied in steps of $50\,\mathrm{cm}^{-3}$. We would like to note that we only describe a stationary density profile of the *charged* dust in our model, while a self-consistent model of the electron absorption is out of the scope of this paper and will be addressed in chapter 6. Some implications of this approximation are also discussed in section 4.3 in *Simon et al.* [2011b]. The spatial density profile of the dust is similar to the neutral density profile (eq. (5.24)). However, due to the ejection speeds of the dust grains being comparable to the escape velocity of Enceladus, the influence of gravitation and inertia forces is larger for the dust grains than for the gas, leading to complicated trajectories around Enceladus [*Kempf et al.* 2010]. We account for that by setting $H_\vartheta = 15°$ for the dust. Moreover, the charging time depends on grain size and the ambient plasma conditions. Therefore, the spatial profile of the dust *charge* density in the plume may be different from the profile of the dust *number* density. We find that our results are in better agreement with Cassini MAG data, if we replace the geometric r^{-2} decrease (see eq. (5.24)) by r^{-1}. The resulting profile does not claim to be a quantitatively realistic image of the charged dust population at Enceladus. This would require a much more sophisticated model of the grain-size-distribution of the dust, the dust motion in the three-body-problem and the dust charging process, which is presented in chapter 6.

5.5 Results for Selected Enceladus Flybys

In order to understand the magnetic field measurements and model calculations along Cassini's 1D-trajectories, we present the results of our 3D simulations together with 1D comparisons between model and observations. We show that considering the electron

absorption is necessary to quantitatively explain the observations. However, before we can understand the magnetic field structures, we have to consider the corresponding structures of plasma density and velocity.

Since upstream and plume parameters are different for each flyby discussed here, we arbitrarily choose the E9 best fit case with an upstream density of $n_0 = 75\,\mathrm{cm}^{-3}$ and a base density of $n_{n,0} = 6 \cdot 10^{10}\mathrm{cm}^{-3}$ for all color plots shown in this section. The simulation including dust has an additional dust base density of $\xi n_{D,0} = 5.5 \cdot 10^2\,\mathrm{cm}^{-3}$.

5.5.1 Density and Velocity

Figure 5.5 displays the densities of ions and charged dust in the ($y = 0$) and ($z = -4R_E$) planes. Plots 5.5(b) and 5.5(e) visualize the gas plume as the region where the ion density is enhanced due to the creation of new ions by electron impacts and photoionization (mass loading). Near the south pole, the ion density is about an order of magnitude larger than upstream. The slightly enhanced density downstream of the plume results from pick-up of the newly created ions [*Kriegel et al.* 2009]. The dust charge density ξn_D (plots 5.5(c) and 5.5(e)) has a maximum of $\xi n_D > 100\,\mathrm{cm}^{-3}$ near the south pole and assumes a value of about $\xi n_D = 50\,\mathrm{cm}^{-3}$ at $z = -4R_E$. Thus, the dropout in the electron density due to electron absorption by dust, which is required by our model to achieve agreement with MAG data (see next sections), is on the order of 10% – 20% in the center of the plume. It is therefore possible to have a noteable difference in electron and ion densities while both are larger than the background density. This finding is in agreement with results from RPWS presented by *Shafiq et al.* [2011]. Since we can only provide dust charge densities, it is not easily possible to compare our results with dust measurements (for example by CDA). In order to relate our model densities of the *charged* dust to *number* densities, one would need to consider the number of electrons on grains of different sizes and the grain-size distribution of the dust which will be done in chapter 6.

Ion velocity and electric field are presented in the lower row of figure 5.5. In plot 5.5(g), one can see the deflection of the ion flow in ($-y$) direction (away from Saturn), as discussed in section 5.3. The twist of the electric field in ($-x$) direction in plot 5.5(h) results from the Anti-Hall effect. As can be seen from plots 5.5(g) and 5.5(h), the pickup tail and the associated decrease in the electric field strength are essentially confined to the ($|y| < 1R_E$)-region, i.e. the tail exhibits a two-dimensional shape. This finding is in agreement with our previous hybrid simulation results where it has been shown that the small gyroradii of the pick-up ions (on the order of 10 km) prevent the tail from a significant expansion in y direction [*Kriegel et al.* 2009]. Within the plume, ion velocity and electric field decrease to approximately zero, in agreement with observations of flow stagnation by CAPS [*Tokar et al.* 2009]. To further illustrate the effect of flow stagnation, figure 5.5(i) displays the ion velocity in the ($z = -4R_E$) plane along the corotation axis ($y = 0$ line): the ion velocity decreases sharply below 1 km/s from $x = -1R_E$ to $x = 0.5R_E$, before it assumes a value of $u_i = 17\,\mathrm{km/s} = 60\%\,u_0$ in the pick-up tail.

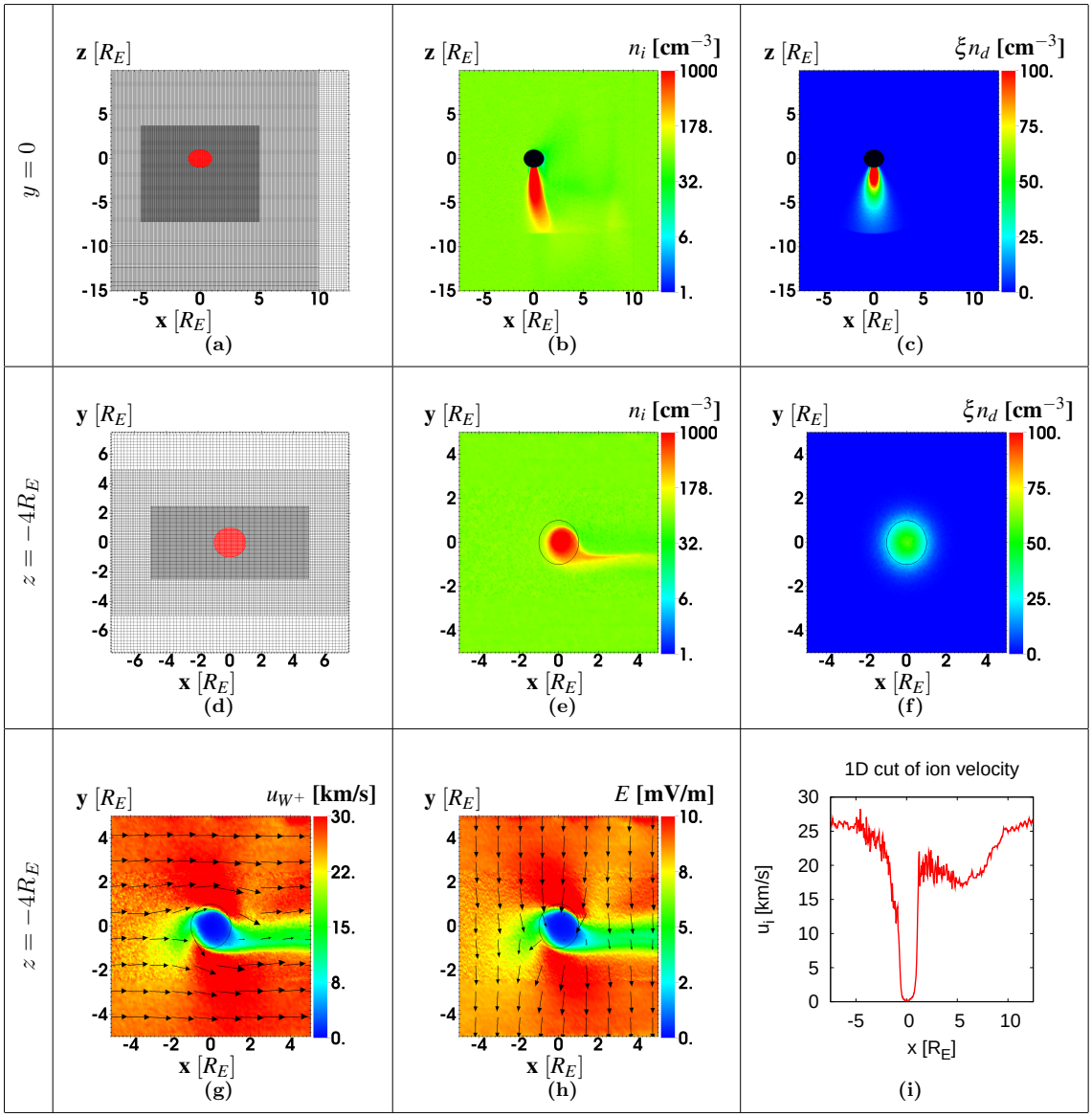

Figure 5.5: Simulation grid and dusty plasma near Enceladus: plots (a) and (d) show the simulation mesh with the different levels of refinement. Plots (b) and (e) display the ion number density, which is enhanced in the plume by about an order of magnitude due to electron impact and photoionization. The dust charge density in plots (c) and (f) is comparable to the upstream plasma density. Plots (g) – (i) show ion velocity and electric field along the $y = 0$ line and in two dimensions. The ion velocity decreases to stagnation within the plume.

5.5.2 Magnetic Field: E5 and E6

All Enceladus flybys in 2008 had trajectories basically in the (x, z) plane. For a better understanding of the perturbations visible in the MAG data, figure 5.6 shows the results for the components of the magnetic field in that plane. For clarity, the color plots only show the magnetic field perturbations $(\Delta B_x, \Delta B_y, \Delta B_z)$, the background field has been subtracted by fitting a dipole field. The black lines represent the projections of Cassini's trajectories during E5 and E6 on the (x, z) plane. The first row shows the results for a pure gas plume without dust. In plot 5.6(a), the Alfvén wing can clearly be seen in the ΔB_x component. ΔB_y (plot 5.6(b)) assumes positive and negative signs in both, the northern and the southern wing, which results from the clockwise rotation of the quadrupole-like structure of ΔB_y due to the Hall effect. The positive sign of ΔB_y in the center of the northern wing as well as the negative sign in the center of the southern wing are consistent with the results for the test scenario (see figure 5.3). We would like to note that an ideal MHD model (i.e. without Hall effect) would yield $\Delta B_y \approx 0$ at $y = 0$. The ΔB_z component in plot (c) assumes a negative value in the magnetic pile-up region in front of the plume and a positive value at the downstream side (since it is $B_z < 0$ for the background field). These structures have already been described in detail in our previous study [*Kriegel et al.* 2009] as well as by *Jia et al.* [2010c].

The middle row of figure 5.6 (plots (d) – (f)) shows the results of a simulation with dust included. As expected, the ΔB_y component inside the Alfvén fluxtube has reversed its sign. On the other hand, no modification of ΔB_x is visible. In section 5.7, we will discuss in which regions the condition for the occurrence of the Anti-Hall effect (inequality (5.8)) is fulfilled . The most important result, especially with respect to the work presented in *Simon et al.* [2011b], is that the reversal of ΔB_y due to electron absorption by dust also occurs for a more realistic, inhomogeneous plume model.

In contrast to what is claimed in recent literature [*Jia et al.* 2010a,b,c], it is therefore *not* necessary to account for the large-scale, centrifugally driven dynamics of the flux tubes in Saturn's magnetosphere in order to understand magnetic field observations within the Enceladus plume. However, for a realistic description of Enceladus' magnetospheric interaction, (at least) three plasma species need to be taken into account: electrons, water group ions, and the dust grains, where the dust grains include a wide distribution of charge-to-mass ratios.

We would also like to point out that our results show that the northern wing (negative ΔB_x) does not begin at Enceladus' south pole, but about 2 R_E below. Thus, our simulation confirms that the draping center is shifted about 2 R_E downward from the south pole, in agreement with the findings of *Khurana et al.* [2007] for E0 – E2. It is remarkable that our simulation succeeds in reproducing this aspect of the interaction without reducing the neutral density near the south pole to account for a reduced ionization efficiency in that region, as proposed by *Jia et al.* [2010c]. By comparing the ΔB_z components in plots 5.6(c) and 5.6(f), one can see that the region of magnetic field decrease is shifted downward, if dust is considered.

A quantitative comparison between MAG data from E5 and E6 and simulation results is provided in the bottom row of figure 5.6. MAG data are colored in black, the other colors indicate different simulation setups: no dust (green), with dust (blue) and the best fit with

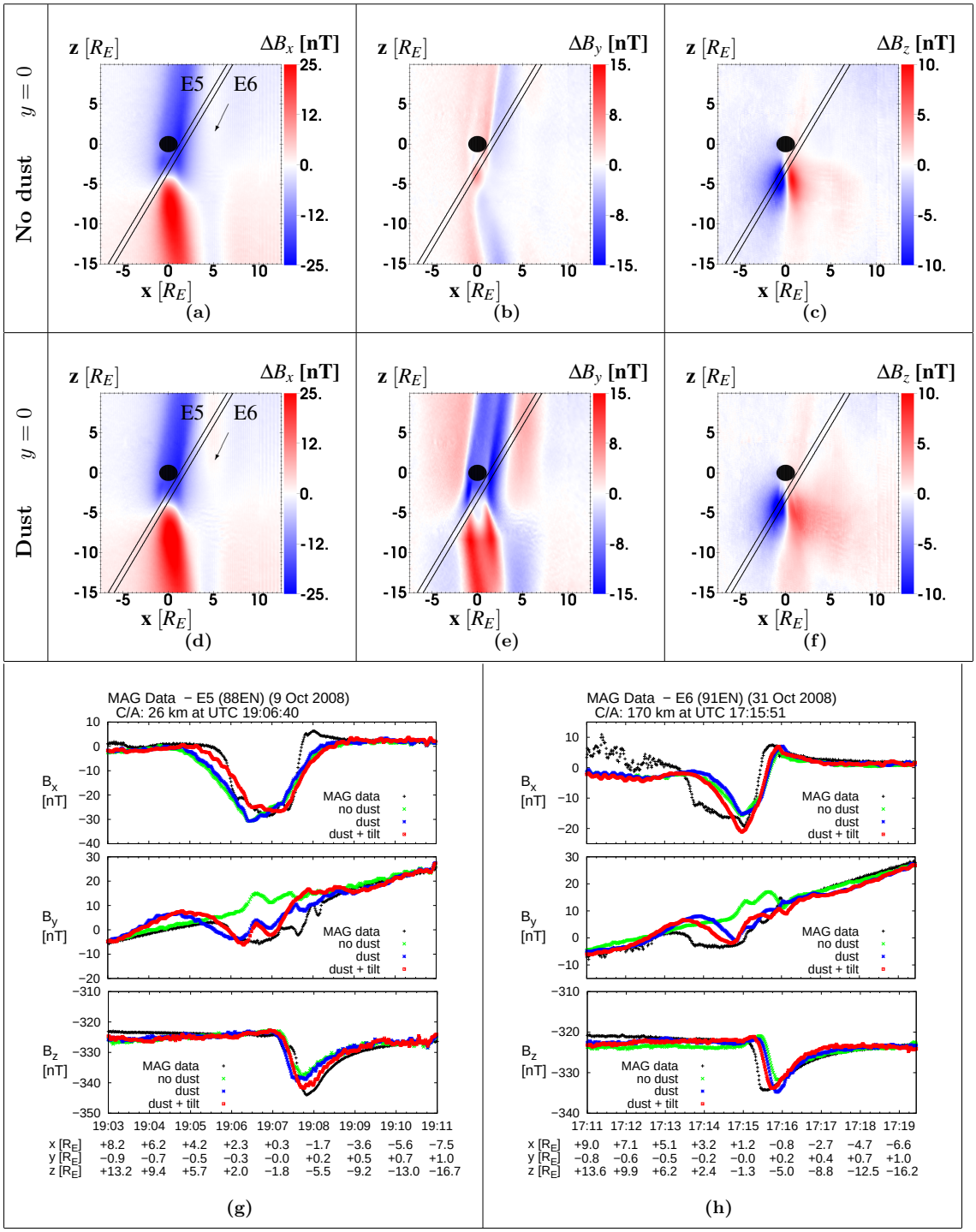

Figure 5.6: Simulated magnetic field components in the (x, z) plane together with the trajectories of E5 and E6 (plots (a)–(f)). The upper row displays the results without dust, while the lower row shows the reversal of the B_y component when the presence of the negatively charged dust is considered. Plots (g) and (h) show a comparison of simulation results with Cassini MAG data (black) for E5 (left) and E6 (right) for a simulation without dust (green), with dust (blue) and the best fit including dust and a tilted plume (red).

dust and a tilted plume (red). By comparison of the observations from both flybys it is evident that the perturbation is stronger for E5 (up to 30 nT) than for E6 (less than 20 nT), see also *Jia et al.* [2010a]. This might not only be an effect of a variable plume activity, but also of the different upstream densities for these flybys: for strong perturbations (as the observed flow stagnation) and a symmetric interaction geometry, the bending of the magnetic field lines is identical to the inclination of the Alfvén wing ($M_A = \tan\Theta_A \cong \Delta B_x/B_0$, cf. section 5.2), which yields

$$\Delta B_x \cong M_A B_0 \sim \sqrt{n_0} \quad . \tag{5.26}$$

Thus, a higher upstream density yields a stronger perturbation. For E5 and E6, the densities were $n_0 = 90\,\mathrm{cm}^{-3}$ and $n_0 = 45\,\mathrm{cm}^{-3}$, respectively [*Jia et al.* 2010b]. Based on the densities alone, one would expect the B_x perturbation during E5 to be about a factor of $\sqrt{2}$ stronger than during E6, which matches well with the observed field perturbation ($30\,\mathrm{nT}/20\,\mathrm{nT} = 1.5 \approx \sqrt{2}$). However, in order to reproduce the strength of the measured perturbations (in particular ΔB_x), different source strengths of the plume of $n_{n,0} = 1 \cdot 10^{11}\mathrm{cm}^{-3}$ (E5) and $n_{n,0} = 7 \cdot 10^{10}\mathrm{cm}^{-3}$ (E6) were required. Thus, the stronger perturbation measured during E5 is not only an effect of the higher upstream density as suggested by eq. (5.26), but also of a stronger plume activity by a factor of 1.5. This also implies that equation (5.26) is not strictly applicable. The reason is that the wing-aligned currents flowing towards Saturn's northern hemisphere are partially blocked by the solid body of Enceladus [*Saur et al.* 2007]. According to eq. (5.25), the plume densities correspond to production rates of about $Q = 3.7 \cdot 10^{29}$ H_2O/s (E5) and $Q = 2.4 \cdot 10^{29}$ H_2O/s (E6). The absolute values are about an order of magnitude larger than those derived by other authors [*Saur et al.* 2008, *Omidi et al.* 2010, *Jia et al.* 2010b]. This mainly results from our narrow plume, since for a larger opening angle (e.g. $H_\vartheta = 15°$), eq. (5.25) yields a production rate that is an order of magnitude lower for the same neutral base density. A summary of the best fit parameters is given in table 5.2.

Data from both flybys (black) show a steep decrease of the B_x component at the downstream side ($x > 0$, inbound), which is not seen in the simulation results (in particular for E6). This is also visible in the results of the analytical model presented in *Simon et al.* [2011b]. Both models have in common that they assume the collision frequency to be the same upstream and downstream. However, in reality the ion composition and therefore also reaction rate and collision frequency vary due to changes in the ion composition when moving through the plume from upstream to downstream. This is confirmed by the fact that downstream mainly H_3O^+ is present [*Cravens et al.* 2009]. Thus, this discrepancy could be due to the rough description of the ion-neutral chemistry in these two models. Including a more sophisticated model of the chemistry will be subject to future studies. At the upstream side ($x < 0$, outbound), the simulations reproduce the sharp increase in B_x during E6, while it is smoother for E5. This can also be seen in plot 5.6(d), where the upper trajectory (E5) passes through a region of negative ΔB_x upstream of the plume. In contrast, the lower trajectory (E6) passes along the uppermost end of the southern wing (positive ΔB_x).

The plots also show that the dust does not have any influence on the B_x and B_z components along E5 and E6 when comparing the simulations with (blue) and without dust (green). In the B_y component, it can be seen that the dust not only qualitatively reverses the sign of

ΔB_y, but also quantitatively explains the magnitude of the measured B_y perturbation. The base densities of the charged dust particles in the simulations are $\xi n_{D,0} = 8.5 \cdot 10^2\,\mathrm{cm}^{-3}$ for E5 and $\xi n_{D,0} = 5.5 \cdot 10^2\,\mathrm{cm}^{-3}$ for E6. The variation of the dust base densities is about a factor 1.5 and therefore, the variability of gas and dust plume is the same. However, for both flybys our simulations are not able to reproduce the extension widths of the B_y perturbation: for E5, our modeled B_y only matches the location of the decrease (downstream), while for E6, only the position of the increase to the background value in the upstream region is reproduced. This may result from a larger extend of the dust plume near the surface. Furthermore, in plot 5.6(e) it appears as if the trajectories pass through the southern Alfvén wing with $\Delta B_y > 0$, while the 1D comparisons only exhibit negative B_y perturbations. This striking difference only results from Cassini's motion in y direction and can be understood when the 3D geometry of the flyby is taken into account: upstream of the plume ($x < 0$), Cassini is located at $y > 0$. There, the B_y perturbation is negative, while it is positive along the projection on $y = 0$.

For B_z, simulations and data match very well. As the modeled perturbation in the B_z component is negative along the entire trajectories, our simulations are also successful in reproducing that Cassini only penetrated through the magnetic pile-up region, but did not intersect the magnetic field decrease. The location of the flyby trajectories with respect to the magnetic pile-up region and the field decrease is also illustrated in plot 5.6(f). For E5, our simulations do not show any further dips before or during the main perturbations around 19:07:20 UTC in B_x and B_z in contrast to the data. A reason for this might be that the trajectory of E5 was so close to the south pole (C/A distance of only 25 km) that these structures are caused by single jets which are not resolved by our plume model.

The red curves show that for both flybys, a tilt of the plume improves the agreement between data and simulation. In particular, the positions of the outbound flank of the region with reduced B_x, the entry into the pile-up region in B_z and its magnitude match observations better when introducing a tilt of the plume. However, the tilt applied for E5 (Lat. = −85°, Lon. = 270°, upstream) has the opposite direction as for E6 (Lat. = −85°, Lon. = 90°, downstream). These different tilts correspond to different plume activities. We therefore propose that during E5, other and possibly stronger jets were active than during E6. For a further investigation of this finding, a multi-jet gas and dust plume model within a plasma simulation is required.

5.5.3 Magnetic Field: E7 and E9

The second group of flybys on which we focus are E7 and E9. The upstream densities are $n_0 = 60\,\mathrm{cm}^{-3}$ for E7 and $n_0 = 75\,\mathrm{cm}^{-3}$ for E9. Figure 5.7 displays the components of the magnetic field perturbation in the plane of these flybys ($z = -1.5R_E$) together with the flyby trajectories. Analogous to figure 5.6, the first row displays the results without dust, while dust is included in the results shown in the second row. In ΔB_x and ΔB_y, the Alfvénic structures caused by the wing-aligned currents are clearly visible: within the northern Alfvén fluxtube, ΔB_x is negative. At the flanks at about $y = \pm R_E$, ΔB_x sharply assumes a small positive value, while along the x-axis, it smoothly gets to zero. Again our simulation therefore confirms that the draping center is located below $z = -1.5R_E$. ΔB_y exhibits a quadrupole-like structure, slightly rotated around the z axis due to Hall or

Anti-Hall effect. As discussed in section 5.3, the direction of this rotation depends on the sign of Σ_H: clockwise without dust and counter-clockwise for the Anti-Hall effect. When comparing the ΔB_y component of the simulations with and without dust (plots 5.7(e) and 5.7(b)), it is also evident that the symmetric quadrupole-like structure is stretched in y direction by the influence of the dust, yielding a larger region with negative ΔB_y (cf. plot 5.7(e)). In B_z, the magnitude of the perturbation is less than 5 nT = 1.5%B_0 in this plane. This is because the strongest magnetic pile-up is located ahead of the draping center, which can be found south of this plane (see also figure 5.6). Moreover, plot 5.7(f) shows that pile-up and field decrease region are also twisted by the Anti-Hall effect, such that the two flybys did not pass through the center of either of them.

The comparison between data and simulations is shown in figures 5.7(g) and 5.7(h). Again, MAG data are colored in black, the other colors indicate different simulation setups: no dust (green) and the best fit with dust (blue). We achieve very good agreement for the perturbations in B_x. The magnitude and the sharpness of the jumps in B_x match exactly for both flybys. It is $\Delta B_x = 20 - 25$ nT for E7 and $\Delta B_x \sim 20$ nT for E9. Since the upstream density is smaller, but the perturbation is stronger for E7 than for E9, we expect the plume activity to be slightly stronger for E7 according to the discussion in section 5.5.2. This is confirmed by our results: in order to reproduce the strength of the B_x perturbation, a neutral base density of $n_{n,0} = 7 \cdot 10^{10} \mathrm{cm}^{-3}$ and $n_{n,0} = 6 \cdot 10^{10} \mathrm{cm}^{-3}$ was required for E7 and E9, respectively. The corresponding production rates are $Q = 2.4 \cdot 10^{29}$ H_2O/s (E7) and $Q = 2.1 \cdot 10^{29}$ H_2O/s (E9). Therefore, the variability of the plume activity between E7 and E9 of about a factor of 1.2 is smaller than between E5 and E6 (factor 1.5). The strong positive spikes seen by the analytical model presented in *Simon et al.* [2011b] inbound and outbound of the Alfvénic fluxtube are only weak in our simulation results (< 5 nT versus > 10 nT). Therefore, these spikes can be regarded an effect of the simplified plume model used by these authors, which concentrates the field-aligned currents on the surface of a cylindrical plume.

Again, the B_y perturbation clearly shows the effect of the electron-absorbing dust on the outcome of the simulation (blue), compared to a scenario without dust (green). Without dust, the sign of the B_y perturbation in our simulation is completely different from the observations, while we achieve very good agreement with the data when dust is included. The base densities of the charged dust particles in the simulations are $\xi n_{D,0} = 5.5 \cdot 10^2$ cm^{-3} for E7 and $\xi n_{D,0} = 5.5 \cdot 10^2$ cm^{-3} for E9. Therefore, our simulations reveal no change in the activity of the dust plume from E7 to E9, in agreement with the small variability in the gaseous part of the plume. The smooth increase to zero in the B_y component for $y < 0$ during E9 is in good agreement with MAG data, while the simulations (blue) show a sharper decrease for $y > 0$ than the data (in particular for E7). We suppose this to be due to the geometry of our dust plume, since in reality most dust particles fall back onto the surface, leading to a wider plume close to the moon [*Kempf et al.* 2010].

Despite the good agreement in B_x and B_y, our simulation is not able to reproduce the observed small pile-up in B_z. In our simulations (blue, green), Cassini only passed at the edge of the field decrease region (positive ΔB_z), without intersecting the region of enhanced $|B_z|$. The stair-case in the observed B_z for E7 is due to a range switch of the instrument. We do not present a best fit simulation with a tilted plume here, since any tilt we tested did not yield a substantial improvement of the fit.

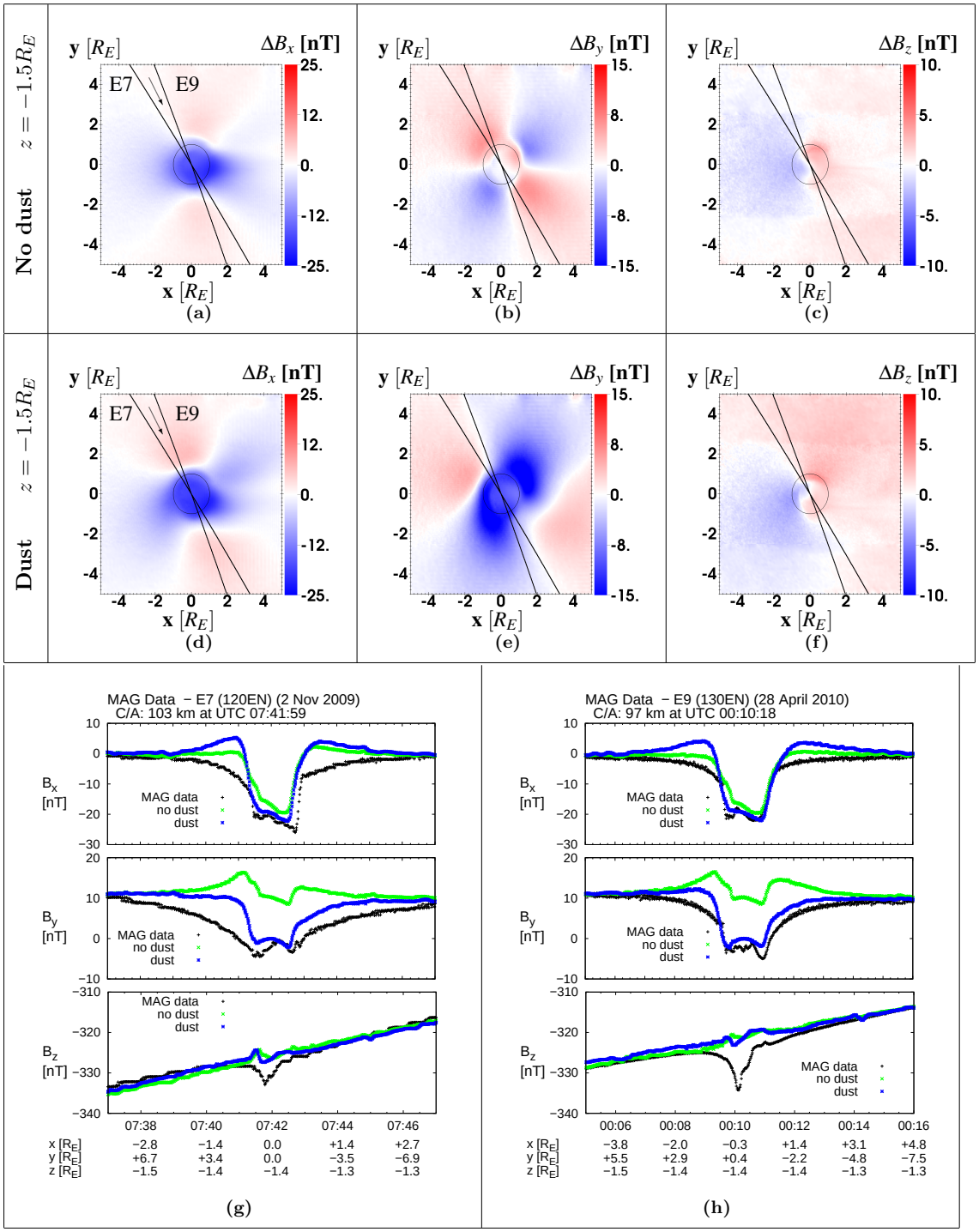

Figure 5.7: Simulated magnetic field components in the ($z = -1.5R_E$) plane together with the projected trajectories of E7 and E9 (plots (a)–(f)). The upper row displays the results without dust, while the lower row shows the counter-clockwise rotation of the magnetic field structures due to the Anti-Hall effect when electron absorption by dust is considered. Plots (g) and (h) show a comparison of simulation results with Cassini MAG data (black) for E7 (left) and E9 (right) for a simulation without (green) and with dust (blue).

5.5.4 Magnetic Field: E8 and E11

The last pair of flybys that we discuss in this paper is E8 and E11. Both occurred far below the moon's orbital plane. So far, E8 and E11 are the only flybys which intersected the southern Alfvén wing. Since the trajectory of E8 was nearly parallel to the equatorial plane at $z = -7.3R_E$, we show our 2D results in that plane in figure 5.8. The black lines indicate the projected trajectories of E8 and E11, the symbols mark the positions of features visible in the data. The magnetic field perturbations in the southern Alfvén wing (ΔB_x and ΔB_y) reveal the same structures as seen in figure 5.7 for the northern Alfvén wing (when including dust), but with opposite signs: ΔB_x is positive inside the fluxtube and negative at the flanks at $y = \pm R_E$. In addition, ΔB_x assumes small positive values in the $(x, y > 0)$ region and decreases with increasing distance to the Alfvén fluxtube. In ΔB_y, the positive perturbation is stretched in y direction. The B_z perturbation in plot 5.8(c) is similar to plot 5.7(f), but the magnitude of ΔB_z at $z = -7.3R_E$ is a little stronger than at $z = -1.5R_E$ (≈ 5 nT compared to ≈ 2 nT). This means that the location of pile-up and field decrease region does not change when moving from $z = -1.5R_E$ (E7, E9) to $z = -7.3R_E$ along the z axis. We do not show 2D results for the simulation without dust, as these plots contain no new information.

The comparison between data and simulations for E8 is shown in figure 5.8(d). Similar to Fig. 5.6 and 5.7, MAG data are colored black and the three simulation setups are as follows: without dust (green), with dust (blue), best fit with dust and a tilted plume (red). The measured B_x component shows a narrow and sharp decrease from −4 nT to −8 nT at about $(0.8, -0.9, -7.3)R_E$ (02:09:32 UTC, diamond in Fig. 5.8(a)), which occurs within 30 km centered around $(x - M_A|z|)^2 + y^2 = R_E^2$, that is around the Enceladus fluxtube. Such a discontinuity-like jump in the magnetic field is likely caused by a very confined or even surface current tangential to the body of Enceladus. This current is supposed to be part of the hemisphere-coupling current system proposed by *Saur et al.* [2007], which arises from the partial blockage of the Alfvénic currents by the body of the moon. As a northward current, it produces auroral hiss observed by the Cassini Radio and Plasma Wave Science (RPWS) instrument [*Gurnett et al.* 2011]. The subsequent increase of the B_x component to a sharply peaked maximum of 15 nT at $(1.1, -0.1, -7.3)R_E$ (rectangle in Fig. 5.8(a)) and the following decrease are associated with nearly field-aligned southward and northward Alfvénic currents. The latter could also in principle contribute to the southward field-aligned electron beams generating auroral hiss. An outbound southward hemisphere coupling current cannot be distinguished from the Alfvénic current in the magnetic field data. It would also be invisible in the hiss observation because of the wrong electron beam direction.

Both, the simulation with (blue) and without dust (green) succeed in reproducing the structure of the perturbation as well as the magnitude of the positive peak, while the magnitude of the negative B_x perturbation in our simulation is stronger than measured. Furthermore, in our simulation the B_x perturbation starts earlier, that is at smaller y than observed by Cassini. This can also been seen in plot 5.8(a), where the diamond is located above the edge of the negative ΔB_x. The measured B_y perturbation during E8 shows a steady increase to a maximum of 29 nT at $(1.4, 0.8, -7.3)R_E$ (02:10:31 UTC, circle in Fig. 5.8(b)), which is interrupted by a small negative dip of 3 nT at $(1.0, -0.2, -7.3)R_E$ (02:09:58 UTC, cross in Fig. 5.8(b)). By comparing with figure 5.8(b), these structures

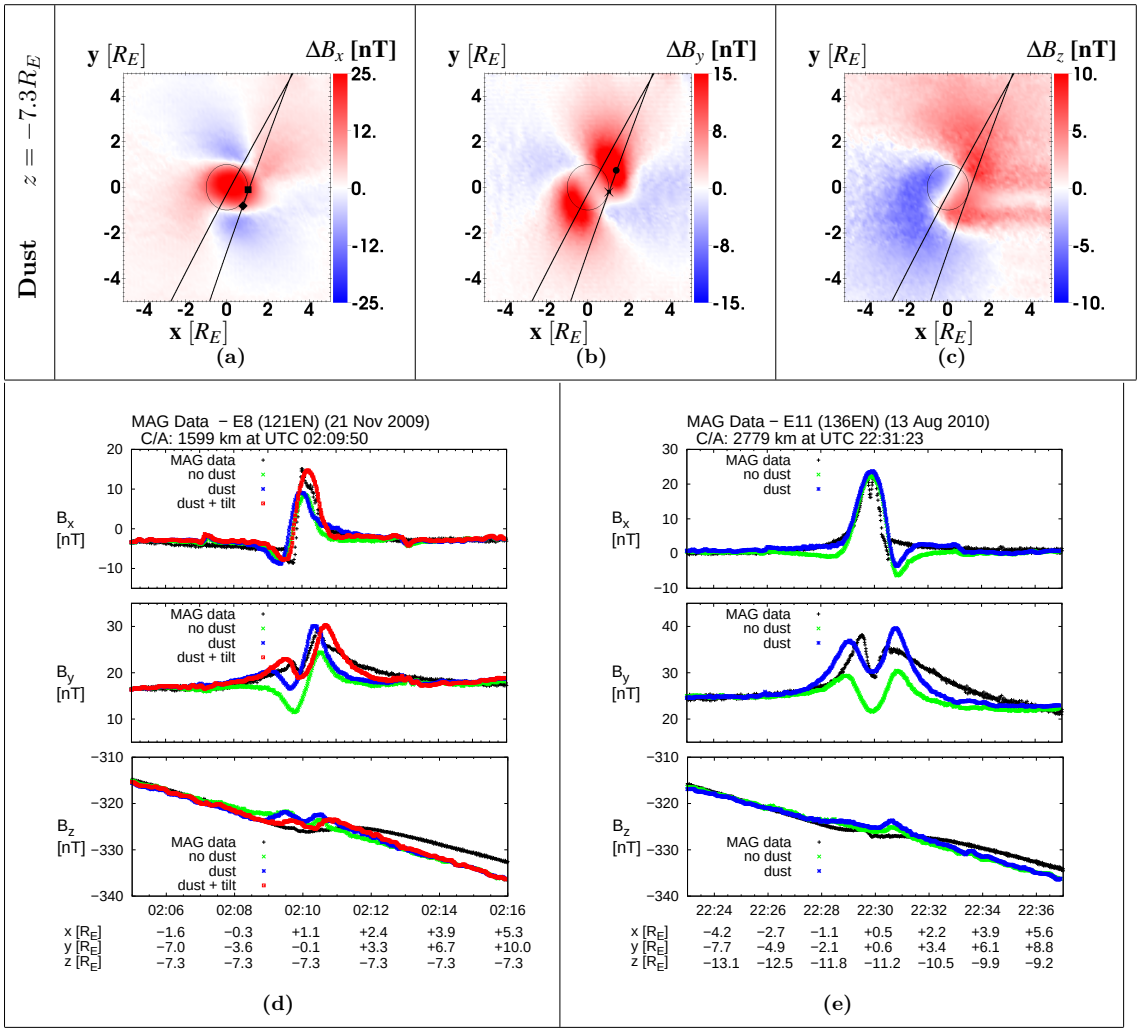

Figure 5.8: Simulated magnetic field components in the ($z = -7.3R_E$)-plane together with the projected trajectories of E8 and E11 (plots (a)–(c)). The symbols mark the positions of features visible in the data. Plots (d) and (e) show a comparison of simulation results with Cassini MAG data (black) for E8 (left) and E11 (right) for a simulation without dust (green), with dust (blue) and the best fit including dust and a tilted plume (red, only E8).

can be explained as follows: inbound, Cassini passed through the outer positive part of the warped quadrupole-like B_y structure, where the perturbation increased as the spacecraft approached the fluxtube. At $(1.0, -0.2, -7.3)R_E$ (cross in in Fig. 5.8(b)), Cassini was located at the edge of the fluxtube where the negative part of the warped quadrupole-structure begins. Thus, B_y decreases, before the spacecraft enters the opposite region of positive B_y. This has already been described in *Simon et al.* [2011b]. These structures are different in our simulation without dust (green), since the direction of rotation as well as the stretching of the quadrupole-like B_y is not seen without dust (see plot 5.7(b)). With dust (blue), our simulation reveals a similar structure as visible in the data. Similar to B_x, the location of the perturbation is slightly displaced.

The simulation with dust and a tilted plume (red) shows that the locations of the features in B_x and B_y match better with the data when the plume is tilted downstream and a little

towards Saturn, i.e. the plume center is located at Lat. $= -80°$ and Lon. $= 67.5°$. The base densities used to reproduce the magnitude of the perturbations measured during E8 are $n_{n,0} = 2 \cdot 10^{10}\text{cm}^{-3}$ and $\xi n_{D,0} = 2.0 \cdot 10^2\ \text{cm}^{-3}$.

For the B_z component, the data show a small decrease of 3 nT around $(1.1, -0.1, -7.3)R_E$ (02:10 UTC), which means that even $1R_E$ downstream, $|\underline{B}|$ is enhanced. This is neither expected nor reproduced by our simulations, since any magnetic pile-up is thought to occur at the upstream side of the plume. As mentioned above, we think that the measured locations of pile-up and field decrease might be reproduced when considering the different reaction rates of the water group ions.

For the E11 encounter, the comparison between data and simulations is shown in figure 5.8(f). MAG data from E11 have already been presented by *Gurnett et al.* [2011] within the context of auroral hiss observations. Since any tilt of the plume yielded no better match with the data, we only show the results for simulations without (green) and with dust (blue). The observed B_x component (black) shows a strong but steady increase with a sharp dip of -7 nT at $(0.4, 0.4, -11.3)R_E$ near the maximum perturbation of 23 nT. In the outbound region at $(1.0, 1.4, -11.3)R_E$ another sharp dip to a minimum value of -1 nT was observed, before B_x returns to its background value. Since the trajectory of E11 is located about $1R_E$ upstream of E8 in the interval considered here, Cassini did not pass through the region of negative ΔB_x inbound, but outbound (see figure 5.8(a)). Similar to the inbound increase during E8, the outbound decrease by 18 nT during E11 is located in a region of 90 km centered around $(x - M_A|z|)^2 + y^2 = R_E^2$. Again we suppose this to be caused by the hemisphere-coupling surface currents. The steep flanks of the major peak in B_x are well reproduced by both simulation setups. However, the sharp dip at the top of the enhancement is not seen in our high-resolution simulations. The outbound dip is reproduced by our simulations, but appears much broader and deeper.

B_y exhibits a similar structure as B_x, but the dip imposed on the maximum perturbation of 15 nT is broadened to an 'M'-like structure and is with -8 nT also deeper than in the data. The outbound dip in B_x is located at the same position as the second maximum (14 nT) of the 'M' in B_y (i.e. $(1.0, 1.4, -11.3)R_E$ at 22:30:30 UTC). Without dust (green), our results reveal a similar 'M'-like pattern, but centered around $\Delta B_y = 0$ nT, whereas the simulation with dust (blue) matches well with the data.

In the B_z component, MAG data show a small bipolar signature of 1 nT magnitude at $(0.3, 0.3, -11.3)R_E$ (22:29:44 UTC), while in our simulations, Cassini passes through a region with reduced magnetic field of 2 nT according to figure 5.8(c).

The base densities used to match the magnitude of the perturbations measured during E11 are $n_{n,0} = 5 \cdot 10^{10}\text{cm}^{-3}$ and $\xi n_{D,0} = 4.0 \cdot 10^2\ \text{cm}^{-3}$. Thus, gas and dust plume seem to have been between a factor of 2 – 3 times more active during E11 than during E8. Similar as for E7 and E9, any tilt of the plume yielded no improvement of the fit.

5.6 Variability of the Plume

Table 5.2 summarizes the parameters used for the best fit simulations presented in the previous sections. We would like to point out that we do not intend to provide *absolute* numbers for the neutral density or amount of dust in reality. That would require a more

Table 5.2: Upstream density n_0 (from RPWS electron densities, cf. table 2.2) and best fit parameters for each flyby. $n_{n,0}$ and $\xi n_{D,0}$ denote the base densities of neutral H_2O molecules and charged dus,t respectively. Some flybys (E5, E6, E8) match better with the data when a tilt of the plume is considered. The plume is then centered at the respective planetographic latitudes (Lat.) and longitudes (Lon.) on Enceladus' surface.

Flyby	Date	n_0 [cm^{-3}]	$n_{n,0}$ [cm^{-3}]	$\xi n_{D,0}$ [cm^{-3}]	Lat. (°)	Lon. (°W)
E5	9 Oct 08	90	$11 \cdot 10^{10}$	$8.5 \cdot 10^2$	−85°	270°
E6	31 Oct 08	45	$7 \cdot 10^{10}$	$5.5 \cdot 10^2$	−85°	90°
E7	2 Nov 09	60	$7 \cdot 10^{10}$	$5.5 \cdot 10^2$	–	–
E8	21 Nov 09	45	$2 \cdot 10^{10}$	$2.0 \cdot 10^2$	−80°	67.5°
E9	28 Apr 09	75	$6 \cdot 10^{10}$	$5.5 \cdot 10^2$	–	–
E11	13 Aug 10	60	$5 \cdot 10^{10}$	$4.0 \cdot 10^2$	–	–

sophisticated model of the plume. Based on our results, we can instead analyze the *relative* variations of the gas production rate between the flybys studied in this paper and use the absolute numbers only as an estimate for the order of magnitude of these quantities.

We find that the variability of the gas production rate lies within a factor of two (with E5 having the strongest and E8 the weakest plume activity). During all analyzed pairs of similar flybys, gas and dust plume have a similar variability: a factor of about 1.5 between E5 and E6 as well as a factor of 2 – 3 for E8 and E11 and an even smaller variation when comparing E7 and E9. Between E5 and E8, the activity even varies by a factor of five. However, the degree to which the results are affected by our model assumptions may differ between flybys of different geometry. Therefore, we only would like to underline the variability between similar flybys by a factor of 2 or less, but not the variability between all flybys.

This variability of the plume intensity is consistent with the different tilts which improved the agreement between MAG data and simulations for some of the flybys (E5, E6, E8). Any tilt of our single-plume model means that different jets or active regions contribute to the plume. If we assume that the jets have a small inclination against the surface normal, our results imply a stronger activity of the 'Damascus' tiger stripe for E5, while during E6 'Alexandria' was more active. For E8, our simulations reveal a tilt direction similar to E6, but even stronger.

We would like to close this section with a cautionary remark: our model includes a high number of parameters ($n_{n,0}, N_D, H_\vartheta, H_d, \vartheta_0, \varphi_0$) which characterize the plume, while our results show that the measured magnetic field signatures are strongly affected by even minor changes in the plume geometry. We therefore cannot rule out the possibility that there are other sets of parameters which also explain the observed magnetic field perturbations or that a multi-plume model is able to match the data for all flybys without using different jets and tilts.

5.7 Anti-Hall Condition at Enceladus

Finally, we would like to analyze in which parts of the plume the Anti-Hall condition (5.6) is fulfilled. For the E9 best fit case, figure 5.9 displays the ratio of the effective collision

frequency and the gyrofrequency $\tilde{\nu}_i/\Omega_i$ (panel (a), see also *Simon et al.* [2013]). Only in a very narrow region around the symmetry axis of the plume (noticeably smaller than the moon's diameter), the effective collision frequency is exceeded by the gyrofrequency. In z direction, this regions extends to about $z = -6R_E$. Plot 5.9(b) shows the ratio of the dust charge density ξn_d and the right hand side of the Anti-Hall condition in the single-ion-species case, i.e. $n_i\,\tilde{\nu}_i^2/(\tilde{\nu}_i^2 + \Omega_i^2)$. Note that values larger than one imply that the Anti-Hall condition is fulfilled, whereas for values smaller one, this is *not* the case. The narrow region with high effective collision frequency is clearly visible as a region with values smaller than one in the plot of the Anti-Hall condition in panel (b). In the outer regions of the plume, the quotient of the Anti-Hall condition assumes values clearly larger than one. Outside the plume, the dust density approaches zero and the values of the quotient again decrease. Therefore, the condition for the occurrence of the Anti-Hall effect (inequality (5.8)) is surprisingly not fulfilled in the center of the plume.

To investigate this finding, we perform a rough estimate of the ratio $\tilde{\nu}_i/\Omega_i$ and the Anti-Hall condition. The ionization frequency is on the order of $\nu_{io} \sim 10^{-8}\,\mathrm{s}^{-1}$, and the reaction rate coefficient is about $k_i \sim 10^{-9}\,\mathrm{cm}^3/\mathrm{s}$. Thus, for an ion density of at least $n_i = 10^2\,\mathrm{cm}^{-3}$, the effective collision frequency (equation (3.46)) is mainly determined by the reactions, i.e.

$$\tilde{\nu}_i = \left(\frac{\nu_{io}}{n_i} + k_i\right) n_n(\underline{x}) \approx k_i n_n(\underline{x}) \quad . \tag{5.27}$$

As can be depicted from figure 5.9, the dependence on the polar angle seems to be more important than the radial decrease. Thus, we consider only the terms from the expression of the plume density (equation (5.24)) which depend on the polar angle ϑ, i.e.

$$n_n(\vartheta) \approx n_{n0} \exp\left[-\left(\frac{\vartheta}{H_\vartheta}\right)^2\right] \quad . \tag{5.28}$$

For $\vartheta \lesssim H_\vartheta$, the exponential function is approximately equal to one and thus, $n(\vartheta) \approx n_{n0} \sim 10^{11}\,\mathrm{cm}^{-3}$ (cf. table 5.2). The effective collision frequency then assumes values of the order of $\tilde{\nu}_i \sim 10^2\,\mathrm{s}^{-1}$. The gyrofrequency is $\Omega_i \sim 1\,\mathrm{s}^{-1}$ (see table 2.4), yielding a ratio $\Omega_i/\tilde{\nu}_i \sim 10^{-2}$. For $\vartheta > H_\vartheta$, the exponential function leads to a rapid decrease of the neutral density and consequently to the decrease of the effective collision frequency, yielding $\Omega_i/\tilde{\nu}_i \gg 1$.

In the same manner we compare the two sides on the Anti-Hall condition (5.6) and obtain

$$\xi n_D \approx \xi n_{D0} > n_i \frac{\tilde{\nu}_i^2}{\tilde{\nu}_i^2 + \Omega_i^2} \rightarrow n_i \approx n_{i0} \tag{5.29}$$

for $\vartheta < H_\vartheta$. Since the ion charge density is always larger than the dust charge density, the Anti-Hall condition is never fulfilled in the case $\tilde{\nu}_i \gg \Omega_i$, corresponding to the region with $|x| \lesssim 0.5R_E$ in figure 5.9(b). This conclusion is also in agreement with the picture sketched in figure 5.2: if $\tilde{\nu}_i \gg \Omega_i$, the ion current density is approximately zero and the small, but non-zero electron current density leads to Hall current in negative x direction, i.e. the 'common' Hall effect without dust. In the opposite case of $\tilde{\nu}_i \ll \Omega_i$, i.e. for $\vartheta > H_\vartheta$, the Anti-Hall condition becomes

$$\xi n_{D0} \exp\left[-\left(\frac{\vartheta}{H_\vartheta}\right)^2\right] > n_{i0} \exp\left[-\left(\frac{\vartheta}{H_\vartheta}\right)^2\right] \frac{\left(k_i n_{n0} \exp\left[-\frac{\vartheta}{H_\vartheta}\right]\right)^2}{\Omega_i^2} \quad . \tag{5.30}$$

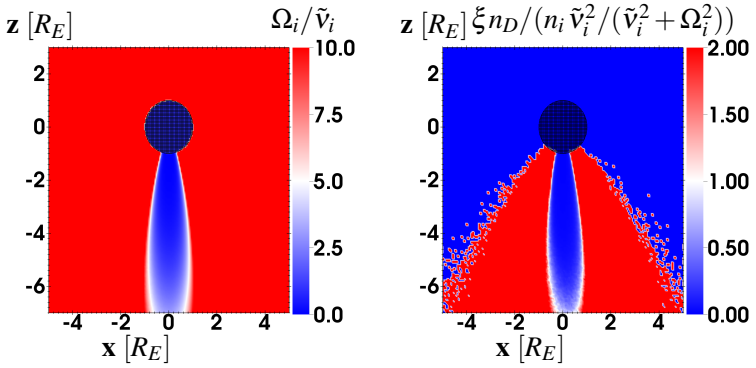

(a) (b)

Figure 5.9: (a) Ratio of effective collision frequency and gyrofrequency (cf. *Simon et al.* [2013]). (b) Anti-Hall condition.

In the above expression it is assumed that to first order, the ion density has a similar shape than the neutral density, since the enhancement of n_i in the plume arises mainly from ionization. Inserting the values yields

$$10^2 \exp\left[-\left(\frac{\vartheta}{15^\circ}\right)^2\right] > 10^4 \left(\exp\left[-\left(\frac{\vartheta}{7.5^\circ}\right)^2\right]\right)^3 \tag{5.31}$$

In particular the larger opening angle of the dust plume therefore allows to fulfill inequality (5.8) in the outer regions of the plume. That is in turn an à posteriori justification of our differences in the models of the neutral gas and the charged dust.

Figure 5.9(b) also shows that the Anti-Hall condition is fulfilled in the outer regions (about $|x| > 0.5R_E$) as long as the dust density is larger than zero. In reality, this would even include the whole E ring. This is a direct consequence of inequality (5.8) for an almost vanishing ion-neutral collision frequency. Yet the Anti-Hall condition for these regions is of no practical significance, since $\tilde{\nu}_i \to 0$ implies negligible or zero Hall current.

Furthermore, it is interesting to note that although the Anti-Hall condition is not fulfilled in the center of the plume, the results presented in the previous sections clearly exhibit a negative ΔB_y for the northern Alfvén wing in these regions. Hence, the negative (positive) B_y perturbations in the northern (southern) Alfvén flux tube within $\sqrt{x^2+y^2} < 0.5R_E$ may be strongly influence by the fields at $\sqrt{x^2+y^2} > 0.5R_E$. Our illustrative interpretation of this finding is that the segments of the magnetic field lines outside this circle are rotatated by the Anti-Hall effect in counterclockwise direction. Thus, if the segment within the circle was not rotated as well, a build-up of magnetic tension would occur within $\sqrt{x^2+y^2} < 0.5R_E$. To reduce the magnetic tension, the field lines within that cylinder are also rotated in counterclockwise direction, even though the Anti-Hall condition is not fulfilled within this region. This in turn shows that the analytical treatment is limited to simplified profiles of the conductivities and emphasizes that numerical simulations are necessary to describe the magnetic field signatures for a realistic plume geometry.

6 Ion Densities and Magnetic Signatures of Dust Pick-up at Enceladus

Wide parts of the following chapter have been submitted for publication before submission of the thesis. The publication is referred to as:
Kriegel, H., S. Simon, P. Meier, U. Motschmann, J. Saur, A. Wennmacher, D. F. Strobel, and M. K. Dougherty, Ion Densities and Magnetic Signatures of Dust Pick-Up at Enceladus, *submitted to Journal of Geophysical Research (Space Physics)*

The main result presented in the previous chapter was the successful reproduction of the field perturbations associated with the Anti-Hall effect, although simplified analytical expressions adopted from the work of *Saur et al.* [2008] for the neutral and dust plumes were applied. The free parameters in these expressions were adjusted to MAG data from selected Enceladus flybys. A major drawback of this method is that the modification of the plume due to the pick-up motion of charged dust grains is not included. Furthermore, only one instrument of Cassini – MAG – has been used to analyze the plasma interaction. Here we present an improved version of the model which includes Monte-Carlo simulations of the neutral gas and dust plumes. The resulting neutral plume is consistent with INMS data and the parameters of the dust plume are chosen in agreement with CDA and CAPS observations. In particular, the model now contains the full dust-plasma coupling in both directions, i. e. the dust is affected by the electromagnetic fields and plasma moments and vice versa. Thus we are now able to address several open questions on Enceladus' plasma interaction:

- *Ion and dust charge densities in the plume*: We combine our plume model with realistic ionization frequencies to impose constraints on the ion and dust charge densities in the plume and compare these expectations against the values directly or indirectly derived from data collected by Cassini's CAPS, RPWS and INMS instruments.

- *Magnetic signatures of dust pick-up*: In the previous chapter, we have shown that the *presence* of negatively charged dust is responsible for the Anti-Hall effect, i. e. the reversal of the (anti-)Saturnward magnetic field component. Here we are going to discuss how the *shape of the dust plume* is responsible for the observed magnetic field signatures and deduce properties of the dust plume.

- *The missing magnetic field decrease*: During E0 – E19, the Cassini magnetometer has observed only the magnetic pile-up region at the ramside of the plume. Despite a good flyby coverage at the moon's wakeside, the corresponding magnetic field decrease has not yet been detected. We demonstrate that the modification of the current systems by the charged dust grains shifted the magnetic field decrease out of Cassini's path during all available Enceladus encounters.

Within this chapter we are going to focus on a few selected flybys which are particularly suitable to deal with the aforementioned issues. These flybys are E3, E5, E7, and the more recent encounters E14, E15, E17, E18 and E19. All flybys not addressed in this or the previous chapter are discussed in appendix B. The reason for our selection of these particular flybys is that for E3 and E5, INMS, CAPS and RPWS data are available, what allows us to constrain the ion densities in the plume [*Morooka et al.* 2011, *Teolis et al.* 2010, *Hill et al.* 2012]. Magnetic field data and simulations for E7 and E9 have already been presented in section 5.5.3. Therefore, E7 provides a reference to illustrate the effect of the improvements included in the model. The magnetic field signatures observed during the encounters E14, E17 and E18 show only minor quantitative differences. For this reason, we decided to discuss E14 and E17 in detail, while magnetic field data from E18 is used only for a brief analysis of plume variability. The comparison of these flybys with E19 is especially important for an understanding of the magnetic field decrease. The distant E15 encounter provides the unique opportunity to analyze the pick-up tail of the plume at large distances to Enceladus. In contrast, the north polar E12 and E13 flybys did not pass through the plume and are therefore discussed only in appendix B. Furthermore, since the trajectory of E16 is very similar to E1 and E10, the magnetic field signatures obtained during this flyby do not contain any new substantial information. Therefore, data and simulations for E16 are shown in appendix B only for completeness.

6.1 Simulation Model

In this chapter a new simulation principle is introduced: we combine the plasma simulation with Monte-Carlo simulations of both, the H_2O and the dust plume. In contrast to our previous study, we do not only consider the influence of electron absorption by dust grains on the electromagnetic fields and plasma flow patterns, but the feedback of the local plasma environment on the motion and charging of the dust. The major challenge of such a model arises from the differences of the involved time scales: on the one hand, the time scale for stationarity of the plasma simulation is roughly defined by the time τ_p that is required by the decelerated plasma flow to travel through the plume in corotation direction, i. e. $\tau_p = 2R_E/1\ \mathrm{km\,s^{-1}} \approx 500\,\mathrm{s}$. On the other hand, the Monte-Carlo simulations achieve stationarity on a time scale τ_{MC} corresponding to the time that the slow neutral molecules or dust grains need to cross the plume in north-south direction, i. e. $\tau_{MC} = 20R_E/0.5\ \mathrm{km\,s^{-1}} \sim 10000\,\mathrm{s}$. With the available computational resources it is not possible to combine both time scales in a single simulation. Instead, we have developed an iterative scheme of *three different types of simulations* which provide the input for each other:

(1) A "downgraded" version of our plasma simulation code is used for a Monte-Carlo

Particle-in-Cell simulation which produces a 3D density and velocity profile of the neutral plume (see section 6.2).

(2) A plasma simulation with A.I.K.E.F. is carried out. Here, the 3D profile of the gas plume obtained by simulation (1) is used as stationary input. In this first step, the dust plume is provided by the model used for the previous simulations (see section 5.4.3).

(3) Subsequently, a Monte-Carlo simulation is carried out for the dust plume (see section 6.3). These simulations, however, require the electromagnetic fields and plasma densities from the hybrid simulations (2) as input to compute the grain dynamics by the Lorentz force and the grain charging according to the plasma densities.

(4) Next, we perform an improved plasma simulation with the gas and dust plumes from steps (1) and (3).

(5) Then an improved simulation of the dust plume with the electromagnetic fields and plasma densities from (4) is made.

(6) A final hybrid simulation with the gas and dust plumes from steps (1) and (5) is carried out.

We find that after steps (5) and (6), the iteration scheme has reached a consistent state, i. e. a third simulation of the dust plume using the results from the hybrid simulation (6) does not lead to noticeable changes of the dust plume.

Apart from the iterative simulation principle, the description of the ion-neutral chemistry within the plasma simulations has been improved and will be discussed in sections 6.1.2 and 6.1.3. The physical and numerical input parameters of the simulations are summarized in the following section.

6.1.1 Simulation Parameters

Although we have used a dipolar background magnetic field in the previous chapter, we decided to use the more simple case of a constant background field $\underline{B}_0 = -B_0\underline{e}_z$ for the simulations presented in this chapter since both approaches do not make any difference for the results. The magnitude of the background field as well as other physical parameters of the upstream plasma are listed in table 6.1. Again, we adjust the upstream density for the simulation of each flyby according to the upstream electron densities derived from RPWS measurements of the upper hybrid frequency, which are listed in table 2.2. In contrast to our previous simulations, we now consider the finding that the speed of the upstream plasma relative to Enceladus is about 80% of the rigid corotation velocity of 26.4 km/s, i. e. $u_0 = 21.1$ km/s [*Wilson et al.* 2009]. From these numbers and for water group ions with an average mass of $m_{W^+} = 17.5$ amu, we derive an Alfvén Mach number between $M_A = 0.08$ and $M_A = 0.13$. Furthermore, we now take into account the temperature anisotropy, i.e. the ratio of the water group ion temperatures perpendicular and parallel to the ambient magnetic field is about $T_{i\perp}/T_{i\parallel} = 5$, see equation (2.4) and *Sittler et al.* [2006].

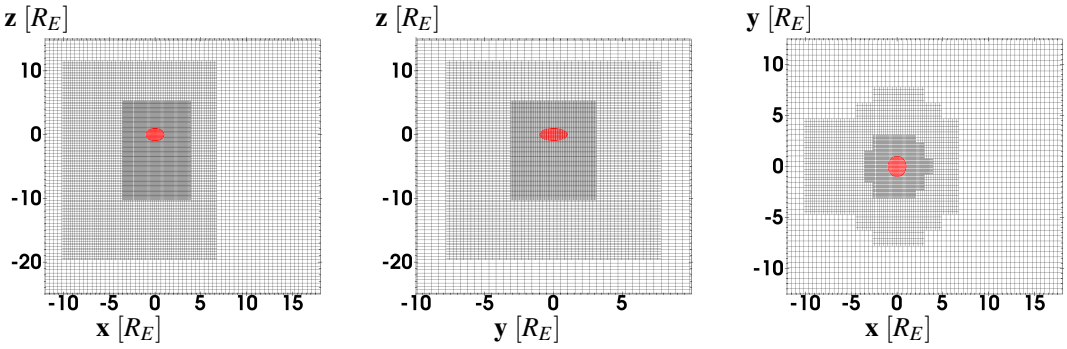

(a) ($y = 0$) (b) ($x = 0$) (c) ($z = 0$)

Figure 6.1: Simulation mesh with three levels of refinement applied for the simulations of Enceladus' plasma interaction in chapter 6.

In agreement with these authors we set $k_B T_{i\parallel} = 7\,\text{eV}$ and $k_B T_{i\perp} = 35\,\text{eV}$. In addition, we found that the contribution of the suprathermal electron population [*Schippers et al.* 2009, *Gustafsson and Wahlund* 2010] to the electron pressure can be neglected. Therefore, our electron fluid consists only of a cold Maxwellian population with a temperature $k_B T_{ec} = 1.35\,\text{eV}$. However, the suprathermal population is important for ionizing the neutrals, as will be discussed in section 6.1.3.

Compared with the simulations presented in the previous chapter, our simulation box is slightly enlarged and has now a size of $L_X \times L_Y \times L_Z = 30R_E \times 25R_E \times 100R_E$ (see also table 6.1 for a summary of the most important numerical parameters). Again, Enceladus is not placed at the center of the box, but offset by 4/7 of the box's height from the bottom of the box. A hierarchical mesh (L_0, L_1, L_2) that is adaptive in space but static in time is used. At the coarsest level (L_0), the resolution is $\Delta_{L_0} = 53\,\text{km} = 0.21R_E$, while $\Delta_{L_2} = \frac{1}{4}\Delta_{L_0} = 13\,\text{km} = 0.05R_E$ is achieved at the highest level. The spatial extension of the refinement levels is illustrated by the plots of our mesh in figure 6.1. In each cell, the ions are represented by about 100 macroparticles, yielding a total of more than one billion macroparticles in the plasma simulation. With a time step of 0.015 inverse gyro frequencies (Ω_0^{-1}), the ion density becomes stationary after about 40000 time steps, i. e. after 600 Ω_0^{-1} or about 330 s. Thus, we increased the simulation time by a factor of four to make sure that the ion density (which we will discuss in detail in section 6.4.2) becomes stationary. A smoothing with a strength of 6% is applied to the electromagnetic fields (see section 4.4).

The Monte-Carlo simulations allow for a larger time step than the plasma simulations since the stability of these simulations is not defined by the stability of the field solvers, but only by the Courant-Friedrichs-Lewy criterion which states that a numerical particle is not allowed to cross one cell within one time step. Therefore, a time step of 0.2 Ω_0^{-1} is used for those simulations requiring 100000 time steps or about 11000 s to achieve stationarity of the neutral and dust densities.

Table 6.1: Main physical and numerical parameters of the simulations. [1]Upstream density adjusted for each flyby according to values listed in table 2.2.

Parameter	Symbol and Value
Plasma velocity	$u_0 = 21.1\,\mathrm{km/s}$
Plasma number density	$n_0 = 45 - 110\,\mathrm{cm}^{-3}$ [1]
Magnetic field	$\underline{B}_0 = (0, 0, -325)\,\mathrm{nT}$
Species included	H^+,O^+, OH^+, H_2O^+, H_3O^+
Ion mass	$m_i = 15.85\,\mathrm{amu}$
Alfvénic Mach number	$M_A = 0.08 - 0.12$
Perpendicular ion temperature	$k_B T_{i\perp} = 35\,\mathrm{eV}$
Parallel ion temperature	$k_B T_{i\parallel} = 7\,\mathrm{eV}$
Electron temperature	$k_B T_{ec} = 1.35\,\mathrm{eV}$
Box (x)	$-12R_E \leq x \leq +18R_E$
Box (y)	$-12.5R_E \leq y \leq +12.5R_E$
Box (z)	$-55R_E \leq z \leq +45R_E$
Mesh spacing L_2	$\Delta_{L_2} = \frac{1}{4}\Delta_{L_0} = 13\,\mathrm{km} = 0.05R_E$
Time step	$\Delta t = 0.015\Omega_i^{-1} = 8.4 \cdot 10^{-3}\,\mathrm{s}$
Simulation time	$40000\Delta t = 600\Omega_i^{-1} = 335\,\mathrm{s}$
Smoothing	$\eta_{sm} = 6\%$
Conductivity of interior	$\sigma = 7 \cdot 10^{-7}\,\mathrm{S/m}$
Macroparticle per Cell	100
Time step (Monte-Carlo simulation)	$\Delta t_{MC} = 0.2\Omega_0^{-1}$
Monte-Carlo simulation time	$100000\ \Delta t_{MC} = 11000\,\mathrm{s}$

6.1.2 Ion-Neutral Chemistry

In contrast to the previous simulations, where a single ion species of mass $m_{W^+} = 17.5$ amu was applied, protons (H^+) and the four water group ion species (O^+, OH^+, H_2O^+, H_3O^+) are now considered separately. In agreement with CAPS observations by *Tokar et al.* [2006], we assume that upstream of Enceladus, the protons contribute 10% to the total ion number density, while the four water group ion species have equal abundances of 22.5%. Since the reaction between an ion of species j_1 and a neutral molecule of the plume produces a new ion of species j_2, the ion abundances within the plume are substantially different when compared to the upstream situation. As a result, the exact values of the upstream abundances have only a minor impact on the ion composition within the plume (see section 6.4.2).

Each of the possible reactions has a different, velocity-dependent reaction rate $k_{j_1 j_2}(v_{rel})$, yielding a complex chemical network within the plume which becomes even more complex due to photoionization and electron impact ionization of the neutrals (see e.g., *Fleshman et al.* [2010a]). Here, v_{rel} denotes the relative velocity between the ion and the neutral. However, for a study of the plasma interaction, we found that it is not necessary to include the most detailed model of the chemical processes in Enceladus' plume. Instead, the neutral plume is assumed to consist purely of H_2O, because the other neutral species possess

Table 6.2: Ion-neutral reactions considered in the model. Upstream of Enceladus, H^+ has an abundance of 10% while the four water group ion species have equal abundances of 22.5%. The expressions for the reaction rate $k_{j_1 j_2}(v_{rel})$ at arbitrary relative velocity v_{rel} are discussed in appendix A. Here, the rates at the upstream speed u_0 are listed for reference.

upstr.	j_1						j_2	$k_{j_1 j_2}(u_0)$ [cm^3/s]
10%	H^+	+	H_2O	→	H	+	H_2O^+	$6.67 \cdot 10^{-9}$
22.5%	O^+	+	H_2O	→	O	+	H_2O^+	$1.33 \cdot 10^{-8}$
22.5%	OH^+	+	H_2O	→	OH	+	H_2O^+	$1.25 \cdot 10^{-8}$
	OH^+	+	H_2O	→	O	+	H_3O^+	$0.82 \cdot 10^{-9}$
22.5%	H_2O^+	+	H_2O	→	H_2O	+	H_2O^+	$1.61 \cdot 10^{-9}$
	H_2O^+	+	H_2O	→	OH	+	H_3O^+	$1.05 \cdot 10^{-9}$
22.5%	H_3O^+	+	H_2O	→	H_2O	+	H_3O^+	$1.02 \cdot 10^{-9}$

a cumulated abundance of less than 10% [*Waite et al.* 2009]. Thus, only the reactions of protons and the four water group ion species with water are included (see table 6.2). The full expressions for the velocity-dependent rates $k_{j_1 j_2}(v_{rel})$ used in our model are provided in appendix A. In table 6.2 only the rates $k_{j_1 j_2}(u_0)$ at the upstream speed u_0 are listed for reference. For the two reactions producing H_3O^+ and the elastic collisions of H_3O^+, the reaction rates are constant, $k_{j,H_3O^+}(u_0) = k_{j,H_3O^+}$.

6.1.3 Photo- and Electron Impact Ionization

Again, we also include photoionization and electron impact ionization. The Enceladus flybys E0 – E13 took place during a time of low solar activity, while the more recent ones occurred around solar maximum. Thus, we approximate the ionization frequency by using $\nu_{ph} = \nu_{ph,min} = 4.4 \cdot 10^{-9}\,\mathrm{s}^{-1}$ for encounters E0 – E13, corresponding to solar minimum conditions. For E14 – E16, however, we apply $\nu_{ph} = 0$, since these flybys occurred in Saturn's geometric shadow. The photoionization rates for E17 – E19 are adjusted to solar maximum conditions, i.e. $\nu_{ph} = \nu_{ph,max} = 1.1 \cdot 10^{-8}\,\mathrm{s}^{-1}$. Note that this simple description of the photoionization does not take into account the response time of the ion densities in the plume to the change of the ionization frequency, i. e. whether Enceladus was long enough within Saturn's shadow that the ions generated due to preceding photoionization were no longer present in the plume. However, it should be pointed out that the photoionization rate is exceeded by ν^* and in consequence, considering the shadow has negligible impact on the results. The relative photoionization rates of H_2O for the different ions which can be produced are listed in table 6.3. We neglect the low opacity of the plume, since for the line-of-sight of the 2010 solar occultation, UVIS measured a decrease in the solar flux intensity that corresponds to an optical thickness of only approximately 0.2 [*Hansen et al.* 2011].

The electron impact ionization rate ν_e is highly sensitive to the local electron energy distribution, because the ionization potential of H_2O is about 13 eV. Thus, only the dilute high energy tail of the cold Maxwellian electrons ($k_B T_{ec} = 1.35\,\mathrm{eV}$, cf. section 5.4.1) can

contribute to the ionization while the major ionizing component is the suprathermal population with electron energies of 10 – 70 eV. Recently, *Ozak et al.* [2012] applied a two-stream electron transport model to the suprathermal electrons within the plume in agreement with data obtained by the Electron Spectrometer (ELS) of CAPS. These authors concluded that the total ionization rate by electrons is in the range of $\nu_{e,min} = (1.2-2)\cdot 10^{-9}\,\mathrm{s}^{-1}$ for solar minimum conditions. The interval of the $\nu_{e,min}$ values results from the opacity of the plume with respect to the ionizing electrons. As the opacity is again rather low, we simply use an average value of $\nu_{e,min} = 1.5 \cdot 10^{-9}\,\mathrm{s}^{-1}$. Since the suprathermal electrons are mainly generated by photoionization of neutrals [*Schippers et al.* 2009], we increase the rate by the same factor of 2.5 as the photoionization rate for solar maximum yielding $\nu_{e,max} = 3.75 \cdot 10^{-9}\,\mathrm{s}^{-1}$. As these electrons are not necessarily produced at Enceladus, but somewhere around its orbit, Saturn's shadow is not considered for the electron ionization. The electron impact rates for the different ion species are obtained by using the same fraction of the total rate as for the photoionization (see table 6.3). This is also in agreement with electron impact ionization cross sections from *Itikawa and Mason* [2005]. Note that we do not include a modification of the electron impact rate due to electron absorption by dust. This would require a model of the electron energy distribution that considers cooling or heating of the electrons by the dust as well as the energy dependence of the electron absorption.

Since the model of *Ozak et al.* [2012] underestimates the electron fluxes at energies between 100 eV and 1000 eV compared to CAPS measurements (see figures 11 and 12 in that work), it shall be analyzed if this regime contributes significantly to the electron impact ionization. The ionization frequency can be calculated as (cf. eq. (4) of *Burger et al.* [2007])

$$\nu_e = n_e \int \sigma(v) f(v) v \mathrm{d}v \quad , \tag{6.1}$$

where $\sigma(v)$ is the velocity-dependent ionization cross section and $f(v)$ the velocity distribution of the electrons with $< v >= \int f(v) v \mathrm{d}v$. We are interested in a rough estimate of the upper limit of ν_e, considering contributions by electrons with energies only between 100 eV and 1000 eV. Furthermore, we assume that the electron flux F_e is isotropic and of the order of $F_e = 10^2\,\mathrm{cm}^{-2}\mathrm{s}^{-1}\mathrm{eV}^{-1}\mathrm{sr}^{-1}$ within this energy interval in agreement with the CAPS observations presented by *Ozak et al.* [2012]. The flux can then be converted into an electron density according to

$$n_e \int f(v) v \mathrm{d}v = F_e 4\pi \Delta E \quad . \tag{6.2}$$

For this energy interval, the electron impact cross section is nearly constant, $\sigma(v) \sim 10^{-16}\,\mathrm{cm}^{-2}$ [*Itikawa and Mason* 2005]. Inserting equation (6.2) in (6.1) yields the ionization rate in the interval between 100 eV and 1000 eV,

$$\nu_e = 4\pi F_e \Delta E \sigma(v) \sim 1 \cdot 10^{-10}\,\mathrm{s}^{-1} \quad . \tag{6.3}$$

Thus, the electron impact ionization by electrons with energies larger than 100 eV yields an ionization frequency that is about one order of magnitude lower than the ionization frequency of the suprathermal electron population.

In addition to the ion species included in the model, data obtained by INMS and CAPS suggest the presence of heavier water cluster ions (H_2O^+-H_2O or H_3O^+-H_2O), with count

Table 6.3: Overview of the different reactions for the ionization of water by photoionization ($h\nu$) and electron impacts (curly brackets), leading to production of protons and water group ions. The ionization rate $\nu_{io} = \nu_{ph,min} + \nu_{e,min} + \nu^*$ is applied for flybys E0 – E13 (solar minimum conditions). For flybys E17 – E19, we set $\nu_{io} = \nu_{ph,max} + \nu_{e,max} + \nu^*$ according to solar maximum conditions. Please note that E14 – E16 took place in Saturn's geometric shadow and therefore, ν_{ph} is set to zero for these flybys, i. e. $\nu_{io} = \nu_{e,max} + \nu^*$. The values for the frequencies are $\nu_{ph,min} = 4.4 \cdot 10^{-9}\,\mathrm{s}^{-1}$, $\nu_{ph,max} = 1.1 \cdot 10^{-8}\,\mathrm{s}^{-1}$, $\nu_{e,min} = 1.5 \cdot 10^{-9}\,\mathrm{s}^{-1}$ and $\nu_{e,max} = 3.75 \cdot 10^{-9}\,\mathrm{s}^{-1}$, see *Burger et al.* [2007] and *Itikawa and Mason* [2005]. Furthermore, the additional contribution ν^* is required to obtain ion densities which are consistent with Cassini observations (see section 6.4.2).

$h\nu\ \{e\}$	+	H_2O	$\rightarrow$	H^+	+	OH	+	$\{2e\}e$	$0.03 \cdot \nu_{io}$
$h\nu\ \{e\}$	+	H_2O	$\rightarrow$	O^+	+	H_2	+	$\{2e\}e$	$0.01 \cdot \nu_{io}$
$h\nu\ \{e\}$	+	H_2O	$\rightarrow$	OH^+	+	H	+	$\{2e\}e$	$0.82 \cdot \nu_{io}$
$h\nu\ \{e\}$	+	H_2O	$\rightarrow$	H_2O^+	+	$\{2e\}e$			$0.14 \cdot \nu_{io}$

rates almost comparable to those of H_3O^+ [*Cravens et al.* 2009, *Tokar et al.* 2009]. However, these water cluster ions are neither produced by ion-neutral reactions with H_2O nor by ionization of H_2O (see *Fleshman et al.* [2010a]). Therefore mechanisms leading to the formation of these ions are not yet clear. Despite being produced, the water cluster ions are not detected downstream of Enceladus and also require an unknown process leading to their conversion into other ion or neutral species. Thus, water cluster ions are not considered in our model.

As will be discussed in sections 6.4.2 and 6.5, various Cassini observations require an effective ionization frequency of at least $\nu^* = 3 \cdot 10^{-8}\ \mathrm{s}^{-1}$ which is even larger than the sum of the photoionization rate and the electron impact rate derived by *Ozak et al.* [2012]. Note that the electron impact rate is proportional to the electron density, and therefore an increase in the density also leads to a higher ionization frequency. Although this aspect is in principle considered by the model of *Ozak et al.* [2012], it was originally not designed to derive ionization frequencies and might underestimate the total electron impact rate. In addition, *Coates et al.* [2013] reported on the detection of a population of plume photoelectrons, i. e. photoelectrons directly produced within plume. These electrons lead to an increase of the electron fluxes around energies of 20 eV by about a factor of two, thereby also enhancing the ionization. Hence, ν^* may also (partially) include an increased electron impact ionization. However, we have to choose ν^* a factor of 20 larger than $\nu_{e,min}$, which may point to an alternative ion source. This ion source may account for the contribution of the aforementioned water cluster ions to the total ion density or may also include modifications of the ion density by dusty plasma effects (see section 6.4.3).

6.2 Modeling of Neutral Plume

In this section, we discuss the Monte-Carlo simulations of the neutral plume which generate the neutral density and velocity profiles for the plasma simulations. In these simulations, we simultaneously calculate the dynamics of millions of water molecules until a

stationary density and velocity profile is achieved.

Similar – and in parts more detailed – Monte-Carlo simulation models of the neutral plume have already been presented by a number of authors: *Tian et al.* [2007] developed a first model to analyze UVIS observations from the E2 flyby. These authors suggest a surface velocity of the ejected gas molecules of 300 – 500 m/s and a total escape rate of about $5 \cdot 10^{27}$ H_2O/s. *Burger et al.* [2007] applied a simulation model to UVIS and INMS observations from E2 which also considered dissociation and ionization by solar UV radiation. They obtained a plume source rate of $\sim 10^{28}$ H_2O/s or 300 kg/s. *Smith et al.* [2010] used a 3D Monte-Carlo multi-species neutral particle model to determine the source rate and ejection velocity of the jets from INMS data of the E2, E3, and E5 encounters. With that model, they also derived the large-scale neutral density distribution in Saturn's magnetosphere by including accurate lifetimes for the different neutral species. They found a variability of the plume source rate by a factor of four, ranging between $6 \cdot 10^{27}$ H_2O/s for E3 and $2.5 \cdot 10^{28}$ H_2O/s for E5. With focus on the initial parameters of the different jets, *Tenishev et al.* [2010] modeled E3 and E5 INMS and E2 UVIS observations. In addition to these numerical studies, analytical approximations of the neutral density profile of the plume have been presented by *Saur et al.* [2008] and *Dong et al.* [2011]. The expression given by *Saur et al.* [2008] combines the geometrical density decrease of a radially expanding atmosphere with an exponential factor for the angular width of the plume which has been adjusted to match MAG data from E0, E1 and E2. This model has also been applied in our previous simulations, cf. equation (5.24). *Dong et al.* [2011] presented an analytical neutral density distribution based on a radially flowing Maxwellian velocity distribution to explain INMS data from E2, E3, E5 and E7. Compared to the aforementioned studies, these authors obtain a higher surface velocity of 550 – 750 m/s and a total source rate of about $(1.5 - 3.5) \cdot 10^{28}$ H_2O/s.

We would like to point out that our plume model does not aim to be more sophisticated than any of the studies discussed above. Our major purpose is to develop a 3D density and velocity profile of the plume in good agreement with available INMS data, which can be used as stationary input for the plasma simulations.

Our approach works as follows: a certain number of particles, which represent a certain production rate Q_0, is inserted into the simulation during each time interval. The particles then move under the influence of the gravitational forces of Saturn and Enceladus. As our frame of reference (ENIS) rotates synchronously with Enceladus, we also consider centrifugal and Coriolis forces. The equation of motion for the neutral particles then reads

$$\begin{pmatrix} \ddot{x} \\ \ddot{y} \\ \ddot{z} \end{pmatrix} = -\gamma \frac{M_E}{|\underline{r}|^3} \begin{pmatrix} x \\ y \\ z \end{pmatrix} - \gamma \frac{M_S}{|\underline{r} - \underline{r}_S|^3} \begin{pmatrix} x \\ y - y_S \\ z \end{pmatrix} + \omega_z^2 \left|\underline{r}_{SE}\right| \begin{pmatrix} 0 \\ -1 \\ 0 \end{pmatrix} + \omega_z^2 \begin{pmatrix} x \\ y \\ 0 \end{pmatrix} - 2\omega_z \begin{pmatrix} -v_y \\ v_x \\ 0 \end{pmatrix} \quad . \tag{6.4}$$

In this equation γ denotes the gravitational constant, M_E and M_S are the masses of Enceladus and Saturn, respectively, $\underline{r}_S = (x_S, y_S, z_S)$ is the distance to Saturn's center, $\underline{r}_{SE}$ is the distance between Enceladus and Saturn and ω_z is Enceladus' rotation rate. This equation

is solved by using a fourth-order Runge-Kutta scheme. The implementation and accuracy tests have been carried out in the work of *Harms* [2010].

After the simulation has reached a stationary state (after ≈ 3h), density and bulk velocity are stored on a 3D mesh with a cell size of $\Delta g = 13$ km. The contribution of each particle to the density and velocity at a certain mesh node is calculated by the same Cloud-in-Cell scheme that is applied in the A.I.K.E.F. code [*Müller et al.* 2011]. Although our simulation grid may not resolve the distance between the sources of the particles at Enceladus' surface, the positions of the particles are not affected since we use a Particle-in-Cell code. Only the stationary density and velocity profiles are "washed out" by our finite mesh resolution. Since our modeled neutral density $n_{H_2O}(\underline{x})$ at a certain position $\underline{x}$ is proportional to the production rate Q, we carry out the simulations with an initial production rate Q_0 and then determine Q by a least mean squares fit of our modeled densities to the densities measured by INMS.

In our model, the initial locations and velocities of the particles at the surface of Enceladus are defined by the locations and directions of the eight dust jets observed in ISS images [*Spitale and Porco* 2007]. As derived from the UVIS observation of a stellar occultation in 2007, these dust jets are very likely associated with water vapor jets [*Hansen et al.* 2008]. More recently, *Hansen et al.* [2011] modeled high resolution UVIS data obtained during the 2010 solar occultation. These authors conclude that gas is ejected along the whole length of the tiger stripes, making up a broad diffuse plume. However, the jets observed by *Spitale and Porco* [2007] are still clearly visible in the data, having a $2-5$ times higher density than the diffuse part. This finding is also in agreement with CDA data [*Postberg et al.* 2011]. Therefore, we also consider 80 point sources distributed uniformly along the tiger stripes (see figure S2 by *Postberg et al.* [2011]). Each particle's starting velocity is given by the superposition of the bulk velocity u_{gas} and a random velocity component v_{th} according to a Maxwellian distribution with a temperature of $T_{H_2O} = 180$ K. This temperature is in agreement with Cassini infrared images of the south polar region [*Spencer et al.* 2006] and corresponds to a thermal velocity of $u_{th} = \sqrt{(8k_B T_{H_2O})/(\pi m_{H_2O})} = 460\,\mathrm{m/s}$. The sonic speed c_s is given by $c_s = \sqrt{(\kappa k_B T_{H_2O})/(m_{H_2O})} = 330\,\mathrm{m/s}$, where $\kappa = 4/3$ is assumed for the water molecules. The sonic Mach number M_s is then defined as the ratio of bulk velocity and sonic speed: $M_s = u_{gas}/c_s$. A high Mach number therefore corresponds to a narrow beam while lower Mach numbers yield a distribution with a larger opening angle. UVIS observations and modeling of INMS data suggest a Mach number of about $M_s = 2$ for the diffuse plume [*Hansen et al.* 2008, *Dong et al.* 2011], while the jets may have a higher Mach number in the range of $M_s = 5-8$ [*Hansen et al.* 2011]. In agreement with these findings, we set the sonic Mach number of the diffuse plume (along the tiger stripes) to $M_{s,d} = 2$ and the sonic Mach number of the eight jets to $M_{s,j} = 6$. The remaining free parameters of the model are the total production rate Q and the strength of the jets relative to each other and relative to the diffuse tiger stripe sources.

Since our eventual goal is a study of Enceladus' plasma interaction, it is beyond the scope of this paper to test a huge number of combinations of the jet strengths. Instead, we choose three representative setups and determine the total production rate Q by fitting our results to the INMS data: plume #1 includes all eight jet locations suggested by *Spitale and Porco* [2007] as well as the diffuse sources (abbreviation for plume #1: I–VIII, d). The

production rate of the jets is set ten times higher than for the diffuse sources. Following the work of *Dong et al.* [2011] and *Tenishev et al.* [2010], plume #2 includes only the jets I, II, III and VI from *Spitale and Porco* [2007] with a Mach number of $M_{s,j} = 2$ (#2 = I, II, III, VI). As will be shown below, this setup yields the best fit to the E3 and E5 data. Plume #3 is designed to give the best fit to the E7 data. It considers jets I, II, III, IV, V and the additional source IV' described by *Dong et al.* [2011] with $M_{s,j} = 6$ and the diffuse sources (#3 = I, II, III, IV, IV', VI, d). Again the jets possess a ten times higher source rate than the diffuse sources.

Our results for the density and velocity of plume #1 are displayed for the planes $y = 0$, $x = 0$ and $z = -1.5R_E$ in the first two rows of figure 6.2. The density contours in panels (a) and (b) show the familiar shape of the plume for a production rate of $Q = 1 \cdot 10^{28}\,\mathrm{H_2O/s}$. The density assumes values up to $10^9\,\mathrm{cm^{-3}}$ close to the south pole and decreases to values below $10^6\,\mathrm{cm^{-3}}$ roughly at $\sqrt{x^2 + y^2} < 5R_E$ and $z < -15R_E$. The small density enhancement at the north pole is formed by a small fraction of particles with velocities very close to the three-body escape speed (see *Kempf et al.* [2010]). This feature was also present in the simulations by *Tenishev et al.* [2010]. The weak asymmetry of the density in y direction (cf. panels (b) and (c)) results from the influence of the centrifugal and Coriolis forces and the slightly asymmetric source regions. The bulk velocity components u_x, u_y and u_z are shown in plots (d) – (f). In the central cone (around the z axis), the bulk velocity assumes values of $u_x \approx u_y \approx 0$ and $u_z \approx -1000\,\mathrm{m/s}$. Outside the cone, the molecules spread in $\pm x$ and $\pm y$ direction with a velocity of about $|u_x| \approx |u_y| \approx 400\,\mathrm{m/s}$.

Plots (g), (h) and (i) of figure 6.2 display our results for the E3, E5 and E7 encounters in a logarithmic scale. For better visualization, model and INMS data around closest approach of E7 are also plotted in a linear scale in panel (j). The projections of the E3 and E5 trajectories onto the $y = 0$ plane and the E7 trajectory onto the $z = -1.5R_E$ plane are shown in the density plots 6.2(a) and 6.2(c), respectively. For E3 and E5, all three setups are in good agreement with the width of the observed peak. However, in agreement with the analytical model of *Dong et al.* [2011] we find that considering only the jets I, II, III and VI with $M_{s,j} = 2$ (plume #2) yields a slightly better fit to the data in the outbound region. In contrast to that, plumes #1 and #3 agree better with INMS densities for E7. In the linear plot, one can see that the location and steepness of the density increase in the inbound region is in excellent agreement with the measured values when considering the high Mach number jet sources. The magnitude of the second peak is not reached by plume #1, but well reproduced by plume #3 where especially jet IV' contributes to the second peak. The profile of plume #2 can neither explain the formation of two separate peaks along the E7 trajectory, nor does it reproduce the observed narrow width of the first peak. The strong fluctuations of our modeled density profiles in the inbound regions of E3 and E5 arise from the low number of particles reaching these regions.

Our results for the production rate Q obtained by the least mean squares fit and the associated minimum χ^2 values are listed in table 6.4. The χ^2 values are defined by $\chi^2 = \mathrm{Min}\{\sum_i (n^{INMS}_{\mathrm{H_2O}}[i] - Q/Q_0\, n^{Q_0}_{\mathrm{H_2O}}[i])^2 / (\sum_i n^{INMS}_{\mathrm{H_2O}}[i])\}$ where the sum is taken over all data points $n^{INMS}_{\mathrm{H_2O}}[i]$, and $Q_0 = 1 \cdot 10^{28}\,\mathrm{H_2O/s}$ denotes the original production rate of the simulation. For E7, however, we found that the fit underestimates the peak density due to the local minimum around closest approach. We therefore decided to adjust the

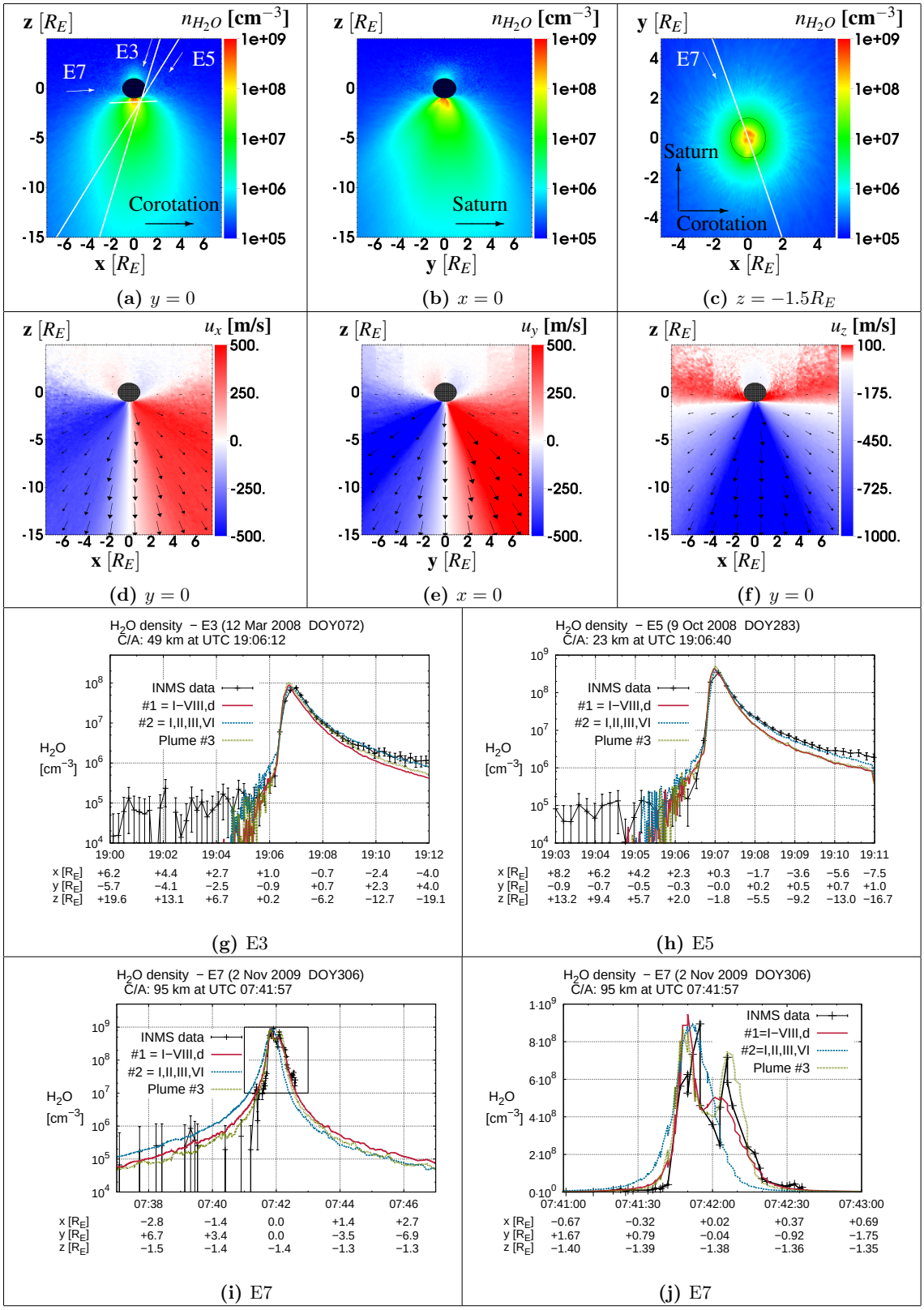

Figure 6.2: Results of the Monte-Carlo simulations of the neutral plume. The color plots (a) – (f) display the density and velocity components of plume #1 (see text for further description of the plume parameters). A comparison between INMS data and plume setups #1, #2 and #3 for E3, E5 and E7 is provided in panels (g) – (i) in a semi-logarithmic scale. The neutral density around closest approach of E7 is also shown on a linear scale in plot (j).

Table 6.4: Production rates of H_2O molecules obtained by least mean squares fits of our modeled densities to the densities measured by INMS. The corresponding χ^2 values are given in brackets. For E7, we find that a manual fit reproduces the peak densities better than the least mean squares method. The three plume setups are described by their active sources, i. e. the jets from *Spitale and Porco* [2007] (roman numbers) and diffuse sources along the tiger stripes (d).

	Q [$10^{28}$$H_2O$/s] ($\chi^2$)		
Plume	E3	E5	E7
#1 = I - VIII + d	1.6 (0.13)	4.3 (0.03)	2.4 (-)
#2 = I,II,III,VI	1.3 (0.03)	4.1 (0.04)	1.2 (-)
#3 = I,II,III,IV,IV',VI+d	1.8 (0.16)	4.9 (0.07)	1.9 (-)

production rate manually to the peak density, as it was also done by *Dong et al.* [2011]. For all three plumes, the production rate for E5 is at least two times larger than for E3. All rates for plumes #1 and #3 exceed those for plume #2. The reason is that plume #2 includes only jets with a Mach number of $M_{s,j} = 2$, while the two other setups have a significant contribution of jets with a Mach number of $M_{s,j} = 6$. According to the continuity equation, faster particles require a higher production rate to yield the same density as slower ones. The derived rates are in good agreement with recent modeling by *Dong et al.* [2011], who suggest rates of $Q = 1.7 \cdot 10^{28}$ H_2O/s for E3 and E7 and $Q = 3.5 \cdot 10^{28}$ H_2O/s for E5.

In principle, each of the nine combinations of plume geometry and production rate could be regarded a reasonable input for the plasma simulations. In section 6.5.1, we will present a comparison between the magnetic field signatures obtained with the three plumes. However, it is not feasible to simulate each combination of plasma and dust parameters with each neutral plume setup. Instead, we pick one setup for all further plasma simulations presented in this work. Plume #3 reproduces the double-peak structure of E7 best and should therefore also be used for a comparison with MAG data from E7. Therefore, using plume #3 with a production rate of $Q = 4.9 \cdot 10^{28}$ H_2O/s is the natural choice for a study of the plasma interaction. We also find that this high production rate yields better agreement with CAPS and MAG data than the lower production rates. We will discuss our simulated ion densities for E5 in section 6.4.2.

We would like to note that once a particle has left the simulation box, it is no longer considered for the density computation (even if the particle would re-enter the domain at a later time). To ensure that these particles do not noticeably modify the total density, we carried out a simulation with a considerably larger box, i. e. $L_x \times L_y \times L_z = 60R_E \times 60R_E \times 210R_E$. In figure 6.3, the results are compared with those of the smaller box. Plot (a) shows INMS data (black), simulation results for the smaller box (red) and results for the larger box (blue) in a short interval around the closest approach of E5 on a linear scale. Plot (b) compares the two simulations along three lines parallel to the x axis, but at different altitudes of $z = -2R_E$, $z = -6R_E$ and $z = -10R_E$. Obviously, there is no visible difference between the simulated densities. Therefore, the box size does not impact our results. Particles that leave the simulation box form the Enceladus torus which has a negligible density ($\sim 10^5$ cm^{-3}) compared to the central plume ($\sim 10^8$ cm^{-3}) [*Smith et al.*

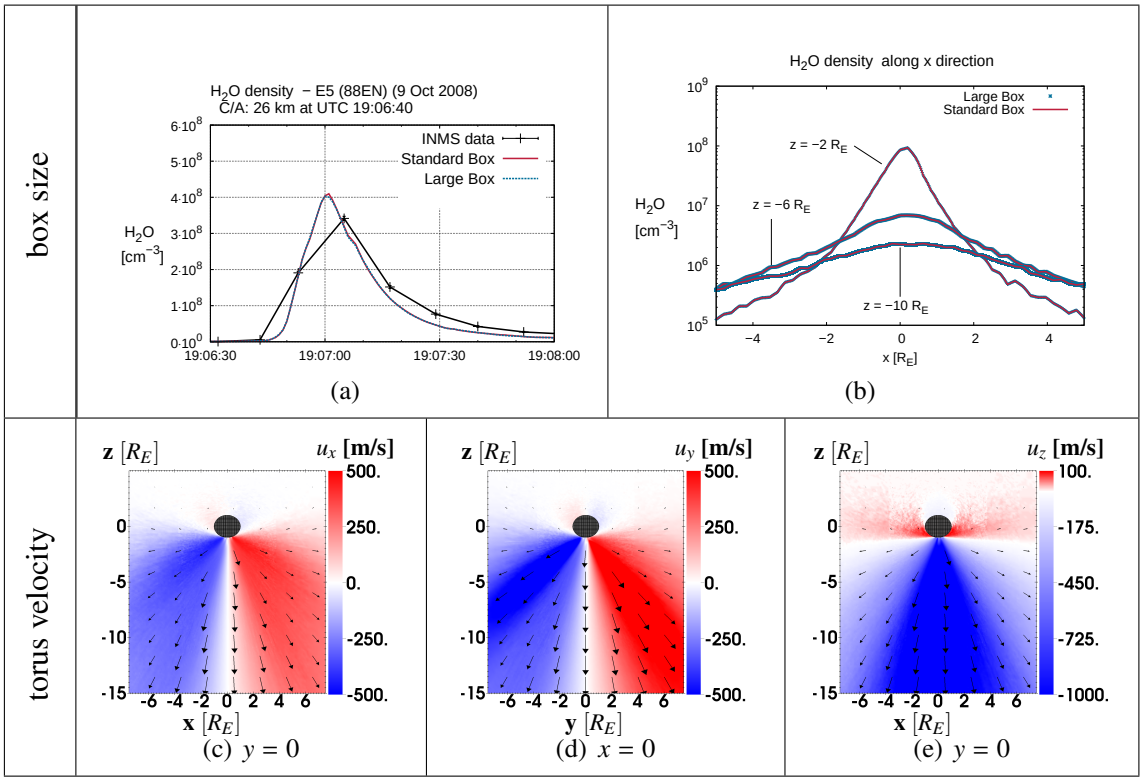

Figure 6.3: Influence of box size and velocity of torus particles on the neutral plume. First row: densities along E5 (a) and three lines parallel to the x axis (b). Shown are the results for the same simulation box as in figure 6.2 (red) and the results for a larger simulation box (blue). Second row: neutral bulk velocity from the same simulation as shown in figure 6.2(d)–(f), but a neutral torus with a density of $n_{torus} = 1 \cdot 10^5\,\mathrm{cm}^{-3}$ and zero velocity is taken into account.

2010]. The bulk velocity of the neutrals, however, is indeed influenced by the torus. In panels 6.2(d)–(f), the velocity is largest away from the plume center due to a low number of particles with high velocities in these regions. In contrast, the torus particles are on Keplarian orbits, implying zero velocity in the ENIS. The correct velocity bulk velocity should therefore be calculated from the mean velocity of the resting torus particles and the fast particles originating directly from the plume. Panels 6.3(c)–(e) show the same bulk velocity as in figure 6.2, but corrected for the molecules of the torus with a constant density of $10^5\,\mathrm{cm}^{-3}$. In contrast to the results presented in figure 6.2, the velocity now decreases with distance to the south pole axis. However, it should be pointed out that the difference in the neutral bulk velocity at large distances to the plume center does not affect the outcome of the plasma simulations for two reasons: first, the velocity of the neutrals only enters the plasma simulations when a new ion is created due to ionization. The correction of the neutral velocity is strongest where the torus density is equal or larger than the plume density. In these regions, however, ionization occurs very rarely. Second, the neutral velocity of about 1 km/s is small compared to the ion velocity which is about 20 km/s upstream or downstream of the plume. Hence, it does not make a noticeable difference whether the torus molecules are considered.

Furthermore, the ion-neutral collisions may also act back on the neutral plume by means of an ion drag force as has been discussed by *Saur et al.* [2002] for Io's atmosphere.

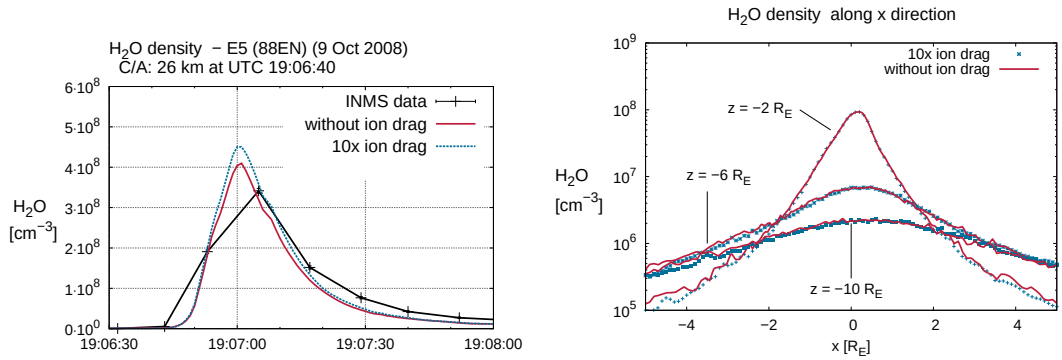

(a) (b)

Figure 6.4: Influence of an ion drag force (equation (6.5)) on the neutral plume densities, illustrated in a similar way as in figure 6.3. Shown are a simulation without drag force (red) and a simulation including the drag force artificially increased by a factor of ten (blue).

Therefore, we analyzed the influence of the ion-neutral collisions on the neutral density in a second simulation of the neutral plume in a new step (2b) of the iteration cycle, in which we used the ion density and velocity of a plasma simulation from step (2). The impact of the ions is considered by adding a drag force (cf. eq. (4.23)) to equation (6.4), i.e.

$$\ddot{\underline{x}} = -k_i n_i \left(\underline{v} - \underline{u}_i \right) \quad . \tag{6.5}$$

To overestimate the effect of the drag force, the collision rate is set to $k_i = 3 \cdot 10^{-8}\,\mathrm{cm}^3/\mathrm{s}$, which is about one order of magnitude larger than the value used for the ion-neutral collisions in the previous chapter (see section 5.4.1). The results are displayed in figure 6.4 in a similar way as in figure 6.3. Although the rate coefficient k_i and in consequence, the strength of the drag force are increased by a factor of ten, the densities of the two simulations are nearly identical. Hence, we conclude that even a ten times increased ion drag does not cause a noticeable effect on the motion of the neutrals and the resulting density profile of the plume.

To illustrate the improvement achieved by simulating the neutral plume, figure 6.5 shows a comparison of the INMS data along E5 and E7 with the analytical plume model from equation (5.24) used in the previous chapter. The parameters of that plume correspond to the best fit with MAG data from E5 and E7, i. e. $H_\vartheta = 7.5°$ (E5, E7) and $n_{n0} = 11 \cdot 10^{10}\,\mathrm{cm}^{-3}$ (E5) and $n_{n0} = 7 \cdot 10^{10}\,\mathrm{cm}^{-3}$ (E7). These parameters yield a peak density which is more than two orders of magnitude larger than the peak density observed during E5 (panel 6.5(a)) and about one order of magnitude larger than during E7 (panel 6.5(b)). In addition, the previous plume model overestimates the steepness of the increase and decrease before and after the peak density was assumed. Therefore, the value of $H_\vartheta = 7.5°$ – which resulted from the adjustment of the plume to MAG data – generated a significantly narrower density profile than measured by INMS. The adjustment of the plume parameters n_{n0} and H_ϑ of equation (5.24) to MAG data has led to a neutral density which is strikingly different from the plume observed by INMS – and in consequence also extremely different from the plume modeled by the Monte-Carlo simulations. To present

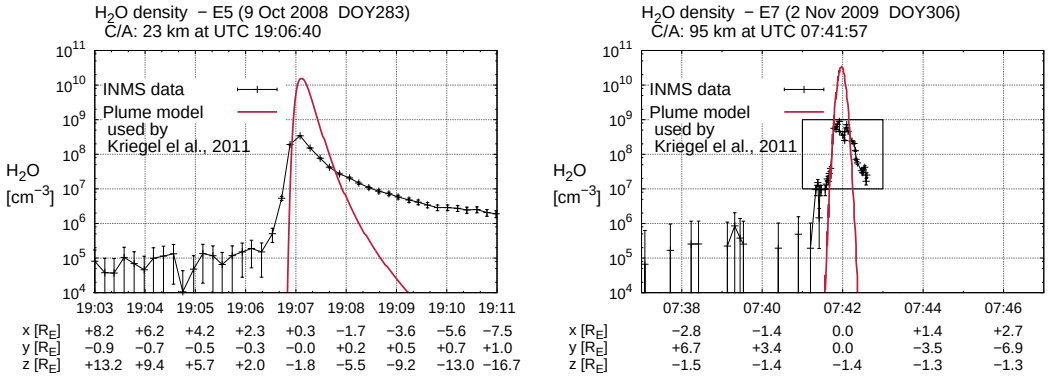

(a) (b)

Figure 6.5: Neutral plume density along E5 (panel (a)) and E7 (panel (b)). Shown are the INMS data and the neutral plume resulting from equation (5.24) as it has been used in the previous chapter to successfully reproduce MAG. According to table 5.2, the parameters of that equation are set to $H_\vartheta = 7.5°$ (E5,E7) and $n_{n0} = 11 \cdot 10^{10}\,\mathrm{cm}^{-3}$ (E5) and $n_{n0} = 7 \cdot 10^{10}\,\mathrm{cm}^{-3}$ (E7). The striking discrepancy between this model and the INMS data demonstrates the necessity for the improved plume model shown in figure 6.2.

a model which is not only in agreement with MAG data but also takes into account the INMS observations, the improvement of the neutral plume model was thus definitely necessary.

6.3 Modeling of the Dust Plume

In this section, we discuss the Monte-Carlo simulations of the dust plume in iteration steps (3) and (5) which are used as a stationary input for the plasma simulations in steps (4) and (6), respectively. These simulations are very similar to the model of the neutral plume (previous section): the initially uncharged dust particles are ejected at the same south polar sources as the neutral gas and their motion is determined by the gravitational and inertia forces. However, in two aspects, the dust model is more complex than the model for the neutral gas:

- Dust grains have different sizes, ranging from nm to μm.
- Dust grains may become charged during their motion through the local plasma environment and are therefore subject to the Lorentz force.

Therefore, the parameter space required to describe the dust plume is significantly enlarged, and a detailed description of the impact of the plasma environment as well as a thorough discussion of the initial dust properties are beyond the scope of this work and contain significant results on their own which will be addressed in a separate study. Here, we will only give a brief overview of the main aspects of the dust model.

Since the acceleration of a dust grain due to gravitation and inertia forces is independent of its mass, the effect of these forces is the same as for the gas molecules. The initial

velocity u_{D0} of the dust grains, however, is probably generated by collisions with the ambient gas flow and is therefore a function of the grain size. This is considered by applying the velocity-size distribution from *Postberg et al.* [2011] (equation S11), who modeled the composition of the grains to match the CDA data. In their model, nanograins have an initial velocity very close to that of the gas molecules ($u_{D0}(R \sim \text{nm}) \approx u_{gas}$), but larger grains may be significantly slower, e. g. a grain of radius $R = 1\,\mu$m has an average velocity of about $u_{D0}(R = 1\,\mu\text{m}) = 0.4 u_{gas}$ when leaving the surface of Enceladus.

To analyze the magnetic field signatures of the dust plume, we apply three different parameter sets for the initial conditions of the dust grains. The first setup comprises only the diffuse tiger stripe sources with $u_{D0} = 660\,\text{m/s}$, while the second setup includes only the jet locations and associated directions from *Spitale and Porco* [2007] with $u_{D0} = 2000\,\text{m/s}$. These choices correspond to a temperature of 180 K and sonic Mach numbers of the gas of $M_s = 2$ and $M_s = 6$, respectively. In the following, the model dust plumes resulting from these initial parameters will be referred to as 'diffuse dust (plume)' and 'jet dust (plume)'. The two setups have been chosen to be consistent with the finding of *Postberg et al.* [2011] that the slow (salt-rich) particles originate from the diffuse sources while the faster (salt-poor) grains originate from the discrete jets. In their model, the grains leave the tiger stripe sources with a mean ejection angle of $\psi = 35°$ with respect to the surface normal, while this angle is $\psi = 15°$ for the jet sources. To account for these angles, we assume that the grains acquire an additional random velocity component corresponding to a Gaussian distribution with a standard deviation of $\sigma = 500\,\text{m/s}$. In cases with only interest in the general effect of the dust we apply a mixture of the two former setups and consider both source types (default dust). Each jet source is assigned a four times higher source rate. In addition, we will employ an analytical model of the dust charge density similar to the one used in the simulations of the previous chapter (see section 5.4.3),

$$\xi n_D(\underline{x}) = \xi n_{d0} \frac{R_E}{r'} \exp\left(-\frac{\vartheta'^2}{H_\vartheta^2}\right) \exp\left(\frac{R_E - r'}{H_d}\right) \quad . \tag{6.6}$$

The prime indicates that r' and ϑ' are the radial distance and the polar angle with respect to the south pole, not the center of Enceladus. Although eq. (6.6) diverges at the south pole from the analytical point of view, it does not do so in our simulation due to the finite grid resolution, where no mesh node is located exactly at $r' = 0$. We set $\xi n_{d0} = 750\,\text{cm}^{-3}$, $H_\vartheta = 20°$ and $H_d = 948\,\text{km}$. We would like to emphasize that we do not intend to regard this profile as realistic or physically justified, yet, a comparison of this simple profile with the results from the Monte-Carlo simulations allows interesting conclusions on the impact of the dust on the magnetic field in section 6.5.

CDA measurements show that the size distribution of grains larger than 1 μm follows a power law according to $\text{d}n_d \sim R^{-\mu}\text{d}R$ [*Kempf et al.* 2010]. The dust charge density ξn_D, that is the number of electrons absorbed per volume by the dust grains is then obtained from integration over the size distribution multiplied by the charge $q_d(R)$ carried by a grain of a certain size R. Thus we get

$$\xi n_D \sim \int_{R_{min}}^{R_{max}} \frac{q_d(R)}{R^\mu}\,\text{d}R \quad . \tag{6.7}$$

The lower and upper cutoffs of our size distribution are set to $R_{min} = 1\,\mathrm{nm}$ and $R_{max} = 5\,\mu\mathrm{m}$, respectively. Modeling of the dust formation by *Schmidt et al.* [2008] suggests that the slope of the logarithmic size distribution may not be constant within the whole range of sizes, but μ is a function of the grain radius, $\mu = \mu(R)$. In our Monte-Carlo simulations of the dust plume, we therefore use a piecewise constant $\mu(R)$:

$$\mu(R) = \begin{cases} 7 & ; \quad 1\,\mathrm{nm} \leq R < 2\,\mathrm{nm} \\ -5 & ; \quad 2\,\mathrm{nm} \leq R < 200\,\mathrm{nm} \\ -4 & ; \quad 200\,\mathrm{nm} \leq R < 5\,\mu\mathrm{m} \end{cases} . \tag{6.8}$$

The magnitude of the dust density is mainly controlled by the mass production rate of the dust which is set to

$$\dot{M}_d = \begin{cases} 0.5\,\mathrm{kg/s} & ; \quad 1\,\mathrm{nm} \leq R < 2\,\mathrm{nm} \\ 7.7\,\mathrm{kg/s} & ; \quad 2\,\mathrm{nm} \leq R < 200\,\mathrm{nm} \\ 8.0\,\mathrm{kg/s} & ; \quad 200\,\mathrm{nm} \leq R < 5\,\mu\mathrm{m} \end{cases} . \tag{6.9}$$

On the one hand, the values for grains larger than $R = 200\,\mathrm{nm}$ are adjusted to modeling of CDA data, e.g. the mass production rate has been adjusted to CDA measurements along the E2 flyby [*Kempf et al.* 2010] and to the peak density seen along E7 [*J. Schmidt; priv. comm.*]. The slope of $\mu = -4$ is in agreement with the model by *Postberg et al.* [2011]. On the other hand, the parameters of the dust with $0.5\,\mathrm{nm} \leq R < 2\,\mathrm{nm}$ are chosen to match the CAPS/ELS nanograin observations along E3 and E5 presented by *Hill et al.* [2012]. From figures 6 and 7 in that work, the slope can be estimated to be approximately $\mu \approx 7$. As will be discussed by *Meier et al., in preparation*, the value of $\dot{M}_d = 0.5\,\mathrm{kg/s}$ for $R < 2\,\mathrm{nm}$ is a lower limit derived from the CAPS nanograin densities. The values for $2\,\mathrm{nm} \leq R < 200\,\mathrm{nm}$ are then obtained by assuming a continuous size distribution.

Of course, the real parameters of the nanograin size distribution might be different from our values. However, with the reasonable constraints that first, the slope of the size distribution is positive for the nanograins and second, the total mass production rate of the dust must not get too large (we assume $M_{d,total} < 50\,\mathrm{kg/s}$), the peak of any size distribution is located at radii smaller than 3 nm and thus, most of the dust particles are small nanograins. For our size distribution, even more than 99% of the grains are smaller than 10 nm.

The grains are charged and discharged dynamically during their motion according to

$$\frac{\mathrm{d}q_d(R)}{\mathrm{d}t} = I_e + I_i + I_{sec} + I_{ph} \quad . \tag{6.10}$$

The currents on the right-hand side of equation (6.10) are the local electron and ion collection currents I_e and I_i, the secondary electron current I_{sec} and the photoionization current I_{ph} (see e. g. *Shukla and Mamun* [2002]). A major advantage of our iterative simulation technique is that these currents and the maximum number of available "free" electrons are constrained by the realistic plasma environment from the hybrid simulations.

We would like to note that many of the nanograins do not attain their equilibrium charge while being located within the central plume. Field emission limits the charge of grains

smaller than 2 nm to a single elementary charge [*Hill et al.* 2012]. In contrast, the equilibrium charge of larger grains is proportional to their radius [*Shukla and Mamun* 2002]. Although the nanograins are not in equilibrium, the dust charge density resulting from all nanograins within a certain volume reaches a steady state. A consequence of the size distribution defined by equations (6.8) and (6.9) is that 99% of the equilibrium charge density is carried by grains smaller than 10 nm.

For singly-charged nanograins of $R = 2\,\mathrm{nm}$ and a corresponding mass $m = 110\,m_{\mathrm{H_2O}}$, the acceleration by the Lorentz force F_L in the upstream plasma dominates the gravitational force of Saturn (F_G) at $3.95 R_S$ by about two orders of magnitude ($F_L/m \sim 10^1\,\mathrm{m/s^2}$ vs. $F_G/m \sim 10^{-1}\,\mathrm{m/s^2}$). The electromagnetic fields are therefore crucial for the motion of the nanograins and the shape of the charged dust plume. We would like to note that our model in principle also allows for positively charged nanograins. As they are clearly outnumbered by the negatively charged particles, the positive nanograins are not visible in the total dust charge density.

The resulting spatial distribution of the dust charge density will be shown in the discussion of the plasma densities (see section 6.4).

6.4 Results I: Plasma Densities

We commence the discussion of our results with the densities of the various ion species and the charged dust. For the macroscopic scales ($\sim$ km) we discuss here, these densities are related by the quasi-neutrality condition

$$\sum_{\alpha} n_\alpha = n_i = n_e + \xi n_D \quad , \tag{6.11}$$

where n_α denotes the density of the ion species α with $\alpha = \{\mathrm{H^+}, \mathrm{O^+}, \mathrm{OH^+}, \mathrm{H_2O^+}, \mathrm{H_3O^+}\}$, n_i is the total ion density, n_e the electron density and ξn_D the number of electrons absorbed by the dust grains per volume. First, we discuss the effect of the ion-neutral chemistry on the relative abundances n_α/n_i of the various ion species. Second, we present our results for the total ion density n_i in the context of the Cassini observations. Finally, we describe the dust plume resulting from the Monte-Carlo simulations for different initial conditions of the dust.

We would like to note that all results presented in the following sections (6.4 and 6.5) are obtained from step (6) of our iteration scheme. If not stated otherwise, the simulations are based on neutral plume #3 with a production rate of $Q = 4.9 \cdot 10^{28}\,\mathrm{H_2O/s}$ (cf. section 6.2) and the default dust plume which considers diffuse and jet dust sources (see section 6.3).

6.4.1 Ion Composition

As described in section 6.1.2, the upstream plasma composition is set to 10% protons and 22.5% of each of the four water group ion species. Due to ion-neutral reactions and ionization in the plume, these relative abundances change. Our simulation results for the relative abundances n_α/n_i of the different ion species are shown in panels (a)–(e) of figure 6.6. As can be seen in plots (a), (b) and (c), the relative abundances of $\mathrm{H^+}$, $\mathrm{O^+}$ and $\mathrm{OH^+}$

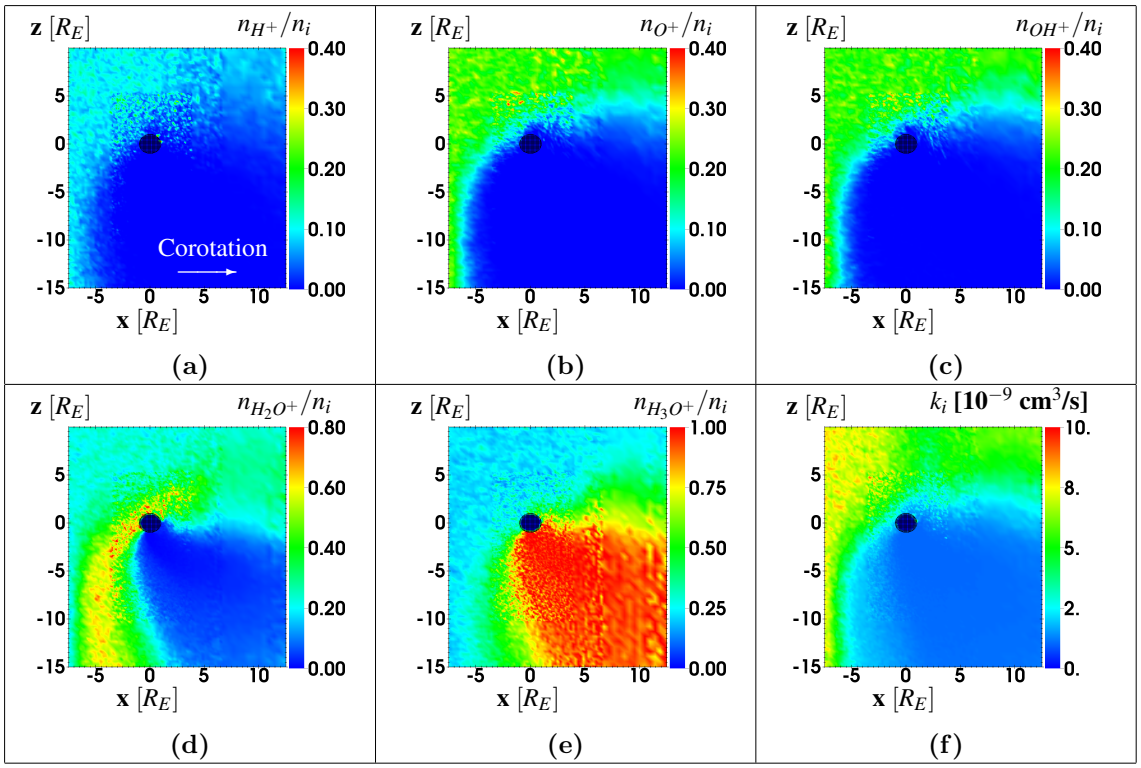

Figure 6.6: Effects of ion-neutral chemistry: plots (a) – (e) show the simulation results for the abundances of the five ion species included in the model in the $y = 0$ plane. Plot (f) displays the average reaction rate k_i.

start to decrease at about $x = -5R_E$ from their upstream values to approximately zero within and downstream of the plume. The abundance of H_2O^+ (cf. panel (d)) increases from the background value to about $n_{H_2O^+}/n_i = 0.6$ in the region between $x = -5R_E$ and $x = -3R_E$. For $x > -3R_E$, $n_{H_2O^+}/n_i$ decreases and nearly vanishes for $x \geq 0$. In contrast to the other species, the abundance of H_3O^+ increases monotonically when entering the plume and assumes a value of nearly one for $x \geq 0$. Panel (f) of figure 6.6 displays the reaction rate k_i, which is calculated as $k_i = \frac{1}{n_i}\left(\sum_\alpha n_\alpha k_\alpha(u_\alpha)\right)$ for the reactions listed in table 6.2. In this expression, u_α denotes the local bulk velocity of species α. The reaction rate decreases from about $k_i = 8 \cdot 10^{-9}\,\mathrm{cm}^3/\mathrm{s}$ upstream of the plume to $k_i = 1 \cdot 10^{-9}\,\mathrm{cm}^3/\mathrm{s}$ within the plume.

The morphology of the relative abundances of the different species visible in figure 6.6 follows directly from the reaction rates (cf. table 6.2): the reactions of O^+ and OH^+ to H_2O^+ have the highest rates, leading to the decrease of the abundance of O^+ and OH^+ and the increase of $n_{H_2O^+}/n_i$ upstream of the plume from $x = -5R_E$ to $x = 0$. Since H^+ has a lower relative density than the other species, its reaction to H_2O^+ makes only a minor contribution to the increase of the H_2O^+ abundance. Similarly, the reaction of OH^+ to H_3O^+ also leads to the upstream increase of $n_{H_3O^+}/n_i$. H_2O^+ can either undergo charge exchange, simply replacing the original H_2O^+ ion by a newly born one, or react to H_3O^+. The latter process is responsible for the decrease of the H_2O^+ abundance and the

increase of $n_{H_3O^+}/n_i$. When approaching $x = 0$ from upstream, these reactions occur so frequently that nearly all H_2O^+ ions are converted to H_3O^+. Finally, H_3O^+ does not react with water at these energies and thus, it undergoes only elastic collisions with the neutral H_2O molecules, yielding no change in its abundance. The high abundance of H_3O^+ within the center of the plume also explains the spatial profile of the reaction rate: k_i is calculated as an average over the different rates of the ion species. Within the plume, however, the average is dominated by the collisions of H_3O^+ which possess one of the smallest rates in the reaction scheme: $k_i \approx k_{H_3O^+} = 1.02 \cdot 10^{-9}\,\mathrm{cm}^3/\mathrm{s}$.

The ion-neutral chemistry relevant for Enceladus' plasma interaction can therefore be summarized as follows: (1) all reactions of the upstream ions with H_2O produce either H_2O^+ or H_3O^+, (2) H_2O^+ also reacts to H_3O^+, (3) H_3O^+ does not react any more. Therefore, the reaction chain ends up in the production of H_3O^+ which is the predominant ion species in the plume (abundance of $n_{H_3O^+}/n_i \approx 1$). This finding is in agreement with INMS data [*Cravens et al.* 2009].

We would like to point out that the velocity of the plasma has only a minor impact on the total reaction rate within the plume, since the rate of H_3O^+ is independent of the velocity (see appendix A). It is also interesting to note that the production of new ions within the plume by photo- and electron impact ionization has a negligible impact on the abundances of the different species. Although these processes produce primarily H_2O^+, these newly born ions then quickly react to H_3O^+ and do not yield a noticeable abundance of H_2O^+.

6.4.2 Ion Densities

Before presenting our simulation results for the total ion density n_i, we will derive an analytical estimate of the maximum ion density in the plume based on ionization of a neutral plume model.

In stationary state, the continuity equation for the ions reads

$$\partial_{\underline{x}} \cdot (n_i \underline{u}_i) = \nu_{io} n_{H_2O}(\underline{x}) \quad , \tag{6.12}$$

where we have neglected the contribution of the upstream plasma and loss terms arising from recombination. To specify $\underline{u}_i$, we assume that in the center of the plume, ion-neutral collisions occur so frequently that the ions are not accelerated to speeds above the velocity of the neutrals. This is in agreement with CAPS observations of flow stagnation [*Tokar et al.* 2009] and our previous simulation results. Furthermore, we have shown in section 6.2 that the neutral bulk velocity $\underline{u}_n$ is mainly directed radially away from the south polar sources, i. e. $\underline{u}_n = u_n \underline{e}_r$ with the radial unit vector $\underline{e}_r$. The neutral density above the sources is approximated by the geometrical decrease of the density according to

$$n_{H_2O}(r) = n_{n0} \left(\frac{R_E}{r} \right)^2 \quad . \tag{6.13}$$

According to the discussion in section 6.1.3, we assume ν_{io} to be constant. Setting $\underline{u}_i = u_n \underline{e}_r$ and $u_n = \mathrm{const}$, it is then possible to integrate eq. (6.12) in spherical coordinates, yielding

$$n_i(r) = \frac{\nu_{io} n_{n0} R_E}{u_n} \frac{R_E}{r} + \frac{K}{r^2} \quad . \tag{6.14}$$

To determine the integration constant K, we consider two extreme boundary conditions: (1) the ion density is zero directly at the surface ($n_i(r = R_E) = 0$), or (2) it achieves its maximum at the surface ($\frac{dn_i(r=R_E)}{dr} = 0$). In both cases, the ion density becomes

$$n_i(r) = \frac{\nu_{io} n_{n0} R_E}{u_n} \left(\frac{R_E}{r} - \frac{R_E^2}{\kappa r^2} \right) \quad , \tag{6.15}$$

with $\kappa = 1$ for case (1) and $\kappa = 2$ for case (2). The maximum which can be assumed by $n_i(r)$ is

$$n_{i,max} = \frac{\nu_{io} n_{n0} R_E}{2 u_n} \tag{6.16}$$

for case (2) at $r = R_E$. We would like to emphasize that this equation provides an *upper limit* for the ion density generated by ionization, because no pick-up of the ions is considered.

The base density n_{n0} can be obtained from eq. (6.13) and the INMS data from the E3, E5 and E7 flybys. We choose r according to the distances where the neutral densities peak along the flyby trajectories. The data displayed in figure 6.2 give $n_{H_2O} = 7.6 \cdot 10^7\,\mathrm{cm}^{-3}$ at 19:07:00 UTC for E3, $n_{H_2O} = 3.4 \cdot 10^8\,\mathrm{cm}^{-3}$ at 19:07:05 UTC for E5 and $n_{H_2O} = 8.9 \cdot 10^8\,\mathrm{cm}^{-3}$ at 07:41:55 UTC for E7. The corresponding radial distances are $r = 3.0 R_E$ (E3), $r = 2.1 R_E$ (E5) and $r = 1.4 R_E$ (E7). These values yield $n_{n0} = 3.0 \cdot 10^8\,\mathrm{cm}^{-3}$ (E3), $n_{n0} = 4.2 \cdot 10^8\,\mathrm{cm}^{-3}$ (E5) and $n_{n0} = 1.3 \cdot 10^8\,\mathrm{cm}^{-3}$ (E7).

Considering only photoionization and electron impacts, the total ionization rate is $\nu_{io}^{(0)} = \nu_{ph} + \nu_e = 5.9 \cdot 10^{-9}\,\mathrm{s}^{-1}$ for these three flybys (see section 6.1.3). Furthermore, we assume a constant neutral bulk velocity of $u_n = 1\,\mathrm{km/s}$ according to our results for the neutral plume in figure 6.2(f). When adding the density of the upstream plasma (n_0) to eq. (6.16) according to the values provided in table 2.2, the maximum ion densities for the three flybys are given by

$$n_{i,max}^{(0)} = \frac{\nu_{io}^{(0)} n_{n0} R_E}{2 u_n} + n_0 = \begin{cases} 310\,\mathrm{cm}^{-3} & (E3) \\ 400\,\mathrm{cm}^{-3} & (E5) \\ 160\,\mathrm{cm}^{-3} & (E7) \end{cases} \quad . \tag{6.17}$$

In the following, we will focus on E3 and E5 due to the availability of CAPS and RPWS Langmuir Probe (LP) observations.

Morooka et al. [2011] reported on Langmuir Probe measurements with peak ion densities of $30,000\,\mathrm{cm}^{-3}$ and $100,000\,\mathrm{cm}^{-3}$ along the E3 and E5 trajectories, respectively. These values are two orders of magnitude larger than our estimated upper limits for the ion densities (cf. eq. (6.17)). The ionization frequency required to achieve the high LP densities is on the order of $\nu_{io}^{LP} = 10^{-6}\,\mathrm{s}^{-1}$ which is in turn two orders of magnitude larger than $\nu_{io}^{(0)}$. We do not have an explanation for this huge discrepancy in the densities and ionization rates, but leave this as an open question.

Another constraint on the ion densities in the plume is imposed by CAPS observations of negatively charged nanograins [*Hill et al.* 2012]. From figure 8 of that work, we derive peak nanograin densities of more than $1,000\,\mathrm{cm}^{-3}$ for E3 and about $800\,\mathrm{cm}^{-3}$ for E5. Due to the quasi-neutrality condition (6.11), the ion density has to be equal to or larger than the density of these nanograins. However, it should be noted that the nanograin densities derived by these authors need to be regarded as a lower limit because only grains smaller than about 2 nm can be detected within the energy range of the CAPS instrument. For a dust-size distribution like the one applied in our model (see section 6.3), more than 50% of the charge density could be carried by grains larger than 2 nm. Therefore, the total number density of charged nanograins (including those with $2\,\mathrm{nm} < R \lesssim 10\,\mathrm{nm}$) might be significantly larger than the values derived by *Hill et al.* [2012].

Obviously, it is a strong contradiction that our estimated *upper* limits for the peak densities in eq. (6.17) are clearly exceeded by the *lower* limits deduced from CAPS. To resolve this discrepancy, the effective ionization frequency needs to be enhanced by an additional contribution ν^*. This contribution might describe the production of the observed $H_xO_2^+$ ions, where $x = 1 - 4$ [*Tokar et al.* 2009, *Cravens et al.* 2011], cf. section 6.1.3. Another explanation for the necessity of this ion source might be associated with dusty plasma effects (see last paragraph of section 6.4.3). The enhanced ionization frequency might also be due to a significantly stronger electron impact ionization. We set ν^* to the lowest value for which the combination of our simulated ion densities and the CAPS nanograin densities does not violate the quasi-neutrality condition (6.11). As will be illustrated in the following, this is the case for $\nu^* \approx 3 \cdot 10^{-8}\,\mathrm{s}^{-1}$, yielding $\nu_{io}^{(2)} = \nu_{ph} + \nu_e + \nu^* = 3.59 \cdot 10^{-8}\,\mathrm{s}^{-1}$. Note that this value is a factor of six larger than $\nu_{io}^{(0)}$. When taking into account both, nanograins larger than 2 nm and the Langmuir Probe ion densities, it is likely that ν^* needs to be set to even a larger value. Due to the unknown physical process underlying this "ionization source", however, we prefer to choose ν^* as small as possible. It should also be pointed out that it is *not* possible to choose ν^* large enough to explain the LP densities under the contraint that the generated magnetic field perturbations are in agreement with MAG data (see section 6.5).

After these initial considerations on ion density and ionization frequency, we move on to our simulation results. Figure 6.7 shows our results for the ion density in the $y = 0$ plane for three simulations with different ionization frequencies. Panel 6.7(a) displays a run with $\nu_{io}^{(0)}$, i. e. only photoionization and electron impacts are considered. Near to the south pole, the ion density is only sightly enhanced and reaches peak values of about $300\,\mathrm{cm}^{-3}$, compared to the background density of $90\,\mathrm{cm}^{-3}$. The simulations shown in plots 6.7(b) and 6.7(c) include the additional ion source ν^* with $\nu^* = 1 \cdot 10^{-8}\,\mathrm{s}^{-1}$ and $\nu^* = 3 \cdot 10^{-8}\,\mathrm{s}^{-1}$, respectively. In both scenarios, the ion density assumes values of at least $1000\,\mathrm{cm}^{-3}$ in the center of the plume. Due to the stronger ionization, the region of increased ion density has a diameter of about $2R_E$ for $\nu_{io}^{(2)}$, while this region has a width of less than $1R_E$ for $\nu_{io}^{(1)}$. In all three plots, the enhanced ion density exhibits a clearly visible tilt towards downstream (positive x direction) which results from the pick-up of the ions (cf. *Kriegel et al.* [2009]). When comparing panels (a)–(c), one can see that the higher the ionization frequency, the smaller is the extension of the wakeside plasma cavity along the corotation direction. Therefore, the refilling of the wake is enhanced by the density gradients.

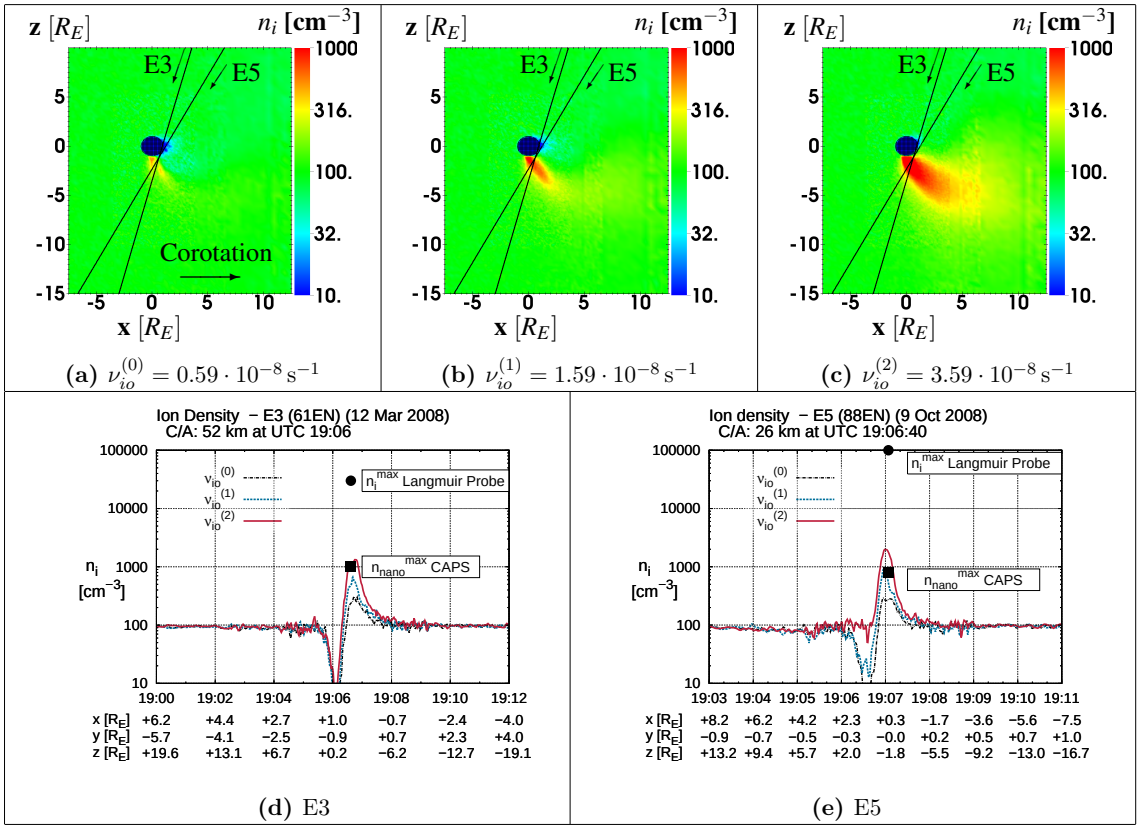

Figure 6.7: Results for the ion density obtained from simulations with three different ionization frequencies. From photoionization and electron impacts, we derive $\nu_{io}^{(0)} = 5.9 \cdot 10^{-9}\,\mathrm{s}^{-1}$, while $\nu_{io}^{(1)} = 1.59 \cdot 10^{-8}\,\mathrm{s}^{-1}$ and $\nu_{io}^{(2)} = 3.59 \cdot 10^{-8}\,\mathrm{s}^{-1}$ include an additional (unspecified) ionization source. Plots (a) – (c) display the ion density in the $y = 0$ plane together with the projections of the E3 and E5 trajectories on this plane. Panels (d) and (e) show the simulated densities along these trajectories. Peak ion densities derived from the Langmuir Probe [*Morooka et al.* 2011] are marked by black circles and CAPS densities of negative nanograins [*Hill et al.* 2012] are marked by a black square.

The simulated ion densities along the E3 and E5 trajectories are presented in panels 6.7(d) and 6.7(e). The colors indicate the three different simulation setups: the dashed black lines display the ion densities for the ionization frequency $\nu_{io}^{(0)}$, while the solid red lines are from the run which uses $\nu_{io}^{(2)}$. The dashed blue lines show the results for the intermediate ionization frequency $\nu_{io}^{(1)}$. In addition, the peak ion densities from the Langmuir probe as well as the peak nanograin densities derived from CAPS are indicated by black circles and squares, respectively.

Except for the simulation with $\nu_{io}^{(2)}$ along E5, the ion density first decreases when Cassini passes through Enceladus' geometric wake. This is followed by a steep increase of the ion density when entering the plume and a gradual decrease of the density in the outbound region, i. e. south of the central plume. In addition, for E5 a partly refilled wake with ion densities around 20 cm^{-3} can be seen only for ionization frequency $\nu_{io}^{(1)}$, but not in the simulations with $\nu_{io}^{(0)}$ or $\nu_{io}^{(2)}$. The reason that the wake is not visible for $\nu_{io}^{(2)}$ along E5 is that at $x = 2R_E$, where the E5 trajectory intersects the $z = 0$ plane, the wake is

already completely refilled (see plot 6.7(c)). However, due to the larger inclination of the E3 trajectory with respect to the $z = 0$ plane, the E3 trajectory intersects the plasma cavity in Enceladus' geometric shadow even when the highest ionization frequency $\nu_{io}^{(2)}$ is applied. Because of the different inclinations of the trajectories, the spacecraft penetrated deeper into the region of enhanced density during E5, explaining why the modeled E5 peak densities are about 50% larger than those for E3. Furthermore, our simulated peak densities for $\nu_{io}^{(0)}$ of about 300 cm^{-3} for E3 and E5 agree well with our estimated densities from eq. (6.17). Therefore, the assumptions made in the derivation of eq. (6.17) are a posteriori justified by the simulations. The peak densities for the simulations with $\nu_{io}^{(1)}$ and $\nu_{io}^{(2)}$ also demonstrate that only the simulation considering an effective frequency of $\nu^* = 3 \cdot 10^{-8}\,\mathrm{s}^{-1}$ is able to produce ion densities larger than the CAPS nanograin densities for both flybys. With an effective frequency of $\nu^* = 1 \cdot 10^{-8}\,\mathrm{s}^{-1}$, the densities are sufficiently large just for E5. We conclude that with photoionization and electron impacts only ($\nu_{io}^{(0)}$), the ion densities are definitely too small for explaining the CAPS nanograin densities derived by *Hill et al.* [2012]. In the remainder of this paper, we therefore apply $\nu_{io}^{(2)}$.

6.4.3 Dust Charge Density

The discussion of the plasma densities is continued with the dust charge density. However, we would like to point out that the dust charge density should always be placed in the context of electron and ion densities, since these densities are linked by the quasi-neutrality condition (6.11). Especially, this means that the local ion density constitutes an upper limit for the charge density that may be accumulated by the dust grains. Therefore, the dust charge density is presented together with the corresponding fraction of "free" electrons n_e/n_i. However, the reader should keep in mind that a minimum electron density of $n_{e,min} = 0.15 n_0^*$ is applied to avoid that the hybrid equations diverge (see section 4.1). In addition, the dust density and the electromagnetic fields constitute a strongly coupled system. We describe the dust charge density obtained from simulations at iteration step (5) here, while the associated electromagnetic fields are discussed in section 6.5.

The three clearly different profiles of the dust charge density introduced in section 6.3 turn out to be most instructive for our analysis: (1) the analytical dust profile defined by eq. (6.6); (2) the simulated profile using the diffuse dust sources only; (3) the simulated plume with the jet dust sources only. Figure 6.8 shows the results for these three setups. Dust plume (1) is presented in the left-hand column, whereas the results for plumes (2) and (3) are displayed in the middle and right-hand columns, respectively. The first row displays the dust charge density in the $x = 0$ plane, while the second row provides the corresponding fraction of free electrons. Similarly, the last two rows show the results in the $z = -2R_E$ plane.

The dust charge density of the analytical model (see panel 6.8(a)) assumes values above $\xi n_D = 100\,\mathrm{cm}^{-3}$ only in a narrow region with an extension of about $0.5R_E$ in x direction. However, at $z = -10R_E$ the density ξn_D of the plume is still larger than 10 cm^{-3}. According to eq. (6.6), this profile possesses rotational symmetry around the z axis. In contrast to that, the two simulated dust plumes (cf. panels 6.8(b) and 6.8(c)) feature a more extended region with a density of $\xi n_D \geq 1000\,\mathrm{cm}^{-3}$. This region is nearly spherical in shape with a diameter of about $2R_E$ and is centered at $(0, 0, -2R_E)$. In both cases, the region

of increased dust density is stretched towards the positive y direction. The main difference between the plume resulting from the diffuse dust sources and the plume with the jet sources is the southward extension of increased charge density. For plume (2), the charge density drops below $\xi n_D = 1\,\mathrm{cm}^{-3}$ at about $z = -5R_E$, while for plume (3) this happens at $z \approx -8R_E$. The corresponding ratios n_e/n_i are displayed in panels 6.8(d)–6.8(f). For the analytical dust profile, $n_e/n_i > 0.7$ is fulfilled in the entire interaction region. Near the south pole, the ratio is close to one. Therefore, only an insignificant fraction of the electrons is attached to the dust grains. This is different for the two simulated dust plumes, where n_e/n_i drops below 50% in that region. When comparing the n_e/n_i ratios with the corresponding charge densities, one notes that the relative number of absorbed electrons does not peak directly below the south pole where the dust charge density is highest, but rather in the peripheral region of the dust plume where ξn_D decreases. The reason is that directly below the south pole, the ion density also achieves its maximum (cf. fig. 6.7). Due to the quasi-neutrality condition, the total number of electrons available for absorption below the south pole is therefore larger than in any other region. Thus, although the *absolute* number of absorbed electrons achieves its maximum directly below the south pole, the *relative* number n_e/n_i does not achieve its minimum in this region due to the large number of electrons initially available for absorption. This again emphasizes that the dust charge density always has to be placed in the context of the ion density.

Many of these aspects can also be found in the results for the $z = -2R_E$ plane (cf. panels 6.8(g)–6.8(l)). However, the difference between the two dust plumes obtained from the Monte-Carlo simulations is even more evident. The charge density in panel 6.8(h) is clearly asymmetric, with the density enhancements of about $10\,\mathrm{cm}^{-3}$ mainly concentrated in three "finger"-like regions, extending into the Saturn-facing hemisphere. In contrast, the density resulting from the jet dust plume is confined to $y < 2R_E$ in this plane. The n_e/n_i ratio of the analytical model (see panel 6.8(j)) shows that within a small part of the Enceladus flux tube at $z = -2R_E$ only about 10% of the electrons are attached to the dust grains. Finally, panels (k) and (l) reveal that for the two simulated plumes, it is $n_e/n_i \approx 0.8$ in the "fingers" and also in parts of the flux tube. In a region roughly defined by the Saturn-facing surface of the fluxtube, the ratio drops to $n_e/n_i = 0.5$.

The asymmetric dust charge density profiles obtained from the Monte-Carlo simulations are caused by the pick-up of nanograins. As the convective electric field $\underline{E} = -\underline{u} \times \underline{B}$ is mainly directed in the negative y direction even when a strong Anti-Hall effect is present (cf. figure 5.4), the negatively charged nanograins are initially accelerated towards $+y$. The corresponding gyroradius for 2 nm grains in the upstream electromagnetic fields is about $50R_E$. This is consistent with the "finger"-like structure in plot 6.8(h), marking the begin of the pick-up cycloids. The concentration of the picked-up nanograins within the three "finger"-like structures arises from the inhomogeneous electric field in the outer regions of the Alfvén wing which focuses the grain trajectories [*Meier et al., in preparation*]. The main reason for the differences between the two Monte-Carlo plumes is the surface velocity of $u_{D0} = 660\,\mathrm{m/s}$ and $u_{D0} = 2000\,\mathrm{m/s}$ for diffuse and jet sources, respectively. Since the time until a grain captures the first electron is independent of the velocity of the grain, it covers a different distance before it becomes charged. Our simulations show that the average charging time for a nanograin of 2 nm is about 450 s. Therefore, the grains are on average charged at distances of $1.2R_E$ ($z = -2.2R_E$) and $3.6R_E$ ($z = -4.6R_E$)

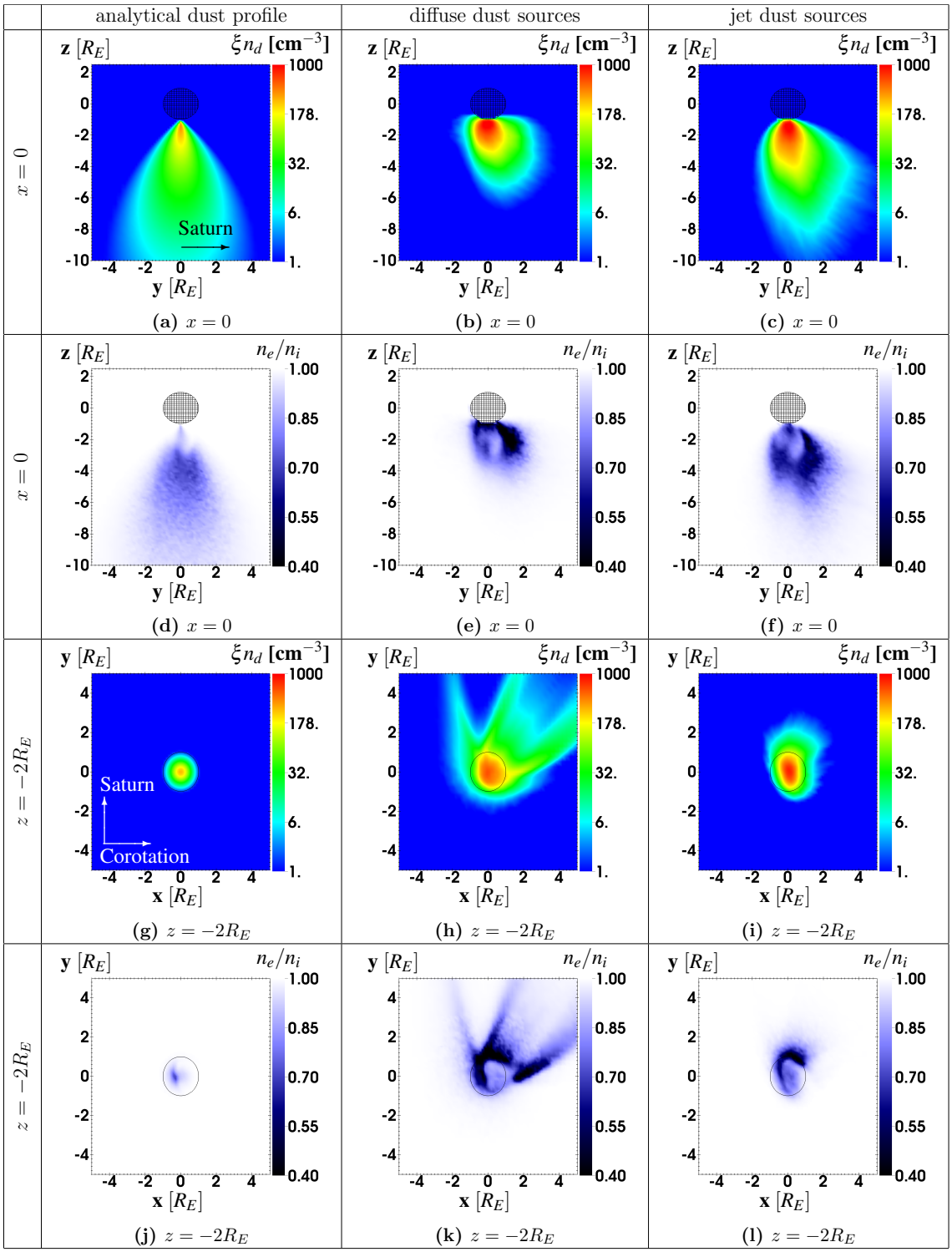

Figure 6.8: Dust charge density ξn_D and corresponding electron-to-ion ratio n_e/n_i in the $x = 0$ and $z = -2R_E$ planes. The first column displays results for an analytical model of the dust charge density defined by eq. (6.6). The second and third columns show the results obtained from Monte-Carlo simulations of the dust plume for different initial conditions of the grains (cf. section 6.3). All grains are either ejected at the diffuse tiger stripe sources with a maximum velocity of $u_{D0} = 660\,\mathrm{m/s}$ or at the jet locations from *Spitale and Porco* [2007] with a maximum velocity of $u_{D0} = 2000\,\mathrm{m/s}$.

for the diffuse sources and for the jet sources, respectively. After the grains have become charged, they are immediately picked-up. This results in a clearly visible pick-up tail in the $z = -2R_E$ plane for the lower grain surface velocity (see panel 6.8(h)). For the higher surface velocity, the pick-up tail is shifted to lower z values and is therefore not visible in panel 6.8(i).

Finally, we shall briefly address the question which additional effects may arise from the high dust charge densities in the plume. Since the dust significantly modifies the quasi-neutrality condition with respect to the situation without dust, it is qualitatively clear that we deal with a dusty plasma. A quantitative measure of the importance of dusty plasma effects is given by the 'Havnes parameter' [*Havnes et al.* 1984]. This parameter crucially depends on the electron density and on the plasma temperatures. Since we impose a lower limit on n_e and assume an adiabatic law for the electrons, a reliable calculation of the Havnes parameter is not possible in the hybrid model. However, we are able to discuss an important consequence of dusty plasma effects for the electron and ion densities in the plume: the overlap of the Debye spheres of the dust grains results in a potential Φ_c of the dust cloud relative to the plasma potential far away from the dust cloud [*Havnes et al.* 1984]. The effect of this potential can be illustrated with a simple example: many nanograins become negatively charged close to the south pole and subsequently these grains move to a region where their density is higher than the density of the surrounding ions. To maintain quasi-neutrality, these grains ought to become discharged. For low plasma densities and small grains, however, the (de)-charging time might be so large that quasi-neutrality is violated on scales of km. Therefore, the dust cloud potential repels electrons and attracts ions to ensure quasi-neutrality. For this reason, dusty plasma effects may cause higher ion densities and may partially explain the additional ion source modeled by the effective ionization frequency ν^* (see section 6.4.2). Unfortunately, dusty plasma effects become most important for $n_e \to 0$ and thus a hybrid model is not suitable to directly model these effects.

6.5 Results II: Magnetic Field Signatures

The second part of the discussion of the simulation results focuses on the magnetic field in Enceladus' vicinity. First, the impact of the three *neutral* plumes described in section 6.2 on the magnetic field structures will be analyzed for the example of the E7 flyby. This flyby has already been discussed in section 5.5.3 in the previous chapter and therefore allows to illustrate the improvements of the model.

Second, we will elaborate on how the measured magnetic field can be used as a sensitive probe of the *dust* plume. A comparison between modeled and observed magnetic field signatures from the horizontal E14, E17 and E19 flybys will allow to constrain the influence of dust pick-up on the magnetic perturbations near Enceladus. The southward extension of the dust plume as well as the location of the expected magnetic field decrease with respect to the flyby trajectories will also be discussed for these flybys. Furthermore, it will be demonstrated that dust pick-up may be responsible for the magnetic field perturbations observed during the distant E15 flyby. By comparing MAG data from E14, E17 and E18 we will also briefly address the variability of the plume.

Like in section 5.1, we will only show the magnetic field *perturbations* ($\Delta B_x, \Delta B_y, \Delta B_z$) throughout this section for better visualization.

6.5.1 Magnetic Field Signatures for Different Neutral Plumes (E7)

Figure 6.9 shows the simulated magnetic field perturbations together with Cassini MAG data for the E7 flyby. MAG data are represented by black lines. The three colored lines denote the field perturbations for the three neutral plumes #1 (red), #2 (blue), and #3 (green), which have been described in section 6.2. The vertical orange lines mark the surface of the Enceladus flux tube, i. e. the region where Cassini was located below Enceladus. The vertical black line denotes the location of closest approach at 07:41:57 UTC.

When comparing the magnetic field signatures generated by the three neutral plume setups with the results of our previous model (cf. fig. 5.7(g)), we note some obvious differences: our preceding simulations, applying an analytical neutral plume model, produced an overshoot of ΔB_x before entering and after leaving the central region of the northern wing where $\Delta B_x < 0$. However, the new results based on the neutral plumes from the Monte-Carlo simulations generate a gradual decrease of B_x on both sides of the flux tube in agreement with MAG data. The overshoots are no longer present. Especially the simulation based on plume #1 shows very good agreement with the data in the inbound region. This improvement can be attributed to the shape of the neutral plume obtained from the Monte-Carlo simulations which is significantly broader compared to the very narrow plume used by in the previous chapter (cf. figure 6.5).

Surprisingly, the agreement between simulations and MAG data for the B_y component was better in the previous chapter, where observed and simulated field perturbations were of the same strength. Our preceding simulation also reproduced the symmetric shape of the B_y perturbation. Especially in the outbound segment of the E7 trajectory, the B_y perturbations shown in figure 6.9 are weaker than the observed perturbations. As demonstrated in the previous chapter, however, ΔB_y is mainly determined by the dust plume and will be discussed in more detail in section 6.5.3. In contrast to the previous work, the new simulations also show both, an enhancement ($\Delta B_z < 0$) and a decrease ($\Delta B_z > 0$) in the B_z component. However, only the region of enhanced B_z is present in MAG data. In section 6.5.5, ΔB_z will be discussed in a 3D context.

When comparing the results for the three neutral plumes (see figure 6.9), we find that the magnetic field perturbations generated by plumes #1 and #3 are nearly identical. This finding is in agreement with the very similar large-scale density profiles of these plume setups (cf. figure 6.2(i)). The minor differences in the fine structure of the density between plume #1 and plume #3 (cf. figure 6.2(j)) are not visible in the magnetic field signatures. The B_x and B_z perturbations generated by plume #2 reveal a more gradual decrease in the inbound segment of the E7 trajectory than the other plume setups. Moreover, the "W"-like decrease of the B_y component assumes its minimum value already about $0.5R_E$ outside of the flux tube while the two minima of the "W"-like B_y perturbations from plumes #1 and #3 are located at the surface of the flux tube. In the outbound region, the B_y perturbations of all three plumes are nearly identical. These differences are probably caused by the larger neutral density of plume #2 in the inbound region of E7 (cf. plots 6.2(i) and 6.2(j)).

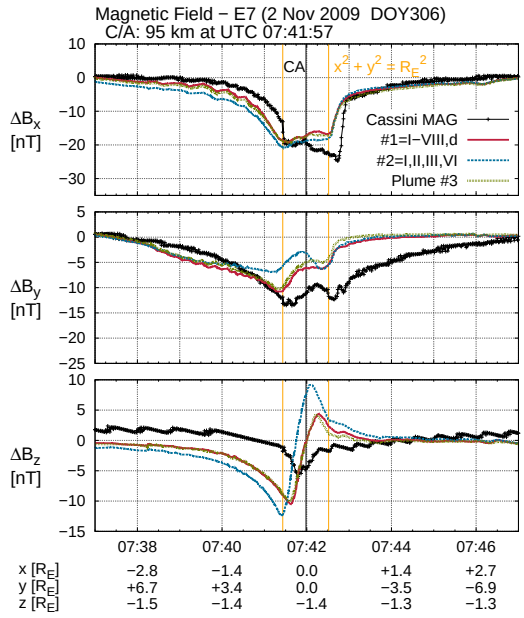

(a)

Figure 6.9: Magnetic field data (black) and simulation results (red, blue, green) for the three neutral plumes (cf. section 6.2) along the E7 trajectory.

The fact that the density profile of plume #2 does not reproduce the second peak seen in INMS data from E7 (cf. figure 6.2(j)) may also explain the larger discrepancy between the B_z perturbations of plume #2 and MAG data around closest approach, compared to the other two plume setups. Out of the three neutral plume setups, plume #3 agrees best with INMS data and as good as plume #1 with MAG data. Therefore, plume #3 will be used as our default neutral plume for all plasma simulations presented in this study.

6.5.2 Influence of Dust Current (E17)

Before we discuss the magnetic field signatures generated by the dust, we first explain the basic idea of how the dust can influence the magnetic field. In principle, the dust can contribute to the currents in two different ways:

- Modification of the quasi-neutrality condition (QN) eq. (6.11) and therefore the current as
$$\underline{j} = e\left(n_i\underline{u}_i - (n_i - \xi n_D)\underline{u}_e\right) \quad . \tag{6.18}$$
- Modification of the quasi-neutrality condition *and* a direct contribution of the dust velocity $\underline{u}_D$ to the current. This yields
$$\underline{j} = e\left(n_i\underline{u}_i - (n_i - \xi n_D)\underline{u}_e - \xi n_D\underline{u}_D\right) \quad . \tag{6.19}$$
For simplicity, in the following we will refer to the term $-e\xi n_D\underline{u}_D$ as "dust pick-up current".

The first case has already been analyzed in the previous chapter. However, the results for the dust plume (see section 6.4.3) have shown that a significant amount of the dust grains is being charged and picked up. These grains possess a non-negligible velocity perpendicular to the magnetic field and we need to investigate if this velocity makes a noticeable contribution to the currents and magnetic field perturbations.

For this reason, figure 6.10(a) shows a comparison between Cassini observations (black) and the results of two simulation runs for the E17 flyby. These simulations are characterized by: (1, red) the hybrid simulation uses only the dust density profile $\xi n_D(\underline{x})$ obtained from the Monte-Carlo simulations. The corresponding dust velocity $\underline{u}_D$ is set to zero in the hybrid simulation. (2, blue) the identical dust profile $\xi n_D(\underline{x})$ is applied, but the dust pick-up current is also included. This is our default setup. Again, the vertical orange and black lines indicate the surface of the Enceladus flux tube and closest approach, respectively.

Since the magnetic field observations from the E17 flyby have not yet been presented in the literature, we discuss them in some more detail here. The shape of the ΔB_x signature is very similar to the "U"-shape of ΔB_x from E7 and corresponds to Cassini's passage through the center of the northern Alfvén wing. However, the B_x decrease observed during E17 possesses a depth of about 30 nT, i. e. the perturbation is about a factor of 1.5 stronger than during E7 ($\Delta B_x = -20\,\mathrm{nT}$). This finding is consistent with a positive correlation between upstream density n_0 and the B_x perturbation (in the far field Alfvén wing solution, it is $\Delta B_x \sim \sqrt{n_0}$), since the upstream density was $n_0 = 110\,\mathrm{cm}^{-3}$ for E17 and only $n_0 = 60\,\mathrm{cm}^{-3}$ during E7 (cf. table 2.2). Inbound, B_x decreases gradually from $\Delta B_x = 0$ to $\Delta B_x = -30\,\mathrm{nT}$. Outbound, however, ΔB_x increases by more than 10 nT within 10 km around 18:30:44 UTC across the surface of the Enceladus flux tube. This discontinuity-like jump probably results from the hemisphere coupling current system predicted by *Saur et al.* [2007]. Furthermore, this behavior is consistent with MAG data from E7 and E9 which also exhibit such a discontinuity-like jump across the ($y > 0$) surface of the flux tube, but not across the ($y < 0$) surface [*Simon et al.* 2011b]. The B_y perturbation exhibits an even more asymmetric shape. Inbound, ΔB_y decreases by about 10 nT from 18:29:00 to 18:29:30 UTC. This decrease is followed by a very sharp dip reaching $\Delta B_y = -20\,\mathrm{nT}$ near closest approach. After closest approach ΔB_y increases to $\Delta B_y = -10\,\mathrm{nT}$. Across the ($y > 0$) surface of the flux tube, one can again see a discontinuity-like decrease of the B_y component by 5 nT. Outbound, ΔB_y gradually increases until the perturbation vanishes at $y \geq 10 R_E$. The observed B_z perturbation possesses a "W"-like shape with a peak magnitude of about $\Delta B_z = -12\,\mathrm{nT}$. The local maximum in the middle of the "W" of $\Delta B_z = -5\,\mathrm{nT}$ was observed at closest approach. This B_z perturbation is consistent with the pile-up of the magnetic field at the ramside of the plume, as will be discussed in section 6.5.5.

The two simulations shown in figure 6.10(a) reproduce the key features of the data. The inbound decrease of B_x is perfectly matched by our model. Outbound, however, the simulations do not show the sharp B_x increase seen in the data and increase more gradual to the background value in the ($x > 1R_E, y > 1R_E$) sector. The peak strength of the simulated B_x perturbations is about 5 nT too weak in both cases. For the B_y component, the simulations show a similar inbound-outbound asymmetry as the observation. In the outbound segment, the B_y perturbations are few nT stronger than in the observation. Within the flux tube, however, our simulations do not reproduce the dip in ΔB_y. In panel 6.10(b), we dis-

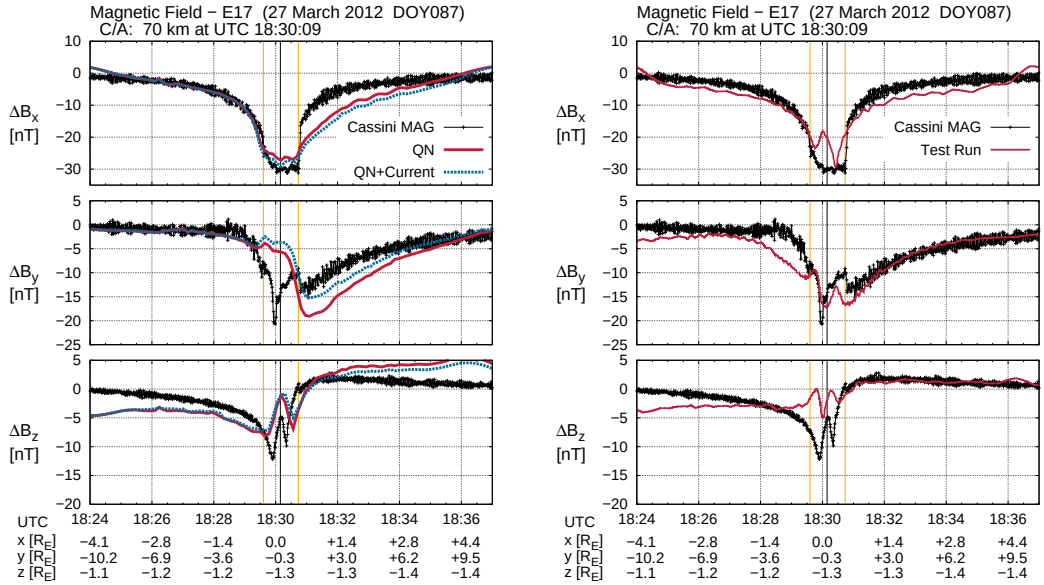

Figure 6.10: Magnetic field data (black) and simulation results (red,blue) along the E17 flyby. The two simulations illustrate how the dust can influence the currents and magnetic field structures: (1, red) only by electron absorption and the corresponding modification of the quasi-neutrality condition (QN); (2, blue) by electron absorption and a contribution of the dust velocity to the currents (QN+current). Plot (b) displays a simulation (red line) with the analytical dust plume and an arbitrarily chosen lower ionization frequency $\nu_{io} = 2 \cdot 10^{-8}\,\mathrm{s}^{-1}$ to show that the simulation could in principle generate the observed B_y perturbation.

play a run that uses a lower ionization frequency of $\nu_{io} = 2 \cdot 10^{-8}\,\mathrm{s}^{-1}$ and the analytical dust profile. From this simulation, we learned that this spike can in principle be generated by our simulations and therefore results from the spatial distribution of n_e/n_i. However, we have argued in section 6.4.2 that the effective ionization frequency $\nu_{io}^{(2)}$ or an even larger value is required for consistency with CAPS nanograin observations. Unfortunately, we have not yet found a set of simulation parameters that simultaneously explains CAPS nanograin observations and the B_y dip observed within the Enceladus flux tube. In the B_z component, the observed "W"-like structure is qualitatively reproduced by the simulations. However, the magnitudes of the simulated perturbations are about 5 nT too weak. The simulated ΔB_z returns to zero within the center of the "W", whereas the measured field perturbation remains negative.

The key issue revealed by figure 6.10(a), however, is that both simulations produce very similar magnetic field structures. Especially for B_x and B_z, the differences are negligible. Only in the $y > 0$ half-space which is populated by picked-up dust grains (i. e. outbound), the simulated B_y perturbation without dust pick-up current (red) is a few nT stronger. This leads to an important conclusion: although the spatial distribution of the dust charge density has a strong impact on the magnetic field structures, the contribution $-e\xi n_D \underline{u}_D$ of the dust to the total current generates a measurable effect only in the pick-up region.

There, the dust velocity is large enough to have a small influence on the strength of the B_y perturbation. The overall shape of the B_y perturbations, however, remains completely unaffected by the inclusion of the non-vanishing dust velocity. This finding can be explained with the analytical description of the currents associated with dust according to equation (5.12). For convenience, the expression for the current j_x is repeated here,

$$j_x = -en_i u_i \left(\frac{\tilde{\nu}_i^2}{\tilde{\nu}_i^2 + \Omega_i^2} - \frac{\xi n_D}{n_i} \left(1 - \frac{u_{D,x}}{u_i} \right) \right) \quad . \tag{6.20}$$

The negative B_y perturbation measured along E17 implies a positive j_x (cf. section 5.2). From equation (6.20), it is then clear that the second term in brackets has to be larger than the first one (Anti-Hall effect). If the x component of the dust velocity $u_{D,x}$ is significantly smaller than the ion bulk velocity, the major effect of the dust on j_x arises from the dust charge density ξn_D. South of Enceladus, $|u_{D,x}| \ll u_i$ is well fulfilled. In that region, only the spatial distribution of the dust charge density $\xi n_D(\underline{x})$ has a non-negligible impact on the magnetic field structures. Outside the flux tube at $y > 1R_E$, the part of the "finger"-like structure in ξn_D intersected by E17 is tilted towards positive x (cf. figure 6.8(h)). This implies a non-vanishing $u_{D,x} > 0$ due to dust pick-up. The second term in eq. (6.20) is therefore reduced (but is still larger than the first term, since the Anti-Hall effect is still present) and leads to a weaker B_y perturbation in the simulation including the dust pick-up current (cf. figure 6.10(a)).

The B_x perturbation is mainly generated by the current in y direction which can be expressed as (cf. eq. (5.14))

$$j_y = -en_i u_i \left(\frac{\tilde{\nu}_i \Omega_i}{\tilde{\nu}_i^2 + \Omega_i^2} + \frac{\xi n_D}{n_i} \frac{u_{D,y}}{u_i} \right) \quad . \tag{6.21}$$

A positive $u_{D,y}$ component of the nanograins therefore leads to a stronger current in agreement with the slightly stronger ΔB_x in the simulation including $\underline{u}_D$ (see figure 6.10).

To sum up, only in the $(x > 0, y > 0)$ sector the dust velocity due to pick-up has a noticeable influence on the magnetic field structures. Anywhere else, only the modification of the quasi-neutrality condition due to the absorption of electrons by the dust grains is important for the magnetic field perturbations.

6.5.3 Pick-up and Length of Dust Plume (E14 and E19)

To analyze how the spatial distribution of the dust charge density ξn_D affects the magnetic field structures, we apply the three dust distributions described in section 6.4.3. Figure 6.11 displays 2D plots of the B_x and B_y components from our simulations as well as MAG data and results for E14 and E19. The first column (panels (a),(d),(g)) shows the results for the analytical dust plume from eq. (6.6). The middle column displays the results for the dust plume from the Monte-Carlo simulations with the diffuse sources only and the third column shows the results for the dust plume using only the jet sources. Panels (a)–(f) display ΔB_x and ΔB_y at $z = -1.5R_E$, i. e. approximately in the plane where the E7, E14, E17 and E19 flybys took place. The projections of the flyby trajectories on this plane are also plotted. ΔB_y is also provided in the $y = 0$ plane in panels (g)–(i) along with the

projection of the E5 trajectory on this plane. The 2D plots 6.11(a)–6.11(i) were obtained from simulations where the upstream ion density has been set to $n_0 = 85\,\mathrm{cm}^{-3}$, according to the value for E14. Plots (j) and (k) display the B_x and B_y perturbations from MAG data and three simulations for E14 and E19, respectively. The corresponding B_z perturbations will be analyzed in section 6.5.5.

The color plots of ΔB_x (panels 6.11(a)–(c)) look very similar for the three simulations. The negative B_x perturbations in the center of the flux tube indicate a cut through the northern Alfvén wing (cf. figure 5.7). In contrast to that work, our new results do not show regions with positive ΔB_x outside both, the Saturn-facing and the Saturn-averted side of the flux tube. This is consistent with MAG data from E7, where our new result did not show an overshoot of the B_x perturbation at the surface of the flux tube (see section 6.5.1). Within the flux tube, a maximum field decrease of $\Delta B_x \approx -20\,\mathrm{nT}$ is achieved. In addition, the B_x perturbations from the two simulations with the Monte-Carlo dust plumes exhibit similar "finger"-like structures as the dust charge density (cf. figures 6.8(h) and 6.8(k)). The magnitude of the B_x perturbations is about $|\Delta B_x| = 15\,\mathrm{nT}$ in these narrow regions of high dust charge density. The wave structures visible in panels 6.11(b) and (c) at about $x > 0$ and $y > 3$ are numerical artifacts, which, however, do not affect our conclusions.

In contrast to ΔB_x, the B_y perturbations of the three simulations are quite different from each other. In the simulation with the analytical dust profile (panels (d) and (g)), the B_y component is perturbed in a broad region that extends into both, the Saturn-facing and the Saturn-averted hemisphere of Enceladus. This result is very similar to figure 5.7e. In contrast, the B_y perturbations generated by the Monte-Carlo dust plumes of $|\Delta B_y| \leq 5\,\mathrm{nT}$ are hardly visible in the Saturn-averted half-space ($y < 0$), cf. panels (e) and (f). For $y > 0$, the regions of maximum $|\Delta B_y|$ coincide again with the "finger"-like structure of increased dust charge density. There, ΔB_y assumes values of up to $\Delta B_y = -15\,\mathrm{nT}$. Note that these structures are also visible in the results for the dust plume which considers only the jet sources, although this plume does not exhibit the "finger"-like structure in the dust charge density at $z = -2R_E$ (see panel 6.8(i)). The B_y perturbations therefore reveal a clear imprint of the height-integrated dust distribution.

This effect is also visible when comparing the B_y perturbations generated by the three dust plumes in the $y = 0$ plane (panels 6.11(g)–(i)). In this plane, one can clearly identify the transition region between the northern ($\Delta B_y < 0$) and southern Alfvén wing ($\Delta B_y > 0$).For the analytical dust profile, a perturbation of the B_y component as strong as $|\Delta B_y| > 10\,\mathrm{nT}$ can still be seen at large distances from Enceladus ($z \approx -6R_E$). The southern Alfvén wing even begins at $z = -8R_E$. For the diffuse dust plume, the magnitude of $|\Delta B_y|$ in the $y = 0$ plane is always smaller than 5 nT, cf. panel 6.11(h). Here, the transition between southern and northern wing is located at $z \approx -3R_E$. The B_y perturbations generated by the jet dust plume constitute a mixture of the former two. As can be seen in panel 6.11(i), a region of strongly enhanced $|\Delta B_y|$ is formed below Enceladus' south pole, which extends to $z \approx -4R_E$. In this case, the transition to the southern Alfvén wing takes place at about $z = -5R_E$.

Before we relate the 2D structures seen in panels (a)–(i) to the observations, we will briefly discuss the magnetic field perturbations observed during E14 and E19 (black lines in panels 6.11(j) and 6.11(k)). The shape of the measured ΔB_x signature from E14 is very

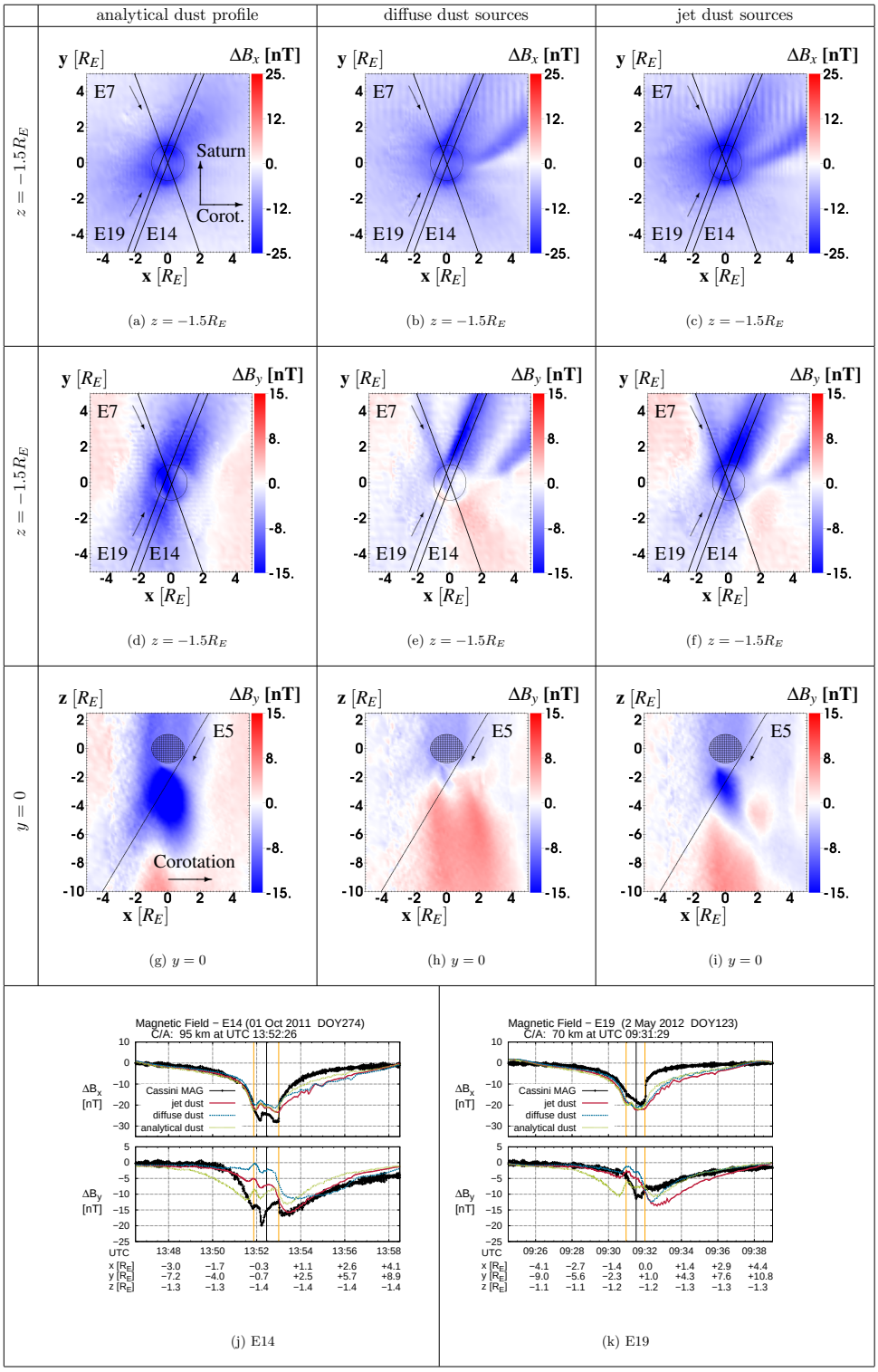

Figure 6.11: Magnetic field perturbations generated by different dust plumes: the first column displays the results for the analytical dust profile from eq. (6.6); the second and third columns show the results obtained with the dust plumes from the Monte-Carlo simulations. The grains either originate only from the diffuse tiger stripe sources (second column) or only from the jet sources (third column). The corresponding dust charge densities are shown in figure 6.8. ΔB_x and ΔB_y are presented in the $z = -1.5R_E$ plane together with the projections of horizontal flybys E7, E14 and E19 on this plane. ΔB_y is also shown in the $y = 0$ plane. Panels (j) and (k) display the B_x and B_y perturbations along the E14 and E19 trajectories, respectively.

similar to E7 and E17. However, the peak magnitude of the perturbation seen during E14 ($\Delta B_x = -25$ nT) is about 5 nT smaller than for E17. This difference might partially arise from the different upstream densities of $n_0 = 85\,\mathrm{cm}^{-3}$ for E14, compared to $n_0 = 110\,\mathrm{cm}^{-3}$ for E17 (cf. table 2.2). In the center of the flux tube, the Alfvén wing far field solution fulfills $\Delta B_x \sim \sqrt{n_0}$. This estimation is roughly consistent with the observed perturbations: $\Delta B_x(E14)/\Delta B_x(E17) = 0.8 \approx \sqrt{n_0(E14)}/\sqrt{n_0(E17)} = 0.9$. Inbound of E19, the observed decrease to the maximum perturbation of about $\Delta B_x = -20\,\mathrm{nT}$ occurs rather gradual compared to the "U"-shape seen during the other flybys (fig. 6.11(k)). In addition, the B_x perturbation observed during E19 does not show the small local maximum around closest approach which was seen during E7, E14 and E17. The reason is the slight upstream displacement of the E19 trajectory compared to E14 and E17. In the outbound regions of E14 and E19, the magnetometer detected a discontinuity-like jump of more than 5 nT when crossing the surface of the Enceladus flux tube. In both cases, this structure possesses a thickness of less than 10 km. The B_y perturbation observed during E14 looks quite similar to the signature seen during E17 (see figure 6.10), but is about 5 nT stronger. However, the sharp dip of $\Delta B_y = -20\,\mathrm{nT}$ before closest approach has the same magnitude as seen during E17. This is different for E19, where the measured B_y is $|\Delta B_y| < 10\,\mathrm{nT}$.

The colored lines which are also plotted in panels 6.11(j) and 6.11(k) are the magnetic field signatures from the three simulations with the different dust plumes. For ΔB_x, all three simulations produce a very similar signature. The strength of the simulated perturbations of $\Delta B_x \approx -20\,\mathrm{nT}$ is weaker than the perturbation of $\Delta B_x \approx -25\,\mathrm{nT}$ observed during E14. The magnitude of the dip seen during E19 is well reproduced. The simulations succeed in reproducing both, the location and the steepness of the inbound decrease in B_x. The simulated ΔB_x also shows the small local maximum around closest approach of E14. The location of the ΔB_x minimum seen during E14 and E19 at the outbound edge of the flux tube is reproduced as well. Outside the flux tube at $y > 0$, the discrepancies between data and simulations are larger for both flybys: the simulated fields gradually increase to the background value while the data reveal a discontinuity-like enhancement of B_x across the flux tube. Again, the observed structure is probably caused by hemisphere coupling currents [*Saur et al.* 2007].

The B_y component exhibits stronger differences between the three simulations. For E14 (panel 6.11(j)), the inbound perturbation caused by the analytical dust plume (green) already commences at about 13:49 UTC, whereas the measured field is still unperturbed until 13:51 UTC. In the outbound region, the magnitude of the B_y perturbations is slightly underestimated by the analytical dust plume. Within the Enceladus flux tube, however, the analytical dust plume yields a better fit to the data than the simulated dust plumes. Unlike the analytical profile, both Monte-Carlo dust plumes succeed in reproducing the B_y perturbation in the outbound region of E14. Below the south pole, however, the diffuse dust plume (blue) does not produce a noticeable ΔB_y, while the jet dust plume (red) generates a B_y perturbation with a strength of about 50% of the measured ΔB_y, i. e. this is still weaker than the perturbations generated by the analytical dust profile.

These results lead to number of important conclusions, especially when one considers the underlying dust densities (fig. 6.8). The asymmetry of the B_y perturbations inbound and outbound of E14, E17 and E19 is reproduced only by the simulated dust plumes. Therefore, these asymmetries are associated with the deformation of the plume due to

dust pick-up. It is, however, surprising that even for the analytical dust plume – i. e. without pick-up – we find that B_y is also perturbed in the ($y > 1R_E$) sector (see panel 6.11(d)). Since for the analytical plume, this perturbation can also be seen at ($y < -1R_E$), we conclude that dust pick-up is not only responsible for generating the B_y perturbations in the Saturn-facing hemisphere ($y > 1R_E$), but the pick-up process also leads to the absence of B_y perturbations in the Saturn-averted hemisphere. Due to pick-up, this sector is essentially devoid of charged grains which results in a weaker or vanishing B_y perturbation. Thus, the asymmetry of the observed B_y perturbations is a direct consequence of the pick-up of negatively charged dust grains.

The results for the southward extension and strength of the B_y perturbations seem to be even more surprising. Compared to the Monte-Carlo plume models, the dust charge density directly below the south pole is much smaller for the analytical model (cf. figure 6.8). Nevertheless, the analytical plume model generates much stronger and more extended negative B_y perturbations south of Enceladus than the other two plumes (cf. plots 6.11(g)–(i)). In particular, the high dust charge density and strong electron absorption of the diffuse dust plume does not produce a noticeable negative B_y directly below the south pole. The dust charge densities of the three dust plumes (see figure 6.8) suggest that neither the absolute value of the charge density ξn_D nor the relative amount of free electrons directly below Enceladus determines the location of the draping center (i.e., the location of the transition between northern and southern Alfvén wing, cf. panels 6.11(g)–(i)), but the *southward extension* of the region where a considerable fraction of the electrons is attached to the dust (see panels 6.8(d)–(f)).

Furthermore, MAG data from E14 and E17 reveal a strong ΔB_y directly below the south pole (see plots 6.10 and 6.11(j)). Therefore, even the observed magnetic field perturbations from these horizontal flybys require a sufficiently large southward extension of the dust plume. In addition, MAG data from the steep encounters E3 – E6 exhibit a negative B_y perturbation even at $z \approx -4R_E$ (see previous chapter). In combination with the results presented in panels 6.11(h) and 6.11(i), these observations imply that the southward extension of the dust plume is larger than seen in the results with the Monte-Carlo dust plume that uses only the diffuse sources. Hence, Enceladus' dust plume is probably better described by the model that comprises only the jet sources. Most of the nanograins might therefore be ejected with velocities as high as $u_{D0} = 2000\,\mathrm{m/s}$, implying a Mach number of $M = 6$ for the neutral gas. This finding is roughly consistent with the model of *Postberg et al.* [2011], who concluded that small, non-salty grains are ejected in the fast jets with $u_{D0} = 1200\,\mathrm{m/s}$ while the larger grains are ejected from the tiger stripe sources at lower velocities. However, it is possible that – apart from the high surface velocity – other effects like changes in the value of ionization rate in combination with a different dust production rate lead to lower numbers of "free" electrons and in consequence, a sufficiently long charging time of the grains. This would result in a further southward extension of the charged dust plume and could therefore also explain the magnetic field observations. Furthermore, additional or stronger jets pointing towards upstream and in the anti-Saturnward direction could in principle produce a stronger B_y perturbation below the south pole as well.

6.5.4 Distant Nanograin Pick-Up (E15)

In contrast to all other flybys discussed in this paper, the E15 encounter did not pass through the center of the plume, but it occurred far downstream of Enceladus. This makes E15 particularly suitable to analyze if the magnetic signatures of nanograin pick-up can still be observed at large distances to Enceladus. In figure 6.12(a), we therefore show the measured magnetic field signatures (black) along the E15 trajectory togehter with the simulation results (red). In addition, the simulated magnetic field perturbations ΔB_x and ΔB_y in the $z = -1.5R_E$ plane are shown in panels 6.12(b) and 6.12(c), respectively. The presentation is similar to figure 6.11, but the range is shifted to $x \in [2R_E, 12R_E]$ to enclose the E15 trajectory.

The magnetic field signatures measured during E15 are quite remarkable considering that the perturbations occurred far away from the center of the neutral plume. Both, B_x and B_y exhibit a sharply pronounced decrease at about ($x = 7R_E$, $y = 2R_E$) and achieve minimum values of $\Delta B_x \approx -10\,\mathrm{nT}$ and $\Delta B_x \approx -8\,\mathrm{nT}$, respectively. Outbound, the perturbations gradually decrease to zero. ΔB_z exhibits a small dip of about $\Delta B_z = -3\,\mathrm{nT}$ at $y \approx 0$, i.e., it is displaced with respect to the perturbations in B_x and B_y.

Our simulation is in qualitative agreement with MAG data for the B_x and B_y components, while the model does not show any perturbations of B_z. Panels 6.11(b) and 6.11(c) show

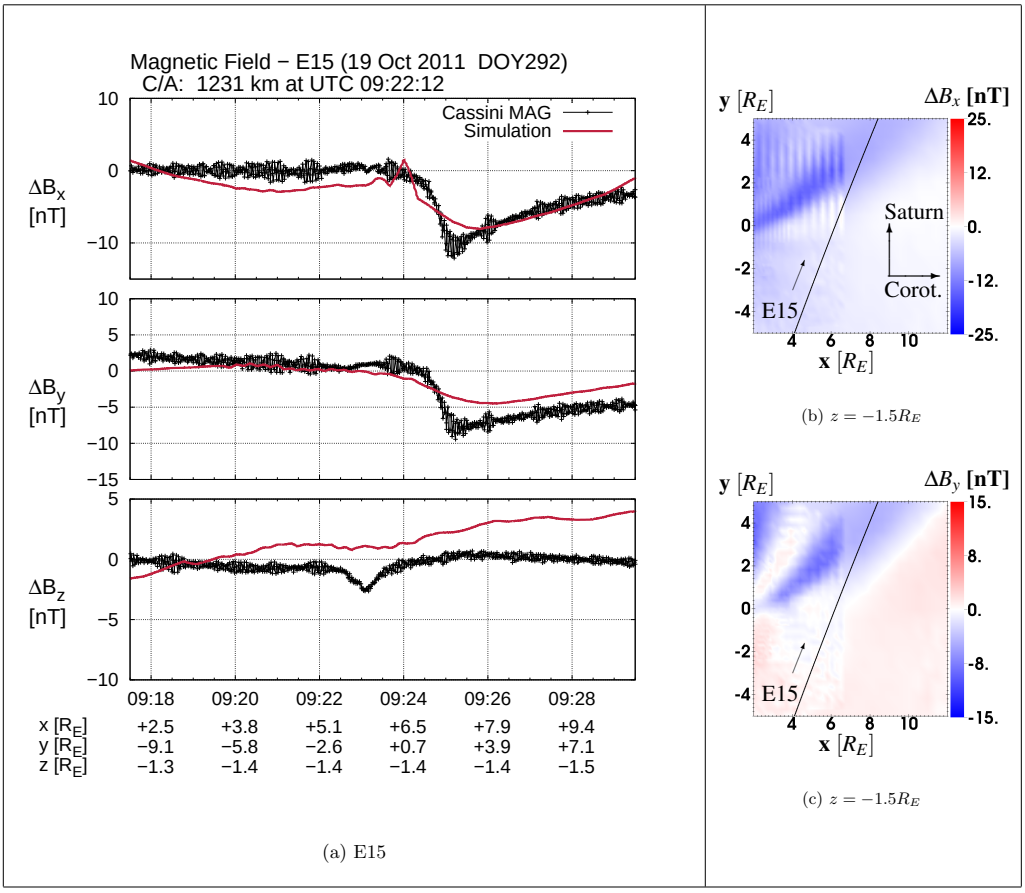

Figure 6.12: Magnetic field perturbations along the E15 trajectory: (a) MAG data (black) and simulation results (red), (b) and (c) B_x and B_y perturbations in the $z = -1.5R_E$ plane.

that the B_x and B_y perturbations originate from the plume. They coincide with the rightmost part of the "finger"-like structure in the dust charge density (cf. fig 6.8). The onset of these structures in ΔB_x and ΔB_y is also visible in the plots for E14 in figure 6.11. Therefore, it is very likely that the magnetic field perturbations observed during E15 arise from Cassini's passage through the distant nanograin pick-up tail of Enceladus. The wave structures visible in panels 6.12(b) and (c) as well as the increase of ΔB_z outbound of the trajectory are numerical artifacts, which, however, do not affect our conclusions.

6.5.5 The "Missing" Magnetic Field Decrease (E14 and E19)

A very puzzling feature of the measured magnetic field signatures at Enceladus is the fact that during all 20 flybys which took place until 2012 only a negative perturbation of the B_z component has been observed. Since $\underline{B}_0 = -B_0\underline{e}_z$, a region with $\Delta B_z < 0$ corresponds to an enhancement of the magnetic field strength, i. e. a pile-up of the magnetic field at the ramside of the obstacle. In other words, the corresponding decrease of the magnetic field has not been observed by Cassini. According to Ampère's law, however, the perpendicular currents in the plume have to generate both, positive and negative ΔB_z somewhere in the vicinity of the plume. In this section, we therefore investigate how the dust influences the location of the magnetic field decrease which needs to be present at Enceladus.

Figure 6.13 shows 2D cuts through the simulation box and a comparison between MAG data and modeled fields for the three dust plumes along E14 and E19. The B_z perturbations presented in that figure correspond to the B_x and B_y perturbations shown in figure 6.11. Panels (a)–(c) display ΔB_z in the $z = -1.5R_E$ plane for the three different dust plumes. Plots (d) and (e) show the B_z perturbations along the E14 and E19 trajectories, respectively. Similar to figure 6.11, MAG data are colored black, and the three simulations consider the analytical dust profile (green), the diffuse dust plume (blue) and the jet dust plume (red). At first glance, the color plots of ΔB_z look rather similar for all three dust plumes. Upstream, the magnetic field piles up to a peak value of about 10 nT. In the downstream half-space ($x > 0$), a large region of reduced B_z is formed. When using the analytical plume model (cf. panel 6.13(a)), the magnetic field enhancement is confined to the upstream half-space ($x < 0$), but the transition region from field enhancement to field decrease already exhibits a slightly curved shape. When using the diffuse dust plume, the magnetic pile-up region exhibits several "tongue"-like extensions into the downstream half-space at both, the Saturn-facing and the Saturn-averted side of Enceladus (cf. panel 6.13(b)). The longest of these "tongues" (located at $y = 1R_E$) generates a field enhancement as far as $x = 3R_E$ downstream of the moon. Although these structures are less prominent for the jet dust plume, the magnetic pile-up region is more extended towards downstream in the ($y < 0$) half-space than in the ($y > 0$) half-space. Although these differences seem to be insignificant, they are quite apparent along the trajectory of E14 (see panel 6.13(d)). The measured B_z perturbations (black) exhibit a "W"-like shape with a similar strength as seen along E17. While the analytical dust profile (green) does not reproduce the "W"-structure, the two simulated dust plumes (red and blue lines) do.

This "W"-like structure is readily explained by plots 6.13(b) and 6.13(c): for the dust plumes obtained from the Monte-Carlo simulations, the dust pick-up goes along with an extension of the pile-up region towards downstream for $y < -1R_E$ as well as $y > 0$. The

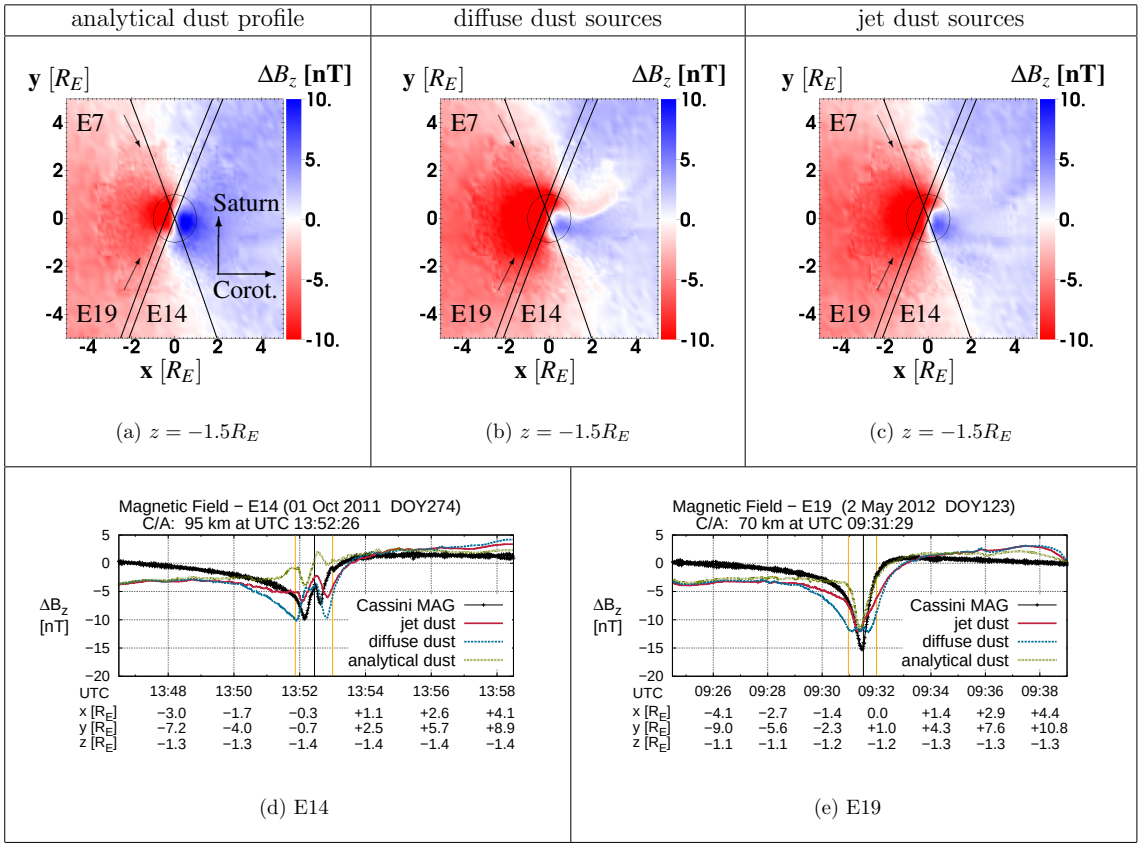

Figure 6.13: Continuation of figure 6.11: simulated B_z perturbations for the three different dust profiles in the $z = -1.5R_E$ plane (panels (a)–(c)) and along the E14 and E19 trajectories (panels (d) and (e)).

figure reveals that E14 (and also E17, see fig. 6.10) passed through a region with $\Delta B_z < 0$ inbound and outbound, which leads to the two minima of the "W"-like structure. Near closest approach, however, Cassini briefly penetrated the outer edge of the field decrease, which led to the local maximum of the "W"-like structure. In contrast to that, MAG data from E19 exhibit a "V"-like ΔB_z signature and a stronger maximum perturbation of about $|\Delta B_z| = 15$ nT (plot 6.13(e)). This can be explained with the slight upstream displacement of the E19 trajectory, compared to E14 and E17: Cassini was embedded in the magnetic pile-up region during the entire duration of the E19 flyby and did not cross the outer edges of the wakeside field decrease. Thus, the "W"-like B_z structures seen during E14 and E17 arise from the curved shape of the boundary between the magnetic pile-up region and the wakeside field decrease, which allowed the spacecraft to intersect a localized "tongue" of the magnetic field decrease around closest approach.

The spikes in the center of the "W" seen during E14 and E17 (and E18, cf. figure 6.14) are the only signatures of the wakeside field decrease which have so far been detected at Enceladus. For E19, the B_z perturbations of all three simulations are in good agreement with MAG data. In particular, the analytical dust profile and the jet dust plume match the steep outer flanks of the "V"-shaped decrease of ΔB_z very well.

The color plots also explain the bipolar signature of the simulated B_z perturbations for E7 (see fig. 6.9). In the model picture, Cassini passed through the pile-up region on

the inbound leg of E7, while it intersected the field decrease on the outbound leg. Since the field decrease is not present in MAG data from E7, this implies that the upstream extension of the field decrease for $y < 0$ may be slightly overestimated by our model. As discussed in section 6.5.3, in that region our dust model does not reproduce the observed magnetic field structures in the B_x and B_y components either. It is therefore very likely that the dust plume is also responsible for the discrepancies between data and simulations of the B_z perturbations.

Note that the B_z perturbations along the various flyby trajectories through the center of plume are extremely sensitive to the exact location and shape of the field decrease region which is in turn dependent on the combination of ionization rate and dust plume.

6.5.6 Plume Variability

Recently, *Hedman et al.* [2013] found a variation in the plume activity which is correlated to varying tidal stresses caused by Enceladus' slightly eccentric orbit (cf. section 2.1). Note that the orbital period of Enceladus of about 33 h is significantly larger than the simulation time of 330 s and therefore, our model assumes quasi-stationarity of the plume within the simulation time. Thus, studying plume variability by means of our model is possible only on a flyby-to-flyby base. Although in the previous chapter, we used Cassini MAG data to derive a plume variation of a factor of 2.5 between different flybys, we refrain from studying the plume variability by applying our improved model to MAG data. The major reason is that a reliable study of plume variability based on our new multi-jet plume model would require systematic parameter studies with different jet and diffuse sources. Such a study, however, is not feasible due to the large number of necessary simulations.

Although we cannot analyze plume variability with our simulation model, it is possible to search MAG data from different flybys for indications of plume variability. Figure 6.14 displays the magnetic field observations of three flybys with nearly identical trajectories: E14 and E17 as well as the E18 encounter. The data are displayed as a function of time relative to closest approach. The B_x perturbations seen during E14 and E18 have nearly the same strength, while for ΔB_y and ΔB_z, E18 is nearly identical to E17. Only the sharp spike in ΔB_y near closest approach of E17 was absent during E18.

We have demonstrated that the B_z perturbations along E14, E17 and E18 are highly sensitive to the location and extension of the field decrease. It requires extensive modeling to determine how this region reacts to plume variability and changes in the upstream density. Thus, B_z does not contain easily accessible information on plume variability. The B_y perturbations are associated with the Anti-Hall effect, i. e. they depend in a non-linear way on the dust charge density ξn_D and the neutral density (through the effective collision frequency, $\tilde{\nu}_i$). Moreover, changes in the *charge* density ξn_D are not necessarily proportional to changes of the total dust density (charged + uncharged). Therefore, it is not clear how a simultaneous increase of the neutral and dust production rate would be related to an increase or decrease of $|\Delta B_y|$. For these reasons, we do not regard ΔB_y as suitable to analyze plume variability.

If no plume variability were present, we would expect the magnitudes of the B_x perturbations from the three flybys to be ordered by their respective upstream densities n_0 of

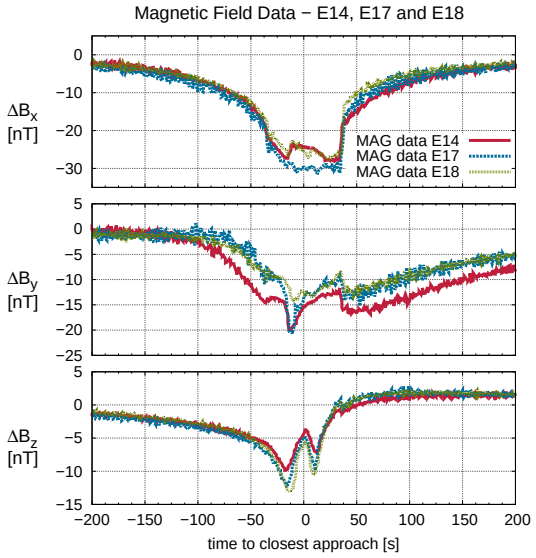

Figure 6.14: Comparison of Cassini MAG data from E14, E17 and E18.

$85\,\mathrm{cm}^{-3}$(E14) $< 100\,\mathrm{cm}^{-3}$(E18) $< 110\,\mathrm{cm}^{-3}$(E17). Since the magnitude of the B_x perturbations observed during E17 is larger than for the two other flybys, this is at least partially fulfilled. The magnitude of ΔB_x of E14, however, is equal to that of E18. This would suggest a higher plume activity during E14 compared to E18. But due to uncertainties in the upstream densities of at least $\Delta n_0 \sim 5\,\mathrm{cm}^{-3}$, the upstream densities may also have been nearly identical during both flybys. Therefore, we are not able to infer any kind of plume variability from MAG data without extensive modeling efforts.

7 Analysis of Cassini magnetic field observations over the poles of Rhea

 The publication can be found under the following reference:
Simon, S., **H. Kriegel**, J. Saur, A. Wennmacher, F. M. Neubauer, E. Roussos, U. Motschmann, and M. K. Dougherty (2012), Analysis of Cassini magnetic field observations over the poles of Rhea, *Journal of Geophysical Research (Space Physics)*, *117*, A07211, doi: 10.1029/2012JA017747

During the first close Rhea flyby (R1 on 26 November 2005), Cassini passed through the plasma wake downstream of the moon at a distance of about $0.7R_{RH}$ (see figure 2.11). Observations made by MAG during this encounter suggested Rhea to be an electromagnetically inert object that interacts with the impinging magnetospheric plasma mainly by absorbing the particles incident upon its surface in agreement with section 3.1. Subsequently, Cassini accomplished the two polar flybys R2 and R3 (see section 2.3.2). During both polar flybys, the Cassini MAG instrument detected significant magnetic field perturbations inside the Rhea fluxtube, the surface of which is defined by the bundle of field lines tangential to the solid body of the moon. While *Santolík et al.* [2011] applied Cassini particle and magnetic field observations to demonstrate the presence of intense plasma wave emissions at the time of the R2 encounter, the origin of the large-scale magnetic field perturbations seen during R2 and R3 has so far not been addressed in the literature. Especially, MAG data from both flybys contain strong perturbations of the flow-aligned magnetic field component ("draping"). At first glance, this seems untypical for the plasma interaction of an obstacle that affects the incident magnetospheric plasma mainly by absorbing it (see, e.g. *Khurana et al.* [2008], *Roussos et al.* [2008a], *Simon et al.* [2009a]).

Here, we present a detailed analysis of the Cassini magnetic field observations acquired during the two polar Rhea flybys R2 and R3. The origin of the observed field perturbations is discussed, on the one hand, by applying simple analytical models of the interaction between an inert moon and the incident flow. On the other hand, we continue the work of *Roussos et al.* [2008a] and present new hybrid simulations of Rhea's interaction with the magnetospheric plasma, taking into account the upstream flow conditions observed during R2 and R3.

This chapter is organized as follows: in section 2, we classify the interaction between Rhea and the incident magnetospheric flow. After providing a brief overview of the ambient magnetospheric plasma parameters at Rhea's L shell (section 2.2), we derive an upper limit for the contribution of Rhea's exosphere to the observed magnetic field perturbations (section 7.1). In section 3, we focus on the interpretation of MAG data from R2 and R3. A brief discussion of the two flyby trajectories (section 2.3.2) is followed by an analysis of MAG data from the south polar R3 flyby in section 7.2.1 and results from complementary hybrid simulation runs in section 7.2.2. Our analysis of MAG data from the north-polar R2 encounter is provided in section 7.2.3.

7.1 Magnetic visibility of Rhea's exosphere

As discussed in section 2.1, INMS data indicate the presence of a tenuous, sputtering-induced atmosphere around Rhea, consisting mainly of molecular oxygen [*Teolis et al.* 2010]. Simultaneously, the Cassini Plasma Spectrometer (CAPS) observed outflowing positive and negative pick-up ions. However, *Khurana et al.* [2008] as well as *Roussos et al.* [2008a] succeeded in explaining MAG data from the first close Rhea encounter (R1) by considering Rhea an electromagnetically inert object that does not possess an atmosphere.

One reason for this apparent discrepancy is that the trajectory of the R1 encounter was not suitable for identifying signatures of a possible gas envelope around Rhea in the magnetic field data. During R1, Cassini passed through Rhea's plasma wake, with the spacecraft trajectory being confined to the ($z = 0$) plane. If a flyby above or below Rhea's equatorial plane had been available, the orientation of the measured B_y perturbations could have been employed to clearly discriminate between a mainly plasma-absorbing obstacle and an interaction scenario that is dominated by mass/momentum loading (see figure 10 in *Khurana et al.* [2008] and figure 1 in *Simon et al.* [2009a]). However, for a flyby like R1 that occurred in Rhea's orbital plane, the B_y perturbation is almost zero in both cases (assuming that a possible atmosphere does not possess a pronounced north-south asymmetry).

Thus, if Rhea's atmosphere caused any measurable magnetic field perturbations, the polar flybys R2 and R3 would have been suitable to identify such signatures. However, based on the parameters provided by *Teolis et al.* [2010], we expect the gas envelope around Rhea to be magnetically invisible even during these close encounters. In order to estimate if Rhea's exosphere/ionosphere could generate any noticeable magnetic field perturbations, we calculation the interaction strength parameter $\overline{\alpha}$ (see section 3.2.2) for Rhea.

Based on the upstream flow parameters provided in section 2.2, we obtain a value of $\Sigma_A = 13.2\,\mathrm{S}$ for the Alfvén conductance in the Rhea scenario. An order-of-magnitude estimate for the Pedersen conductance Σ_P can be obtained from the atmospheric parameters of *Teolis et al.* [2010] who derived a total atmospheric O_2 content of $N_{tot} = 2.5 \cdot 10^{29}$ molecules. For our estimate, we assume the spatial distribution of the neutral gas around Rhea to be spherically symmetric and to be prescribed by equation 1 in the work of *Saur and Strobel* [2005], i.e.

$$n_n(r) = n_{n,0}\left(\frac{R_{RH}}{r}\right)^2 \exp\left(\frac{R_{RH}-r}{D}\right) \quad , \tag{7.1}$$

where r denotes the distance to the center of Rhea. From the work of *Saur and Strobel* [2005], we adopt a value of $D = 100\,\mathrm{km}$ for the depletion length scale, while the base density n_0 can be derived from the total gas content of the atmosphere N_{tot} according to

$$n_{n,0} = \frac{N_{tot}}{4\pi R_{RH}^2 D} \quad . \tag{7.2}$$

From the work of *Simon et al.* [2011a], we adopt a value of $\kappa = 1 \cdot 10^{-8}\,\mathrm{cm}^3/\mathrm{s}$ for the reaction rate between magnetospheric water group ions and oxygen molecules at a relative velocity of $u_0 = 40\,\mathrm{km/s}$, considering charge-exchange reactions and elastic collisions. This allows to compute the (effective) ion-neutral collision frequency according to $\tilde{\nu}_i(r) = \kappa n_n(r)$. The ratio of the ion gyrofrequency and the collision frequency is then applied to compute the local Pedersen conductivity according to

$$\sigma_P(r) = \frac{e n_0}{B_0} \cdot \frac{\frac{\Omega_i}{\tilde{\nu}_i(r)}}{\left(\frac{\Omega_i}{\tilde{\nu}_i(r)}\right)^2 + 1} \quad , \tag{7.3}$$

see equation (3.56). By numerically integrating eq. (7.3), we now compute the Pedersen conductance Σ_P along a magnetic field line that intersects Rhea at the north pole, i.e.

$$\Sigma_{P,1} = \int_{r=R_{RH}}^{\infty} \sigma_P(r)\,\mathrm{d}r \quad , \tag{7.4}$$

and along a magnetic field line that is tangential to the solid body of the moon:

$$\Sigma_{P,2} = \int_{z=0}^{\infty} \sigma_P\left(\sqrt{z^2 + R_{RH}^2}\right)\mathrm{d}z \quad . \tag{7.5}$$

These two values constitute a lower ($\Sigma_{P,1}$) and an upper ($\Sigma_{P,2}$) limit for the Pedersen conductance in the Rhea scenario, see figure 6 in the work of *Neubauer* [1998] for illustration. The estimated values of the Pedersen conductance range between $\Sigma_{P,1} = 0.11\,\mathrm{S}$ and $\Sigma_{P,2} = 0.43\,\mathrm{S}$, respectively, corresponding to an interaction strength of $4.2 \cdot 10^{-3} \leq \overline{\alpha} \leq 1.6 \cdot 10^{-2}$. Thus, the contribution of Rhea's atmosphere to the magnetic field signatures arising from the moon's interaction with the upstream flow can be considered negligible. The pick-up ions generated at Rhea can be treated as test particles that are inserted in a pre-defined electromagnetic field configuration. For comparison, the parameters provided by *Saur et al.* [2007] suggest an interaction strength of $\overline{\alpha} = 0.6$ for Enceladus' magnetospheric interaction. Besides, as will be shown in section 7.2, the key features of the magnetic field observations made during the R2 and R3 flybys can be explained by means of a numerical model that considers only the plasma-absorbing body of Rhea, but not its exosphere. Apart from the estimations provided above, the analysis of the magnetic field data therefore provides independent evidence that Rhea's exosphere was indeed "magnetically invisible" at the times of the R2 and R3 encounters.

We would briefly like to note that Rhea's exosphere might exhibit some degree of time variability, similar to what *Simon et al.* [2011a] found at Dione due to the time-dependency of energetic particle fluxes in Saturn's radiation belts. If at certain time periods Rhea's energetic particle environment is similar to what Voyager 1 saw, then both the atmospheric particle content and the associated magnetic field perturbations will be significantly stronger [*Saur and Strobel* 2005]. For the conditions of the Voyager 1 flyby, these authors derived an interaction strength of $\overline{\alpha} = 0.4$. Voyager 1 estimates for the energetic particle influx to Saturn's icy satellites showed to be consistently much higher than what has been measured by Cassini (e.g. *Roussos et al.* [2008b]), thereby possibly generating an atmosphere around Rhea that was "magnetically visible" at that time.

7.2 Rhea flybys R2 and R3

In this section, we shall present the Cassini magnetic field observations from the two polar Rhea encounters. We will commence our discussion with the R3 flyby, since the data acquired during this passage allow for a much easier depiction of the key features of the interaction than the R2 dataset.

7.2.1 Flyby R3: MAG data

The magnetic field signatures observed during R3 are displayed in the right-hand panels of figure 7.1. The vertical orange lines indicate Cassini's passages through the surface of the Rhea fluxtube $\sqrt{x^2 + y^2} = R_{RH}$. Although the R3 trajectory was located below the south pole and did not intersect the moon's geometric plasma shadow, the magnetic field observations reveal several features immediately indicative of a plasma-absorbing obstacle. The B_z component exhibits a compression signature inside the Rhea fluxtube, i.e. $|B_z|$ is enhanced. Similar enhancements of $|B_z|$ have also been observed in the plasma wakes of Tethys and Dione as well as during the R1 flyby of Rhea [*Khurana et al.* 2008, *Roussos et al.* 2008a, *Simon et al.* 2009a, 2011a]. Such signatures arise from a void in the magnetospheric plasma density due to the absorption of the incident flow at the moon's surface. The resulting deficit of plasma pressure is then compensated by an enhanced magnetic pressure, i.e. the field lines are dragged into the density cavity (see also section 3.1). While for the interaction between the Terrestrial moon and the supersonic solar wind, such field compression signatures occur only in the downstream region [*Kallio* 2005], they expand to above and below the poles, if the flow incident upon the obstacle is subsonic. In this case, the bulk speed of the plasma is exceeded by its thermal speed, i.e. a significant number of particles possess large field-aligned velocities. Therefore, particles which were initially located north or south of Rhea can be absorbed as well, yielding an expansion of the density depletion region to the polar regions of the moon as illustrated in figure 3.1.

The compression signature seen in B_z possesses a magnitude of about 2 nT. This value can be compared to the maximum field compression expected for the void region of the central wake which is (almost) completely evacuated, see figure 3 in the work of *Khurana et al.* [2008]. Based on the pressure balance equation

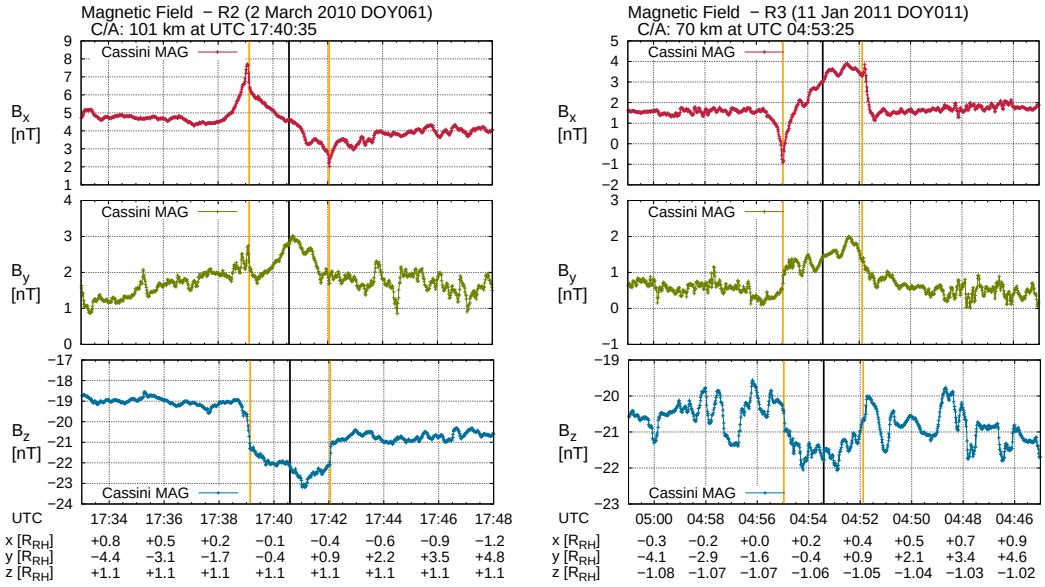

Figure 7.1: Cassini MAG observations during Rhea flybys R2 (left) and R3 (right) in RHIS coordinates. The magnetic field components are shown in red (B_x), green (B_y) and blue (B_z), respectively. The vertical orange lines denote Cassini's passages through the surface of the Rhea fluxtube $\sqrt{x^2 + y^2} = R_{RH}$. Despite the slight deviations of $\underline{B}_0$ from being aligned with the negative z axis, this expression provides a very good approximation for the surface of the fluxtube.

$$n_0 k\,(T_i + T_e) + \frac{B_0^2}{2\mu_0} = \frac{(B_0 + \delta B)^2}{2\mu_0} \tag{7.6}$$

and the upstream parameters provided in section 2.2, we find that a peak field perturbation δB of

$$\frac{\delta B}{B_0} = \sqrt{\beta_i + \beta_e + 1} - 1 \approx 0.47 \qquad , \tag{7.7}$$

i.e. $\delta B \approx 9.8\,\mathrm{nT}$, can be achieved in Rhea's central wake, i.e. the perturbation observed below the south pole is about a factor of 5 smaller. This finding is consistent with the idea of the plasma in the south polar region being only partially depleted: only particles that impinge on Rhea's northern hemisphere with large field-aligned velocities are "missing" there. It should also be noted that additional B_z perturbations of nearly the same magnitude as in the central wake were observed outside the Rhea fluxtube near $y = -2.1 R_{RH}$, $y = +3.0 R_{RH}$ and $y = +9.0 R_{RH}$. These signatures may possibly arise from fresh plasma injections in Saturn's equatorial plane, which may have occurred coincidentally (see, e.g. *Burch et al.* [2007]). Similar events were found to "contaminate" the interaction signatures observed during a recent wakeside flyby of Dione [*Simon et al.* 2011a].

Equation 7.6 also illustrates why the magnitude of the B_z perturbations observed *over the poles* of Rhea (compared to the background field strength) is much larger than the compression signatures detected in the *wake* of Tethys during the only targeted flyby

[*Khurana et al.* 2008, *Simon et al.* 2009a]. The above expression can be rewritten as

$$\frac{B_0 + \delta B}{B_0} = \sqrt{1 + \beta_i + \beta_e} \quad . \tag{7.8}$$

Hence, the relative magnitude of the maximum field perturbation is determined by the total plasma beta of the ambient magnetospheric flow. The more important the impact of flow dynamics, the larger are the compression signatures in the magnetic field. While at Rhea, the value of $\beta_i + \beta_e$ is of the order of one, the by far stronger magnetospheric field near Tethys' orbit ($B_0 = 167\,\mathrm{nT}$) yields a value of $\beta_i + \beta_e = 0.02$, thereby allowing for a peak field perturbation of only 1% of the background field (see also *Simon et al.* [2009a]).

The slight enhancement of B_y observed within the Rhea fluxtube (see figure 7.1) arises from the aforementioned field compression due to plasma absorption. In the ($z < 0$) half space, the field compression yields a region of $B_y < 0$ for $y < 0$ and a region of $B_y > 0$ for $y > 0$, see *Simon et al.* [2009a]. As can be seen from the (x, y) projection in figure 2.11, Cassini crossed regions of both ($y < 0$) and ($y > 0$) while being located inside the Rhea fluxtube. Therefore, one would expect the spacecraft to pass through both the ($B_y > 0$) and the ($B_y < 0$) perturbation region. The fact that only the ($B_y > 0$) distortion was detected is consistent with CAPS observations from R1 and R1.5 [*Wilson et al.* 2010], suggesting a slight tilt of the ambient bulk speed away from Saturn. Such a tilt would rotate the interaction signatures around the z axis in clockwise direction, thereby shifting the region of positive B_y further into the Rhea fluxtube. The region of ($B_y < 0$) was then probably missed by Cassini due to the slight tilt of the trajectory. We will address this feature again when discussing our hybrid simulation results in section 7.2.2.

It is very important to note that Cassini also observed a non-vanishing, positive B_x perturbation below Rhea's south pole, possessing nearly the same magnitude as the perturbation seen in B_z. In general, one would expect such a B_x distortion to arise from field line draping, i.e. from the formation of an Alfvén wing due to an interaction between the obstacle's ionosphere or intrinsic magnetic field and the incident plasma (cf. section 3.2). However, as inferred in section 7.1, Rhea's gas envelope is far too dilute to cause such strong perturbations of the magnetospheric field, and the moon was also found to be devoid of an internal magnetic field by *Khurana et al.* [2008]. Nonetheless, the observations shown here suggest that the interaction gives rise to a draping-like broad enhancement in B_x, being comparable to or even stronger than the distortions detected in the B_z and B_y components. As will be shown in the following, this B_x enhancement arises from the finite extension of Rhea's plasma wake along the corotational flow direction.

In contrast to the Terrestrial moon –the wake of which is nearly devoid of plasma even at distances of several satellite radii [*Kallio* 2005]–, the wake of a plasma-absorbing moon embedded in a submagnetosonic flow is refilled at rather short distances to the obstacle. As already discussed in section 3.1, the reason for the different refilling of the wake is the higher sonic Mach number of about $M_S = 1$ for the plasma around Rhea (cf. table 2.4). As demonstrated by preceding hybrid simulations of Rhea's plasma interaction during the R1 flyby (for slightly different upstream parameters than provided in section 2.2, cf. *Roussos et al.* [2008a]), the number density of the plasma in Rhea's wake has already returned to 75% of the background value at a distance (in x direction) of only $1R_{RH}$ to the surface of the obstacle. The resulting pressure gradient $\partial_{\underline{x}} p = \frac{\partial p}{\partial x}\underline{e}_x$ along the corotation

direction gives rise to a diamagnetic current $\underline{j}_{dia}$ in $(-y)$ direction,

$$\underline{j}_{dia} = \frac{\underline{B} \times \partial_{\underline{x}} p}{B^2} \approx \frac{\underline{B}_0 \times \partial_{\underline{x}} p}{B_0^2} = -\frac{1}{B_0} \frac{\partial p}{\partial x} \underline{e}_y \quad , \tag{7.9}$$

where $\underline{B}$ in the first expression denotes the locally perturbed field in the interaction region. As a first approximation, we have assumed the magnetic field $\underline{B}$ in the expression for $\underline{j}_{dia}$ to be equal to the background magnetic field $\underline{B}_0$ outside the interaction region. As discussed above, a peak field strength of about $1.5B_0$ may locally be achieved in Rhea's central wake. In the central wake, this would yield an additional factor of $1/1.5$ in eq. (7.9). However, this deviation from the background field strength and the associated bending of the field lines towards the $(y = 0)$ plane are neglected for the order-of-magnitude estimate of the diamagnetic current provided below. The diamagnetic current $\underline{j}_{dia}$ is thus parallel to the convective electric field $\underline{E}_0 = -\underline{u}_0 \times \underline{B}_0 = -u_0 B_0 \underline{e}_y$ of the undisturbed flow.

The orientation of the density gradient as well as the current $\underline{j}_{dia}$ in the wake and the associated magnetic field perturbations are illustrated in figure 7.2. This figure shows that below the south pole, the B_x perturbation arising from the diamagnetic current in Rhea's central wake is parallel to the positive x axis, whereas above the north pole, the associated B_x perturbation points in negative x direction. Thus, the diamagnetic current arising from the finite length of Rhea's wake produces field perturbations above the northern and southern poles that are qualitatively similar to what would be expected for field line draping around a conducting obstacle (cf. red dashed circles in figure 7.2).

To demonstrate that the proposed current $\underline{j}_{dia} \propto -\underline{e}_y$ can produce a sufficiently strong magnetic field below the south pole to explain the B_x enhancement observed during R3, let us assume that the thermal pressure $p(x)$ in the wake (note that the contributions of ram and magnetic pressure do not enter the pressure gradient term in the momentum equation of MHD and thus eq. (7.9)) increases linearly from $p\,(x = 1R_{RH}) = 0$ at the surface of Rhea to $p\,(x = 4R_{RH}) = p_0 = n_0 k\,(T_i + T_e)$ at a distance of $3R_{RH}$ to the surface. This estimate for the length of the wake is in good agreement with new hybrid modeling results for Rhea discussed in section 7.2.2. We also verified from the simulations that the pressure gradient term and the Lorentz term indeed make up the dominant contributions in the momentum equation of the hybrid model within Rhea's wake.

To obtain a simple analytical estimate for the magnetic field associated with the current j_{dia}, let us further assume that j_{dia} is constant within a cylinder of Radius $1R_{RH}$ in y direction whose axis intersects the x axis at $x = 2.5R_{RH}$. The circular intersection area of this wire with the (x, z) plane covers a large fraction of the density depletion region downstream of Rhea, see section 3.1. The magnitude δB_{dia} of the magnetic field perturbation outside the current-carrying region is then given by

$$\delta B_{dia} = \frac{\mu_0 R_{RH}^2}{2\sqrt{(x - 2.5R_{RH})^2 + z^2}} \cdot \frac{p_0}{3B_0 R_{RH}} \quad . \tag{7.10}$$

This equation follows directly from Ampère's law by integrating along the circular magnetic field lines around the cylinder's axis (along which $\left|\delta \underline{B}_{dia}\right|$ is constant), yielding

$$\delta B_{dia} = \frac{\mu_0 j_{dia} \pi R_{RH}^2}{2\pi\sqrt{(x - 2.5R_{RH})^2 + z^2}} \quad . \tag{7.11}$$

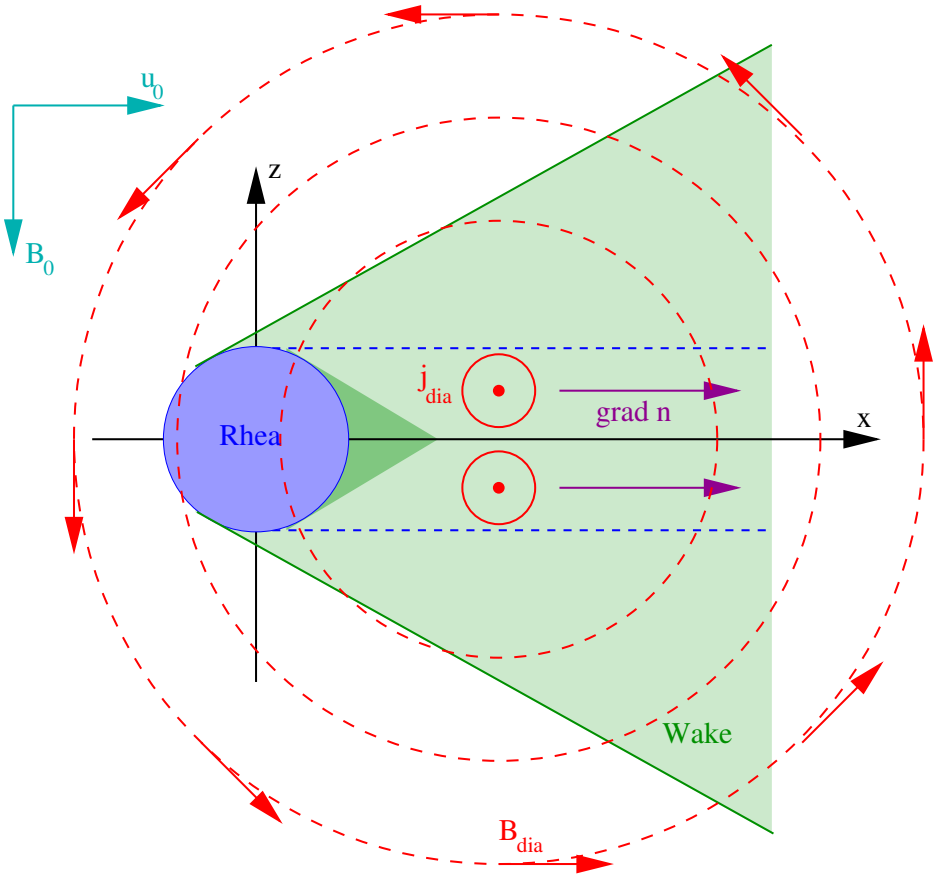

Figure 7.2: Diamagnetic currents arising from the finite length of Rhea's plasma wake along the corotational flow direction. For the ($y = 0$) plane of the RHIS (containing the background magnetic field $\underline{B}_0$ and the (co)rotational flow speed $\underline{u}_0$), the figure provides a schematic illustration of the magnetic field perturbations that arise from the refilling of Rhea's wake by magnetospheric particles with large field-aligned velocities. The void region of nearly zero plasma density is denoted in dark green, while the area shaded in light green depicts the rarefaction cone where the number density of the magnetospheric ions gradually increases with increasing distance to the moon in x direction. Within Rhea's geometric shadow (denoted by the cylinder $\sqrt{y^2 + z^2} < R_{RH}$, dashed blue lines) the resulting density gradient along the positive x axis (magenta arrows) gives rise to a system of diamagnetic currents $\underline{j}_{dia}$, pointing out of the paper plane. By applying the right-hand rule to j_{dia}, one verifies that above the north pole, the B_x component of the magnetic field generated by this current is negative, whereas below the south pole, it assumes a positive value. This field orientation is similar to what would be expected for the draping of the magnetic field around a conducting obstacle, as observed e.g. at Dione [*Simon et al.* 2011a] and the plume of Enceladus [*Dougherty et al.* 2005, *Kriegel et al.* 2009]. The dashed circles and the arrows along them illustrate the magnetic field that would arise from j_{dia} alone. Outside Rhea's geometric shadow, the effect of the density gradient in ($+x$) direction is partially attenuated by the density gradient in ($-x$) direction along the outer flanks of the wake (boundaries of light green region), producing a diamagnetic current in ($+y$) direction. However, these perpendicular current systems do not fulfill $\partial_{\underline{x}} \cdot \underline{j}_{\perp} = 0$ by themselves. As revealed by our hybrid simulations, the diamagnetic currents in Rhea's wake are connected to the currents along the characteristics of an Alfvén wing.

In this expression, $\sqrt{(x - 2.5R_{RH})^2 + z^2}$ denotes the distance from the observer at point (x, y, z) to the axis of the cylinder and

$$j_{dia} = \frac{p_0}{3B_0 R_{RH}} \tag{7.12}$$

is the diamagnetic current according to eq. (7.9).

Below the south pole ($x = 0, z = -1R_{RH}$), this yields a perturbation field of about $\delta B_{dia} \approx 0.75\,\mathrm{nT}$, which is of the same order of magnitude as the enhancement of B_x observed within the Rhea fluxtube during R3. Hence, we suggest that the B_x perturbations observed below Rhea's south pole mainly arise from currents in the moon's intermediate wake. The question of how these diamagnetic currents are closed by field-aligned currents will be addressed in the discussion of our hybrid simulation results in section 7.2.2.

However, we would like to point out that this estimation is only meant to demonstrate that a diamagnetic current arising from the finite length of Rhea's wake is able to produce a measurable B_x perturbation below the south pole that can in principle explain the observed increase of B_x. In reality, the geometry of the diamagnetic currents is far more complex than assumed here. Fully self-consistent hybrid simulations, as discussed in section 7.2.2, are required to determine the precise shape of the current systems in Rhea's wake and the field perturbations generated by them.

The Rhea interaction scenario is particularly suitable for observing the magnetic field perturbations that arise from the finite length of the obstacle's wake. Although hybrid simulations suggest the extension of Tethys' plasma wake to be comparable to or even smaller than the length of Rhea's wake [*Simon et al.* 2009a], one would not expect to observe any strong perturbations of the flow-aligned field component at Tethys. As can be seen from eq. (7.9), the magnitude of the diamagnetic current is inversely proportional to the magnetospheric field strength, which at Tethys is almost 8 times larger than at Rhea, yielding a plasma beta of only 0.02 [*Khurana et al.* 2008, *Simon et al.* 2009a]. Thus, the current j_{dia} is not expected to make any measurable contributions to the magnetic field distortions at Tethys. One should therefore keep in mind that the extension of the wake is not the only controlling parameter for the magnitude of the diamagnetic current, but the magnetic field plays a key role as well.

As demonstrated above, the finite extent of Rhea's wake along the corotation direction allows for a considerable flow-aligned field perturbation. However, as can also be seen from figure 7.2, such a flow-aligned perturbation may occur only outside the $(z = 0)$ plane. Within the $(z = 0)$ plane, it leads to a field-aligned perturbation (i.e. $\delta\underline{B} \propto \underline{e}_z$) that strengthens the field upstream and decreases it downstream. The downstream decrease is probably obscured by the enhancement due to reduced plasma pressure. Upstream, the perturbation is without "competition" and should show an enhancement signature, as it would also be caused by mass/momentum loading (e.g. *Kriegel et al.* [2009], *Simon et al.* [2011a]).

As can also be seen from figure 7.2, the density gradient along the outer flanks of the interaction region (boundaries of the light green cone) possesses a component in *negative* x direction. Thus, it generates a diamagnetic current in positive y direction and a magnetic field that counteracts the effects of the finite wake extension along the corotation direction. In order for the B_x perturbation below the south pole to become positive (as observed

during R3), the effect caused by the currents at the outer flanks of the wake must be overcompensated by the field arising from the density gradient in $(+x)$ direction in the central wake. This is especially important in the polar regions where the wake flanks "touch" the solid body of the moon, cf. figure 7.2. While outside Rhea's geometric shadow, i. e. at $\sqrt{y^2+z^2} > R_{RH}$ (and $x > 1R_{RH}$), density gradients in $(+x)$ and $(-x)$ direction occur, the density gradient inside the shadow region points exclusively in $(+x)$ direction and may even cause strong field perturbations above Rhea's poles. Numerical simulations (see section 7.2.2) are required to understand the magnetic field distortions caused by this complex system of wakeside currents.

Finally, we would briefly like to note that the field perturbations seen in B_y and B_z are also caused by a diamagnetic current system, arising from the finite extension of the density cavity in y direction [*Colburn et al.* 1967]. In the $(y > 0)$ half space, the pressure gradient points in $(+y)$ direction, i.e. the resulting diamagnetic current is parallel to $\underline{e}_x$. In the $(y < 0)$ half space, the directions of both the density gradient and the resulting current are reversed. By applying the right-hand rule to these two current systems, one can easily verify that they are responsible for enhancing $|B_z|$ in the central wake and depressing the field at the flanks of the interaction region. They are also responsible for generating the quadrupolar pattern of different B_y orientations illustrated in figure 1 of *Simon et al.* [2009a]. The diamagnetic currents in x direction are closed within a current loop around the ramside of the satellite (see figure 11.8 in *Mauk et al.* [2009]).

7.2.2 Flyby R3: Hybrid simulations

So far, our analysis of the R3 magnetic field observations is mainly based on analytical estimates of the effects generating the perturbation signatures. In this way, we have been able to explain numerous features seen in the dataset. However, to confirm that our interpretation is quantitatively realistic and to gain further insights into the current systems arising from the finite length of the wake –especially how j_{dia} is closed–, the interaction needs to be treated within the framework of a fully self-consistent plasma simulation. In addition, there is one feature in the R3 dataset which has not yet been addressed: coincident with Cassini's outbound passage $(y < 0)$ through the surface of the Rhea fluxtube, the magnetometer detected a sharply pronounced dip in the B_x component with a magnitude of $\delta B_x \approx -2.1$ nT, i.e. comparable to the strength of the B_x enhancement seen within the Rhea fluxtube.

To clarify these remaining issues, we carry out new simulations of Rhea's magnetospheric interaction, amplifying the pilot study by *Roussos et al.* [2008a]. Since the hybrid code treats the ions as individual particles, it is particularly suitable for reproducing effects associated with finite ion gyroradii, especially asymmetries in the flow deflection pattern and non-Maxwellian particle distribution functions (e.g., the ring distributions associated with ion pick-up or the counter-stream distribution in the wake of an inert moon, cf. *Simon et al.* [2009a]).

Since the key features and basic equations of this code have been elaborated on in detail in chapter 4, we shall provide only a brief discussion of how the code is adapted to the Rhea scenario.

7.2.2.1 Model description and input parameters

The magnetospheric upstream conditions applied in the simulations are provided in section 2.2. For the simulation of R3, however, three slight adjustments have been included: first, the weak tilt of the background magnetic field with respect to the z axis (see upper-right panel of figure 7.1) has been taken into account and we set $\underline{B}_0 = (1.8, 0.6, -20.8)\,\mathrm{nT}$, i.e. the magnitude is again $B_0 \approx 21\,\mathrm{nT}$. Second, the upstream plasma density observed during R3 was also slightly larger than the value of $n_0 = 6\,\mathrm{cm}^{-3}$ derived by *Wilson et al.* [2010] for R1 and R1.5. Measurements of Cassini's Radio and Plasma Wave Science Instrument suggest a value of $n_0 = 7\,\mathrm{cm}^{-3}$ [*Roussos et al.* 2012], which we adopt as input parameter for our model. Third, while data from the R1 flyby [*Wilson et al.* 2010] suggest an ion temperature of about $kT_i = 200\,\mathrm{eV}$, we achieved better agreement between simulation and MAG data for R3 by applying a value of $kT_i = 100\,\mathrm{eV}$, as proposed by *Roussos et al.* [2008a]. At the time of this writing, no measurements of the ion temperature were available for the R3 encounter. For this reason, we have used the ion temperature as a free parameter (within the range of values provided by *Wilson et al.* [2010], *Khurana et al.* [2008] and *Roussos et al.* [2008a]) to achieve best possible agreement between simulation and magnetic field data. An overview about the used parameters is provided in table 7.1. The applied value of kT_i yields an ion gyroradius of $r_g = 0.45 R_{RH}$. The modified upstream conditions yield an only slightly increased Alfvénic Mach number of $M_A = 0.95$ and a magnetosonic Mach number of $M_{MS} = 0.73$. While these changes have negligible qualitative influence on the overall structures seen in the simulations, they may nonetheless strongly affect the magnitudes of the signatures. The minor hydrogen component identified in CAPS ion data from R1 and R1.5 by *Wilson et al.* [2010] is not included in our simulations.

As discussed in sections 3.1 and 4.5.1, Rhea is treated as an electromagnetically inert and plasma-absorbing body, i.e. the tenuous atmosphere described by *Teolis et al.* [2010] is not included. The simulation applies a hierarchical Cartesian grid with three different refinement levels. The extent and location of these levels is shown in figure 7.3. At the highest level, a peak resolution of $0.05 R_{RH}$ is achieved near the surface of the moon. The cell size in the other two levels is two/four times larger. The simulation domain is cubic, possessing an extension of $-5 R_{RH} \leq x \leq +10 R_{RH}$ and $-7.5 R_{RH} \leq y, z \leq +7.5 R_{RH}$.

7.2.2.2 Discussion of simulation results

The results of our hybrid simulations can be seen in figures 7.4, 7.5 and 7.6, respectively. Panels (a) and (b) of figure 7.4 display the magnetospheric plasma density and the corresponding B_x perturbation in the ($z = 0$) plane of the RHIS. For a downstream cut through the wake at $x = 2 R_{RH}$, panels (c) and (d) show the distortions of the B_x and B_y components.

To explore the influence of the large ion gyroradii on the signatures seen in panels (c) and (d), the final row of figure 7.4 displays results from a test simulation where the radius of Rhea has been artificially increased by a factor of 3, while the incident flow parameters were left unchanged. Thus, the ion gyroradius is now $r_g = 0.15 \tilde{R}$, where $\tilde{R}$ is the radius of the artificially enlarged obstacle. The purpose of this test scenario is to isolate

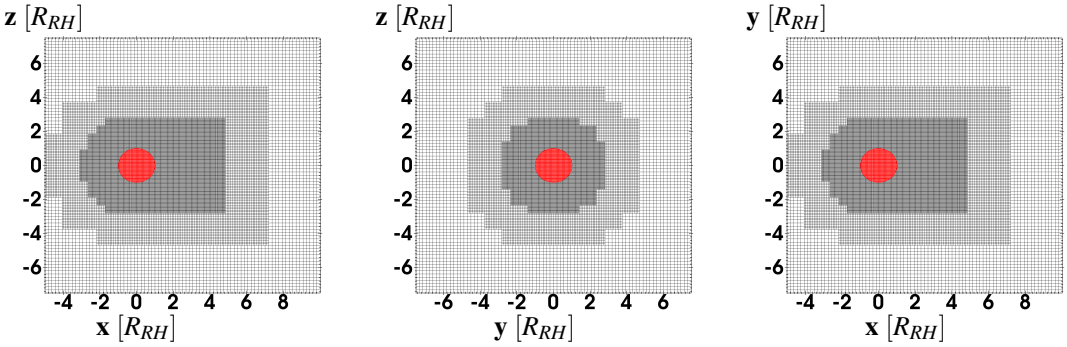

(a) ($y = 0$) (b) ($x = 0$) (c) ($z = 0$)

Figure 7.3: Simulation mesh with three levels of refinement applied in the simulations of Rhea's plasma interaction.

Table 7.1: Physical and numerical parameters used in the simulations of Rhea's plasma interaction.

Parameter	Value
Plasma velocity	$u_0 = 50\,\mathrm{km/s}$
Plasma number density	$n_0 = \begin{cases} 4\,\mathrm{cm}^{-3} & (R2) \\ 7\,\mathrm{cm}^{-3} & (R3) \end{cases}$
Magnetic field	$B_0 = \begin{cases} (4.5, 1.7, -0.2y/R_{RH} - 20)\,\mathrm{nT} & (R2) \\ (1.8, 0.6, -20.8)\,\mathrm{nT} & (R3) \end{cases}$
Species included	water group ions = W^+
Ion mass	$m_i = 17\,\mathrm{amu}$
Alfvénic Mach number	$M_A = 0.90 - 1.19$
Ion temperature	$k_B T_i = \begin{cases} 200\,\mathrm{eV} & (R2) \\ 100\,\mathrm{eV} & (R3) \end{cases}$
Electron temperature	$k_B T_e = 10\,\mathrm{eV}$
Box (x)	$-5R_{RH} \leq x \leq +10R_{RH}$
Box (y)	$-7.5R_{RH} \leq y \leq +7.5R_{RH}$
Box (z)	$-7.5R_{RH} \leq z \leq +7.5R_{RH}$
Mesh spacing L_0	$\Delta_{L_0} = 143\,\mathrm{km} = 0.19R_{RH}$
Mesh spacing L_2	$\Delta_{L_2} = \frac{1}{4}\Delta_{L_0} = 36\,\mathrm{km} = 0.05R_{RH}$
Time step	$\Delta t = 0.0005\Omega_i^{-1} = 4.2 \cdot 10^{-3}\,\mathrm{s}$
Simulation time	$15000\Delta t = 7.5\Omega_i^{-1} = 63\,\mathrm{s}$
Smoothing	$\eta_{sm} = 0.3\%$
Conductivity of interior	$\sigma = 9 \cdot 10^{-7}\,\mathrm{S/m}$
Macroparticle per Cell	200

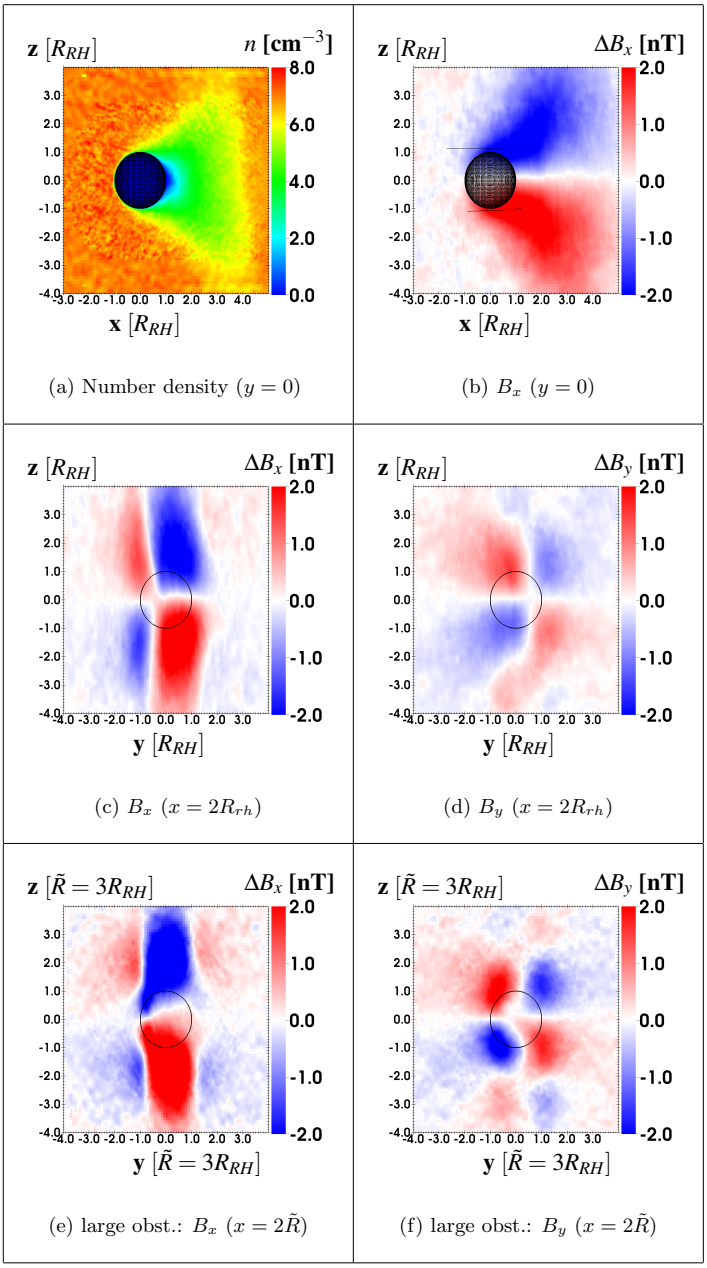

(a) Number density ($y = 0$)

(b) B_x ($y = 0$)

(c) B_x ($x = 2R_{rh}$)

(d) B_y ($x = 2R_{rh}$)

(e) large obst.: B_x ($x = 2\tilde{R}$)

(f) large obst.: B_y ($x = 2\tilde{R}$)

Figure 7.4: Hybrid simulation of Rhea's magnetospheric interaction for the conditions of the R3 encounter. The figure displays (a) the magnetospheric plasma density in the ($y = 0$) plane, (b) the magnetic B_x component in the ($y = 0$) plane, (c) the B_x component downstream of Rhea at $x = 2R_{RH}$ and (d) B_y at $x = 2R_{RH}$. Panels (e) and (f) display the results of a test simulation where the radius of Rhea has been artificially increased by a factor of 3 to investigate the influence of finite ion gyroradii on the interaction. In these two panels, the symbol $\tilde{R}$ refers to 3×764 km. The panels show (e) the B_x and (f) the B_y component in the ($x = 2\tilde{R}$) plane. In panels (b)–(f), only the *perturbations* of the magnetic field are shown, i.e. the background magnetic field $\underline{B}_0$ has been subtracted. The cutting planes shown in panels (c), (d), (e) and (f) are intersected by Rhea's geometric shadow $\sqrt{y^2 + z^2} = R_{RH}$ along the black circles. The outer, circle-like boundary visible in plots (e) and (f) arises from different resolution levels of the simulation grid on either side.

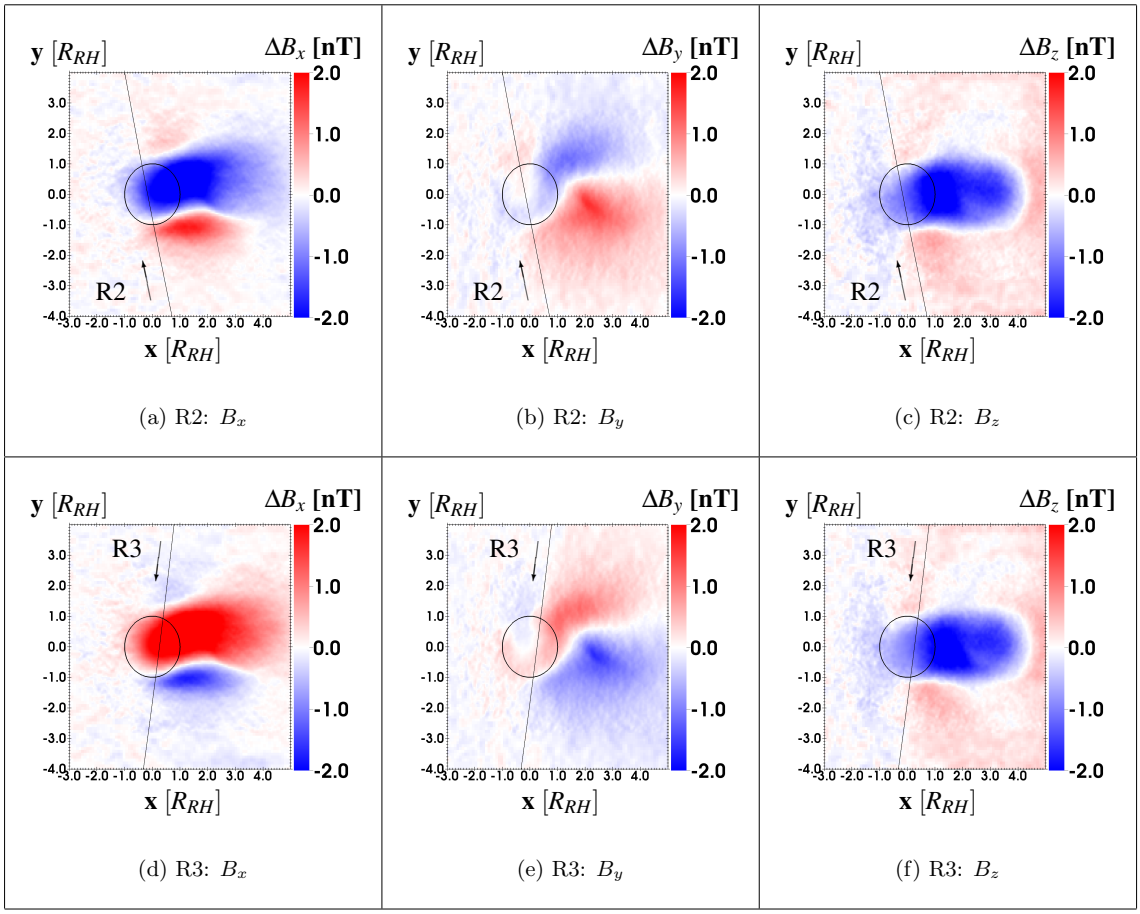

Figure 7.5: Perturbation magnetic field components (background field $\underline{B}_0$ subtracted) in the planes of the R2 ($z = +1.1R_{RH}$, panels (a), (b) and (c)) and the R3 flyby ($z = -1.1R_{RH}$, panels (d), (e) and (f)). The flyby trajectory is denoted by the black line, while the black circle $\sqrt{x^2 + y^2} = R_{RH}$ marks the projection of Rhea on the cutting planes.

the influence of finite gyroradius effects (i.e., highly asymmetric plasma absorption) on the structure of the magnetic field perturbations: while in the real Rhea scenario (panels (c) and (d), large gyroradii), the absorption process and the associated magnetic field perturbations feature a prominent asymmetry between the Saturn-facing ($y > 0$) and the Saturn-averted ($y < 0$) hemisphere, these signatures are nearly symmetric in the case of small ion gyroradii (panels (e) and (f)).

The lower row in figure 7.5 displays the perturbation magnetic field components in the plane of the R3 encounter (i.e. at $z = -1.1R_{RH}$), while figure 7.6 shows a comparison between our model results and MAG data from R3 along the flyby trajectory. For the run illustrated by the solid red, green and blue lines (the results of this run are also shown in figs. 7.4 and 7.5), the upstream particle population is represented by a drifting Maxwellian distribution, i.e. the temperature is assumed to be isotropic and has a value of $kT_i = 100\,\mathrm{eV}$.

In addition, the dashed lines illustrate the results of a test scenario where an anisotropic ion temperature has been included ($kT_{i,\perp} = 150\,\mathrm{eV}$, $kT_{i,\parallel} = 50\,\mathrm{eV}$). The applied values

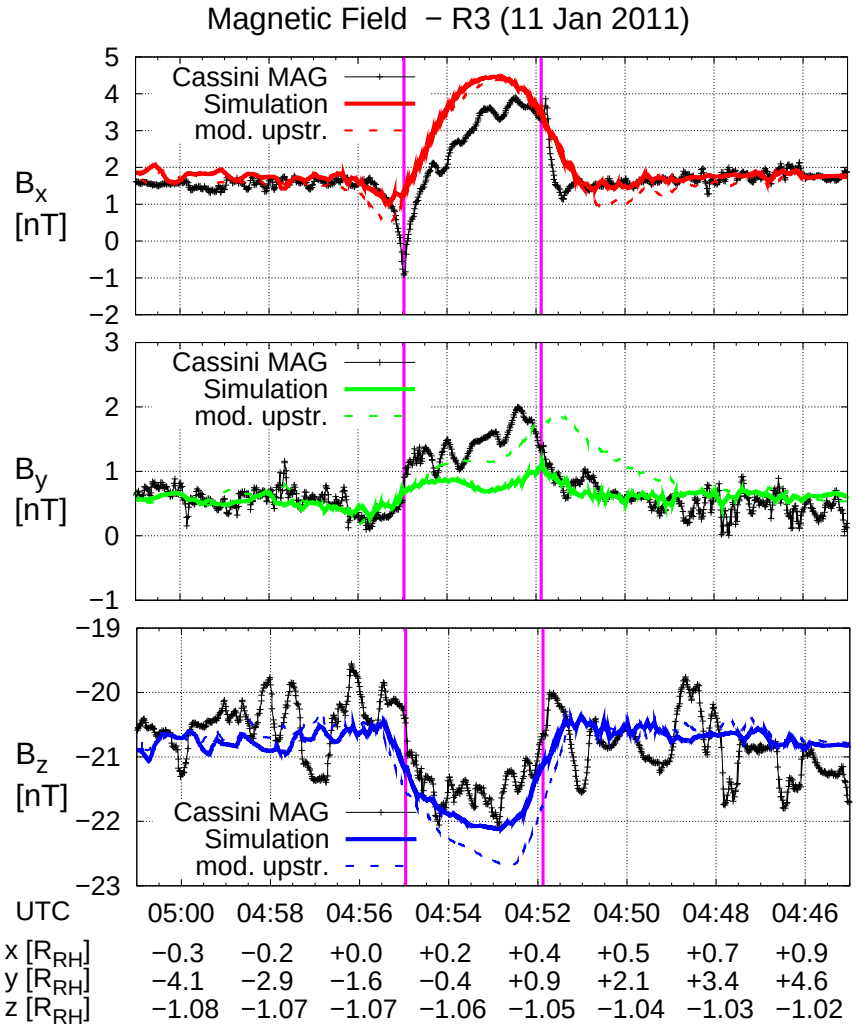

Figure 7.6: Cassini magnetic field observations (black) versus hybrid simulation results (B_x: red, B_y: green, B_z: blue) along the R3 trajectory. The solid lines show the results of the model run that yielded best agreement with MAG data. The dashed lines illustrate the results of a test scenario with an anisotropic temperature in the upstream flow. The vertical magenta lines denote Cassini's passages through the surface of the Rhea fluxtube $\sqrt{x^2 + y^2} = R_{RH}$. Similar to figure 7.1, the data are shown from negative to positive y values (i.e. the time axis is reversed).

of the temperature components are similar to those shown in figures 5 and 6 of *Wilson et al.* [2010] for the conditions of the R1 and R1.5 encounters. However, the results of this simulation obviously overestimate the magnitude of the observed B_z perturbation (indicative of the "strength" of the interaction) and are only meant to illustrate the general effect of an anisotropic temperature on the sharpness and depth of the simulated dip in the B_x component. Therefore, these results will only be briefly discussed at the end of the section. If not stated otherwise, the following discussion always refers to the case of an *isotropic* temperature, as illustrated by the *solid* red, green and blue lines in figure 7.6.

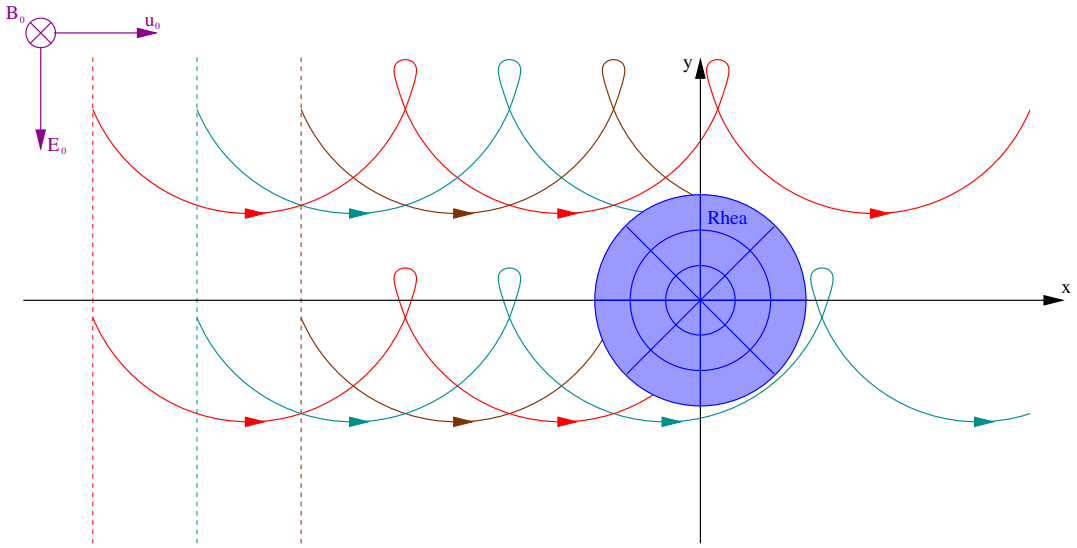

Figure 7.7: Asymmetric particle absorption at Rhea's surface. For the ($z = 0$) plane of the RHIS, the figure illustrates the trajectories of several representative magnetospheric ions in the vicinity of Rhea. In each x = const plane upstream of the moon, the two red, cyan and brown particles possess the same gyrophase. However, in the ($y > 0$) half space only the red particle "survives" the passage through the interaction region, while for $y < 0$ the cyan particle is the only one that does not get absorbed. Thus, the particle population reaching the downstream region in the Saturn-averted half space possesses different gyrophases than the "surviving" particles in the Saturn-facing half space. In the Saturn-averted half space, particles which travel close to Rhea's surface (since the moon is located within a "bulge" of their trajectory) can reach the moon's wakeside, causing an asymmetry in the refilling of the density cavity. The cyan particle in the ($y < 0$) half space possesses such a trajectory.

Figure 7.8 illustrates the number density of the magnetospheric plasma in the ($z = 0$) plane for both the real Rhea scenario (panel (a)) and for the case of an artificially enlarged obstacle (panel (b)). The influence of large ion gyroradii on the plasma absorption is also illustrated schematically in figure 7.7.

In accordance with preceding hybrid simulation results by *Roussos et al.* [2008a], figure 7.4(a) illustrates that the region of depleted plasma density expands to far north and south of Rhea along the magnetic field lines. This rarefaction region arises from the excitation of fast mode waves (see *Khurana et al.* [2008] and section 3.1). Its opening angle (measured against the x axis) is roughly given by $\arctan M_{MS} = \arctan 0.73 = 36°$, which is in good agreement with our simulation result. The cone-like void region in Rhea's geometric shadow (denoted in blue, see also figure 3.1) is clearly visible in the simulated density profile as well. Although not shown here again, the corresponding magnetic field enhancement in this region is similar to figure 1(D) in the work of *Roussos et al.* [2008a].

In addition to the aforementioned structures, the simulation reveals two prominent regions of a reduced (for $z > 0$) or enhanced (for $z < 0$) B_x component, connecting to the near-Rhea region between the poles ($x = 0$) and $x \approx 4R_{RH}$, cf. figure 7.4(b). The sign of B_x corresponds to that of a magnetic draping pattern or an Alfvén wing, as it also arises from the interaction between the plume of Enceladus and the ambient magnetospheric flow (see

section 5.2). Indeed, the tilt angle of the simulated wings against the ambient magnetic field direction ($\approx \underline{e}_z$) corresponds well to a value of $\arctan M_A \approx 44°$, cf. equation (3.3). It should be noted that the Alfvénic field perturbation within these wings is rather weak, i.e. only about 10% of the magnetospheric background field.

In order for an Alfvén wing to be formed, the currents along the wing characteristics need to be closed by transverse currents in the local interaction region. In the case of Enceladus, this closure is mediated by the Pedersen and Hall currents in the plume. At Rhea, however, we encounter a scenario where the current system of the wing is not closed within the obstacle's ionosphere, but by the diamagnetic current in $(-y)$ direction that arises from the finite extension of the moon's wake along the corotational flow direction.

The hybrid simulation revealed this Alfvénic interaction signature that was not considered in our original discussion of $\underline{j}_{dia}$. The formation of this Alfvén wing also implies that the diamagnetic currents in $(+y)$ direction at the outer flanks of the wake are not strong enough to close the entire current system in $(-y)$ direction, but the additional inclusion of the currents along the wing characteristics is required to fulfill the $\partial_{\underline{x}} \cdot \underline{j} = 0$ condition. In general, an Alfvén wing can form when the transverse currents $\underline{j}_\perp$ do not fulfill $\partial_{\underline{x}} \cdot \underline{j}_\perp = 0$, no matter whether the satellite possesses an atmosphere or not. It should be noted that in the scenario considered here, gradient and curvature drifts may also make a minor contribution to the perpendicular currents. Only for particles with energies in the keV range, these drift motions start to take major influence on particle dynamics, cf. table 1 and section 7 in the work of *Khurana et al.* [2008].

To further understand this peculiar structure, let us at first have a look at the simulated magnetic field configuration in a cut through the intermediate wake region at $x = 2R_{RH}$, see panels (c) and (d) in figure 7.4 for the asymmetric case (large gyroradii) and panels (e) and (f) where the gyroradii are small with respect to the artificially enlarged obstacle. In panel (e), one can recognize the magnetic field features typical for an Alfvén wing. In planes perpendicular to the wing characteristics, the magnetic field configuration corresponds to a two-dimensional dipole whose magnetic moment has a component parallel (southern wing) or antiparallel (northern wing) to the positive x axis of the RHIS. Correspondingly, a region of negative B_x is encountered within the center of the northern wing tube (dark blue region above Rhea in figure 7.4(e)), while at the flanks of the northern wing tube, the field changes its orientation and points in positive x direction. In the southern hemisphere, the orientation of B_x is reversed inside and outside the wing. The quadrupolar pattern in the B_y component (see figure 7.4(f)) corresponds to the field compression/plasma absorption pattern discussed in the preceding section.

It is most important to note that if the gyroradii are small compared to the size of the obstacle, the magnitudes of the B_x and B_y perturbations are symmetric with respect to the $(x = 0)$ plane, as illustrated by figs. 7.4(e) and (f). In the real Rhea scenario, however, the large gyroradii of the magnetospheric upstream ions give rise to an asymmetrization of the B_x and B_y patterns with respect to the direction of the convective electric field $\underline{E}_0 \approx -u_0 B_0 \underline{e}_y$. As can be seen from figure 7.4(c), the draping pattern is clearly shifted in the $(y < 0)$ half space where the electric field points away from Rhea. The regions of perturbed B_x outside the Rhea fluxtube become more prominent in the $(y < 0)$ half space, whereas for $y > 0$, both the magnitude and the extent of the B_x perturbations are reduced. In a similar way, the absorption pattern in the B_y component exhibits a slight asymmetry

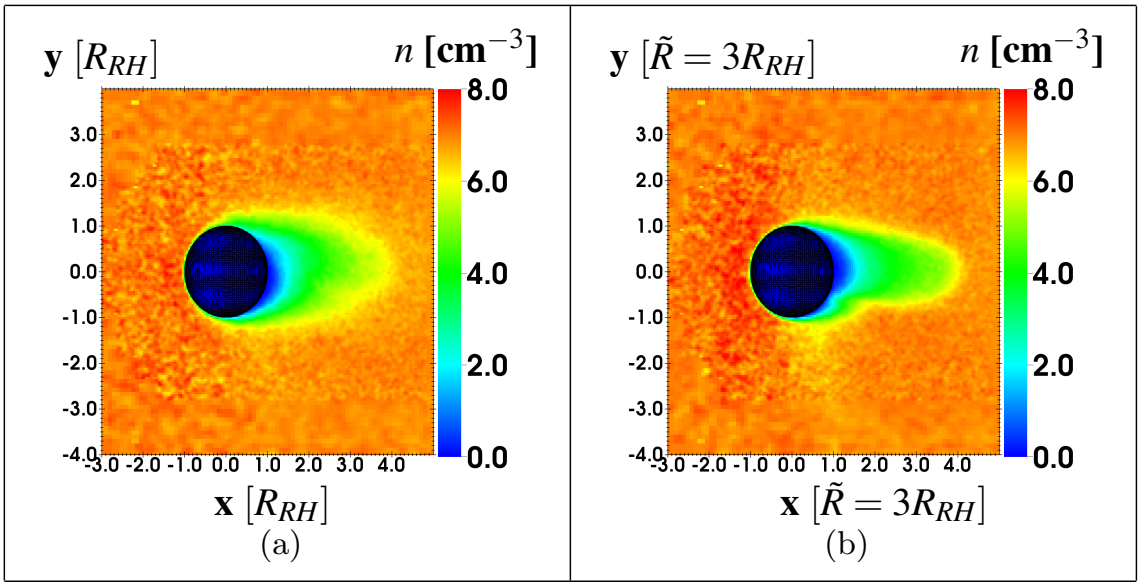

Figure 7.8: Number density of the magnetospheric plasma in the (z = 0) plane for the upstream conditions of the R3 flyby: (a) real Rhea scenario, (b) test scenario with artificially enlarged obstacle.

with respect to the direction of the convective electric field as well (see figure 7.4(d)).

A similar asymmetrization of the magnetic draping pattern with respect to the direction of the convective electric field occurs at Titan, where the gyroradii of both magnetospheric upstream ions and exospheric pick-up ions exceed the radius of the obstacle to the flow. By applying a hybrid simulation, *Simon et al.* [2007], *Simon et al.* [2008] showed that in this case, both the ramside magnetic pile-up region and the wakeside magnetotail structure are shifted in the direction of the convective electric field. These authors also found evidence for the asymmetric structure of Titan's interaction region in Cassini magnetic field observations.

As can be seen from figure 7.4(c), the two wings near Rhea are not aligned with the direction of the background magnetic field, but they are both tilted away from Saturn. Since in the far field, an Alfvén wing exhibits translation symmetry along its characteristics $\underline{u}_0 \pm \underline{v}_A$ (see section 5.2), this feature clearly illustrates that the B_x perturbations shown in figure 7.4(c) cannot be exclusively ascribed to the current systems in the wing. In the rather small region around Rhea investigated here the transverse currents in the local interaction region make a noteworthy contribution that needs to be superimposed.

While the asymmetries of Rhea's plasma interaction are clearly visible in the magnetic field (after subtraction of $\underline{B}_0$), they appear less prominent in the simulated plasma density near the moon. Overall, figure 7.8 shows that in the real Rhea scenario, the wake is refilled at shorter distances to the moon than in the test scenario. This is best visible in the extension of the green density depletion region along the corotational flow direction. An explanation for this behavior is provided in figure 7.7, showing that in the case of large gyroradii, the ions can refill the wake more easily by avoiding collisions with the moon on their spiral trajectories. Even in the case of small gyroradii, the density depletion region

features a slight asymmetry. The occurrence of this effect is consistent with our preceding simulations of Tethys' magnetospheric interaction and arises from the Hall term [*Simon et al.* 2009a]. In the real Rhea scenario, this effect is still present (visible in the outer boundary of the green region in figure 7.8(a)), although the outer flanks of the wake are more blurred. However, comparing the locations of the central density void downstream of the moon (dark blue region) between the real Rhea scenario (cf. figure 7.8(a)) and the case of an artificially enlarged obstacle (cf. figure 7.8(b)) also shows that in the real scenario, the central density void is more prominent in the Saturn-averted half space where the convective electric field points away from Rhea. This effect may give rise to a slightly steeper density profile (along the corotation direction) for $y < 0$ than in the test scenario, generating a stronger diamagnetic current in the Saturn-averted half space and thereby contributing to the asymmetry in the magnetic field pattern. Given the weakness of these visible modifications in the density profile (compared to the background density), it is also important to notice that the change in the magnitude of the B_x perturbation in the ($y < 0$) half space between asymmetric and symmetric case (figure 7.4(c) versus 7.4(e)) is on the order of only 1 nT, i.e. less than 5% of the background field.

Based on these results, we can now investigate the origin of the spiky dip in B_x detected by Cassini when leaving the Rhea fluxtube ($y < 0$). As can be seen from figure 7.5(d), Cassini only grazed the weakly pronounced region of reduced B_x in the inbound region of R3 ($y > 0$). However, after leaving the Rhea fluxtube where B_x was enhanced, the spacecraft passed through the more prominent region of reduced B_x in the ($y < 0$) half space. A comparison between measured and simulated B_x component (see upper panel of figure 7.6) shows that our simulation result is in good agreement with the measured B_x signature. Especially, both the magnitude and the width of the B_x enhancement inside the Rhea fluxtube are quantitatively reproduced by the simulation. The location of the B_x dip at the ($y < 0$) surface of the Rhea fluxtube is reproduced by the simulation as well, but its magnitude and sharpness are underestimated. A possible reason for this may be the finite level of numerical diffusion in the simulations or the occurrence of effects on electron scales which are not covered by the hybrid model. However, it is important to notice that our model qualitatively reproduces this dip by considering plasma-absorption at the moon's surface alone.

To further illustrate that the effect producing the B_x spike seems to be reproduced by the hybrid simulation, let us have a brief look at the results of the test scenario with an *anisotropic* temperature (dashed red, green and blue lines in figure 7.6). This run overestimates the width of the enhancement in B_y and especially the compression signature in B_z. Due to the increased perpendicular temperature (150 eV versus 100 eV), the pressure loss at Rhea's surface is larger than in the first simulation run, therefore requiring a stronger magnetic field enhancement.

However, this run also produces a more prominent spike at the ($y < 0$) flank of the Rhea fluxtube. These results illustrate that although the global features of the interaction remain qualitatively unaffected by the modified temperature, the magnitudes of the simulated magnetic field signatures are highly sensitive to the incident magnetospheric flow conditions. To a high degree, the discrepancy between simulation and measurement near the ($y < 0$) passage through the Rhea fluxtube may probably be ascribed to uncertainties in the ambient flow conditions. Of course, we cannot definitely exclude that additional

effects which are not taken into account by the model –such as currents due to non-zero surface potentials [*Roussos et al.* 2010, *Santolík et al.* 2011]– might also play a role in causing the spikey shape of the observed signature. We would also like to point out that –based on the available data and modeling results– the question of why these spikes coincide almost precisely with Cassini's passage through the surface of the Rhea fluxtube cannot be answered.

As can be seen from figure 7.6, the simulation also reasonably reproduces the positions and magnitudes of the perturbations seen in B_y and B_z. The contour plots in the lower row of figure 7.5 place these spacecraft observations within the context of the three-dimensional interaction scenario. As discussed in section 7.2.1, the spacecraft only passed through the region of enhanced B_y during its south polar flyby. The simulation illustrates that this is not only a result of the inclination of the R3 trajectory against the y axis, but due to the large ion gyroradii, the B_y perturbations also exhibit a slight asymmetry between the ($y > 0$) and the ($y < 0$) half spaces. Panel 7.5(c) illustrates that the maximum perturbation in B_z is indeed not achieved below the south pole where R3 took place, but further downstream in the central void region.

7.2.3 Flyby R2: MAG observations and hybrid simulations

In this section, we shall focus on Cassini's magnetic field observations during the north polar R2 encounter, as shown in the left-hand column of figure 7.1. At first glance, the B_y and B_z perturbations are familiar to what is expected for the plasma interaction of an electromagnetically inert moon. Again, the magnetic field along the trajectory is compressed (i.e. $|B_z|$ is enhanced) within the Rhea fluxtube, this time due to the depletion of magnetospheric particles incident upon Rhea's south pole. Even far outside the Rhea fluxtube, the observed B_y component was highly perturbed. Although a slight enhancement of about 1 nT was detected within the Rhea fluxtube, the magnitude of this perturbation is comparable to the B_y perturbations observed e.g., at $y = -5R_{RH}$ or at $y = +7R_{RH}$. The slight enhancement of B_y observed within the Rhea fluxtube possibly arises from plasma absorption at Rhea's surface. The presence of a corresponding region of negative B_y (see upper sectors in figure 1(ii) of *Simon et al.* [2009a]) might have been obscured by the rather high fluctuation level that was present in the B_y component at the time of R2, cf. figure 7.1.

In contrast to B_y and B_z, the B_x signature observed during R2 looks unusual. As can be seen from figure 7.1, the magnetometer detected a bipolar perturbation in this component, with the positions of the maximum and the minimum coinciding with Cassini's passages through the surface of the Rhea fluxtube. Considering that the spacecraft was moving mainly in y direction, the perturbation seen in B_x is similar to the magnetic field of a straight, infinitely long wire with the same diameter as the Rhea fluxtube, carrying a homogeneous current in ($+z$) direction (see also *Santolík et al.* [2011]). However, the occurrence of such an unidirectional current would be inconsistent with our interpretation of MAG data from the R3 flyby, involving a bipolar current system towards and away from Rhea in each of the two Alfvén wings. Note also that the variation in the observed B_x component outside the Rhea fluxtube disagrees with the model of a cylindrical homogeneous current in z direction particularly before entering the fluxtube (see figure 3 in

the work of *Santolík et al.* [2011]). Also the model of a homogeneous wire predicts only weak variations in B_y, contrary to observations.

To shed light on the origin of these puzzling B_x perturbations, we have carried out an additional hybrid simulation run for the R2 flyby. Again, the upstream flow conditions in the model differ slightly from the "average" set of parameters provided in section 2.2. First, the background magnetospheric field has been set to $\underline{B}_0 = (4.5, 1.7, -0.2y/R_{RH} - 20)$ nT, accounting for the spatial inhomogeneity of the observed B_z component (see lower left panel in figure 7.1). The fundamental $\partial_{\underline{x}} \cdot \underline{B}_0 = 0$ condition is of course fulfilled by this setting. Second, the number density of the incident flow has been set to $n_0 = 4\,\mathrm{cm}^{-3}$ according to table 2.3. However, these modifications of the upstream flow conditions again do not change the overall picture of the interaction, but only have quantitative impact on the magnitudes of the simulated field perturbations.

As can be seen from figure 7.9, both the width and the magnitude of the compression signature in B_z are well reproduced by the hybrid simulation. The model magnetic field also shows a slight enhancement of B_y within the Rhea fluxtube, in agreement with our expectations and Cassini MAG data. The simulated B_x signature exhibits a bipolar perturbation which is at least in rough qualitative agreement with Cassini observations. Although the magnitude of the peak field perturbation is quantitatively consistent with the observations as well, the sharpness of the two spikes is clearly underestimated by the model. Especially within the Rhea fluxtube, the simulated B_x component decreases much steeper than the observed one. Overall, the simulated bipolar B_x perturbation is shifted against the measured one in negative y direction, with the displacement of the minimum being stronger than that of the maximum.

A possible reason for this discrepancy may stem from non-stationarities in the incident magnetospheric flow conditions, as clearly visible in the B_y component. Additionally, Cassini Plasma Spectrometer data from preceding (close and non-targeted) Rhea encounters indicate that the ambient magnetospheric flow direction may possess a slight asymmetry between the Saturn-facing and the Saturn-averted half space. *Wilson et al.* [2010] showed that during both, R1 and the non-targeted R1.5 encounter, the ambient flow possessed a radial component of about 10 km/s outward on the Saturn-averted side of Rhea, while no radial component was observed in the Saturn-facing hemisphere. Such asymmetric upstream flow conditions, which certainly impose additional deformations on the magnetic field lines in the interaction region, are not included in our hybrid simulation. Whether the varying radial flow profile derived by *Wilson et al.* [2010] is a result of Rhea's interaction with the magnetospheric flow or indeed a feature already present in the undisturbed upstream plasma is not yet clarified.

However, it is also possible that there is still an important component missing in our understanding of Rhea's magnetospheric interaction during R2. Numerous unexplained features in particle data from R2 –such as the detection of dropouts in energetic particle fluxes outside the wake and the lack of a void region in the electron density downstream of Rhea– are in favor of this hypothesis [*Roussos et al.* 2012]. Nevertheless, it is remarkable to notice that –in analogy to R3– by considering the plasma-absorbing body of Rhea alone, the hybrid model is able to qualitatively reproduce the bipolar nature of the observed B_x signature.

The two-dimensional contour plots of the simulated magnetic field components in the

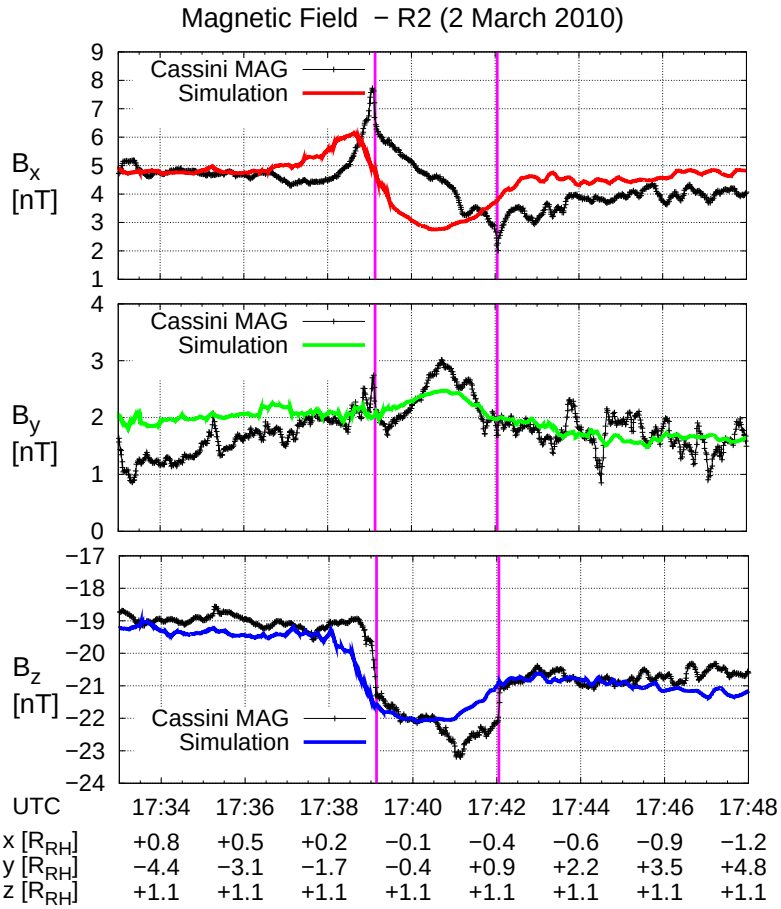

Figure 7.9: Cassini magnetic field observations (black) versus hybrid simulation results (B_x: red, B_y: green, B_z: blue) along the R2 trajectory. The vertical magenta lines denote Cassini's passages through the surface of the Rhea fluxtube $\sqrt{x^2 + y^2} = R_{RH}$.

plane of the R2 flyby (cf. panels (a)–(c) in figure 7.5) illustrate the origin of the simulated B_x perturbation. Again, the spacecraft passed through the Alfvénic perturbation region that arises from the finite length of Rhea's wake. In the northern hemisphere where R2 took place, the B_x perturbation within the Rhea fluxtube is negative, while B_x reverses its sign along the Saturn-facing and Saturn-averted flanks of the interaction region (see figure 7.5(a)). Again, the large gyroradii of the incident ions make the perturbation features appear more prominent in the ($y < 0$) half space.

In analogy to R3, the combined influence of the slight tilt in the R2 flyby trajectory and the asymmetry of the field perturbation gave rise to the bipolar nature of the observed B_x signatures. When approaching Rhea from the Saturn-averted half space, Cassini first intersected the region of positive B_x. Subsequently, the spacecraft penetrated the "core" of the Alfvénic fluxtube, where the B_x perturbation possesses a negative sign. In the Saturn-facing half space, the spacecraft missed the region of enhanced B_x at the flank of the interaction region for two reasons: on the one hand, the spacecraft moved into

the undisturbed upstream hemisphere after closest approach to Rhea. On the other hand, the asymmetry of the Alfvénic perturbations between Saturn-facing and Saturn-averted hemisphere makes the B_x perturbation nearly vanish in the outbound region ($y > 0$) of the R2 flyby. In this sense, we propose that the B_x perturbations observed during R2 arise at least partially from the same mechanism as suggested for R3.

It should be noted that only if a Rhea flyby occurred outside of the ($z = 0$) plane and downstream of about $x = 1R_{RH}$, the spacecraft could potentially intersect the region of positive/negative B_x perturbation inside the southern/northern Alfvénic fluxtube as well as *both* regions of negative/positive B_x perturbation along its flanks. However, neither the trajectories of R2 and R3 nor the preceding R1 flyby (at $z = 0$) meet this criterion. During the upcoming R4 encounter, Cassini will travel mainly in z direction along Rhea's Saturn-averted side with a closest approach altitude of $1.3R_{RH}$, thereby making it most likely impossible to collect further evidence for our interpretation. Available and scheduled flybys of Saturn's icy moons Tethys and Dione do not possess suitable trajectories for the detection of this effect either. In addition, the magnetic field arising from the diamagnetic currents may be much weaker at these moons. However, the idea of a weak, asymmetric Alfvén wing –arising from the finite length of Rhea's wake and the large gyroradii of the incident magnetospheric ions– can consistently explain Cassini MAG observations from the R2 and R3 flybys. Probably, these two encounters constitute the only icy satellite flybys of the entire Cassini mission whose trajectories were suitable to detect these peculiar features of an inert moon's plasma interaction.

Finally, we would briefly like to dwell on an intrinsic limitation of the hybrid approach: while this type of model self-consistently encompasses non-Maxwellian ion distribution functions and the wave modes associated with their decay, it is not able to cover similar effects for the electrons. The decay of non-Maxwellian electron distributions (e.g. loss-cones) may give rise to local inhomogeneities of the plasma temperature, affecting both the flow pattern and the magnetic field. Assessing the influence of these effects on Rhea's magnetospheric interaction would require the application of a full-particle model [*Birch and Chapman* 2001], which –due to limited computing resources– is so far not available in three spatial dimensions. However, since we succeeded in explaining the key features of the magnetic field observations without inclusion of a self-consistent description of the electrons, we are confident that these effects will exert only weak influence on the structure of the interaction region. This assessment is further supported by magnetic field observations from the more distant R1 flyby, which could also be fully reproduced by a hybrid simulation that applies a simple adiabatic law to the electrons [*Roussos et al.* 2008a].

In their hybrid simulation study of Tethys' magnetospheric interaction, *Simon et al.* [2009a] explored the impact of changes in the (spatially homogeneous) electron temperature on the plasma flow and magnetic field pattern in the wake. These authors showed that even an increase of the electron temperature by a factor of 4 had only minor quantitative influence on the magnetic field signatures and the density pattern (see especially figure 3 in that work). Hence, it is reasonable to expect that spatial inhomogeneities of the electron temperature will not introduce additional new features in the large-scale magnetic field environment of Saturn's plasma-absorbing moons.

8 Summary and Outlook

In this thesis, the plasma environments of the Saturnian moons Enceladus and Rhea – which are located deeply within Saturn's magnetosphere – have been studied. Both icy moons have in common that their surfaces are completely covered with water ice. The satellites' interactions with Saturn's magnetospheric plasma, however, represent two completely different types of interaction scenarios. On the one hand, the extended plume of water vapor and dust originating from Enceladus' south polar region gives rise to a sub-alfvénic ionosphere-type interaction: the neutral plume is ionized by means of charge exchange, photoionization and electron impacts. The subsequent pick-up of the ions and electrons and the associated currents generate a non-linear system of standing Alfvén waves, the Alfvén wing. On the other hand, particle absorption at the surface of Saturn's second-largest moon Rhea corresponds to an inert-moon type of interaction, similar to that of the Earth's moon.

Analytical modeling and numerical simulations by means of the hybrid code A.I.K.E.F. (Adaptive Ion-Kinetic Electron-Fluid) have been used to analyze the plasma structures in the vicinity of the icy moons. It turned out that A.I.K.E.F. is particularly suitable to study these plasma interactions, since the charged dust in Enceladus' plume could be easily included in the hybrid model and the treatment of the inner boundary at the surfaces of the satellites allows a correct description of processes associated with plasma absorption by the solid body of Rhea.

The simulation results are compared with various measurements from the Cassini spacecraft. In particular the magnetic field measurements obtained during the 20 Enceladus and five Rhea flybys that were available at the time of this thesis were set into a three-dimensional context. Surprisingly, it turned out that both moons have in common that they generate an Alfvén wing that is unique, either in terms of its properties or with respect to its generation. The study of the underlying processes helped to interpret Cassini data and substantially enlarged our understanding of the respective plasma interaction. The particular results of this thesis are summarized in the following.

8.1 Enceladus

In part one of the study of Enceladus' plasma interaction (chapter 5), the influence of electron absorption by negatively charged dust on the structure of Enceladus' Alfvén wings was investigated. For a first basic analysis, charged dust was included in the analytical modeling of the Alfvén wing as well as in simulations of a corresponding test scenario. The major findings were:

- Due to electron absorption by heavy dust grains, the density of "free" electrons (n_e) is significantly reduced within the plume. If n_e falls below a critical threshold given by

$$\frac{n_i - n_e}{n_i} = \frac{\tilde{\nu}_i^2}{\tilde{\nu}_i^2 + \Omega_i^2} \quad ,$$

  the ion current density becomes larger than the electron current density, thereby reversing the direction of the Hall current. In this expression, n_i, $\tilde{\nu}_i$ and Ω_i denote ion density, effective ion collision frequency and ion gyrofrequency. In contrast, the Pedersen current is not affected by the presence of negatively charged dust. For that reason this effect was termed "Anti-Hall effect".

- The measurable consequence of the Anti-Hall effect is a reversal in the sign of the magnetic field component along the Saturn-Enceladus line (B_y) in Enceladus' Alfvén wings. As a result of the translation invariance of the Alfvén wing along its characteristics, the Anti-Hall effect is present even at large distances to the obstacle.

- The hybrid simulations quantitatively reproduce the predictions of the analytical theory for a simplified test scenario, thereby proving that negatively charged dust can be correctly described within the simulation model.

- In the plane perpendicular to the magnetic field, the "usual" Hall current (without dust) leads to a clockwise rotation of the perpendicular current, a deflection of the magnetospheric ion flow in the anti-Saturnward direction and a deflection of the electrons towards Saturn. In contrast, the reversal of the Hall current by the presence of negatively charged dust causes a counterclockwise rotation of the perpendicular current. Furthermore, the deflection of the ion flow is enhanced, whereas the electrons are also deflected in the anti-Saturnward direction.

In a subsequent quantitative analysis, the previous simulation model of Enceladus' plasma interaction [*Kriegel et al.* 2009] was extended such that it included a population of negatively charged dust. The second major improvement was that in addition to mass loading via photoionization and electron impacts, momentum loading due to charge exchange was also considered. The simulation results were compared against Cassini MAG data for selected pairs of similar Enceladus flybys: (E5,E6), (E7,E9) and (E8,E11). The main results can be summarized as follows:

- The simulations demonstrate that the reversal of the B_y component due to the Anti-Hall effect is indeed present in MAG data from all Enceladus flybys.

- The simulated magnetic field signatures are in good quantitative agreement with the observed field perturbations for the six flybys (E5 – E9 and E11), if and only if negatively charged dust is included.

- Within the plume, the ion flow is slowed down to below 1 km/s.

- The hemisphere coupling current system proposed by *Saur et al.* [2007] and found to be present in MAG data by *Simon et al.* [2011b] is also evident in the simulation results.

- The simulations indicate a small variability in the activity of the plume between all analyzed pairs of similar flybys by about a factor of two.

- For some flybys (E5, E6 and E8) simulations and MAG data match better if a tilt of the plume is considered, yielding a different orientation of the plume for each of these flybys.

The major drawback of this study was that the analytical expressions for the neutral and dust plume were adjusted to MAG data only, while measurements of other instruments from Cassini were not considered.

In the second part (chapter 6), the ion densities and the magnetic signatures of charged dust at Enceladus were analyzed. The model was improved in the sense that it then included two different types of simulations. The output of Monte-Carlo simulations of the neutral and dust plumes was used as input for the hybrid plasma simulations. Since charged nanograins in the plume are strongly affected by the ambient electromagnetic fields and vice versa, the hybrid plasma simulations and Monte-Carlo simulations of the dust were carried out iteratively. In addition, a more detailed description of the ion-neutral chemistry for the water group ions was considered.

The density profiles of the neutral water obtained from the plume simulations agree well with available INMS data for the E3, E5 and E7 flybys. The simulated dust plume could be compared to CDA data for the micron-sized grains and CAPS observations of the charged nanograins. However, the model of the dust plume includes many free parameters, the impact of which will be discussed in a separate study [*Meier et al., in preparation*]. Here, the focus was on the results of the plasma simulations or, more precisely, the impact of the neutral gas and charged dust plumes on the plasma flow pattern and the electromagnetic fields was analyzed.

By combining the simulation results with Cassini INMS and CAPS data it was found that:

- Although the magnetospheric plasma consists of protons and different water group ion species, the reactions between these ions and the neutral water cloud end up in the production of H_3O^+ which has an abundance of nearly 100% within and downstream of the plume. This finding is in agreement with INMS observations by *Cravens et al.* [2009].

- Combining realistic models of the neutral plume and the ionization sources (solar photons, electron impacts) allows to constrain the ion densities in the plume. Based on the densities of about $1000\,\mathrm{cm}^{-3}$ for negatively charged nanograins observed by CAPS during E3 and E5 [*Hill et al.* 2012], it is found that these densities can only be maintained if an effective ionization frequency of at least $\nu^* = 3 \cdot 10^{-8}\,\mathrm{s}^{-1}$ is taken into account. This value is a factor of five larger than the sum of the photoionization rate and the electron impact rate derived by *Ozak et al.* [2012] and might therefore point to an additional ion source. This source might be associated with the production of heavier water cluster ions (H_2O^+-H_2O or H_3O^+-H_2O), as observed by INMS [*Cravens et al.* 2009] and CAPS [*Tokar et al.* 2009]. Dusty plasma effects – such as a dust cloud potential – may also lead to an increase of the effective ionization rate.

- Since the modeled dust size distribution peaks at a grain radius of 2 nm, the plume of charged dust is dominated by small nanograins and therefore significantly affected by the electromagnetic forces. A dense pick-up tail is visible in the dust charge density in the ($x > 0, y < 0$) sector (i. e. downstream and towards Saturn). It was decided not to provide absolute values of the dust charge density, as these are related to the ion density and therefore also to the ionization rate due to charge neutrality. However, it was demonstrated that a fraction of free electrons (n_e/n_i) well above 50% is sufficient to explain the observed magnetic field perturbations.

By comparing the results of the improved simulation model with MAG data from the E7, E14, E15, E17 and E19 flybys, further properties of the plume could be constrained:

- By comparing the magnetic field perturbations produced by three different neutral plume setups, it was found that magnetic field observations alone are inappropriate to uniquely constrain the fine structure of the active jets. This result is consistent with an analysis of MAG data from E0, E1 and E2 by *Saur et al.* [2008].

- The velocity of the dust grains ("dust pick-up current") only makes an insignificant contribution to the transverse currents. Instead, the spatial distribution of the dust charge density determines the magnetic field structures.

- MAG data from the E14, E17 and E19 encounters show a negative B_y perturbation which is related to the presence of negatively charged dust according to the Anti-Hall effect. These perturbations are present only in the $y > 0$ hemisphere where the dust pick-up occurs, but no similar signature exists in the opposite half-space ($y < 0$). Therefore, the B_y perturbations measured during these flybys can be regarded as the magnetic signatures of nanograin pick-up.

- In addition, MAG data from the E15 flyby was analyzed and it was found that the magnetic field signatures observed far downstream of the plume (at $x > 5R_E$) probably arise from nanograin pick-up.

- The magnitude of the B_y perturbations as well as the location of the transition region from northern ($\Delta B_y < 0$) to southern wing ($\Delta B_y > 0$) is not controlled by the dust charge density directly below the south pole. Instead, the southward extension of the dust plume, i. e. the region where a noticeable fraction of the electrons is absorbed by the dust, determines the magnetic field structures. Therefore, even MAG data from the horizontal flybys at $z \approx -1.5R_E$ contain information on the length of the dust plume. Directly south of Enceladus, the modeled B_y perturbation is in agreement with MAG data only if the dust plume extends to at least $z = -4R_E$. Such a large extension of the plume requires the average charging distance of the nanograins to be sufficiently large. Otherwise, most of them would be picked up close to the south pole and be transported out of the interaction region. These necessary charging distances can be achieved if the nanograins leave the surface with velocities of up to 2000 m/s.

- The surprising fact that Cassini did not pass through the region with reduced magnetic field strength downstream of the plume is a consequence of the modification

of the current systems by the nanograins. This effect rotates the region of decreased field away from the path of the flown flyby trajectories. During E14, E17 and E18, however, the spacecraft crossed the outer edge of this region.

8.2 Rhea

In chapter 7, an analysis of Cassini magnetic field data acquired during the only two polar Rhea flybys of the entire Cassini mission was presented. During the R2 flyby on 02 March 2010, Cassini passed through the Rhea fluxtube $\sqrt{y^2 + z^2} = R_{RH}$ above the north pole while moving from the Saturn-averted into the Saturn-facing half space. The trajectory of the subsequent R3 encounter on 11 January 2011 led through the Rhea fluxtube below the moon's south pole. During R3, Cassini moved from the Saturn-facing into the Saturn-averted half space. The trajectories of both flybys were nearly parallel to Rhea's equatorial plane ($z = 0$) and slightly inclined with respect to the y axis. During the entire Cassini mission, there will be no further Rhea flybys that possess similar trajectories. Magnetic field observations from both flybys revealed perturbation signatures inside the Rhea fluxtube with a magnitude of about $10 - 15\%$ of the background field.

To interpret these magnetic field observations, estimations from simple analytical models as well as output from the hybrid simulations were applied. The major results can be summarized as follows:

- Even though data from Cassini's Ion and Neutral Mass Spectrometer suggest Rhea to be embedded in a tenuous exosphere [*Teolis et al.* 2010], the interaction between this gas envelope and the incident magnetospheric flow is not expected to produce any measurable perturbations of the ambient magnetic field. Since the Pedersen conductance of Rhea's exosphere is about two orders of magnitude smaller than the Alfvén conductance of the ambient flow, the weak Alfvén wing arising from the presence of the atmosphere is completely obscured by the magnetic field signatures caused by plasma absorption at the surface.

- Although Cassini did not pass through the wake downstream of Rhea, the magnetometer detected compression signatures in B_z during both flybys. These field perturbations arise from the absorption of magnetospheric particles with large field-aligned velocity components at the surface of the icy moon: particle absorption in the south polar region leads to a partial depletion of the magnetospheric flow above the north pole. On the other hand, absorption of particles impinging with pitch angles near 0° (remember that $\underline{B}_0$ points southward) on the north pole causes a plasma void below the south pole. The resulting pressure deficit within the Rhea fluxtube is compensated by an enhanced magnetic field strength. The magnitude of the observed B_z perturbations is consistent with a simple pressure balance calculation. The signatures seen in B_y during both flybys are also consistent with a compression of the magnetic field lines inside the Rhea fluxtube and a depression along the flanks of the interaction region. This picture agrees well with Cassini MAG observations during flybys of Dione and Tethys as well as during an earlier wakeside Rhea encounter (e.g., *Roussos et al.* [2008a], *Simon et al.* [2009a, 2011a]).

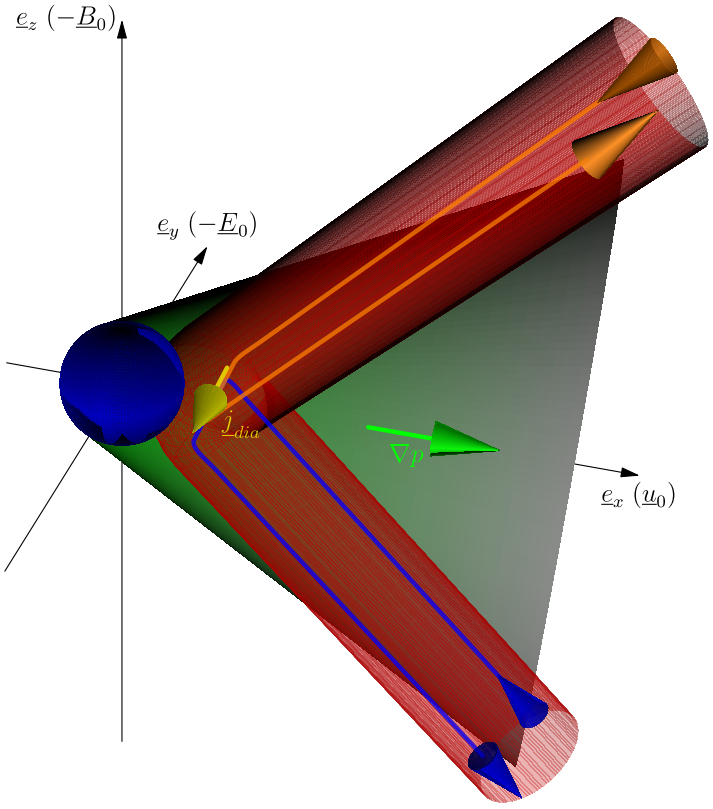

Figure 8.1: Key elements of Rhea's magnetospheric interaction, as described in this thesis. The finite length of Rhea's plasma wake (shaded in green) along the corotational flow direction gives rise to a density gradient ∇p along the positive x axis, corresponding to a diamagnetic current j_{dia} in $(-y)$ direction. This diamagnetic current is (partially) closed by the currents (orange and blue) in a weak Alfvén wing (red tubes), emerging from the regions of depleted plasma density over Rhea's poles and in the wake. For illustration purposes, the wing tubes in the figure are connected to the central plasma void where the density gradient is largest. Figure courtesy of A. Wennmacher.

- Due to the high thermal velocity of the incident magnetospheric flow, the density void downstream and over the poles of Rhea is refilled at rather short distances of 2–3 moon radii along the corotational flow direction. The resulting density gradient in $(+x)$ direction gives rise to a diamagnetic current in $(-y)$ direction, i.e. parallel to the undisturbed convective electric field. This diamagnetic current is connected to the currents along the characteristics of a weak Alfvén wing, arising from the finite length of Rhea's plasma wake in $(+x)$ direction. The presence of this wing corresponds to a negative B_x perturbation above the north pole and to a positive B_x perturbation below the south pole of Rhea. Thus, the finite length of Rhea's plasma wake produces a qualitatively similar perturbation as field line draping around a conducting exosphere/ionosphere. A minor part of the diamagnetic currents is closed at the outer boundaries of Rhea's plasma wake. In these regions, the density gradient points in negative x direction, corresponding to a diamagnetic current in positive y direction.

- The intensity of the flow-aligned magnetic field perturbations is not only proportional to the pressure gradient in the wake, but it also *decreases* with *increasing* strength of the ambient magnetospheric field. The plasma environment of Rhea, featuring a rather large beta value of $\beta_i + \beta_e \approx 1$, is therefore particularly suitable for observing these signatures. Even if flybys of Tethys or Dione possessed suitable trajectories to detect this effect, the stronger background magnetospheric field near the orbits of these satellites ($\beta_i + \beta_e \ll 1$) would most probably prevent the formation of any measurable flow-aligned field perturbations.

- The ion gyroradii in the incident magnetospheric flow are comparable to the size of the Rhea, thereby making plasma absorption at the surface of the moon asymmetric with respect to the direction of the convective electric field. This effect also causes an asymmetry in the structure of the Alfvén wing: in the Saturn-averted hemisphere where the convective electric field points away from Rhea, the magnetic field perturbations are more intense than in the Saturn-facing hemisphere. Magnetic field observations from both R2 and R3 are qualitatively consistent with the presence of this asymmetric Alfvén wing structure, generated by the finite length of Rhea's wake. Additional close flybys of Rhea would be required to further strengthen this prediction of the hybrid simulation.

Figure 8.1 summarizes our current understanding of Rhea's magnetospheric interaction.

8.3 Outlook

Although excellent agreement between the modeled magnetic field signatures and Cassini MAG data was achieved for a number of flybys of Enceladus and Rhea, there are still various features in the data that are not reproduced by the simulations. This points to a still oversimplified model and/or additional processes which are not yet considered.

In appendix B, those Enceladus flybys are discussed, for which the results are (partially) only in rough agreement with MAG data. A few test runs were carried out to analyze the origin of the most apparent discrepancies. From these simulations as well as from the results presented in chapters 5 and 6, it was learned that the following issues should be addressed in future work:

- Even though the simulations discussed in chapter 6 are based on a neutral plume in agreement with INMS data, MAG data from the steep flybys E3 – E6 could be reproduced only for a neutral plume which is almost as narrow as the one applied in chapter 5. Up to now, no simulation setup could be found which simultaneously explains MAG and INMS data for these flybys.

- The B_z perturbations measured above Enceladus' north pole during E12 and E13 as well as during the far downstream encounter E15 feature a puzzling increase of a few nT around closest approach. The magnitude of these perturbations would be roughly consistent with an enhanced magnetic field compensating for a lack of plasma pressure similar to Rhea's wake. However, at Enceladus, the plasma is deflected around the Alfvén wing before it impinges on the surface. In particular

for E15, the simulations would be more likely consistent with an increase of plasma pressure due to the increased ion density in the pick-up tail. It is therefore not clear why a plasma density cavity should be present in these regions.

- The fact that – at least for some of the flybys like E7 – the simplified analytical expression for the dust charge density yields better agreement with MAG data than the dust plume resulting from the Monte-Carlo simulations shows that Enceladus' cloud of charged dust is still considerably different from that generated by the simulations. In particular at the Saturn-averted side of the plume (outbound of E7 and E9, inbound of E14 and E17 – E19), the simulated B_y perturbations are clearly weaker than the measured perturbations. This may indicate that the Anti-Hall effect needs to be stronger in this region, and consequently the dust charge density needs to be higher in the direction opposite to the dust pick-up. The reasons for the differences to our modeling efforts could be manifold: the real dust size distribution could favor larger grains which would imply less pick-up; the ionization frequency (and the resulting plasma densities) might be larger or smaller which would alter the grain charging; the dust jets might be more collimated than assumed or some of them might be oriented away from Saturn.

- MAG data from the horizontal flybys discussed in chapter 6 exhibit magnetic field discontinuities exactly at the Enceladus flux tube which are likely associated with the hemisphere coupling current system proposed by *Saur et al.* [2007]. However, these discontinuities seem to be present only in the Saturn-facing hemisphere. This may be linked to the asymmetric distribution of auroral hiss (strong whistler mode emissions) which are generated by field-aligned currents [*Leisner et al.* 2013]. The cause of these asymmetries should be investigated.

- The high densities of negatively charged dust may also lead to fundamental changes in the nature of the plasma, i.e. dusty plasma effects like the dust cloud potential may play a key role in understanding the details of the physics within the plume. Incorporating the dust cloud potential may also lead to a self-consistent model of the ion source ν^*.

- The future flybys E20 and E22 are going to be located $10R_E$ above and $20R_E$ below Enceladus' poles, respectively. Thus, these flybys are going to provide the unique opportunity to study the northern and southern Alfvén wing in the far field, thereby allowing to further constrain the extent of the plume in the plane perpendicular to the magnetic field.

- Unfortunately, some results also reveal numerical artifacts. For instance, a wave structure with a wave length corresponding to the mesh can be clearly seen in figure 6.12. Furthermore, the offset between simulated B_z component and MAG data inbound of the encounters E14, E17 and E19 (cf. figures 6.10 and 6.13) is associated with an artificial extent of the magnetic field pile-up region. However, it should be pointed out that it has been very thoroughly checked that these artifacts do *not* affect the aspects of the simulated magnetic field structures that are discussed in this thesis, nor do they alter any of the conclusions. Nevertheless, these numerical effects should be eliminated in future work.

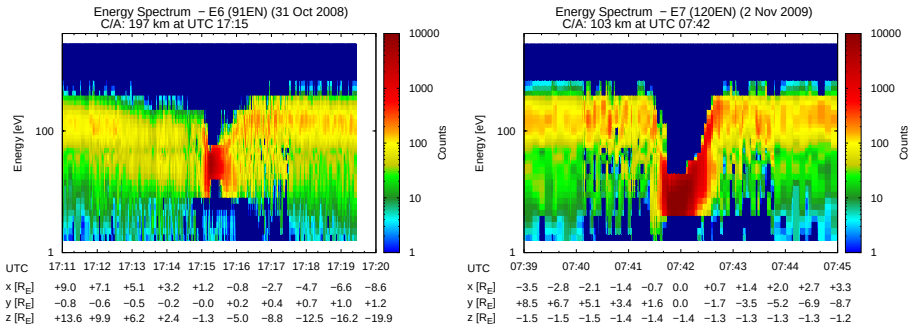

(a) (b)

Figure 8.2: Preliminary simulation results for ion energy spectra along E6 and E7 (instrument pointing not taken into account).

Although the simulation model presented in chapter 6 considers data from various instruments onboard the Cassini spacecraft, the analysis focused on the interpretation of magnetic field data. A comparison of ion energy spectra from the simulations with CAPS spectra has not yet been accomplished and may reveal further aspects of the ion-neutral-dust interactions. Preliminary ion energy spectra along E6 and E7 obtained from the simulations are shown in figure 8.2. Inbound and outbound of the two trajectories, the ion energies range from 1 eV to about 200 eV, whereas most ions possess energies of about 100 eV. This mean energy corresponds to the ion bulk speed of about $u_0 = 20\,\mathrm{km/s}$ superimposed on Cassini's velocity. The scattering of the ion energies is associated with a Maxwellian distribution with a temperature of $k_B T_i = 35\,\mathrm{eV}$. When crossing the plume, only a narrow energy range can be seen. These energies are centered at about $E = 30\,\mathrm{eV}$ and $E < 10\,\mathrm{eV}$, corresponding to Cassini's velocities of $v = 17.7\,\mathrm{km/s}$ and $v = 7.7\,\mathrm{km/s}$ during the E6 and E7 encounters, respectively. Therefore, the narrow energy range results from the nearly stagnant plasma flow within the plume. Due to the higher ion density in the plume, the count rates are increased. These results are generally consistent with CAPS data presented by *Tokar et al.* [2009]. It should be pointed out, however, that these results are preliminary and more work is required to optimize and analyze the simulated spectra.

For Rhea, it should be investigated if the charging of the moon's surface generates noticeable field-aligned currents which contribute to the overall plasma structures, thereby explaining the spiky dips of the observed B_x component which are located exactly at the surface of the Rhea flux tube. Furthermore, a theoretical description of Rhea's asymmetric Alfvén wing with respect to the large ion gyroradii still needs to be developed.

Overall, the findings of this thesis substantially increased the knowledge about the plasma interactions of Saturn's family of icy moons. In particular, additional structures generated by Rhea's wake as well as afore unknown processes in Enceladus' dusty plume have been revealed. The insights into plasma structures within a dust-rich environment that were developed in this thesis will also become increasingly important when the ROSETTA spacecraft arrives at comet 67P/Churyumov-Gerasimenko in spring 2014. However, our understanding of Enceladus and Rhea and their magnetospheric environments is far from complete. Unfortunately, the Cassini mission has already passed its summit with regard

to flybys of the icy moons. The spacecraft is going to perform only three additional Enceladus flybys and no further flyby of Rhea that could provide new in situ data. The huge set of data already collected by Cassini will, however, still allow to make new and spectacular discoveries within the next years or even decades, before we visit these fascinating moons again.

A Reaction and Ionization Rates

The ion-neutral interactions considered in our model are provided in table 6.2 of the main paper. There, the reaction rates $k_{\alpha,\beta}(u_0)$ were listed at the upstream speed u_0 for reference. In this appendix, we provide the expressions for the velocity-dependent reaction rates $k_{\alpha,\beta}(v_{rel})$ which are applied in our model. Two different interaction mechanisms are included: elastic ion-neutral collisions and charge exchange (see section 4.3).

The elastic ion-neutral collisions are approximated by induced dipole interactions (ID), i.e. the approaching ion leads to a polarization of the neutral [*Schunk and Nagy* 2009]. In such a case, the interaction potential V is given by

$$V = -\frac{1}{4\pi\epsilon_0}\frac{\gamma_n e^2}{r} \quad , \tag{A.1}$$

where γ_n denotes the polarizability of the neutral and r the distance between the ion and the neutral. Collisions associated with this interaction potential are also referred to as "Maxwell molecule collisions". The corresponding the cross section $\sigma_\alpha^{ID}(v_{rel})$ in units of cm^2 is (see e. g. *Schunk and Nagy* [2009], eq. (4.88))

$$\sigma_\alpha^{ID}(v_{rel}) = 2.21\pi\sqrt{\frac{\gamma_n \alpha_{fit} e^2}{\mu_\alpha v_{rel}^2}} \quad , \tag{A.2}$$

where v_{rel} is the relative velocity between the reactants in cm/s, $\gamma_n = 1.48\cdot10^{-24}\,\mathrm{cm}^3$ is the polarizability of H_2O and μ_α and $e = 4.8\cdot10^{-10}$ esu denote reduced mass and elementary charge, respectively. CGS units are used in equation (A.2). α_{fit} is a fudge parameter to match the laboratory measured rates (e. g. http://www.udfa.net UMIST database for Astrochemistry). Physically, it accounts for the permanent electric dipole of the water molecules. The values for α_{fit} are listed in table A.1. Since $\sigma_\alpha^{ID} \propto v_{rel}^{-1}$, the corresponding reaction rate $k_{\alpha,\beta}^{ID} = v_{rel}\sigma_\alpha^{ID}$ is independent of the velocity.

The resonant charge exchange cross section $\sigma_\alpha^{CX}(v_{rel})$ (in cm^2) can be expressed as (see e.g., *Schunk and Nagy* [2009], eq. (4.148))

$$\sigma_\alpha^{CX}(v_{rel}) = \left(A_\alpha - B_\alpha \log_{10}(\epsilon_\alpha)\right)^2 - C_\alpha \log_{10}(v_{rel}) \quad , \tag{A.3}$$

where $\epsilon_\alpha = \mu_\alpha v_{rel}^2/2$ (in eV) denotes the relative kinetic energy of the colliding particles. The last term on the right hand side of equation (A.3) has been added to match the laboratory measured rates. Here, the velocity v_{rel} has to be inserted in units of cm/s. The values of the constants A_α, B_α and C_α are listed in table A.1. If different energy states of the ions need to be considered, the expression becomes more complex [*Nakai et al.* 1987]:

Table A.1: Ion-neutral reactions included in the model. Two reaction mechanisms are considered: induced dipole interactions (ID) and charge exchange (CX). Listed are the contributions to each reactions' total cross section $\sigma^{tot}_{\alpha,\beta}(v_{rel})$ and the constants required for the calculation of $\sigma^{ID}_{\alpha}(v_{rel})$, $\sigma^{CX}_{\alpha}(v_{rel})$ and $\sigma^{CX*}_{\alpha}(v_{rel})$. A_α and B_α are given in 10^{-8} cm, C_α in 10^{-17} cm^2. In case one of the parameters is not given in the table, the corresponding term can be omitted for the calculation of the cross section. See text for further explanations.

α		β	$\sigma^{tot}_{\alpha,\beta}(v_{rel})$	α_{fit}	A_α	B_α	C_α	a_1	a_2
H^+	$\rightarrow$	H_2O^+	$\sigma^{ID}_{H^+} + 2\sigma^{CX*}_{H^+}(v_{rel})$	4.58	-	-	-	$5.85 \cdot 10^5$	1.6
O^+	$\rightarrow$	H_2O^+	$\sigma^{ID}_{O^+} + 2\overline{\sigma}^{CX}_{O^+}(v_{rel})$	8.8	9	1.2	1.5	$1 \cdot 10^{10}$	1.7
OH^+	$\rightarrow$	H_2O^+	$0.45\sigma^{ID}_{OH^+} + 2\overline{\sigma}^{CX}_{OH^+}(v_{rel})$	7.44	9	1.2	1.5	$1 \cdot 10^{10}$	1.7
OH^+	$\rightarrow$	H_3O^+	$0.55\sigma^{ID}_{OH^+}$	7.44	-	-	-	-	-
H_2O^+	$\rightarrow$	H_2O^+	$2\sigma^{CX}_{H_2O^+}(v_{rel})$	-	4.3	0.95	-	-	-
H_2O^+	$\rightarrow$	H_3O^+	$\sigma^{ID}_{H_2O^+}$	4.05	-	-	-	-	-
H_3O^+	$\rightarrow$	H_3O^+	$\sigma^{ID}_{H_3O^+}$	4	-	-	-	-	-

$$\sigma^{CX*}_{\alpha}(v_{rel}) = \sigma_0 \left(f(E_1) + a_7 f(E_1/a_8)\right) \quad , \tag{A.4}$$

where $\sigma_0 = 10^{-16}$ cm^2 and

$$f(E) = a_1 \frac{(E/E_R)^{a_2}}{1 + (E/a_3)^{a_2+a_4} + (E/a_5)^{a_2+a_6}} \quad , \tag{A.5}$$

$$E_1 = E_0 - E_t \quad . \tag{A.6}$$

For reactions with the target H_2O, the constants a_3,..., a_8 are $a_3 = 0.1$ keV, $a_4 = 0.441$, $a_5 = 5.86$ keV, $a_6 = 3.82$, $a_7 = 3.2 \cdot 10^{-4}$ keV and $a_8 = 10$ keV. $E_R = 25$ keV is the Rydberg energy multiplied by the ratio of the atomic hydrogen mass to the electron mass, E_0 denotes the projectile energy, and $E_t = -0.001$ keV is the threshold energy of the process. Since no laboratory data are available for the reaction $OH^+ \rightarrow H_2O^+$, we assume the cross sections to be identical to the reaction $O^+ \rightarrow H_2O^+$. The total momentum transfer cross section for charge exchange is finally given by

$$\overline{\sigma}^{CX}_{\alpha}(v_{rel}) = \frac{1}{3}\left(\sigma^{CX*}_{\alpha}(v_{rel}) + 2\sigma^{CX}_{\alpha}(v_{rel})\right) \quad . \tag{A.7}$$

The resulting total momentum transfer cross sections $\sigma^{tot}_{\alpha,\beta}(v_{rel})$ including both, induced dipole interactions and charge exchange, are provided in table A.1. The corresponding reaction rates can be expressed as

$$k_{\alpha,\beta}(v_{rel}) = \frac{\mu_\alpha}{m_\alpha} v_{rel} \sigma^{tot}_{\alpha,\beta}(v_{rel}) \quad . \tag{A.8}$$

The factor $\frac{\mu_\alpha}{m_\alpha}$ is necessary to convert the rates into the laboratory frame of reference, i. e. ENIS in our case. Please note that for $\alpha = H_3O^+$, the induced dipole interactions at energies of a few eV do not describe a reaction but elastic collisions only.

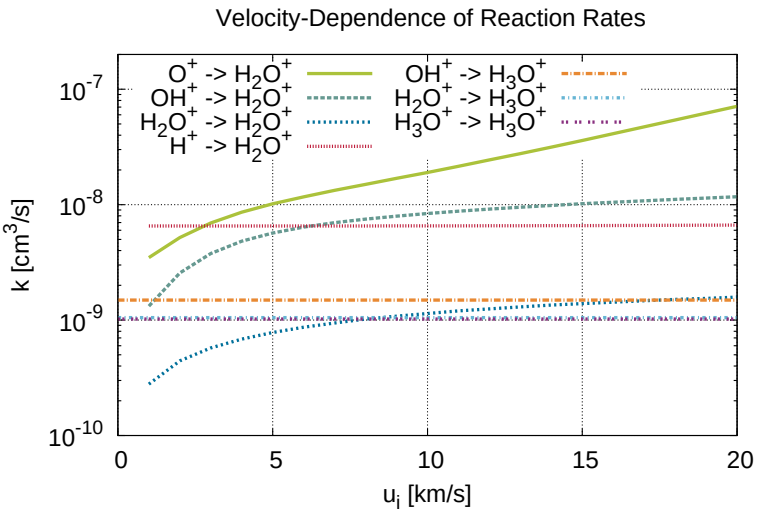

Figure A.1: Velocity-dependence of the various reactions included in the model.

The resulting velocity-dependence of the various reactions is illustrated in figure A.1. In particular for $v_{rel} > 5\,\mathrm{km/s}$, the reaction rates of H^+, O^+ and OH^+ to H_2O^+ are almost one order of magnitude larger than the others. For H_2O^+, the conversion into H_3O^+ dominates the resonant charge exchange for velocities $v_{rel} < 8.5\,\mathrm{km/s}$. The vertical black line marks the upstream speed u_0.

B Magnetic Field Signatures from Further Enceladus Flybys

Although numerous Enceladus flybys have been discussed in chapters 5 and 6, some encounters have not yet been addressed in this thesis, e. g. E12, E13 and E1/E10/E16. Furthermore, the magnetic field signatures observed during the steep flybys E5 and E6 have been compared only to the results based on the analytical plume in chapter 4, but no comparison with the results of the improved model – that was discussed in chapter 6 – was shown. The E2 encounter was even analyzed only in the preceding study to this thesis [*Kriegel et al.* 2009], but no simulated magnetic field perturbations considering negatively charged dust have been presented along E2. For completeness, the magnetic field signatures of these flybys will be discussed in the following.

B.1 The Encounters E1, E10 and E16

The E16 encounter is the only one whose magnetic field signatures have neither been discussed in the literature nor in this thesis. Thus figure B.1(b) displays MAG data (black) together with the default simulation setup from chapter 6 (red) for the E16 flyby. The trajectory of E16 is very similar to that of the E1 and E10 flybys which occurred in 2005 and 2010, respectively. Similar to the other flybys discussed in this paper, the trajectories are parallel to the equatorial plane at $z \approx -1.5 R_E$. In contrast to the other flybys, however, Cassini passed upstream of the plume. MAG data from E10 are shown for comparison in figure B.1(a). The magnetic field signatures for E1 have already been analyzed by e. g. *Kriegel et al.* [2009] (cf. figure 6 in that work), whereas for E10 until now only MAG data [*Jia et al.* 2011] and no simulation results have been discussed. The only difference between MAG data from E1, E10 and E16 is the magnitude of the perturbations which is about three times stronger for E16 than for E1. The strength of the perturbations observed during E10 is in between those of the two other flybys. This results at least partially from the higher upstream density during E16 (see table 2.2). The simulation results are in good agreement with MAG data for all three components for E16, but the simulated perturbations are stronger than the signatures observed during E10. This may indicate that the upstream density for E10 is even lower than the value of $n_0 = 60\,\mathrm{cm}^{-3}$ given in table 2.2. A comparison to figures 6a and 6b of *Kriegel et al.* [2009] also reveals that there are only minor differences to the results of the initial model which did *not* consider electron absorption by dust. Thus, the presence of charged dust has only negligible impact on the magnetic field signatures directly upstream of Enceladus. Since closest approach

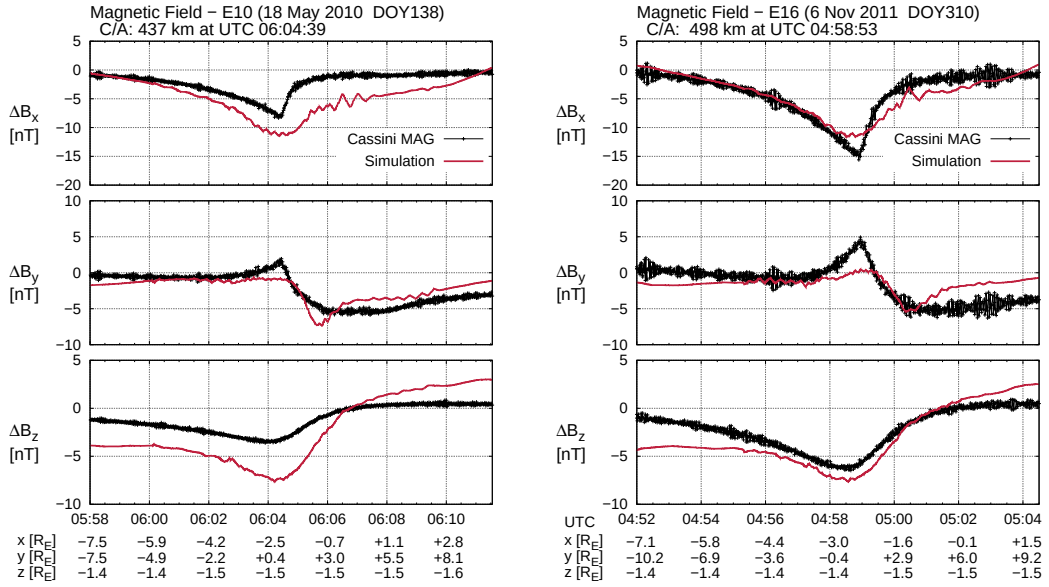

(a) (b)

Figure B.1: Cassini MAG data (black) and simulation results (red) for the E10 flyby (a) and the E16 flyby (b).

of E16 took place $2R_E$ upstream of the moon, this is in agreement with the pick-up of the nanograins that do not reach so far upstream before they are charged and accelerated by the convective electric field.

B.2 Comparison of MAG Data from E5 and E6 with the Results Based on the Simulated Plumes

In section 5.5.2, the magnetic field signatures of the steep flybys E5 and E6 have been discussed. It was shown that the simulated magnetic field perturbations are in good agreement with MAG data for the two flybys (cf. figure 5.6). However, these simulations were based on the analytical plume model which was adjusted to MAG data. As has been pointed out in section 6.2, this adjustment resulted in a neutral plume profile that is significantly different from the neutral plume observed by INMS.

Therefore, figure B.2 displays MAG data (black) from E5 and E6 together with the results of two simulations corresponding to the different modeling approaches of the plume. The simulations denoted by the solid red lines are based on the neutral plume that is obtained from the Monte-Carlo simulations. The simulations also use the jet sources dust plume; further parameters are described in section 6.1.1. In contrast, the simulations corresponding to the dashed blue lines are identical to the best fit cases discussed in section 5.5.2. Therefore, these simulations include the analytical descriptions of the neutral and dust plumes, the parameters of which are adjusted to MAG data. In the following, the

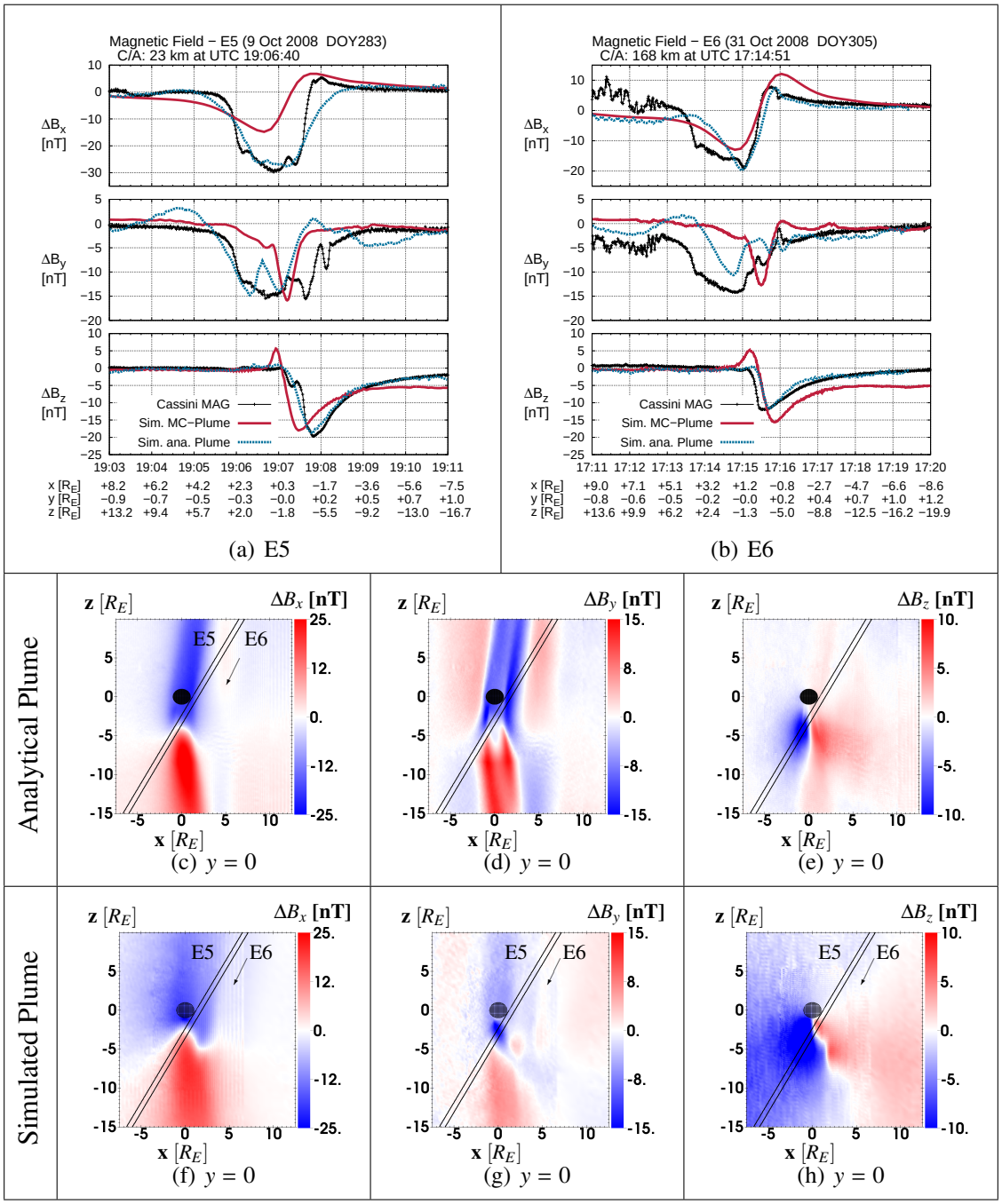

(a) E5 (b) E6

(c) $y = 0$ (d) $y = 0$ (e) $y = 0$

(f) $y = 0$ (g) $y = 0$ (h) $y = 0$

Figure B.2: Magnetic field perturbations along the encounters E5 (a) and E6 (b). Shown are MAG data (black), a simulation based on the Monte-Carlo neutral plume with jet sources only (red), and a simulation including the analytical neutral plume, which is adjusted to MAG (blue). The simulations with the analytical plume are identical to the best fit simulations of figure 5.6. Panels (c)–(h) display the field perturbations of the two simulations in the ($y = 0$)-plane.

two neutral plumes are referred to as "analytical plume" and "simulated or Monte-Carlo plume", respectively. Surprisingly, the agreement between MAG data and simulation for all three components is better for the simulation with the analytical plume than for the simulation based on the Monte-Carlo plume.

For a better understanding of the discrepancies between the simulated field perturbations, panels (c)–(h) of figure B.2 display the field perturbations in the ($y = 0$)-plane. The analytical plume generates a sharply defined Alfvén flux tube with strong B_x and B_y perturbations, whereas the Monte-Carlo plume generates an Alfvén wing which exhibits a rather diffuse transition from the flux tube to the background. The B_y perturbation of the Alfvén wing triggered by the Monte-Carlo plume is even about 10 nT weaker than that of the Alfvén wing generated by the analytical plume. For both cases, the transition region from $\Delta B_x < 0$ to $\Delta B_x > 0$ possesses the shape of a parabola that opens down. For the analytical plume, this parabola is narrower and its vertex is located further south than for the simulated plume. In particular in the inbound region of the E5 trajectory, the observed B_x and B_y perturbations agree better with the narrower Alfvén wing. Both, E5 and E6 intersect also the southern Alfvén wing in the simulation with the Monte-Carlo plume, yielding a disagreement between simulation and data around 19:08 and 17:16, respectively. In the B_y component, MAG data of both flybys show a perturbation of $\Delta B_y < -10\,\mathrm{nT}$ already above Enceladus, in agreement with the perturbation generated by the analytical plume. However, the positive ΔB_y outside the Alfvén flux tube (cf. panel (d)) has not been observed. Furthermore, the results for the simulated plume show only a spiky decrease of B_y along the flybys, corresponding to the small region with $\Delta B_y \approx -10\,\mathrm{nT}$ below Enceladus' south pole (panel (g)). In contrast, MAG data exhibits an extended interval with $\Delta B_y < -10\,\mathrm{nT}$ from about $z = +2R_E$ to $z = -5R_E$ in rough agreement with the perturbations generated by the analytical plume. The B_z perturbation generated by the Monte-Carlo plume exhibits a significantly larger pile-up region (see panel (h)) than the simulation with the analytical plume. In addition, the simulated neutral plume also leads to a short interval with a positive B_z perturbation of about $\Delta B_z = +5\,\mathrm{nT}$ along the flyby trajectories that was not observed by Cassini. This interval corresponds to the small region of positive ΔB_z close to the south pole. As has been discussed in section 6.5.5, the field decrease region is rotated out of Cassini's path for the E14 and E19 flybys due to the modifications of the current systems by the dust. Thus, minor changes in the shape of the dust plume may also resolve the discrepancy of the simulated B_z perturbations and MAG data along E5 and E6. However, the narrower analytical plume shifted both, pile-up and field decrease further southward and in consequence, these simulations do not exhibit a positive ΔB_z along E5 and E6.

Overall, the magnetic field structures generated by the narrower and denser analytical plume match well with MAG data, whereas a neutral plume in agreement with INMS data fails to explain several features of the observed magnetic field perturbations. Thus it seems to be challenging to find a parameter setup which is in agreement with both, MAG and INMS data for E5 and E6. Although not shown here, modeling of the two other steep flybys E3 and E4 led to the same difficulties. To resolve this issue, several explanations could be considered:

- A different orientation of the jets may lead to a narrower plume along the trajectories. However, this is rather unlikely, since the neutral density of the Monte-Carlo

plume is in excellent agreement with INMS data along E3 and E5.

- The INMS instrument may be influenced by dust impacts such that the "real" H_2O densities within the plume and outbound of the trajectories may be different from those presented in section 6.2, possibly leading to a narrower and denser plume. However, by deriving the densities from the count rates *Teolis et al.* [2010] already considered the instrument's mode of operation.

- Changes in the parameters of the dust – that are poorly constrained compared to the parameters of the neutral plume – may cause the dust plume to dominate the magnetic field structures instead of the neutral plume. Although this point is somewhat vague, the results presented in this thesis have already demonstrated that the dust has a tremendous influence on the plasma structures.

Whatever the reason is, the four steep flybys emphasize that further multi-instrument studies are required to understand Enceladus' plasma interaction.

B.3 The E2 Flyby in the Context of Charged Dust

The magnetic field signatures for the E2 flyby have already been discussed by *Jia et al.* [2010c] as well as in a hybrid simulation study preceding this thesis [*Kriegel et al.* 2009]. However, the results of a simulation including negatively charged dust have not yet been presented along E2. Therefore, figure B.3(a) shows MAG data (black) and the results of two simulations for the E2 flyby. The simulation denoted by the solid red line uses the jet sources dust plume (see section 6.5.3), whereas the simulation results denoted by the dashed blue line correspond to a scenario without dust.

Both simulations are in very good agreement with MAG data for the B_x component. The small discrepancies in the B_z component may arise from a higher or lower activity of some of the modeled neutral gas jets, since it has been pointed out by *Kriegel et al.* [2009] that the onset of the B_z perturbation as well as the location of the maximum dip is extremely sensitive to the shape of the neutral plume. As expected, the B_y perturbations of the two simulations are clearly different. Only the simulation including the dust exhibits a negative ΔB_y after 19:56, in agreement with MAG data. However, both simulations show a small dip in the B_y perturbations of about $\Delta B_y = -3\,\mathrm{nT}$ around 19:54:30, i.e. at $(-1.4, 0.3, -1.9)R_E$, which is hardly visible in the data. To understand these structures, figure B.3(b) shows the simulated B_y perturbation from the simulation based on the jet sources dust plume in a plane defined by Cassini's motion in x and z direction during E2. The interval of E2 which corresponds to the small dip is highlighted in yellow, while the negative B_y perturbations in the outbound segment of the trajectory are marked in green. The color plot shows that the observed negative ΔB_y outbound of E2 corresponds to Cassini's passage through the northern Alfvén wing. In contrast, the small dip of negative ΔB_y around 19:54:30 arises from the field perturbations within the plume. Overall, the simulated field perturbations are in good agreement with MAG data if dust is considered.

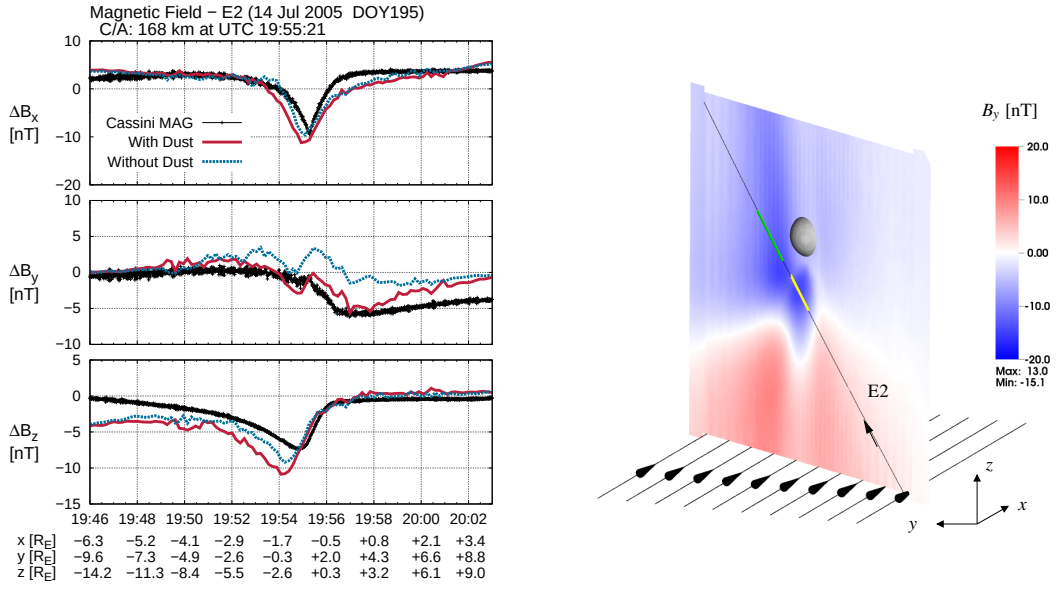

(a) (b)

Figure B.3: Plot (a) displays magnetic field data (black) and simulation results for the jet dust plume (red, solid) and without dust (blue, dashed) along the E2 flyby. See section 6.5.3 for further details of the simulation setup. Panel (b) shows the B_y perturbation from the simulation with dust in a plane defined by Cassini's motion in x and z direction during E2. The segments of the trajectory that are colored yellow and green approximately correspond to the intervals of negative ΔB_y visible in plot (a).

B.4 The North Polar Flybys E12 and E13

Finally, the magnetic field signatures from the two north polar encounters E12 and E13 shall be discussed. Figure B.4 displays MAG data (black) and the simulated magnetic field perturbations along these two flybys for three simulations. The vertical orange lines denote the surface of the Enceladus flux tube. The simulation setup is basically the same as for the simulations shown in chapter 5. The simulation denoted by the solid red lines is based on the jet sources dust plume, the simulation displayed in dashed blue uses the analytical dust plume and the third one (dotted green) is based on the analytical dust plume but does not include the solid body of Enceladus.

For ΔB_x and ΔB_y all three simulations are in reasonable agreement with MAG data. Outside the flux tube at $y < 0$ the simulations, however, fail to reproduce the additional kink in B_x and B_y which was observed by Cassini during E12. At closer look, the agreement between simulated and measured field perturbations is better for the analytical plume than for the jet sources dust. The B_x signatures generated by the latter exhibit a stronger perturbation in the inbound segment than the perturbations generated by the analytical plume and also clearly stronger perturbations than observed by Cassini, whereas the B_y perturbations of the jet dust plume are too weak at the outbound part of the trajectory. Since the spacecraft passed from the Saturnward to the Saturn-averted hemisphere during both flybys (cf. figure 2.9 in section 2.3.1), the outbound segment corresponds to the sector with

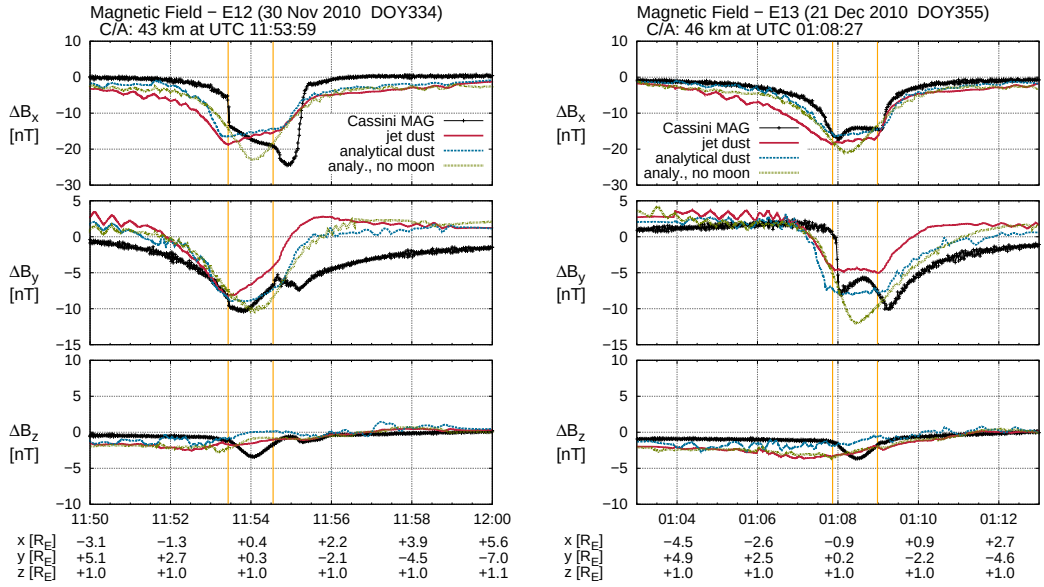

(a) (b)

Figure B.4: Magnetic field perturbations along the encounters E12 (a) and E13 (b). Shown are MAG data (black), and three simulations which based on the jet sources dust plume (solid red), analytical dust plume (dashed blue) and analytical dust plume, but no solid body of Enceladus considered (dotted green).

only few charged nanograins due to the pick-up of these grains towards Saturn. Therefore, the weaker perturbations of the jet dust plume outbound of the trajectories indicate that the jet dust plume includes a too strong pick-up of the nanograins. This finding is consistent with the analysis of MAG data from E14 and E19 presented in section 6.5.3. It should be noted that the dust is not present at the plane of the two flybys (north of Enceladus), but the effect of the dust is mapped from the south polar plume to regions north of Enceladus due to the translation invariance of the Alfvén wing. In addition, the simulation without the solid body of the moon yields stronger perturbations within the flux tube which is most apparent for the B_y component along E13. If the solid body is considered, the Alfvénic currents are not blocked at the surface of the moon and directly feed the northern wing. It should be pointed out that E12 and E13 are the only flybys where the presence of the solid body made a noticeable difference for the simulated magnetic field signatures.

Furthermore, the small dip in ΔB_z of about 3 nT around closest approach is not seen in the simulations. Interestingly, a similar perturbation was observed during E15 at about $(x, y, z) = (6R_E, 0, -1.5R_E)$, i.e. at a completely different place. At the same time, the density of thermal and high-energetic electrons was measured to be reduced [*unpublished data*]. This may indicate that pressure balance between plasma and magnetic field leads to the B_z increase, similar to Rhea's wake. An estimate of ΔB_z based on equation (7.6) yields $\Delta B_z \approx -2$ nT which is comparable to the data. However, we are not aware of any reason why the plasma density should be reduced at these different regions and therefore, the cause of these perturbations remains purely speculative.

C Simulations of the Dione D3 Flyby

Apart from Enceladus and Rhea, we also briefly studied the third largest icy satellite Dione (R_D = 561.5 km) which orbits Saturn at a distance of about $6.28R_S$, between the orbits of Tethys and Rhea. So far, Cassini performed three targeted flybys of Dione, labeled D1, D2 and D3. The magnetic field data obtained during the first two flybys have been analyzed by *Simon et al.* [2011a] who found that the signatures from D1 are consistent with the existence of a tenuous, sputtering-induced atmosphere around Dione.

We applied A.I.K.E.F. to the plasma interaction of Dione in order to contribute to the analysis of Energetic particle measurements in the vicinity of Dione by *Krupp et al.* [2013][1]. These authors compared electron absorption signatures from measurements of the Cassini LEMMS instrument with electron wake profiles resulting from electron guiding center trajectory tracings in our simulated environment of Dione.

The simulation was adjusted to the D3 flyby which occurred on 12 December 2011. The trajectory is shown in figure C.1 in the Dione Interaction System, which can be introduced in analogy to the ENIS and the RHIS (see section 2.3). The encounter passed through Dione's wake in the anti-Saturnward direction parallel to the equatorial plane at $z = 0.1R_D$. The closest approach altitude was only about 100 km.

The parameters applied in the simulation are summarized in Table C.1. In agreement with RPWS measurements of the upper hybrid frequency at Dione's L-shell [*Gurnett et al.* 2007, *Persoon et al.* 2009], an upstream plasma density of $n_0 = 25\,\mathrm{cm}^{-3}$ is used. The plasma is assumed to consist of water group ions with an average mass of $m_i = 17$ amu which impinge on the moon at the ideal corotation velocity of $u_0 = 40\,\mathrm{cm}^{-3}$. The electron temperature is set to $k_B T_{ec} = 6$ eV, and the ion temperature is $k_B T_i = 90$ eV [*Khurana et al.* 2008]. The background magnetic field is modeled as a dipole field and is adjusted to MAG data from the D3 flyby (cf. Figure C.2). Like Enceladus and Rhea, Dione itself is modeled as an absorbing and insulating body (see section 4.5.1). The conductivity of the interior is set to $\sigma = 1{\cdot}10^{-7}$ S/m. The simulation box has a size of $L_x{\times}L_y{\times}L_z = 18R_D{\times}15R_D{\times}15\,R_D$. Two levels of refinement are used, yielding a resolution of $\Delta_{L_2} \approx 0.05R_{Di} = 28$ km. Further numerical parameters are provided in table C.1.

An overview of our simulation results is provided in figure C.3. Panels C.3(a)–(c) show the magnetic field perturbations in the $y = 0$ cross section, panels C.3(j)–(l) display the plane $z = 0$ and in panels (m)–(o) the results are are shown at $z = +0.1R_D$, i.e. approx-

[1]Full reference: Krupp, N., E. Roussos, **H. Kriegel**, P. Kollmann, M.G. Kivelson, A. Kotova , C. Paranicas, D.G. Mitchell, S.M. Krimigis, K.K. Khurana (2013), Energetic particle measurements in the vicinity of Dione during the three Cassini encounters 2005–2011, *Icarus*, *226*, 617–628, doi: 10.1016/j.icarus.2013.06.007

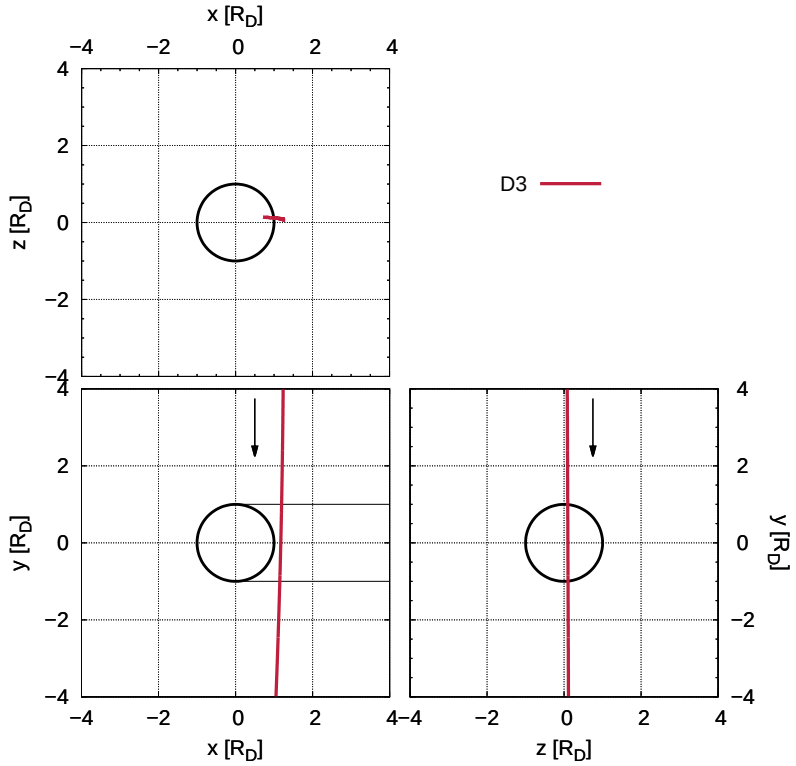

Figure C.1: Trajectory of the D3 Dione flyby.

Table C.1: Paramater used for the hybrid simulation.

Parameter	Value
Plasma velocity	$u_0 = 40\,\mathrm{km/s}$
Plasma number density	$n_0 = 25\,\mathrm{cm}^{-3}$
Magnetic field	$\underline{B}_0 = (0, 0, -75)\,\mathrm{nT}$
Species included	W^+
Ion mass	$m_i = 17\,\mathrm{amu}$
Alfvén Mach number	$M_A = 0.63$
Ion temperature	$k_B T_i = 90\,\mathrm{eV}$
Electron temperature	$k_B T_e = 6\,\mathrm{eV}$
Box (x)	$-4.5R_D \leq x \leq +13.5R_D$
Box (y)	$-7.5R_D \leq x \leq +7.5R_D$
Box (z)	$-7.5R_D \leq x \leq +7.5R_D$
Mesh spacing	$\Delta_{L_2} = 26\,\mathrm{km} = 0.05R_D$
Time step	$\Delta t = 0.004\Omega_i^{-1} = 9.4 \cdot 10^{-3}\,\mathrm{s}$
Simulation time	$\tau = 10000\Delta t = 40\Omega_i^{-1} = 94\,\mathrm{s}$
Smoothing	$\eta_{sm} = 0.5\%$
Conductivity of interior	$\sigma = 1 \cdot 10^{-7}\,\mathrm{S/m}$

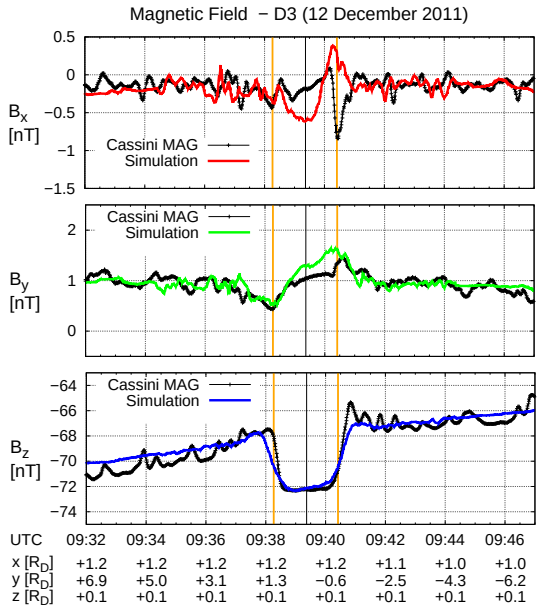

Figure C.2: Magnetic field along D3 flyby.

imately the plane where the D3 flyby was located. The results confirm the picture of an inert moon's plasma interaction discussed in chapter 7. An Alfvén wing (visible in the ΔB_x component in C.3(a)) is triggered in the wake. The enhancement of B_z compensates the loss of plasma pressure in the wake. Furthermore, density and velocity are displayed in the $y = 0$ and $z = 0$ planes (cf. plots C.3(d), (e), (g) and (h)). They structures correspond to the shape of the plasma wake and its refilling described in section 3.1. The resistivity profile used for the inner boundary is shown in panel C.3(f). Because the closest approach took place only $0.2R_D$ above the surface, we made sure that the inner boundary does not affect our results by comparing with a run using only an absorbing half-shell (see section 4.5.1). The overall structures are very similar to Rhea, as expected.

A comparison between the measured and simulated magnetic field signatures is presented in Figure C.2. The vertical black and orange lines mark closest approach and wake boundaries, respectively. In the B_x component, simulated and observed magnetic field are strongly different from each other. Within the wake, the simulation shows a small decrease while MAG data exhibit a ΔB_x of about zero. During the outbound crossing of the wake boundary, Cassini observed a sharp negative spike in the B_x component of about 1 nT. This structure has also been observed at Rhea and may arise from a field-aligned current, the origin of which is not yet clear. For the B_y and B_z components, however, MAG data and hybrid simulation are in excellent agreement. The bipolar signature in B_y can be explained by field lines which are dragged into the wake since the D3 trajectory is located slightly north of the equatorial plane (see Figure 1 of *Simon et al.* [2009b]). The negative B_z perturbation within the wake corresponds to an increase of the magnetic field strength due to the deficit of plasma pressure in the wake.

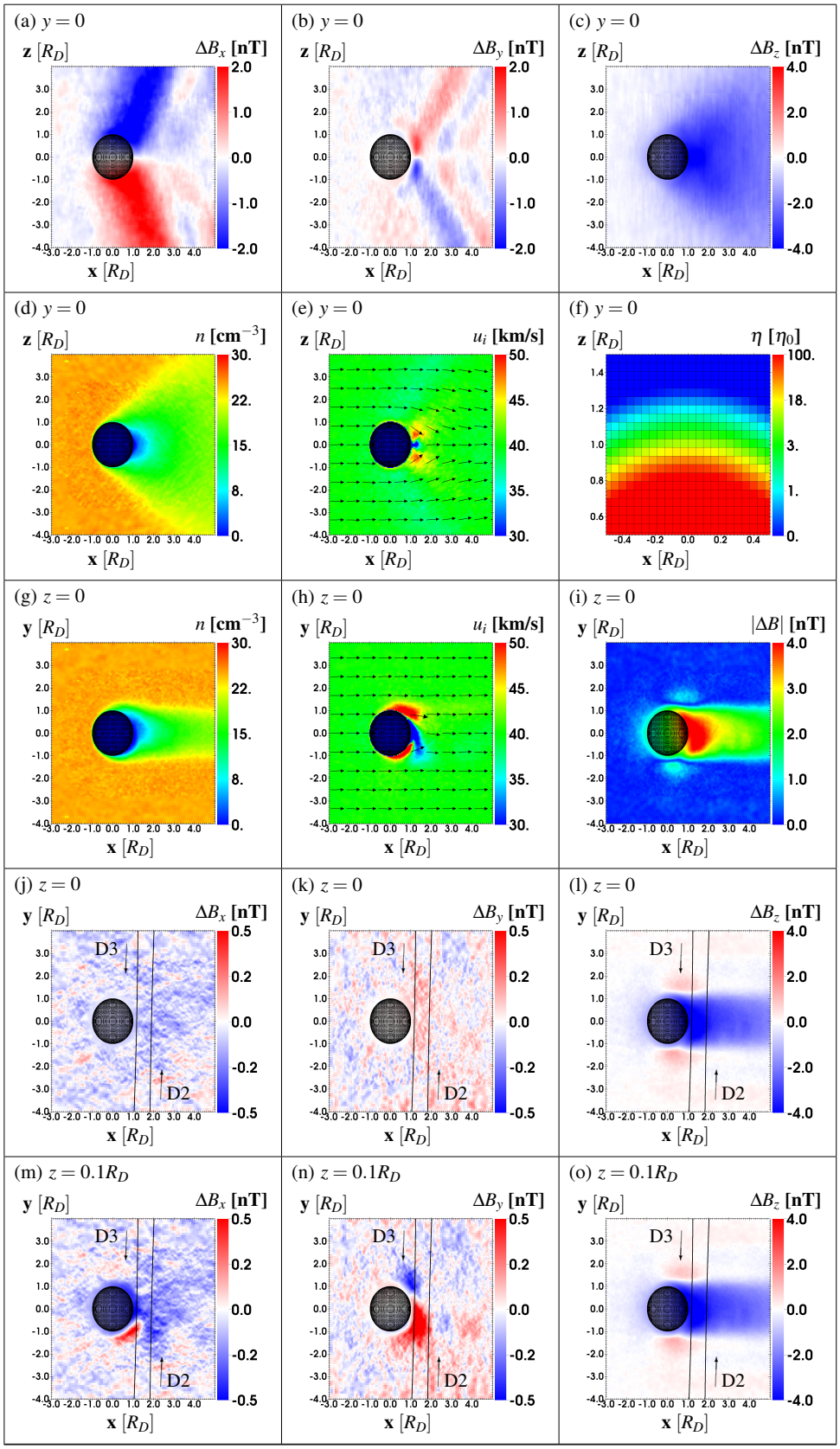

Figure C.3: Simulation results for Dione. The simulation parameters are adjusted to the D3 flyby.

Bibliography

Anderson, J. D., and G. Schubert (2007), Saturn's satellite Rhea is a homogeneous mix of rock and ice, *Geophysical Research Letters*, *34*, 2202, doi: 10.1029/2006GL028100.

André, N., et al. (2008), Identification of Saturn's magnetospheric regions and associated plasma processes: Synopsis of Cassini observations during orbit insertion, *Reviews of Geophysics*, *46*, RG4008, doi: 10.1029/2007RG000238.

Andrews, D. J., A. J. Coates, S. W. H. Cowley, M. K. Dougherty, L. Lamy, G. Provan, and P. Zarka (2010), Magnetospheric period oscillations at Saturn: Comparison of equatorial and high-latitude magnetic field periods with north and south Saturn kilometric radiation periods, *Journal of Geophysical Research (Space Physics)*, *115*, A12252, doi: 10.1029/2010JA015666.

Andrews, D. J., B. Cecconi, S. W. H. Cowley, M. K. Dougherty, L. Lamy, G. Provan, and P. Zarka (2011), Planetary period oscillations in Saturn's magnetosphere: Evidence in magnetic field phase data for rotational modulation of Saturn kilometric radiation emissions, *Journal of Geophysical Research (Space Physics)*, *116*, A09206, doi: 10.1029/2011JA016636.

Arridge, C. S., C. T. Russell, K. K. Khurana, N. Achilleos, N. André, A. M. Rymer, M. K. Dougherty, and A. J. Coates (2007), Mass of Saturn's magnetodisc: Cassini observations, *Geophysical Research Letters*, *34*, L09108, doi: 10.1029/2006GL028921.

Bagdonat, T. (2004), Hybrid Simulation of Weak Comets, Ph.D. thesis, TU Braunschweig.

Bagdonat, T., and U. Motschmann (2002a), From a Weak to a Strong Comet - 3d Global Hybrid Simulation Studies, *Earth Moon and Planets*, *90*, 305–321, doi: 10.1023/A:1021578232282.

Bagdonat, T., and U. Motschmann (2002b), 3D Hybrid Simulation Code Using Curvilinear Coordinates, *Journal of Computational Physics*, *183*, 470–485, doi: 10.1006/jcph.2002.7203.

Birch, P. C., and S. C. Chapman (2001), Detailed structure and dynamics in particle-in-cell simulations of the lunar wake, *Physics of Plasmas*, *8*, 4551–4559, doi: 10.1063/1.1398570.

Blöcker, A. (2013), MHD-Modellierung der Plasmawechselwirkung bei Io und Enceladus, Master's thesis, Universität zu Köln.

Bonfond, B., D. Grodent, J.-C. Gérard, A. Radioti, J. Saur, and S. Jacobsen (2008), UV Io footprint leading spot: A key feature for understanding the UV Io footprint multiplicity?, *Geophysical Research Letters*, *35*, L05107, doi: 10.1029/2007GL032418.

Bonfond, B., D. Grodent, J.-C. Gérard, A. Radioti, V. Dols, P. A. Delamere, and J. T. Clarke (2009), The Io UV footprint: Location, inter-spot distances and tail vertical extent, *Journal of Geophysical Research (Space Physics)*, *114*, A07224, doi: 10.1029/2009JA014312.

Bößwetter, A., T. Bagdonat, U. Motschmann, and K. Sauer (2004), Plasma boundaries at Mars: a 3-D simulation study, *Annales Geophysicae*, *22*(12), 4363–4379.

Burch, J. L., J. Goldstein, W. S. Lewis, D. T. Young, A. J. Coates, M. K. Dougherty, and N. André (2007), Tethys and Dione as sources of outward-flowing plasma in Saturn's magnetosphere, *Nature*, *447*, 833–835, doi: 10.1038/nature05906.

Burger, M. H., E. C. Sittler, R. E. Johnson, H. T. Smith, O. J. Tucker, and V. I. Shematovich (2007), Understanding the escape of water from Enceladus, *Journal of Geophysical Research (Space Physics)*, *112*, A06,219, doi: 10.1029/2006JA012086.

Burton, M. E., M. K. Dougherty, and C. T. Russell (2010), Saturn's internal planetary magnetic field, *Geophysical Research Letters*, *37*, L24105, doi: 10.1029/2010GL045148.

Běhounková, M., G. Tobie, G. Choblet, and O. Čadek (2012), Tidally-induced melting events as the origin of south-pole activity on Enceladus, *Icarus*, *219*, 655–664, doi: 10.1016/j.icarus.2012.03.024.

Cao, H., C. T. Russell, U. R. Christensen, M. K. Dougherty, and M. E. Burton (2011), Saturn's very axisymmetric magnetic field: No detectable secular variation or tilt, *Earth and Planetary Science Letters*, *304*(1 – 2), 22 – 28, doi: 10.1016/j.epsl.2011.02.035.

Clarke, J. T., D. Grodent, S. W. H. Cowley, E. J. Bunce, P. Zarka, J. E. P. Connerney, and T. Satoh (2004), *Jupiter. The Planet, Satellites and Magnetosphere*, chap. Jupiter's aurora, pp. 639–670, Cambridge Univ. Press.

Coates, A. J., G. H. Jones, G. R. Lewis, A. Wellbrock, D. T. Young, F. J. Crary, R. E. Johnson, T. A. Cassidy, and T. W. Hill (2010), Negative ions in the Enceladus plume, *Icarus*, *206*, 618–622, doi: 10.1016/j.icarus.2009.07.013.

Coates, A. J., A. Wellbrock, G. H. Jones, J. H. Waite, P. Schippers, M. F. Thomsen, C. S. Arridge, and R. L. Tokar (2013), Photoelectrons in the Enceladus plume, *Journal of Geophysical Research (Space Physics)*, *118*, 5099–5108, doi: 10.1002/jgra.50495.

Colburn, D. S., R. G. Currie, J. D. Mihalov, and C. P. Sonett (1967), Diamagnetic Solar-Wind Cavity Discovered behind Moon, *Science*, *158*, 1040–1042, doi: 10.1126/science.158.3804.1040.

Cravens, T. E., R. L. McNutt, J. H. Waite, I. P. Robertson, J. G. Luhmann, W. Kasprzak, and W.-H. Ip (2009), Plume ionosphere of Enceladus as seen by the Cassini Ion and Neutral Mass Spectrometer, *Geophysical Research Letters*, *36*, L08106, doi: 10.1029/2009GL037811.

Cravens, T. E., N. Ozak, M. S. Richard, M. E. Campbell, I. P. Robertson, M. Perry, and A. M. Rymer (2011), Electron energetics in the Enceladus torus, *Journal of Geophysical Research (Space Physics)*, *116*, A09205, doi: 10.1029/2011JA016498.

Desch, M. D., and M. L. Kaiser (1981), Voyager measurement of the rotation period of Saturn's magnetic field, *Geophysical Research Letters*, *8*, 253–256, doi: 10.1029/GL008i003p00253.

Dong, Y., T. W. Hill, B. D. Teolis, B. A. Magee, and J. H. Waite (2011), The water vapor plumes of Enceladus, *Journal of Geophysical Research (Space Physics)*, *116*, A10204, doi: 10.1029/2011JA016693.

Dougherty, M. K., et al. (2004), The Cassini Magnetic Field Investigation, *Space Science Reviews*, *114*, 331–383, doi: 10.1007/s11214-004-1432-2.

Dougherty, M. K., et al. (2005), Cassini Magnetometer Observations During Saturn Orbit Insertion, *Science*, *307*, 1266–1270, doi: 10.1126/science.1106098.

Dougherty, M. K., K. K. Khurana, F. M. Neubauer, C. T. Russell, J. Saur, J. S. Leisner, and M. E. Burton (2006), Identification of a Dynamic Atmosphere at Enceladus with the Cassini Magnetometer, *Science*, *311*, 1406–1409, doi: 10.1126/science.1120985.

Farrell, W. M., W. S. Kurth, D. A. Gurnett, R. E. Johnson, M. L. Kaiser, J. Wahlund, and J. H. Waite (2009), Electron density dropout near Enceladus in the context of water-vapor and water-ice, *Geophysical Research Letters*, *36*, L10,203, doi: 10.1029/2008GL037108.

Farrell, W. M., et al. (2010), Modification of the plasma in the near-vicinity of Enceladus by the enveloping dust, *Geophysical Research Letters*, *37*, L20,202, doi: 10.1029/2010GL044768.

Fleshman, B. L., P. A. Delamere, and F. Bagenal (2010a), Modeling the Enceladus plume-plasma interaction, *Geophysical Research Letters*, *37*, 3202–+, doi: 10.1029/2009GL041613.

Fleshman, B. L., P. A. Delamere, and F. Bagenal (2010b), A sensitivity study of the Enceladus torus, *Journal of Geophysical Research (Planets)*, *115*, E04,007, doi: 10.1029/2009JE003372.

Goertz, C. K. (1980), Io's interaction with the plasma torus, *Journal of Geophysical Research (Space Physics)*, *85*, 2949–2956, doi: 10.1029/JA085iA06p02949.

Goldreich, P., and D. Lynden-Bell (1969), Io, a Jovian unipolar inductor, *Astrophysical Journal*, *156*, 59–78, doi: 10.1086/149947.

Gombosi, T. I., T. P. Armstrong, C. S. Arridge, K. K. Khurana, S. M. Krimigis, N. Krupp, A. M. Persoon, and M. F. Thomsen (2009), *Saturn's Magnetospheric Configuration*, p. 203, doi: 10.1007/978-1-4020-9217-6_9.

Gurnett, D. A., and W. R. Pryor (2012), Auroral Processes Associated With Saturn's Moon Enceladus, *Washington DC American Geophysical Union Geophysical Monograph Series*, *197*, 305–313, doi: 10.1029/2011GM001174.

Gurnett, D. A., A. M. Persoon, W. S. Kurth, J. B. Groene, T. F. Averkamp, M. K. Dougherty, and D. J. Southwood (2007), The Variable Rotation Period of the Inner Region of Saturn's Plasma Disk, *Science*, *316*(5823), 442, doi: 10.1126/science.1138562.

Gurnett, D. A., et al. (2011), Auroral hiss, electron beams and standing Alfvén wave currents near Saturn's moon Enceladus, *Geophysical Research Letters*, *38*, L06,102, doi: 10.1029/2011GL046854.

Gustafsson, G., and J.-E. Wahlund (2010), Electron temperatures in Saturn's plasma disc, *Planet. Space Sci.*, *58*, 1018–1025, doi: 10.1016/j.pss.2010.03.007.

Haff, P. K., G. L. Siscoe, and A. Eviatar (1983), Ring and plasma - The enigmae of Enceladus, *Icarus*, *56*, 426–438, doi: 10.1016/0019-1035(83)90164-1.

Hansen, C. J., L. Esposito, A. I. F. Stewart, J. Colwell, A. Hendrix, W. Pryor, D. Shemansky, and R. West (2006), Enceladus' Water Vapor Plume, *Science*, *311*, 1422–1425, doi: 10.1126/science.1121254.

Hansen, C. J., et al. (2008), Water vapour jets inside the plume of gas leaving Enceladus, *Nature*, *456*, 477–479, doi: 10.1038/nature07542.

Hansen, C. J., D. E. Shemansky, L. W. Esposito, I. Stewart, and A. R. Hendrix (2010), The Composition and Structure of Enceladus' Plume from a Cassini UVIS Observation of a Solar Occultation, *AGU Fall Meeting Abstracts*, pp. C9+.

Hansen, C. J., et al. (2011), The composition and structure of the Enceladus plume, *Geophysical Research Letters*, *38*, L11,202, doi: 10.1029/2011GL047415.

Harms, E. (2010), Modellierung des Plumes von Enceladus, Master's thesis, TU Braunschweig.

Hartogh, P., et al. (2011), Direct detection of the Enceladus water torus with Herschel, *Astronomy & Astrophysics*, *532*, L2, doi: 10.1051/0004-6361/201117377.

Havnes, O., G. E. Morfill, and C. K. Goertz (1984), Plasma potential and grain charges in a dust cloud embedded in a plasma, *Journal of Geophysical Research*, *89*, 10,999–11,003, doi: 10.1029/JA089iA12p10999.

Hedman, M. M., C. M. Gosmeyer, P. D. Nicholson, C. Sotin, R. H. Brown, R. N. Clark, K. H. Baines, B. J. Buratti, and M. R. Showalter (2013), An observed correlation between plume activity and tidal stresses on enceladus, *Nature*, *advance online publication*, –.

Herschel, J. F. W., Sir (1847), *Results of astronomical observations made during the years 1834, 5, 6, 7, 8, at the Cape of Good Hope; being the completion of a telescopic survey of the whole surface of the visible heavens, commenced in 1825*, London, Smith, Elder and co.

Herschel, W. (1790), Account of the Discovery of a Sixth and Seventh Satellite of the Planet Saturn; With Remarks on the Construction of Its Ring, Its Atmosphere, Its Rotation on an Axis, and Its Spheroidical Figure, *Philosophical Transactions of the Royal Society of London*, *80*, 1–20.

Hill, T. W. (1979), Inertial limit on corotation, *Journal of Geophysical Research (Space Physics)*, *84*, 6554–6558, doi: 10.1029/JA084iA11p06554.

Hill, T. W., and D. H. Pontius (1998), Plasma injection near Io, *Journal of Geophysical Research*, *103*, 19,879–19,886, doi: 10.1029/98JE00945.

Hill, T. W., et al. (2012), Charged nanograins in the Enceladus plume, *Journal of Geophysical Research (Space Physics)*, *117*, A05209, doi: 10.1029/2011JA017218.

Howett, C. J. A., J. R. Spencer, J. Pearl, and M. Segura (2010), Thermal inertia and bolometric Bond albedo values for Mimas, Enceladus, Tethys, Dione, Rhea and Iapetus as derived from Cassini/CIRS measurements, *Icarus*, *206*, 573–593, doi: 10.1016/j.icarus.2009.07.016.

Howett, C. J. A., J. R. Spencer, J. Pearl, and M. Segura (2011), High heat flow from Enceladus' south polar region measured using 10-600 cm^{-1} Cassini/CIRS data, *Journal of Geophysical Research (Planets)*, *116*, E03003, doi: 10.1029/2010JE003718.

Hurford, T. A., P. Helfenstein, G. V. Hoppa, R. Greenberg, and B. G. Bills (2007), Eruptions arising from tidally controlled periodic openings of rifts on Enceladus, *Nature*, *447*, 292–294, doi: 10.1038/nature05821.

Hurford, T. A., B. G. Bills, P. Helfenstein, R. Greenberg, G. V. Hoppa, and D. P. Hamilton (2009), Geological implications of a physical libration on Enceladus, *Icarus*, *203*, 541–552, doi: 10.1016/j.icarus.2009.04.025.

Itikawa, Y., and N. Mason (2005), Cross sections for electron collisions with water molecules, *Journal of Physical and Chemical Reference Data*, *34*(1), 1–22, doi: 10.1063/1.1799251.

Jacobsen, S. (2011), Three-dimensional Magnetohydrodynamic Simulations of Io's Non-Linear Interaction with the Jovian Magnetosphere, Ph.D. thesis, University of Cologne.

Jia, Y., C. T. Russell, K. K. Khurana, J. S. Leisner, Y. J. Ma, and M. K. Dougherty (2010a), Time-varying magnetospheric environment near Enceladus as seen by the Cassini magnetometer, *Geophysical Research Letters*, *37*, L9203, doi: 10.1029/2010GL042948.

Jia, Y.-D., C. T. Russell, K. K. Khurana, Y. J. Ma, W. Kurth, and T. I. Gombosi (2010b), Interaction of Saturn's magnetosphere and its moons: 3. Time variation of the Enceladus plume, *Journal of Geophysical Research (Space Physics)*, *115*(A14), A12,243, doi: 10.1029/2010JA015534.

Jia, Y.-D., C. T. Russell, K. K. Khurana, Y. J. Ma, D. Najib, and T. I. Gombosi (2010c), Interaction of Saturn's magnetosphere and its moons: 2. Shape of the Enceladus plume, *Journal of Geophysical Research (Space Physics)*, *115*(A12), A04,215, doi: 10.1029/2009JA014873.

Jia, Y.-D., C. T. Russell, K. K. Khurana, G. Toth, J. S. Leisner, and T. I. Gombosi (2010d), Interaction of Saturn's magnetosphere and its moons: 1. Interaction between corotating plasma and standard obstacles, *Journal of Geophysical Research (Space Physics)*, *115*, A04214, doi: 10.1029/2009JA014630.

Jia, Y.-D., C. T. Russell, K. K. Khurana, H. Y. Wei, Y. J. Ma, J. S. Leisner, A. M. Persoon, and M. K. Dougherty (2011), Cassini magnetometer observations over the Enceladus poles, *Geophysical Research Letters*, *38*, L19109, doi: 10.1029/2011GL049013.

Jia, Y.-D., Y. J. Ma, C. T. Russell, H. R. Lai, G. Toth, and T. I. Gombosi (2012), Perpendicular flow deviation in a magnetized counter-streaming plasma, *Icarus*, *218*, 895–905, doi: 10.1016/j.icarus.2012.01.017.

Jones, G. H., et al. (2008), The Dust Halo of Saturn's Largest Icy Moon, Rhea, *Science*, *319*, 1380–, doi: 10.1126/science.1151524.

Jones, G. H., et al. (2009), Fine jet structure of electrically charged grains in Enceladus' plume, *Geophysical Research Letters*, *36*, L16,204, doi: 10.1029/2009GL038284.

Jurac, S., and J. D. Richardson (2005), A self-consistent model of plasma and neutrals at Saturn: Neutral cloud morphology, *Journal of Geophysical Research (Space Physics)*, *110*, A09220, doi: 10.1029/2004JA010635.

Kallio, E. (2005), Formation of the lunar wake in quasi-neutral hybrid model, *Geophysical Research Letters*, *32*, L06107, doi: 10.1029/2004GL021989.

Kanani, S. J., et al. (2010), A new form of Saturn's magnetopause using a dynamic pressure balance model, based on in situ, multi-instrument Cassini measurements, *Journal of Geophysical Research (Space Physics)*, *115*, A06207, doi: 10.1029/2009JA014262.

Kempf, S., U. Beckmann, G. Moragas-Klostermeyer, F. Postberg, R. Srama, T. Economou, J. Schmidt, F. Spahn, and E. Grün (2008), The E ring in the vicinity of Enceladus. I. Spatial distribution and properties of the ring particles, *Icarus*, *193*, 420–437, doi: 10.1016/j.icarus.2007.06.027.

Kempf, S., U. Beckmann, and J. Schmidt (2010), How the Enceladus dust plume feeds Saturn's E ring, *Icarus*, *206*(2), 446–457, doi: 10.1016/j.icarus.2009.09.016.

Khurana, K. K., M. K. Dougherty, C. T. Russell, and J. S. Leisner (2007), Mass loading of Saturn's magnetosphere near Enceladus, *Journal of Geophysical Research (Space Physics)*, *112*, 8203–+, doi: 10.1029/2006JA012110.

Khurana, K. K., C. T. Russell, and M. K. Dougherty (2008), Magnetic portraits of Tethys and Rhea, *Icarus*, *193*, 465–474, doi: 10.1016/j.icarus.2007.08.005.

Kriegel, H. (2009), 3D-Hybridsimulationen der Plasmawechselwirkung des Saturnmondes Enceladus und Vergleich mit Cassini-Magnetometer-Daten, Master's thesis, TU Braunschweig.

Kriegel, H., S. Simon, J. Mueller, U. Motschmann, J. Saur, K.-H. Glassmeier, and M. Dougherty (2009), The plasma interaction of Enceladus: 3D hybrid simulations and comparison with Cassini MAG data, *Planetary and Space Science*, *57*(14-15), 2113 – 2122, doi: 10.1016/j.pss.2009.09.025.

Kriegel, H., S. Simon, U. Motschmann, J. Saur, F. M. Neubauer, A. M. Persoon, M. K. Dougherty, and D. A. Gurnett (2011), Influence of negatively charged plume grains on the structure of Enceladus' Alfvén wings: Hybrid simulations versus Cassini Magnetometer data, *Journal of Geophysical Research (Space Physics)*, *116*, A10223, doi: 10.1029/2011JA016842.

Krupp, N., et al. (2012), The Cassini Enceladus encounters 2005–2010 in the view of energetic electron measurements, *Icarus*, *218*(1), 433 – 447.

Krupp, N., et al. (2013), Energetic particle measurements in the vicinity of Dione during the three Cassini encounters 2005–2011, *Icarus*, *226*, 617–628, doi: 10.1016/j.icarus.2013.06.007.

Kurth, W. S., T. F. Averkamp, D. A. Gurnett, J. B. Groene, and A. Lecacheux (2008), An update to a Saturnian longitude system based on kilometric radio emissions, *Journal of Geophysical Research (Space Physics)*, *113*, 5222–+, doi: 10.1029/2007JA012861.

Ledvina, S. A., S. H. Brecht, and J. G. Luhmann (2004), Ion distributions of 14 amu pickup ions associated with Titan's plasma interaction, *Geophysical Research Letters*, *31*, L17S10, doi: 10.1029/2004GL019861.

Leisner, J. S., G. B. Hospodarsky, and D. A. Gurnett (2013), Enceladus auroral hiss observations: Implications for electron beam locations, *Journal of Geophysical Research (Space Physics)*, *118*, 160–166, doi: 10.1029/2012JA018213.

Lipatov, A. S., E. C. Sittler, R. E. Hartle, J. F. Cooper, and D. G. Simpson (2012), Saturn's magnetosphere interaction with Titan for T9 encounter: 3D hybrid modeling and comparison with CAPS observations, *Planetary and Space Science*, *61*, 66–78, doi: 10.1016/j.pss.2011.08.017.

Martinecz, C., et al. (2009), Plasma environment of Venus: Comparison of Venus Express ASPERA-4 measurements with 3-D hybrid simulations, *Journal of Geophysical Research (Space Physics)*, *114*, 0–+, doi: 10.1029/2008JE003174.

Matson, D. L., J. C. Castillo-Rogez, A. G. Davies, and T. V. Johnson (2012), Enceladus: A hypothesis for bringing both heat and chemicals to the surface, *Icarus*, *221*, 53–62, doi: 10.1016/j.icarus.2012.05.031.

Matthews, A. P. (1994), Current advance method and cyclic leapfrog for 2d multispecies hybrid plasma simulations, *Journal of Computational Physics*, *112*(1), 102 – 116, doi: http://dx.doi.org/10.1006/jcph.1994.1084.

Mauk, B. H., et al. (2005), Energetic particle injections in Saturn's magnetosphere, *Geophysical Research Letters*, *32*, L14S05, doi: 10.1029/2005GL022485.

Mauk, B. H., et al. (2009), *Saturn from Cassini-Huygens*, chap. Fundamental Plasma Processes in Saturn's Magnetosphere, pp. 281–331, Springer Netherlands, doi: 10.1007/978-1-4020-9217-6_11.

McKinnon, W. B. (2013), The shape of Enceladus as explained by an irregular core: Implications for gravity, libration, and survival of its subsurface ocean, *Journal of Geophysical Research: Planets*, *118*(9), 1775–1788, doi: 10.1002/jgre.20122.

Meyer, J., and J. Wisdom (2007), Tidal heating in Enceladus, *Icarus*, *188*, 535–539, doi: 10.1016/j.icarus.2007.03.001.

Moncuquet, M., A. Lecacheux, N. Meyer-Vernet, B. Cecconi, and W. S. Kurth (2005), Quasi thermal noise spectroscopy in the inner magnetosphere of Saturn with Cassini/RPWS: Electron temperatures and density, *Geophysical Research Letters*, *32*, L20S02, doi: 10.1029/2005GL022508.

Morooka, M. W., et al. (2011), Dusty plasma in the vicinity of Enceladus, *Journal of Geophysical Research (Space Physics)*, *116*, A12221, doi: 10.1029/2011JA017038.

Müller, A. L., J. Saur, N. Krupp, E. Roussos, B. H. Mauk, A. M. Rymer, D. G. Mitchell, and S. M. Krimigis (2010), Azimuthal plasma flow in the Kronian magnetosphere, *Journal of Geophysical Research (Space Physics)*, *115*, A08203, doi: 10.1029/2009JA015122.

Müller, J. (2012), A.I.K.E.F.: An Adaptive Hybrid Model with Application to Fossil Fields at Titan and Mercury's Double Magnetopause, Ph.D. thesis, TU Braunschweig.

Müller, J., S. Simon, U. Motschmann, J. Schüle, K.-H. Glassmeier, and G. J. Pringle (2011), A.i.k.e.f.: Adaptive hybrid model for space plasma simulations, *Computer Physics Communications*, *182*(4), 946 – 966, doi: 10.1016/j.cpc.2010.12.033.

Müller, J., S. Simon, Y.-C. Wang, U. Motschmann, D. Heyner, J. Schüle, W.-H. Ip, G. Kleindienst, and G. J. Pringle (2012), Origin of Mercury's double magnetopause: 3D hybrid simulation study with A.I.K.E.F., *Icarus*, *218*, 666–687, doi: 10.1016/j.icarus.2011.12.028.

Nakai, Y., T. Shirai, T. Tabata, and R. Ito (1987), Cross sections for charge transfer of hydrogen atoms and ions colliding with gaseous atoms and molecules, *Atomic Data and Nuclear Data Tables*, *37*(1), 69 – 101, doi: 10.1016/0092-640X(87)90005-2.

Neubauer, F. M. (1980), Nonlinear standing Alfven wave current system at Io - Theory, *Journal of Geophysical Research*, *85*, 1171–1178, doi: 10.1029/JA085iA03p01171.

Neubauer, F. M. (1998), The sub-Alfvénic interaction of the Galilean satellites with the Jovian magnetosphere, *Journal of Geophysical Research*, *103*, 19,843–19,866, doi: 10.1029/97JE03370.

Nimmo, F., and R. T. Pappalardo (2006), Diapir-induced reorientation of Saturn's moon Enceladus, *Nature*, *441*, 614–616, doi: 10.1038/nature04821.

Nimmo, F., J. R. Spencer, R. T. Pappalardo, and M. E. Mullen (2007), Shear heating as the origin of the plumes and heat flux on Enceladus, *Nature*, *447*, 289–291, doi: 10.1038/nature05783.

Omidi, N., C. T. Russell, R. L. Tokar, and J. S. Leisner (2010), Hybrid simulations of the plasma environment around Enceladus, *Journal of Geophysical Research (Space Physics)*, *115*, A05,212, doi: 10.1029/2009JA014391.

Omidi, N., R. L. Tokar, T. Averkamp, D. A. Gurnett, W. S. Kurth, and Z. Wang (2012), Flow stagnation at Enceladus: The effects of neutral gas and charged dust, *Journal of Geophysical Research (Space Physics)*, *117*, A06230, doi: 10.1029/2011JA017488.

Ozak, N., T. Cravens, A. Coates, I. Robertson, and G. Jones (2012), Modeling of Electron Fluxes in the Enceladus Plume, *Journal of Geophysical Research*, *117*, A06,220, doi: 0.1029/2011JA017497.

Pang, K. D., C. C. Voge, J. W. Rhoads, and J. M. Ajello (1984), The E ring of Saturn and satellite Enceladus, *Journal of Geophysical Research (Space Physics)*, *89*, 9459–9470, doi: 10.1029/JB089iB11p09459.

Paty, C. S., J. Dufek, J. H. Waite, and R. L. Tokar (2011), Coupling Eruptive Dynamics Models to Multi-fluid Plasma Dynamic Simulations at Enceladus, *AGU Fall Meeting Abstracts*, p. B2017.

Persoon, A. M., D. A. Gurnett, W. S. Kurth, G. B. Hospodarsky, J. B. Groene, P. Canu, and M. K. Dougherty (2005), Equatorial electron density measurements in Saturn's inner magnetosphere, *Geophysical Research Letters*, *32*, 23,105–+, doi: 10.1029/2005GL024294.

Persoon, A. M., et al. (2009), A diffusive equilibrium model for the plasma density in Saturn's magnetosphere, *Journal of Geophysical Research (Space Physics)*, *114*, A04211, doi: 10.1029/2008JA013912.

Pontius, D. H., and T. W. Hill (2006), Enceladus: A significant plasma source for Saturn's magnetosphere, *Journal of Geophysical Research (Space Physics)*, *111*, 9214–+, doi: 10.1029/2006JA011674.

Porco, C. C., et al. (2006), Cassini Observes the Active South Pole of Enceladus, *Science*, *311*, 1393–1401, doi: 10.1126/science.1123013.

Postberg, F., S. Kempf, J. Schmidt, N. Brilliantov, A. Beinsen, B. Abel, U. Buck, and R. Srama (2009), Sodium salts in E-ring ice grains from an ocean below the surface of Enceladus, *Nature*, *459*, 1098–1101, doi: 10.1038/nature08046.

Postberg, F., J. Schmidt, J. Hillier, S. Kempf, and R. Srama (2011), A salt-water reservoir as the source of a compositionally stratified plume on Enceladus, *Nature*, *474*, 620–622, doi: 10.1038/nature10175.

Pryor, W. R., et al. (2011), The auroral footprint of Enceladus on Saturn, *Nature*, *472*, 331–333, doi: 10.1038/nature09928.

Ranocha, H. (2013), Erweiterung des Hybrid-Codes A.I.K.E.F. um eine Energiegleichung für das Elektronenfluid, Master's thesis, TU Braunschweig.

Richardson, J. D., and E. C. Sittler, Jr. (1990), A plasma density model for Saturn based on Voyager observations, *Journal of Geophysical Research (Space Physics)*, *95*, 12,019–12,031, doi: 10.1029/JA095iA08p12019.

Roberts, J. H., and F. Nimmo (2008), Tidal heating and the long-term stability of a subsurface ocean on Enceladus, *Icarus*, *194*, 675–689, doi: 10.1016/j.icarus.2007.11.010.

Roussos, E., et al. (2008a), Plasma and fields in the wake of Rhea: 3-D hybrid simulation and comparison with Cassini data, *Annales Geophysicae*, *26*, 619–637.

Roussos, E., et al. (2008b), Discovery of a transient radiation belt at Saturn, *Geophysical Research Letters*, *35*, L22106, doi: 10.1029/2008GL035767.

Roussos, E., N. Krupp, H. Krüger, and G. H. Jones (2010), Surface charging of Saturn's plasma-absorbing moons, *Journal of Geophysical Research (Space Physics)*, *115*, A08225, doi: 10.1029/2010JA015525.

Roussos, E., et al. (2012), Energetic electron observations of Rhea's magnetospheric interaction, *Icarus*, *221*, 116–134, doi: 10.1016/j.icarus.2012.07.006.

Rymer, A. M., et al. (2007), Electron sources in Saturn's magnetosphere, *Journal of Geophysical Research (Space Physics)*, *112*, A02201, doi: 10.1029/2006JA012017.

Santolík, O., et al. (2011), Intense plasma wave emissions associated with Saturn's moon Rhea, *Geophysical Research Letters*, *38*, L19204, doi: 10.1029/2011GL049219.

Saur, J. (2004), A model of Io's local electric field for a combined Alfvénic and unipolar inductor far-field coupling, *Journal of Geophysical Research (Space Physics)*, *109*, A01210, doi: 10.1029/2002JA009354.

Saur, J., and D. F. Strobel (2005), Atmospheres and Plasma Interactions at Saturn's Largest Inner Icy Satellites, *The Astrophysical Journal*, *620*, L115–L118, doi: 10.1086/428665.

Saur, J., F. M. Neubauer, D. F. Strobel, and M. E. Summers (1999), Three-dimensional plasma simulation of Io's interaction with the Io plasma torus: Asymmetric plasma flow, *Journal of Geophysical Research*, *104*, 25,105–25,126, doi: 10.1029/1999JA900304.

Saur, J., F. M. Neubauer, D. F. Strobel, and M. E. Summers (2002), Interpretation of Galileo's Io plasma and field observations: I0, I24, and I27 flybys and close polar passes, *Journal of Geophysical Research (Space Physics)*, *107*, 1422, doi: 10.1029/2001JA005067.

Saur, J., B. H. Mauk, A. KaßNer, and F. M. Neubauer (2004a), A model for the azimuthal plasma velocity in Saturn's magnetosphere, *Journal of Geophysical Research (Space Physics)*, *109*, A05217, doi: 10.1029/2003JA010207.

Saur, J., F. M. Neubauer, J. E. P. Connerney, P. Zarka, and M. G. Kivelson (2004b), *Jupiter. The Planet, Satellites and Magnetosphere*, chap. Plasma interaction of Io with its plasma torus, pp. 537–560, Cambridge Univ. Press.

Saur, J., F. M. Neubauer, and N. Schilling (2007), Hemisphere coupling in Enceladus' asymmetric plasma interaction, *Journal of Geophysical Research (Space Physics)*, *112*, A11,209, doi: 10.1029/2007JA012479.

Saur, J., N. Schilling, F. M. Neubauer, D. F. Strobel, S. Simon, M. K. Dougherty, C. T. Russell, and R. T. Pappalardo (2008), Evidence for temporal variability of Enceladus' gas jets: Modeling of Cassini observations, *Geophysical Research Letters*, *35*, L20,105, doi: 10.1029/2008GL035811.

Saur, J., T. Grambusch, S. Duling, F. M. Neubauer, and S. Simon (2013), Magnetic energy fluxes in sub-Alfvénic planet star and moon planet interactions, *Astronomy and Astrophysics*, *552*, A119, doi: 10.1051/0004-6361/201118179.

Schippers, P., N. André, R. E. Johnson, M. Blanc, I. Dandouras, A. J. Coates, S. M. Krimigis, and D. T. Young (2009), Identification of photoelectron energy peaks in Saturn's inner neutral torus, *Journal of Geophysical Research (Space Physics)*, *114*, A12,212, doi: 10.1029/2009JA014368.

Schmidt, J., N. Brilliantov, F. Spahn, and S. Kempf (2008), Slow dust in Enceladus' plume from condensation and wall collisions in tiger stripe fractures, *Nature*, *451*, 685–688, doi: 10.1038/nature06491.

Schubert, G., J. D. Anderson, B. J. Travis, and J. Palguta (2007), Enceladus: Present internal structure and differentiation by early and long-term radiogenic heating, *Icarus*, *188*, 345–355, doi: 10.1016/j.icarus.2006.12.012.

Schunk, R. W., and A. F. Nagy (2009), *Ionospheres*, second edition ed., Cambridge University Press, doi: 10.1017/CBO9780511635342.

Seufert, M., J. Saur, and F. M. Neubauer (2011), Multi-frequency electromagnetic sounding of the Galilean moons, *Icarus*, *214*, 477–494, doi: 10.1016/j.icarus.2011.03.017.

Shafiq, M., J.-E. Wahlund, M. Morooka, W. Kurth, and W. Farrell (2011), Characteristics of the dust-plasma interaction near Enceladus' South Pole, *Planetary and Space Science*, *59*(1), 17 – 25, doi: 10.1016/j.pss.2010.10.006.

Shemansky, D. E., P. Matheson, D. T. Hall, H.-Y. Hu, and T. M. Tripp (1993), Detection of the hydroxyl radical in the Saturn magnetosphere, *Nature*, *363*, 329–331, doi: 10.1038/363329a0.

Shukla, P. K., and A. A. Mamun (2002), *Introduction to dusty plasma physics*, 1st edition ed., Taylor & Francis, doi: 10.1088/0741-3335/44/3/701.

Simon, S. (2007), Titan's highly variable plasma environment: a 3D hybrid simulation study, Ph.D. thesis, TU Braunschweig.

Simon, S., A. Bößwetter, T. Bagdonat, U. Motschmann, and J. Schuele (2007), Three-dimensional multispecies hybrid simulation of Titan's highly variable plasma environment, *Annales Geophysicae*, *25*(1), 117–144.

Simon, S., U. Motschmann, G. Kleindienst, K. Glassmeier, C. Bertucci, and M. K. Dougherty (2008), Titan's magnetic field signature during the Cassini T34 flyby: Comparison between hybrid simulations and MAG data, *Geophysical Research Letters*, *35*, 4107–+, doi: 10.1029/2007GL033056.

Simon, S., U. Motschmann, G. Kleindienst, J. Saur, C. L. Bertucci, M. K. Dougherty, C. S. Arridge, and A. J. Coates (2009a), Titan's plasma environment during a magnetosheath excursion: Real-time scenarios for Cassini's T32 flyby from a hybrid simulation, *Annales Geophysicae*, *27*, 669–685, doi: 10.5194/angeo-27-669-2009.

Simon, S., J. Saur, F. M. Neubauer, U. Motschmann, and M. K. Dougherty (2009b), Plasma wake of Tethys: Hybrid simulations versus Cassini MAG data, *Geophysical Research Letters*, *36*, L04,108, doi: 10.1029/2008GL036943.

Simon, S., J. Saur, F. M. Neubauer, A. Wennmacher, and M. K. Dougherty (2011a), Magnetic signatures of a tenuous atmosphere at Dione, *Geo*, *38*, L15102, doi: 10.1029/2011GL048454.

Simon, S., J. Saur, H. Kriegel, F. M. Neubauer, U. Motschmann, and M. K. Dougherty (2011b), Influence of negatively charged plume grains and hemisphere coupling currents on the structure of Enceladus' Alfvén wings: Analytical modeling of Cassini magnetometer observations, *Journal of Geophysical Research (Space Physics)*, *116*, A04221, doi: 10.1029/2010JA016338.

Simon, S., H. Kriegel, J. Saur, and A. Wennmacher (2013), Energetic aspects of Enceladus' magnetospheric interaction, *Journal of Geophysical Research (Space Physics)*, *118*, 3430–3445, doi: 10.1002/jgra.50380.

Sittler, E. C., et al. (2006), Cassini observations of Saturn's inner plasmasphere: Saturn orbit insertion results, *Planet. Space Sci.*, *54*, 1197–1210, doi: 10.1016/j.pss.2006.05.038.

Sittler, E. C., et al. (2007), Erratum to "Cassini observations of Saturn's inner plasmasphere: Saturn orbit insertion results". [Planetary and Space Science 54 (2006) 1197 1210], *Planet. Space Sci.*, *55*, 2218–2220, doi: 10.1016/j.pss.2006.11.022.

Sittler, E. C., et al. (2008), Ion and neutral sources and sinks within Saturn's inner magnetosphere: Cassini results, *Planetary and Space Science*, *56*, 3–18, doi: 10.1016/j.pss.2007.06.006.

Smith, H. T., et al. (2007), Enceladus: The likely dominant nitrogen source in Saturn's magnetosphere, *Icarus*, *188*, 356–366, doi: 10.1016/j.icarus.2006.12.007.

Smith, H. T., R. E. Johnson, M. E. Perry, D. G. Mitchell, R. L. McNutt, and D. T. Young (2010), Enceladus plume variability and the neutral gas densities in Saturn's magnetosphere, *Journal of Geophysical Research (Space Physics)*, *115*, A10,252, doi: 10.1029/2009JA015184.

Southwood, D. J., and M. G. Kivelson (1987), Magnetospheric interchange instability, *Journal of Geophysical Research (Space Physics)*, *92*, 109–116, doi: 10.1029/JA092iA01p00109.

Spahn, F., et al. (2006), Cassini Dust Measurements at Enceladus and Implications for the Origin of the E Ring, *Science*, *311*, 1416–1418, doi: 10.1126/science.1121375.

Spencer, J. R., et al. (2006), Cassini Encounters Enceladus: Background and the Discovery of a South Polar Hot Spot, *Science*, *311*, 1401–1405, doi: 10.1126/science.1121661.

Spitale, J. N., and C. C. Porco (2007), Association of the jets of Enceladus with the warmest regions on its south-polar fractures, *Nature*, *449*, 695–697, doi: 10.1038/nature06217.

Stevenson, D. J. (1982), Reducing the non-axisymmetry of a planetary dynamo and an application to Saturn, *Geophysical and Astrophysical Fluid Dynamics*, *21*, 113–127, doi: 10.1080/03091928208209008.

Stverak, S., P. M. Travnicek, K. K. Khurana, P. Hellinger, and M. K. Dougherty (2009), Interaction of Enceladus's Water Plume with Kronian Magnetosphere via Hybrid Numerical Simulations, *AGU Fall Meeting Abstracts*, p. C1639.

Tenishev, V., M. R. Combi, B. D. Teolis, and J. H. Waite (2010), An approach to numerical simulation of the gas distribution in the atmosphere of Enceladus, *Journal of Geophysical Research*, *115*, A09,302, doi: 10.1029/2009JA015223.

Teolis, B. D., M. E. Perry, B. A. Magee, J. Westlake, and J. H. Waite (2010), Detection and measurement of ice grains and gas distribution in the Enceladus plume by Cassini's Ion Neutral Mass Spectrometer, *Journal of Geophysical Research (Space Physics)*, *115*, A09,222, doi: 10.1029/2009JA015192.

Terrile, R. J., and A. F. Cook (1981), Enceladus: Evolution and Possible Relationship to Saturn's E-Ring, *LPI Contributions*, *428*, 10.

Thomas, P. C. (2010), Sizes, shapes, and derived properties of the saturnian satellites after the Cassini nominal mission, *Icarus*, *208*, 395–401, doi: 10.1016/j.icarus.2010.01.025.

Tian, F., A. I. F. Stewart, O. B. Toon, K. W. Larsen, and L. W. Esposito (2007), Monte Carlo simulations of the water vapor plumes on Enceladus, *Icarus*, *188*, 154–161, doi: 10.1016/j.icarus.2006.11.010.

Tiscareno, M. S., J. A. Burns, J. N. Cuzzi, and M. M. Hedman (2010), Cassini imaging search rules out rings around Rhea, *Geophysical Research Letters*, *37*, L14205, doi: 10.1029/2010GL043663.

Tokar, R. L., et al. (2006), The Interaction of the Atmosphere of Enceladus with Saturn's Plasma, *Science*, *311*, 1409–1412, doi: 10.1126/science.1121061.

Tokar, R. L., et al. (2008), Cassini detection of water-group pick-up ions in the Enceladus torus, *Geophysical Research Letters*, *35*, L14,202, doi: 10.1029/2008GL034749.

Tokar, R. L., R. E. Johnson, M. F. Thomsen, R. J. Wilson, D. T. Young, F. J. Crary, A. J. Coates, G. H. Jones, and C. S. Paty (2009), Cassini detection of Enceladus' cold water-group plume ionosphere, *Geophysical Research Letters*, *36*, L13,203, doi: 10.1029/2009GL038923.

Verbiscer, A., R. French, M. Showalter, and P. Helfenstein (2007), Enceladus: Cosmic Graffiti Artist Caught in the Act, *Science*, *315*, 815–, doi: 10.1126/science.1134681.

Vernisse, Y., H. Kriegel, S. Wiehle, U. Motschmann, and K.-H. Glassmeier (2013), Stellar winds and planetary bodies simulations: Lunar type interaction in super-Alfvénic and sub-Alfvénic flows, *Planetary and Space Science*, *84*, 37–47, doi: 10.1016/j.pss.2013.04.004.

Wahlund, J., et al. (2009), Detection of dusty plasma near the E-ring of Saturn, *Planet. Space Sci.*, *57*, 1795–1806, doi: 10.1016/j.pss.2009.03.011.

Wahlund, J.-E., et al. (2005), The inner magnetosphere of Saturn: Cassini RPWS cold plasma results from the first encounter, *Geophysical Research Letters*, *32*, L20S09, doi: 10.1029/2005GL022699.

Waite, J. H., et al. (2006), Cassini Ion and Neutral Mass Spectrometer: Enceladus Plume Composition and Structure, *Science*, *311*, 1419–1422, doi: 10.1126/science.1121290.

Waite, J. H., Jr., et al. (2009), Liquid water on Enceladus from observations of ammonia and 40Ar in the plume, *Nature*, *460*, 487–490, doi: 10.1038/nature08153.

Wang, Y.-C. (2012), Solar wind interaction with mercury's magnetosphere and its surface-bounded exosphere, Ph.D. thesis, Institute of Astronomy, National Central University.

Wiehle, S., et al. (2011), First lunar wake passage of ARTEMIS: Discrimination of wake effects and solar wind fluctuations by 3D hybrid simulations, *Planet. Space Sci.*, *59*, 661–671, doi: 10.1016/j.pss.2011.01.012.

Wilson, R. J., R. L. Tokar, and M. G. Henderson (2009), Thermal ion flow in Saturn's inner magnetosphere measured by the Cassini plasma spectrometer: A signature of the Enceladus torus?, *Geophysical Research Letters*, *36*(23), L23,104, doi: 10.1029/2009GL040225.

Wilson, R. J., R. L. Tokar, W. S. Kurth, and A. M. Persoon (2010), Properties of the thermal ion plasma near Rhea as measured by the Cassini plasma spectrometer, *Journal of Geophysical Research (Space Physics)*, *115*, A05201, doi: 10.1029/2009JA014679.

Winske, D., L. Yin, N. Omidi, H. Karimabadi, and K. Quest (2003), Hybrid simulation codes: Past, present and future – a tutorial, in *Space Plasma Simulation*, *Lecture Notes in Physics*, vol. 615, edited by J. Büchner, M. Scholer, and C. Dum, pp. 136–165, Springer Berlin / Heidelberg, doi: 10.1007/3-540-36530-3_8.

Wolf-Gladrow, D. A., F. M. Neubauer, and M. Lussem (1987), Io's interaction with the plasma torus - A self-consistent model, *Journal of Geophysical Research (Space Physics)*, *92*, 9949–9961, doi: 10.1029/JA092iA09p09949.

Yaroshenko, V. V., S. Ratynskaia, J. Olson, N. Brenning, J. Wahlund, M. Morooka, W. S. Kurth, D. A. Gurnett, and G. E. Morfill (2009), Characteristics of charged dust inferred from the Cassini RPWS measurements in the vicinity of Enceladus, *Planet. Space Sci.*, *57*, 1807–1812, doi: 10.1016/j.pss.2009.03.002.

Young, D. T., et al. (2005), Composition and Dynamics of Plasma in Saturn's Magnetosphere, *Science*, *307*, 1262–1266, doi: 10.1126/science.1106151.

Zarka, P., and W. Kurth (2005), Radio wave emission from the outer planets before cassini, *Space Science Reviews*, *116*, 371–397, 10.1007/s11214-005-1962-2.

Danksagung

Ich möchte mich vor allem bei Professor Dr. Uwe Motschmann bedanken, der diese Arbeit als Mentor betreut hat. Insbesondere möchte ich mich für die große inhaltliche und vor allem zeitliche Freiheit, die er mir bei der Bearbeitung meines Themas gelassen hat, bedanken. Sein Vertrauen ermöglichte mir außerdem, bereits in meiner Diplomarbeit Einblicke in Enceladus' Plasmawechselwirkung zu gewinnen. Die Selbstverständlichkeit mit der ich zu den diversen Tagungen fahren durfte sei hier ebenfalls dankend erwähnt. Zudem war es mir immer eine große Freude, seine exzellenten Vorlesungen zur theoretischen Physik als Übungsassistent zu begleiten. Auch bei der gemeinsamen Betreuung von insgesamt sieben Bachelorarbeiten habe ich viel gelernt.

Ich möchte mich weiterhin bei Professor Dr. Joachim Saur dafür bedanken, dass er diese Arbeit als Zweitgutachter betreut hat. In vielen Diskussionen und Kommentaren profitierte ich von seinem umfangreichem Wissen und seinen scharfsinnigen Analysen. Jeder Besuch in Köln gestaltete sich somit extrem lehrreich, sodass ich immer mit neuen Ideen im Gepäck zurück nach Braunschweig fahren konnte. Nebenbei wurde ich auch in die Kölner Arbeitsgruppe adoptiert, so dass ich sogar beim Sieg im Schwinger-Cup dabei war.

Nicht genug danken kann ich PD Dr. Sven Simon. Mit riesengroßer Begeisterung ("Findest du das nicht auch so spannend?") beantwortete er meine zahlreichen Fragen meist bereits nach wenigen Minuten und mit unermüdlichem Eifer widmete er sich dem Korrekturlesen unserer gemeinsamen Artikel sowie dieser Arbeit. Hierdurch habe ich unglaublich viel gelernt. Außerdem sei dankend erwähnt, dass es selbstverständlich wurde, bei meinen Besuchen in Köln Svens Gastfreundschaft in Anspruch zu nehmen. Unsere vielen gemeinsamen Dienstreisen werden zudem immer unvergessliche Erlebnisse bleiben.

Des Weiteren danke ich meinen Kollegen an unseren beiden Theorie-Instituten für die schöne Zeit in der AG NPS. Besonderer Dank geht an Benedikt Probst, der mit seinem Einsatz für den Kaffee-Vollautomaten sorgte, und das ein oder andere Kicker-Spielchen. Cornelia Schmidt danke ich für die morgendlichen Pausen-Gespräche. Auch bei "meinen" Bacheloranden möchte ich mich für die gute Zusammenarbeit bedanken, vor allem bei dem Olfrat sowie Hendrik Ranocha und Willi Fröhlke. Außerdem bedanke ich mich bei meinen Freunden aus dem IGEP dafür, dass ich – obwohl ich aufgrund des Pendelns zwischen Salzgitter und Braunschweig viel zu selten dabei war – immer sofort in die Gruppe integriert wurde. Vor allem Eike Beitz wurde nie müde mich zu den vielen Aktivitäten einzuladen. Christoph Koenders danke ich weiterhin für unsere fast täglichen Gespräche – einschließlich des gemeinsamen Ärgerns über abstürzende Simulationen. Und natürlich danke ich allen Ski-Boardern für die tollen Urlaube.

Nicht zuletzt danke ich auch meiner Freundin Stephanie für die bedingungslose Unterstützung während der letzten fünf Jahre und ihre liebevolle Geduld mit mir, wenn ich mit meinen Gedanken mehr bei meinen Simulationen und meiner Doktorarbeit war.